GL-TR-89-0124(III)
Report PSI-9032/TR-901

CANOES II: DYNAMICS OF ATMOSPHERIC INFRARED THERMOCHEMICAL EXCITATION

W.T. Rawlins
L.G. Piper
M.E. Fraser
H.C. Murphy
T.R. Tucker
A. Gelb

Physical Sciences Inc.
Research Park
P.O. Box 3100
Andover, MA 01810

March 1989

Final Report
24 March 1985 - 24 May 1989

GEOPHYSICS LABORATORY
AIR FORCE SYSTEMS COMMAND
UNITED STATES AIR FORCE
HANSCOM AIR FORCE BASE, MA 01731-5000

"This technical report has been reviewed and is approved for publication"

(Signature)
STEVEN M. MILLER
Contract Manager

(Signature)
William A.M. Blumberg
Branch Chief, Acting

FOR THE COMMANDER

(Signature)
R. EARL GOOD
Director

This report has been reviewed by the ESD Public Affairs Office (PA) and is releasable to the National Technical Information Service (NTIS).

Qualified requestors may obtain additional copies from the Defense Technical Information Center. All others should apply to the National Technical Information Service.

If your address has changed, or if you wish to be removed from the mailing list, or if the addressee is no longer employed by your organization, please notify AFGL/DAA, Hanscom AFB, MA 01731. This will assist us in maintaining a current mailing list.

Do not return copies of this report unless contractual obligations or notices on a specific document requires that it be returned.

REPORT DOCUMENTATION PAGE

1a. REPORT SECURITY CLASSIFICATION UNCLASSIFIED	1b. RESTRICTIVE MARKINGS N/A since unclassified
2a. SECURITY CLASSIFICATION AUTHORITY N/A since unclassified	3. DISTRIBUTION / AVAILABILITY OF REPORT Approved for public release; distribution unlimited
2b. DECLASSIFICATION / DOWNGRADING SCHEDULE N/A since unclassified	
4. PERFORMING ORGANIZATION REPORT NUMBER(S) PSI-9032/TR-901 (Volume III)	5. MONITORING ORGANIZATION REPORT NUMBER(S) GL-TR-89-0124 (III)
6a. NAME OF PERFORMING ORGANIZATION Physical Sciences Inc. 6b. OFFICE SYMBOL (If applicable)	7a. NAME OF MONITORING ORGANIZATION Geophysics Laboratory
6c. ADDRESS (City, State, and ZIP Code) Research Park, P.O. Box 3100 Andover, MA 01810	7b. ADDRESS (City, State, and ZIP Code) Hanscom Air Force Base, MA 01731-5000
8a. NAME OF FUNDING / SPONSORING ORGANIZATION GL 8b. OFFICE SYMBOL (If applicable)	9. PROCUREMENT INSTRUMENT IDENTIFICATION NUMBER F19628-85-C-0032
8c. ADDRESS (City, State, and ZIP Code) Hanscom Air Force Base, MA 01731-5000	10. SOURCE OF FUNDING NUMBERS PROGRAM ELEMENT NO. 61102F; PROJECT NO. 2310; TASK NO. G4; WORK UNIT ACCESSION NO. BJ

11. TITLE (Include Security Classification)
CANOES II: Dynamics of Atmospheric Infrared Thermochemical Excitation

12. PERSONAL AUTHOR(S) Rawlins, Wilson T.; Piper, Lawrence G.; Fraser, Mark E.; Murphy, Henry C.; Tucker, Thomas P.; and Gelb, A.

13a. TYPE OF REPORT	13b. TIME COVERED	14. DATE OF REPORT (Year, Month, Day)	15. PAGE COUNT
Final	FROM 850324 TO 890524	1989 March	256

16. SUPPLEMENTARY NOTATION Volume I: pages 1-92; Volume II: pages 93-372; Volume III: pages 373-624; Volume IV: pages 625-862

17. COSATI CODES		
FIELD	GROUP	SUB-GROUP

18. SUBJECT TERMS (Continue on reverse if necessary and identify by block number)
Infrared emission, Oxygen, Nitrogen, Nitric oxide, Ozone, Molecular dynamics, Vibrational excitation, Atmospheric background

19. ABSTRACT (Continue on reverse if necessary and identify by block number)

In the electron disturbed upper atmosphere, electronically excited metastable forms of oxygen and nitrogen are formed by electron impact processes. These species dissipate their energy into the atmosphere largely by collisional quenching and chemical reaction. Specific species and reactions of interest include: (1) electronically and/or vibrationally excited nitrogen, N_2^*, its spectroscopy, energy pooling and interactions with O, O_2 and trace, infrared-active atmospheric species such as CO, CO_2, and N_2O; (2) metastable atomic nitrogen, $N(^2D, ^2P)$, reaction kinetics and product branching ratios in interactions with the above atmospheric species; (3) various metastable states of O_2, O_2^*, and their potential as auroral precursors of infrared radiation

20. DISTRIBUTION / AVAILABILITY OF ABSTRACT ☒ UNCLASSIFIED/UNLIMITED ☐ SAME AS RPT ☐ OTIC USERS	21. ABSTRACT SECURITY CLASSIFICATION UNCLASSIFIED/UNLIMITED
22a. NAME OF RESPONSIBLE INDIVIDUAL Steven Miller	22b. TELEPHONE (Include Area Code) / 22c. OFFICE SYMBOL CL/OPI

DD FORM 1473, 84 MAR 83 APR edition may be used until exhausted. All other editions are obsolete.

19. ABSTRACT (Continued)

from other atmospheric species; and 4) the role of metastable-metastable O_2/N_2 interactions as potential sources for non-linear infrared effects which might occur in strong aurorae. This document reports on the results from a four-year coupled experimental program using the COCHISE and FAKIR facilities to investigate these issues in fundamental detail.

CONTENTS

APPENDIX J

(SR-407 reproduced in its entirety)

To be submitted to Applied Spectroscopy

PSI-9032/
SR-407

PRODUCTION OF $N_2(A^3\Sigma_u^+)$ IN THE DIELECTRIC BARRIER (OZONIZER) DISCHARGE

William P. Cummings and Lawrence G. Piper

Physical Sciences Inc.
Research Park, P.O. Box 3100
Andover, MA 01810-7100

To be submitted to Applied Spectroscopy

April 1989

ABSTRACT

Several reports in the literature imply extremely large number densities of metastable nitrogen molecules can be found in the effluents of dielectric-barrier or ozonizer discharges in flowing nitrogen. We have constructed a dielectric-barrier discharge which operates at 1 to 10 kV in flowing nitrogen or mixtures of nitrogen in either argon or helium at total pressures between 0.3 and 6 Torr. Spectroscopic observations in the afterglow of this discharge indicate that virtually all observed excitation between 200 and 850 nm results from discharge streamers. All emissions are quenched upon adding a grounded loop down stream from the discharge. The absence of NO Gamma-band emission when NO is added downstream from the grounded loop indicates that $N_2(A)$ number densities in the afterglow are below 10^5 molecules cm^{-3}, some ten orders of magnitude below previous estimates.

I. INTRODUCTION

The dielectric-barrier (ozonizer) discharge is a high voltage ac discharge. A number of groups have investigated the afterglow of dielectric-barrier discharges through flowing nitrogen for application to spectroscopy[1-4] and trace analysis.[5-12] They have reported strong nitrogen second-positive emission ($N_2(C^3\Pi_u) \rightarrow N_2(B^3\Pi_g)$) even at times as long as 100 ms downstream from the discharge. Since the radiative lifetime of $N_2(C^3\Pi_u)$ is 37 ns,[13] these results suggest that $N_2(C^3\Pi_u)$ is being produced somehow in the discharge afterglow. Ung[4] postulated that the strong second-positive emission resulted from energy pooling reactions of $N_2(A^3\Sigma_u^+)$ either with itself or with highly vibrationally excited, ground-electronic state nitrogen:

$$2N_2(A^3\Sigma_u^+) \rightarrow N_2(C^3\Pi_u) + N_2(X^1\Sigma_g^+) \qquad (1)$$

$$N_2(A^3\Sigma_u^+) + N_2(X^1\Sigma_g^+, v' > 20) \rightarrow N_2(C^3\Pi_u) + N_2(X^1\Sigma_g^+) \quad . \qquad (2)$$

Dodge and Allen,[6] noting the fall off from linearity of atomic zinc emissions as a function of added [Zn] estimated $N_2(A)$ number densities to be 10^{15} molecules cm^{-3} or about five to six orders of magnitude greater than is produced by microwave[14] or hollow-cathode[15] discharges. Jurgensen and Winefordner have estimated similarly large $N_2(A)$ number densities, 10^{16} molecules cm^{-3}.

Intrigued by these reports of large $N_2(A)$ number densities, we undertook a spectroscopic study of the dielectric-barrier discharge afterglow in order to determine number densities of metastable nitrogen quantitatively. Our procedure involves determining absolute photon emission rates of various spectroscopic features. In situ calibration of our detection system relies on observations of the air afterglow chemiluminescence under carefully controlled conditions. The absolute photon yields of this reaction at visible wavelengths are well established.[17-20]

II. EXPERIMENTAL

A. Apparatus

The afterglow of the discharge was monitored as it passed through a 1 in. diameter glass flow-tube with quartz windows at various points along its length (see Fig. 1). A wire loop was inserted through a 1/4 in. port at the entrance to the flow-tube. The loop was grounded through a 1 kΩ resistor and served as a groundpoint to ensure the discharge did not extend into the observation region. A Sargent-Welch No. 1402 (160 lpm) mechanical pump exhausted the flow tube, maintaining flow velocities on the order to 300 cm/s^{-1}.

Nitrogen flow rates ranged from 20 to 200 $\mu moles^{-1}$ and total pressures varied between 0.5 and 6 Torr. Most spectra were taken 28 cm (~ 100 ms) downstream from the discharge terminus. These conditions were picked to reproduce those of Dodge and Allen[6] and of Jurgensen and Winefordner.[12]

The discharge, which is based on Dodge and Allen's design,[6] consists of two coaxial glass tubes which form a 2.8 mm annulus (see Figure 2). One electrode is formed by pinching off the bottom of the inner tube, filling it with saturated NaCl solution and immersing a wire from the power supply in the solution. The second electrode is made by wrapping copper foil tape around the outer tube. The electrodes form a discharge region that is 30 cm long.

The ac power supply used with the discharge consisted of a 15 kV neon sign transformer (center tap of secondary grounded) with a variac in the primary circuit to control the output voltage. To reduce interference with nearby electronics, only half of the transformer secondary was used during most of our work. Two 100 kΩ power resistors, placed in the secondary, limited the current.

Spectra were taken using a Spex No. 1269, 1.26m, monochromator (1 to 3 mm slits) and a Hamamatsu No. R955 photomultiplier tube. The photomultiplier tube

was cooled to -40°C and operated at a gain of 1.7×10^6. The output of the photomultiplier tube was measured using a Keithley No. 417 picoameter which fed into a Soltec No. 1242 strip chart recorder.

B. Photometric Calibrations

Calibrating the apparatus for absolute photon emission rates was done in two steps. First, the relative response function (R_λ) of the monochromator was measured using an ultraviolet irradiance standard between 200 and 400 nm and the relative intensities of the continuum produced by the O/NO air afterglow reaction between 400 and 800 nm (reaction (3)).[17-20] This relative response function corrects for wavelength variations in detector efficiency and the transmission of the optical system. Second, the absolute response at 580 nm was measured using the O/NO air afterglow titration.

When oxygen atoms and nitric oxide are mixed, the following reaction acts to produce a continuum that extends from 375 nm to beyond 3000 nm:

$$O + NO \rightarrow NO_2^* + M \qquad (3a)$$

$$NO_2^* \rightarrow NO_2 + h\nu \text{ (a continuum)} \quad . \qquad (3b)$$

The intensity of the emission is

$$I_\lambda^{O/NO} = k_\lambda [O][NO]\Delta\lambda \quad , \qquad (4)$$

where k_λ is the air afterglow rate coefficient ($k_\lambda = 1.25 \times 10^{-19}$ photon cm^{-3} s^{-1} nm^{-1} at 580 nm)[17] and $\Delta\lambda$ is the monochromator bandwidth. Measuring the air afterglow intensity at a fixed wavelength under conditions of known [O] and [NO] place the relative response function on an absolute basis.

In the titration known number densities of O atoms are formed by mixing NO with a constant flow of N atoms. The N atoms are produced by passing nitrogen gas through a microwave discharge. The NO quantitatively converts the N to O through reaction (5),[21]

$$N + NO \rightarrow O + N_2 \quad . \tag{5}$$

Well below the titration point N_2 first-positive emission is observed from the recombination of N atoms:

$$N + N + M \rightarrow N_2(B^3\Pi_g) + M \quad , \tag{6}$$

$$N_2(B^3\Pi_g) \rightarrow N_2(A^3\Sigma_u^+) + h\nu \text{ (first positive)} \quad . \tag{7}$$

As more NO is added the intensity of the first-positive emission drops. At the titration point no emission from the flow is observed and the O-atom number density is equal to the initial N-atom number density. As still more NO is added, the O/NO air afterglow is observed and its intensity varies linearly with the number density of NO added:

$$I_\lambda^{O/NO} = \kappa[N]_o ([NO]-[N]_o) \quad , \tag{8}$$

where subscript o refers to N-atom number density determined from the titration and point. Equation (8) shows that κ will be determined by the ratio of the square of the slope to the intercept of the line determined by the variation in intensity of the air afterglow as a function of added NO number density.

Combining Eqs. (4) and (8) converts the observed intensities (in nA) to absolute photon emission rates:

$$I_{true} = I_{obs} k_{580} \Delta\lambda R_{580}/(\kappa R_{\lambda obs}) \quad . \tag{9}$$

Where I_{obs} is the total integrated band intensity of the spectral feature of interest.

The air afterglow intensities must be corrected for the slow removal of O atoms in the following reactions:

$$O + NO + M \rightarrow NO_2 + M \ (k = 7 \times 10^{-31} \text{ cm}^6 \text{ molecules}^{-2}\text{s}),^{22} \quad (10)$$

and

$$NO_2 + O \rightarrow NO + O_2 \ (k = 9.5 \times 10^{-12} \text{ cm}^3 \text{ molecule}^{-1} \text{ s}^{-1},^{22} \quad (11)$$

where k is the rate coefficient of the corresponding reaction.

III. RESULTS

A. General Observations

Figures 3 and 4 show typical spectra in the afterglow region with the loop floating and with it grounded. The second-positive bands ($N_2(C^3\Pi_u) \rightarrow N_2(B^3\Pi_g)$) were by far the strongest system. Other observed systems included the first-positive system ($N_2(B^3\Pi_g) \rightarrow N_2(A^3\Sigma_u^+)$, N_2^+ first-negative bands at 391 and 428 nm ($v',v'' = 0, 0$ and $0, 1$ of $N_2^+(B^2\Sigma_u^+) \rightarrow N_2^+(X^2\Sigma_u^+)$), and a relatively weak NOγ system ($NO(A^2\Sigma^+) \rightarrow NO(X^2\Pi)$). The presence of the NOγ bands - caused mostly by trace oxygen in the nitrogen - made it impossible to detect the Vegard-Kaplan bands that would have signaled the presence of $N_2(A)$ in the discharge effluent. The output of the discharge was observed for pressures ranging from 0.3 to 6 torr and supply voltages from 1 to 10 kV. The observed intensities were roughly proportional to the voltage but pressure seemed to have the most effect on the discharge output. At higher pressures the output was a purple-pink color. The flow was also very unsteady in appearance. At 0.3 torr the discharge output was bright pink and uniform. At lower pressures the intensities of the first- and second-positive systems were greater than at high pressures and a few bands in each system emitted nearly all of the signal.

With the loop grounded the afterglow was non-existent downstream from the groundpoint. Spectra taken under these conditions showed nothing except scattered light - as was verified when the flow tube was modified to position the ground point upstream from the light trap.

Measurements of the current flowing out of the groundpoint were made by monitoring the voltage drop across a 1 kΩ resistor between the groundpoint and ground. At 6 torr the current was about 60 mA (with 5400V across the discharge). At lower pressures the figure rose to around 400 mA.

B. Estimate of $N_2(A)$ Number Density

We looked for the excitation of NO(A) by $N_2(A)$ to determine if $N_2(A)$ were present in the afterglow:

$$N_2(A) + NO \rightarrow NO(A^2\Sigma^+) + N_2(X^1\Sigma_g^+) \quad , \tag{12}$$

$$NO(A^2\Sigma^+) \rightarrow NO(X^2\Pi) + h\nu \ (\gamma \text{ bands}) \quad . \tag{13}$$

The differential equation governing the number density of $NO(A^2\Sigma^+)$ is

$$\frac{d[NO(A)]}{dt} = k_{ex}\,[N_2(A)][NO] - k_{rad}\,[NO(A)] \quad . \tag{14}$$

k_{ex} (7×10^{-11} cm^3 $molecule^{-1}$ s^{-1})[23] is the excitation rate coefficient and k_{rad} is the radiative decay rate.[24] NO(A) is in steady state in our reactor because the radiative lifetime of NO(A) is short (~ 200 ns) compared to the time the gas resides within the monochromator field of view (~ 1 ms). This means that

$$I_{NO(A)} = k_{rad}\,[NO(A)] = k_{ex}\,[N_2(A)][NO] \tag{15}$$

so

$$[N_2(A)] = \frac{1}{k_{ex}} \frac{dI_{NO(A)}}{d[NO]} \quad . \tag{16}$$

We looked for emission from the 0,1 γ-band at 235 nm when we added NO to the reactor. We could detect no changes in emission intensity as the NO number density was increased to 10^{14} molecules cm^{-3}. We estimate a minimum detectable signal increase of 2×10^{-3} nA which when converted for absolute system response corresponds to an absolute photon emission rate of 1.6×10^9 photons cm^{-3} s^{-1}. Using this value in Eq. (16) along with the NO number density and k_{ex} implies an upper limit to the $N_2(A)$ number density of 2.3×10^5 molecules cm^{-3}. This number is some ten orders of magnitude below previous estimates which were based upon more indirect evidence.

IV. DISCUSSION

The facts of the discharge afterglow's terminating at the groundpoint, the relatively large electron currents observed at the ground point, and the lack of measurable $N_2(A)$ in the afterglow, suggest that the afterglow is actually an extension of the discharge. The $N_2(C^3\Pi_u)$ observed by others and by us in the afterglow region when the loop is ungrounded is continuously formed by electron impact excitation of N_2 by discharge streamers rather than by energy-pooling reactions such as (1) and (2). This fact does not negate the usefulness of the dielectric-barrier discharge as a tool for exciting analytically useful spectra. Useful spectra clearly are excited. The mechanism of this excitation, however, is different from what has been proposed.

The lack of $N_2(A)$ under the conditions employed actually is not particularly surprising. $N_2(A)$ is well known to be quenched with unit efficiency in collisions with reactor walls.[15] In order to transport $N_2(A)$ for any appreciable distance, therefore, one must work either at quite high pressure and, thereby slow diffusion to the reactor walls, or else one's observations must be made only a few milliseconds downstream from the discharge.

Noxon[3] was successful in detecting $N_2(A)$ in the afterglow of a dielectric-barrier discharge. He worked at pressures on the order of an atmosphere and could observe Vegard-Kaplan emission in the afterglow for times on the order of a second. Rice et al.'s[11] configuration for exciting analyte spectra in the afterglow of a dielectric-barrier discharge also employs pressures on the order of an atmosphere and, in addition, quite high nitrogen flow rates. Although they do not report having observed Vegard-Kaplan emission, their conditions should be favorable for the presence of $N_2(A)$ in the afterglow. One sign that $N_2(A)$ is likely to be in their afterglow is their observation of atomic oxygen emission at 557.7 nm. This emission is excited in the energy-transfer reaction between $N_2(A)$ and O atoms.[25]

We moved our dielectric-barrier discharge to a 2 in. diameter flow reactor which has significantly enhanced pumping capabilities[23] to see if $N_2(A)$ would indeed persist in the discharge afterglow. We observed Vegard-Kaplan emission quite readily upon discharging mixtures of nitrogen in argon at pressures on the order of 5 to 10 Torr and times on the order of 10 ms downstream from the grounded loop. Absolute photometric observations of Vegard-Kaplan emission established the $N_2(A)$ number densities in the observation region to be about 10^{10} molecules cm^{-3}. This number density is comparable to what is produced by other laboratory sources. The dielectric-barrier discharges therefore, does not seem to offer significant advantages over other discharge-flow methods of $N_2(A)$ generation. Its one advantage appears to be the ability to generate $N_2(A)$ at pressures on the order of an atmosphere.

V. SUMMARY AND CONCLUSIONS

The dielectric-barrier discharge, as commonly configured for analytical applications, is not a source of $N_2(A)$ for analytically useful spectra. Rather, the spectra are excited by direct electron impact by discharge streamers. When configured for atmospheric pressure operation with short transit times between the discharge and the observation region, $N_2(A)$ energy-transfer reactions may indeed provide the primary excitation source. This high pressure configuration might be preferred if the discharge source is to be used is a gas chromatograph detector. The dielectric-barrier discharge provides no advantages over other common laboratory sources when used to generate $N_2(A)$ to study energy-transfer reactions unless one wants to study these reactions at high pressures.

ACKNOWLEDGEMENTS

We appreciate funding from the Air Force Geophysics Laboratories under Contract F19628-85-C-0032, sponsored by Air Force Office of Scientific Research under Task 2310G4 and by Defense Nuclear Agency under Project SA, Task SA/SDI, Work Unit 00175. Discussions with and encouragement from George Caledonia of PSI were particularly beneficial.

REFERENCES

1. O.R. Wulf and E.H. Melvin, Phys. Rev. 55, 687 (1939).
2. J. Janin, Ann. Phys. (Paris) 1, 538 (1946).
3. J.F. Noxon, J. Chem. Phys. 36, 926 (1962).
4. A. Y-M. Ung, Chem. Phys. Lett. 32, 193 (1975).
5. A.P. D'Silva, G.W. Rice, and V.A. Fassel, Appl. Spectrosc. 34, 578 (1980).
6. W.B. Dodge, III and R.A. Allen, Anal. Chem. 53, 1279 (1981).
7. T.M. Neimczyk and H.C. Na, Appl. Spectrosc. Revs. 19, 363 (1983).
8. J. Kishman, E. Barish, and R. Allen, Appl. Spectrosc. 37, 545 (1983).
9. G.W. Rice, A.P. D'Silva, and V.A. Fassel, Appl. Spectrosc. 38, 149 (1984).
10. G.W. Rice, A.P. D'Silva, and V.A. Fassel, Appl. Spectrosc. 39, 554 (1985).
11. G.W. Rice, J.J. Richard, A.P. D'Silva, and V.A. Fassel, Anal. Chem. 53, 1519 (1981).
12. H.A. Jurgensen, T. Yu, and J.D. Winefordner, Can. J. Spectrosc. 29, 113 (1984).
13. A. Lofthus and P.H. Krupenie, J. Phys. Chem. Ref. Data 6, 113 (1977).
14. J.A. Meyer, D.W. Setser, and W.G. Clark, J. Phys. Chem. 76, 1 (1972).
15. J.A. Meyer, D.H. Klosterboer, and D.W. Setser, J. Chem. Phys. 55, 2084 (1971).
16. H. Jurgensen and J.D. Winefordner, Talanta 31, 777 (1984).
17. A. Fontijn, C.B. Meyer, and H.I. Schiff, J. Chem. Phys. 40, 64 (1964).
18. D. Golomb and J.H. Brown, J. Chem. Phys. 63, 5246 (1975).
19. A.M. Pravilov and L.G. Smirnova, Kinet. Catal. 19, 902 (1978).
20. M. Sutoh, Y. Morioka, and M. Nakamura, J. Chem. Phys. 72, 20 (1980).
21. F. Kaufman and J.R. Kelso, 7th Int. Comb. Symp. 53 (1958).
22. D.L. Balch, D.D. Drysdale, D.G. Horn, and A.C. Loyd, Evaluated Kinetic Data for High Temperature Reaction II, London: Butterworths (1973).

23. L.G. Piper, L.M. Cowles, and W.T. Rawlins, J. Chem. Phys. 85, 3369 (1986).

24. L.G. Piper and L.M. Cowles, J. Chem. Phys. 85, 2419 (1986).

25. L.G. Piper, J. Chem. Phys. 77, 2373 (1982).

FIGURE CAPTIONS

1. Schematic diagram of apparatus used to study dielectric-barrier discharge afterglows.

2. Details of dielectric-barrier discharge.

3. Spectrum of afterglow between 300 and 450 nm with the loop flotaing and with it grounded. The spectrum has not been corrected for variations in monochromator response with wavelength.

4. Spectrum of afterglow between 550 and 800 nm with the loop floating and with it grounded. The spectrum has not been corrected for variations monochromator response with wavelength.

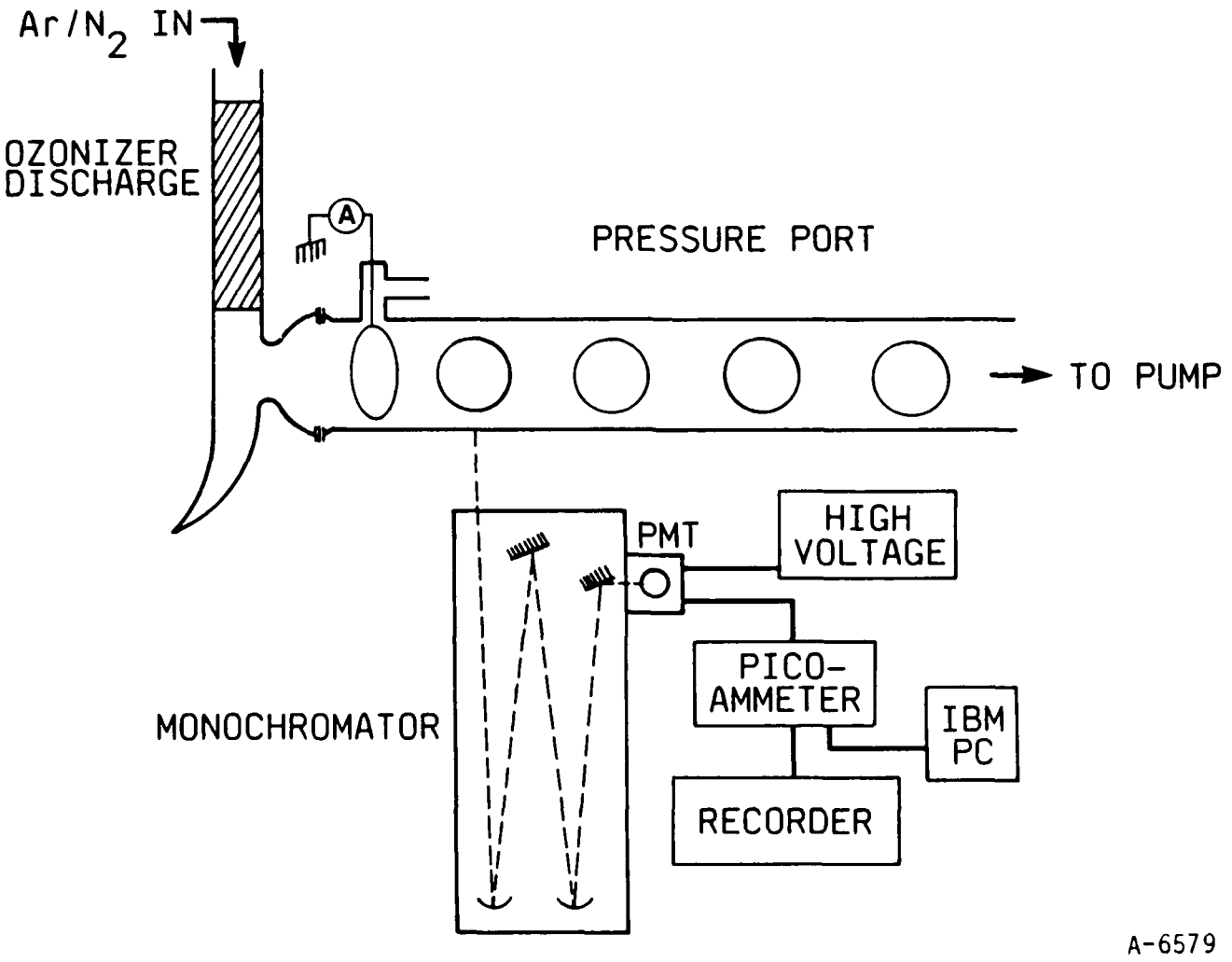
Ar/N2 IN
OZONIZER DISCHARGE
A
PRESSURE PORT
TO PUMP
PMT
HIGH VOLTAGE
PICO-AMMETER
IBM PC
MONOCHROMATOR
RECORDER
A-6579

Figure 1

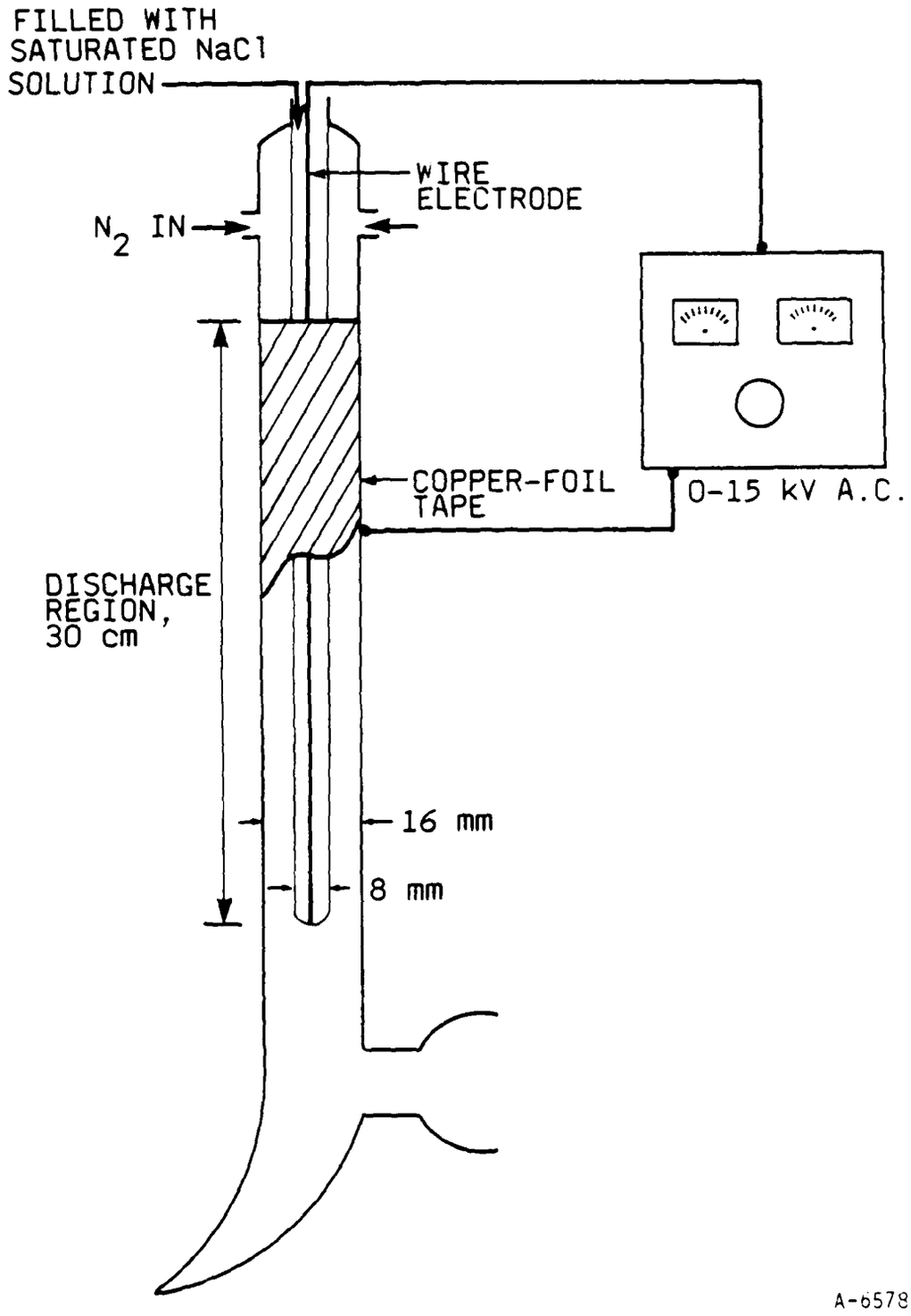
FILLED WITH
SATURATED NaCl
SOLUTION
WIRE
ELECTRODE
N_2 IN
COPPER-FOIL
TAPE
0-15 kV A.C.
DISCHARGE
REGION,
30 cm
16 mm
8 mm
A-6578

Figure 2

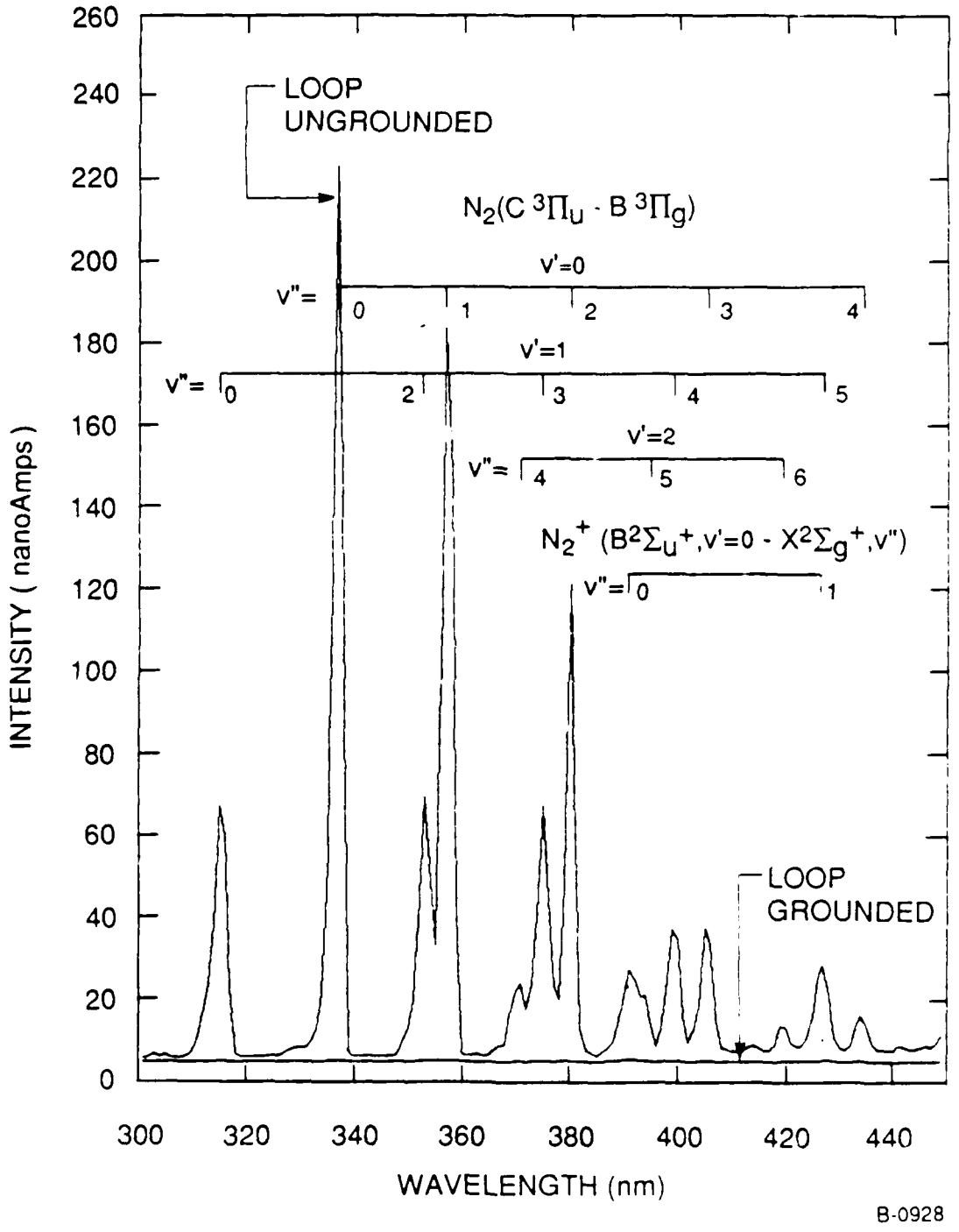
LOOP
UNGROUNDED
$N_2(C\ ^3\Pi_u - B\ ^3\Pi_g)$
v'=0
v"=
0
1
2
3
4
v'=1
v"=
0
2
3
4
5
v'=2
v"=
4
5
6
N_2^+ $(B^2\Sigma_u^+, v'=0 - X^2\Sigma_g^+, v")$
v"=
0
1
LOOP
GROUNDED
INTENSITY (nanoAmps)
260
240
220
200
180
160
140
120
100
80
60
40
20
0
300
320
340
360
380
400
420
440
WAVELENGTH (nm)
B-0928

Figure 3

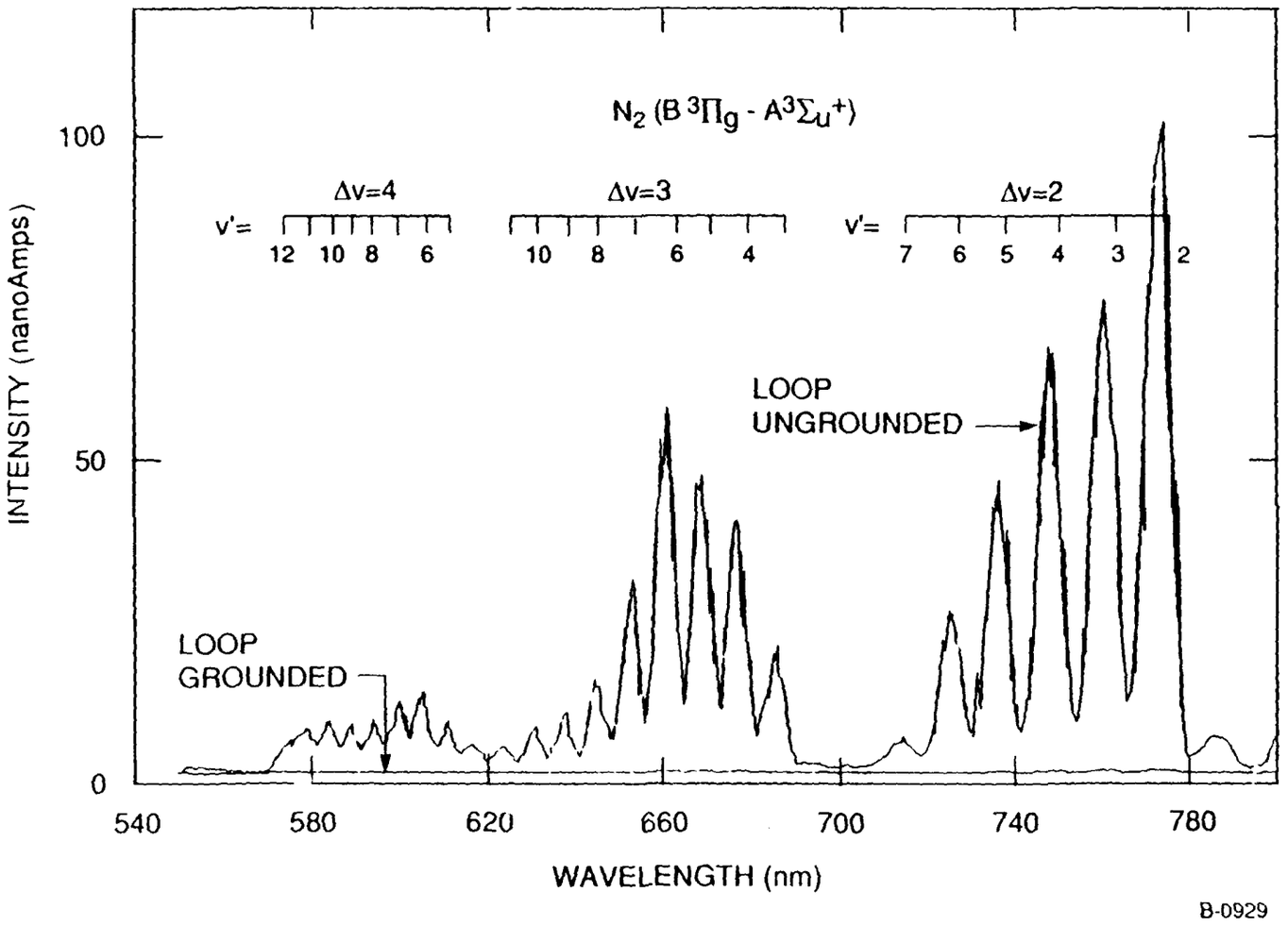
N2 (B 3Πg - A3Σu+)
Δv=4
Δv=3
Δv=2
v'=
12 10 8 6
10 8 6 4
v'=
7 6 5 4 3 2
LOOP
UNGROUNDED
LOOP
GROUNDED
INTENSITY (nanoAmps)
100
50
0
540 580 620 660 700 740 780
WAVELENGTH (nm)
B-0929

Figure 4

APPENDIX K

(SR-324 reproduced in its entirety)

J. Chem. Phys. 89, 2918 (1988)

PSI-9076/
SR-324

DETERMINATION OF NON-BOLTZMANN VIBRATIONAL DISTRIBUTIONS OF $N_2(X,V")$ IN He/N_2 MICROWAVE-DISCHARGE AFTERGLOWS

Lawrence G. Piper

and

William J. Marinelli

Physical Sciences Inc.
Research Park, P.O. Box 3100
Andover, MA 01810

J. Chem. Phys. 89, 2918 (1988)

ABSTRACT

We have extended a technique for studying the vibrational distributions of ground-electronic-state, molecular nitrogen in the afterglow of a microwave discharge through mixtures of helium and nitrogen. The technique is based upon adding metastable helium atoms to the afterglow. The He* (2^3S) excites the $N_2(X,v)$ to $N_2^+(B,^2\Sigma_u^+)$ in a Penning-ionization reaction. Since Penning ionization is a Franck-Condon process, the vibrational distribution of the $N_2^+(B)$ product is determined by that of the $N_2(X,v)$ from which it was produced. The measurements show that the ground-state nitrogen distribution is highly non-Boltzmann, with vibrationally hotter distributions being produced with lower mole fractions of nitrogen in the discharge. We have also observed the production of $N_2^+(C^2\Sigma_u^+)$ from He* Penning ionization of molecular nitrogen. This process is energetically allowed only if the vibrational energy in the ground-electronic-state nitrogen exceeds 3.8 eV or 15 vibrational quanta.

I. Introduction

Our recent observations in discharged nitrogen afterglows showed that $IF(B^3\Pi_{0^+})$[1] and $N_2(B^3\Pi_g)$[1,2] excitation appeared to result from V-E transfer rather than the more conventional E-E transfer from one electronically excited species to another. To investigate these processes more fully, we needed to develop a diagnostic for $N_2(v)$. This report details our development of an $N_2(X,v)$ diagnostic based upon Penning ionization by metastable helium atoms.

Vibration-to-electronic transfer processes, if efficient, could have important implications for chemical laser development as well as for the modeling of disturbed atmospheres because, unlike the lowest electronically excited nitrogen metastable, $N_2(A,^3\Sigma_u^+)$[3], $N_2(v)$ does not destroy itself efficiently in collisions. Indeed, quite high levels of vibrational excitation can be achieved by V-V up-pumping[4-7]. Thus $N_2(v)$ might act as an energy storage medium in a laser system, and $N_2(v)$ created in an atmospheric disturbance could cool only by collisions with unlike species. We note that Starr observed V-E excitation of Na and K by $N_2(v)$[8,9], and the work of Rich and co-workers provides evidence of efficient V-E transfer in systems involving $CO(v)$[10] and $NO(v)$[11].

A number of previous studies of the effluents of active-nitrogen discharge afterglows have shown qualitatively the presence of vibrationally excited nitrogen. Quantitative assessment of the degree of ground-state vibrational excitation, however, generally has proved difficult. Because N_2 is not an infrared active molecule, the degree of vibrational excitation in the active nitrogen has been probed primarily by indirect methods. Kaufman and Kelso[12] remarked on the heated walls of their flow reactor downstream from their discharge and attributed the source of this heat to deactivation of vibrationally excited nitrogen molecules in collisions with the walls. Morgan, Phillips, and Schiff[13,14] noted an excess temperature given to the catalytic probe placed in their flow reactor which could not be attributed N-atom recombination. Again they suggested that the source of this excess

heat was vibrationally excited nitrogen molecules. Starr[8] and Starr and Shaw[9] observed excitation of sodium and potassium electronic transitions when they introduced sodium or potassium atoms to the afterglow of a nitrogen discharge. They suggested that the excitation resulted from a vibrational-to-electronic (V-E) excitation from $N_2(v)$ to Na or K. Bass[15] and Tanaka et al.[16] used vacuum ultraviolet (VUV) absorption spectroscopy, employing the partially forbidden Lyman-Birge-Hopfield bands, to show that $N_2(v)$ was indeed present in nitrogen-discharge afterglows. A number of other diagnostics have been developed in more recent years including photo-ionization[17], photoelectron spectroscopy[18,19], electron energy loss[20], Penning ionization[21-24], Raman[25-27], CARS[28,29], and Multiphoton ionization[30,31], among others. Caledonia et al. have reviewed much of this work in a recent report[32].

Our diagnostic for vibrationally excited nitrogen in discharge afterglows extends the pioneering work of Schmeltekopf et al.[21] and Young and Horn[22,23]. They relied on the vertical nature of Penning-ionization transitions from ground-electronic-state, neutral nitrogen to produce $N_2^+(B^2\Sigma_u^+,v)$ distributions characteristic of the ground-state distributions. Mixing metastable helium atoms with a flow of molecular nitrogen results in strong emission of the nitrogen first-negative system, $N_2^+(B\ ^2\Sigma_u^+ - X^2\Sigma_g^+)$. Since the Penning-ionization process follows a Franck-Condon excitation pathway, the vibrational distribution in the neutral, ground state will determine the distribution observed in the upper, ionic state. One problem with this approach is that care must be taken not to have any He^+ or He_2^+ in the flow of metastable helium. Both of those species also excite $N_2^+(B)$ quite strongly in charge-transfer reactions, but with an $N_2^+(B)$ vibrational distribution that is decidedly non-Franck-Condon[33]. This diagnostic is most sensitive to vibrational excitation of the first six vibrational levels in the ground electronic state. Our goal is to be able to estimate the overall vibrational distribution of the ground-state nitrogen by combining our experimental determination of the vibrational distribution in the lower levels with modeling calculations on the temporal development of the fully coupled vibrational-state manifold[4,5]. Jolly et al.[24] have also re-investigated the Penning-Ionization technique.

II. Experimental

The discharge-flow apparatus used in these experiments has been described in most respects previously[34-39]. We summarize briefly the modifications required for the measurements related to $N_2(v)$. Figure 1 shows the configuration of the flow reactor. A microwave discharge at the upstream end of the flow reactor, through a flow of helium and nitrogen, creates the active nitrogen. It enters a section of 2 in.-diameter Pyrex® containing three side arms. Small amounts of SF_6 flow through the first side arm to attach electrons created in the Penning-ionization reactions and the metastable helium atoms enter through the third side arm to produce the Penning-ionization spectrum. A 0.5m monochromator, mounted on rails, views the region of the flow reactor just downstream from the He^* injector to observe the fluorescence created in the Penning-ionization reaction.

A hollow-cathode, d.c. discharge through a flow of purified helium creates the metastable helium atoms. Flowing the helium through a molecular-sieve trap at liquid nitrogen temperature, upstream from the discharge, removes most of the impurities in the helium, including nitrogen and oxygen. Small amounts of residual neon in the helium ($\leq$10 ppm) have no effect on our observations. The discharge operates at 350V with a current, limited by a 200 kΩ resistor, below a milliamp.

We showed previously[33] that operating the hollow-cathode discharge at high voltage and high current tended to produce significant number densities of atomic and molecular helium ions. These ions are an anathema to the Penning-ionization measurements because they produce highly non-Franck-Condon distributions in the $N_2^+(B)$. Thus one could be led to false conclusions regarding the extent of ground-state vibrational excitation. The absence of significant number densities of helium ions was confirmed by failing to observe $N_2^+(B, v' > 2)$ when the active-nitrogen discharge was off.

Typical conditions comprised flow rates of helium through the microwave discharge and the metastable-producing d.c. discharge of 3600 and 1200 μmol s^{-1} respectively, nitrogen flow rates between 25 and 250 μmol s^{-1}, SF_6 flow rate of 4 μmol s^{-1}, total pressure of 1.5 torr, and transit time between the microwave discharge and observation region of ~11 ms. Generally, the microwave power, which was coupled through a McCarroll cavity, was 75 watts.

A least-squares fitting procedure[35] analyzes the Penning-ionization spectra. We generate basis functions consisting of a synthetic electronic spectrum for a unit population in each vibrational level of each electronic state appearing in the spectral region of interest. A linear least-squares routine then finds the populations of each vibronic band which, when multiplied by the appropriate basis function and summed with overlapping bands, gives a composite spectrum most nearly matching the experimental spectrum.

III. Theory Behind the Penning-Ionization Measurements

The Penning ionization between metastable helium atoms and molecular nitrogen is a vertical process. One can calculate the vibrational distribution in the final state, therefore, knowing only the vibrational distribution in the lower state and the Franck-Condon factors that couple the two states together. Thus

$$N_{v'} \propto \sum_{v''} N_{v''} q_{v'v''} \qquad (1)$$

where v′ and v″ represent the vibrational levels of the upper and lower states, respectively, and $q_{v'v''}$ is the Franck-Condon factor coupling them.

We calculated a set of Franck-Condon factors over the range of ground-electronic-state vibrational levels of 0-18, and $N_2^+(B)$-state vibrational levels of 0-9 using a calculational procedure previously described.[40] Table 1 contains the results of these calculations.

In theory, if one measures the vibrational distribution in the upper state, that in the ground state can be determined simply by inverting the Franck-Condon matrix, and multiplying this inverse matrix on both sides of Eq. (1). This procedure did not work for us because the measurements of the upper-state populations have some uncertainty associated with them, and the uncertainties become greatly magnified by the matrix multiplication. Jolly et al.[24] apparently succeeded in using this approach to analyze $N_2(v)$ distributions created in a glow discharge. We do not understand their success in light of our lack of it. Our spectral fitting approach for determining $N_2^+(B)$ number densities ought to be more accurate than their graphical integration of one branch from each band. We analyzed our data, therefore, using a model to describe the $N_2(X)$ vibrational distributions which we then used to predict $N_2^+(B)$ vibrational distributions. We then compared these predictions with observation.

Using the Franck-Condon factors in Table 1, we computed the $N_2^+(B)$-state vibrational populations relative to that in $N_2^+(B, v' = 0)$ expected for a number of values of vibrational temperature of ground-state nitrogen between 300 and 30,000 K, assuming a Boltzmann distribution among the levels. Figure 2 displays the results of these calculations. If the ground-state vibrational level populations follow a Boltzmann distribution, one can use experimentally derived $N_2^+(B)$ population ratios and Figure 2 to find the vibrational temperatures of ground-state nitrogen which corresponds to those excited-state population ratios.

If the ground-electronic-state vibrational levels do not follow a Boltzmann distribution, one can still compute expected excited-state populations from Eq. (1), if the ground-state distribution is known. Effluents from nitrogen discharges generally have nonequilibrium vibrational distributions, with the higher vibrational levels more strongly populated than would be predicted on the basis of a Boltzmann distribution. Caledonia and Center[4] and Capitelli and Dilonardo[7] have shown that for low vibrational levels the analytical distribution given by Treanor et al.[6] holds:

$$\frac{N_{v''}}{N_{v''=0}} = \exp\left\{- v'' \left[\frac{1.4388\left(\omega_e - 2\omega_e x_e\right)}{\Theta_1} - (v''-1)\,\frac{1.4388\ \omega_e x_e}{T}\right]\right\}, \qquad (2)$$

where Θ_1 is the Boltzmann vibrational temperature referenced to v" = 1, T is the ambient gas temperature, and ω_e and $\omega_e x_e$ are spectroscopic constants in units of cm^{-1}. The Boltzmann vibrational temperature is given by

$$\Theta_1 = - \frac{\omega_e - 2\omega_e x_e}{k \ln\left(N_{v''=1}/N_{v''=0}\right)} \quad . \qquad (3)$$

This distribution goes through a minimum, generally referred to as the Treanor minimum, at vibrational level v^*, given by

$$v^* = \frac{T\left(\omega_e - 2\omega_e x_e\right)}{2\ \omega_e x_e\ \Theta_1} + 0.5 \quad . \qquad (4)$$

For vibrational levels greater than the Treanor minimum, the product $v''N_{v''}$ is essentially constant. The resulting distribution for $v'' > v^*$, therefore, is

$$\frac{N_{v''}}{N_{v''=0}} = \frac{v^*-1}{v''} \exp\left\{\frac{- 1.4388\ \left(v^{*2}-1\right)\ \omega_e x_e}{T}\right\} \quad , \qquad (5)$$

where the various parameters in Eq. 5 are determined by requiring that the two distributions be equal at $v'' = v^*-1$.

The Penning-ionization spectrum calculated from a non-Boltzmann, ground-state distribution based upon Eqs. (2), (4) and (5) is significantly different from what one would calculate from a Boltzmann ground-state distribution. The Penning-ionization technique, therefore ought to differentiate between the two ground-state distributions rather easily.

IV. Results of the Penning-Ionization Measurements

Figures 3 and 4 show a portion of the nitrogen first-negative spectrum with the active-nitrogen discharge off and on, respectively. Clearly, the vibrational development of the emission is greatly enhanced by discharging the gas. We determined vibrational populations in the upper state by fitting the spectrum in the manner described previously[35,38]. While the fits included upper-state vibrational levels 0-8, for the most part, only vibrational levels 0-7 contributed any significant intensity to the spectra.

A number of different and conflicting sets of Einstein coefficients for the $N_2^+(B^2\Sigma_u^+ - X^2\Sigma_g^+)$ fill the literature[41-44]. In particular, the constancy of the electronic transition moment with r-centroid is unsettled[45,46]. To analyze our data, we calculated a set of Einstein coefficients based upon the relative electronic transition moment variation given by Brown and Landshoff[46], which has received some support by Comes and Speier[47] and by Chang et al.[48], the Franck-Condon factors of Albritton et al.[49], and a radiative lifetime of $N_2^+(B,v'=0)$ of 62.5 ns[41]. They are tabulated elsewhere.[24] We are currently investigating this issue of transition-moment variation. The molecular potential constants given in Lofthus and Krupenie[41] were found to be inadequate for predicting band positions accurately. Our fitting program uses the recent potential constants determined by Gottscho et al.[50]

Early in this measurement program, we discovered that moving the monochromator slightly downstream from the injector, through which the He^* entered the reactor, resulted in a much different vibrational distribution in the upper state. There appeared to be no reason why the vibrational distribution in the active nitrogen should change over short distances. A diffuse emission could be seen extending somewhat downstream from the well-defined flame created by the Penning-ionization. Several centimeters downstream from the injector, the Penning-ionization flame disappeared, and only the diffuse emission remained. Figure 5 shows the diffuse-emission spectrum.

On the assumption that the emission was caused by energetic electrons exciting $N_2^+(X)$, a trace of SF_6 was added to act as a scavenger for the electrons. This addition eliminated the diffuse flame, and also resulted in $N_2^+(B)$ vibrational distributions which did not change with the location of the monochromator relative to the He^* injector. Presumably, the electrons created in the Penning-ionization reaction pick up some extra kinetic energy either from stray microwave fields which have penetrated downstream, or else from collisions with energetic species in the active nitrogen. The amount of energy must be fairly considerable, because exciting $N_2^+(B)$ from $N_2^+(X)$ requires more than 3 eV. All the results given below were obtained in the presence of small traces of SF_6.

Analyzing the $N_2^+(B,v')$ vibrational distributions with the help of Figure 2 gave different ground-state vibrational temperatures depending upon which upper-state vibrational level was considered. The data fell into three groups. The temperature determined from $v' = 1$ was only 63 percent of that determined from $v' = 2$ and 3, which were themselves reasonably consistent. Vibrational temperatures determined from $v' = 4$-7 also were reasonably consistent with each other, but were 30 percent larger than temperatures determined from vibrational levels 2 and 3. Clearly, a Boltzmann model for the ground-state vibrational distribution is inadequate.

Fitting our distributions to the analytical model described by Eqs. (2), (4), and (5) was more successful. Figures 6 and 7 show two examples. Clearly, the nonequilibrium model does a reasonable job of fitting observations out through $v' = 6$. We do not understand the sudden discrepancy at $v' = 7$. The dashed lines in Figures 6 and 7 show the distribution which would be predicted were the ground-state to be determined by a Boltzmann distribution. This shows graphically the inadequacy of that model for the ground-state levels. In the future we plan to use an improved model to predict the population distribution up to higher vibrational levels.

Our observations show that effective vibrational temperatures, θ_1, as determined from fits of the data to Eqs. (2) and (5) rather than what one would calculate from Eq. (3), tended to be smaller with larger nitrogen mole fractions flowing through the discharge (Figure 8) and also at higher total pressures. Placing a nickel screen in the reactor, downstream from the discharge, only slightly reduced the effective vibrational temperature of the nitrogen (about 5 percent). The nickel screen, however, reduced atomic nitrogen number densities by more than an order of magnitude. Placing a screen in the afterglow, therefore, is a means to produce a somewhat cleaner flow of $N_2(v)$ in a discharge-flow system. The Penning-ionization technique appears to provide a reasonably accurate monitor of the vibrational distribution of ground-electronic-state nitrogen, at least for the lower vibrational levels. Extending the model to include higher vibrational levels would need experimental confirmation.

To extend the Penning-ionization technique as a diagnostic for $N_2(v)$ containing energies of several eV, we investigated excitation of the nitrogen second-negative system, $N_2^+(C^2\Sigma_u^+ - X^2\Sigma_g^+)$. This system can be excited by collisions between metastable helium and molecular nitrogen only if the nitrogen has at least 3.8 eV of internal energy. Because the $N_2^+(C)$ potential curve is somewhat offset from that of $N_2(X)$, vertical transitions connecting the two states would arise from highly-excited ground-state vibrational levels. Observing the second-negative system, therefore, would provide unequivocal evidence of highly excited ground-state nitrogen in the reactor.

Using a quartz flow reactor we observed the second-negative system in the ultraviolet between 185 and 210 nm. Figure 9 shows the spectral region between 188 and 208 nm with the metastable helium off and on. In both cases, the active-nitrogen discharge is on. The two features appearing at 191 and 199 nm are the $\Delta v = -6$ and -7 sequences, respectively, of the nitrogen second-negative system. The $\Delta v = -8$ sequence at 206 nm is masked by the 2,0 band of the $NO(A^2\Sigma^+ - X^2\Pi)$ system. This system is excited by interactions between

$N_2(A^3\Sigma_u^+)$, created in the active-nitrogen discharge, and some impurity NO also created in the discharge[38].

Scans with the active nitrogen discharge off, but the metastable-helium discharge on, resulted in no observed emissions. This latter observation is important because it establishes the absence of He^+ from the metastable helium flow. Charge-transfer between He^+ and $N_2(X)$ is a well-known source of the second-negative system[33,51].

Observing the nitrogen second-negative system from the interaction between metastable helium atoms and active nitrogen demonstrates the presence of metastable nitrogen in the afterglow containing at least 3.8 eV. In addition to $N_2(X,v)$, the electronic metastables $N_2(A^3\Sigma_u^+)$ or $N_2(a'^1\Sigma_u^-)$ are significantly populated in active nitrogen afterglows. Using alternative sources to generate the electronic metastables, we observed the resulting spectra when they were mixed with helium metastables.

The $N_2(A^3\Sigma_u^+)$ is produced cleanly by adding N_2 downstream from a hollow-cathode, d.c. discharge through a mixture of helium and argon[52,53]. Scans of the Vegard-Kaplan bands between 220 and 400 nm established that the $N_2(A)$ number densities from this source were of comparable magnitude to those obtained from the active-nitrogen discharge. Turning the metastable nitrogen on and off in the presence of metastable helium showed no detectable change in the emissions in the region between 185 and 210 nm.

$N_2(a')$ is made along with slightly enhanced number densities of $N_2(A)$ - about a factor of 3 - when the molecular nitrogen flows through the d.c. discharge with the He/Ar mixture[39,54]. Again, turning the metastable nitrogen on and off indicated no emissions between 185 and 210 nm. We conclude therefore that interactions between metastable helium and $N_2(A)$ and $N_2(a')$ do not produce $N_2^+(C)$.

The appearance of $N_2^+(C)$ from the interaction between metastable helium and active nitrogen, therefore, appears to be the result of Penning ionization of ground-electronic-state nitrogen containing at least 3.8 eV of vibrational energy. This corresponds to ground-electronic-state vibrational levels of $v'' \geq 15$.

V. Summary

In summary, Penning ionization of $N_2(v)$ by metastable helium atoms excites $N_2^+(B)$ up to at least $v' = 8$. Analysis indicates the ground-state nitrogen vibrational distribution follows a Treanor rather than Boltzmann distribution, with effective vibrational temperatures of up to 6,000 K at times up to 30 ms downstream from the active-nitrogen discharge.

The diagnostic is complicated by the presence of free electrons created in the Penning ionization. These free electrons absorb energy from the active-nitrogen medium and produce further excitation of $N_2^+(B)$. Adding traces of SF_6 removes the free electrons from the reactor, and thereby eliminates their interfering effects.

Observing emission from $N_2^+(C)$, excited by Penning-ionization reactions in the afterglow, demonstrates the presence of $N_2(v)$ containing at least 3.8 eV internal energy. Future efforts will be directed towards a more quantitative assessment of the $N_2^+(C)$ observations to identify the range of $N_2(v)$ levels responsible for this excitation.

Acknowledgements

This work was sponsored by SDIO/IST through a contract with Los Alamos National Laboratories, Contract No. 9X25-X451-2 and by the Defense Nuclear Agency (project 5A, task 5A, work unit 115) and the Air Force Office of Scientific Research (Task 2310G4) through the Air Force Geophysics Laboratory Contract No. F19628-85-C-0032. We appreciate analytical and experimental help from Margrethe DeFaccio, Catherine White, and Bill Cummings, and the comments and advice of Dave Green, Steve Davis, and George Caledonia.

REFERENCES

1. a) L.G. Piper, S.J. Davis, H.C. Murphy, W.P. Cummings, L.P. Walkauskas, M.A. DeFaccio, L.M. Cowles, W.T. Rawlins, W.J. Marinelli, and B.D. Green, PSI-076/TR-593, Final report under Air Force Weapons Laboratories Contract No. F29601-84-C-0076 (1987).
   b) L.G. Piper and W.J. Marinelli, manuscript in preparation.

2. L.G. Piper and G.E. Caledonia, Bull. A.P.S. 31, 157 (1986).

3. a) L.G. Piper, J. Chem. Phys. 88, 231 (1988).
   b) L.G. Piper, J. Chem. Phys, 88, xxxx (1988).

4. G.E. Caledonia and R.E. Center, J. Chem. Phys. 55, 552 (1971).

5. R.E. Center and G.E. Caledonia, Appl. Opt. 10, 1795 (1971).

6. C.E. Treanor, J.W. Rich, and R.G. Rehn, J. Chem. Phys. 43, 1798 (1968).

7. M. Dilonardo, and M. Capitelli, Rev. Phys. Appl. 13, 115 (1978).

8. W.L. Starr, J. Chem. Phys. 43, 73 (1965).

9. W.L. Starr and T.M. Shaw, J. Chem. Phys. 44, 4181 (1966).

10. R.L. DeLeon and J.W. Rich, Chem. Phys. 107, 283 (1986).

11. H. Dunnwald, E Siegel, W. Urban, J.W. Rich, G.F. Homicz, and M.J. Williams, Chem. Phys. 94, 195 (1985).

12. F. Kaufman and J.R. Kelso, J. Chem. Phys. 28, 510 (1958).

13. J.E. Morgan, L.F. Phillips, and H.I. Schiff, Discuss Faraday Soc. 33, 118 (1962)

14. J.E. Morgan and H.I. Schiff, Can. J. Chem. 41, 903 (1963).

15. A.M. Bass, J. Chem. Phys. 40, 695 (1964).

16. Y. Tanaka, F.R. Innes, A.S. Jursa, and M. Nakamura, J. Chem. Phys. 42, 1183 (1965).

17. G.R. Cook and R.J. McNeal, J. Chem. Phys. 56, 1388 (1972).

18. J. Dyke, N. Jonathan, A. Morris, and T. Sears, J.C.S. Faraday Trans. II 72, 597 (1976).

19. G.H. Van Lonkhuyzen and C.A. DeLange, Chem. Phys. Lett. 107, 420 (1984).

20. M.D. White, K.J. Ross, E.W. Lewis, and N.B.H. Jonathan, J. Phys. B. 9, 1035 (1976).

21. A.L. Schmeltekoff, E.F. Ferguson, and F.C. Fensenfeld, J. Chem. Phys. 48, 2966 (1968).

22. S.J. Young and K.P. Horn, J. Chem. Phys. 57, 4835 (1972).

23. S.J. Young, J. Chem. Phys. 38, 1603 (1973).

24. J. Jolly, M. Touzeau,, and A. Ricard, J. Phys. B 14, 473 (1981).

25. V.P. Podobedov, A.M. Pyndyk, and Kh. E. Sterin, Opt. Spectrosc. 43, 504 (1977).

26. G. Black, H. Wise, S. Schechter, and R.L. Sharpless, J. Chem. Phys. 60, 3526 (1974).

27. B. Mutel, M. Bridoux, M. Crunelle-Cras, O. Dessaux, F. Grase, P. Goudmand, and G. Moreau, Chem. Phys. Lett. 104, 290 (1984).

28. W.M. Shaub, W.J. Nibler, and A.B. Harvey, J. Chem. Phys. 67, 1883 (1977).

29. T. Dreier, U. Wellhausen, J. Wolfrum, and G. Marowsky, Appl. Phys. B 29, 31 (1982).

30. K.L. Carleton, K.H. Welge, and S.R. Leone, Chem. Phys. Lett. 115, 492 (1985).

31. W.J. Marinelli and W.J. Kessler, PSI TR-669 (1987).

32. G.E. Caledonia, S.J. Davis, B.D. Green, L.G. Piper, W.T. Rawlins, G.A. Simons, and G.M. Weyl, Air Force Wright Aeronautical Labs. report AFWAL-TR-86-2078 (1986).

33. L.G. Piper, L. Gundel, J.E. Velazco, and D.W. Setser, J. Chem. Phys. 62, 3883 (1975).

34. L.G. Piper, G.E. Caledonia, and J.P. Kennealy, J. Chem. Phys. 74, 2888 (1981).

35. L.G. Piper, W.J. Marinelli, W.T. Rawlins, and B.D. Green, J. Chem. Phys. 83, 5602 (1985).

36. L.G. Piper and W.T. Rawlins, J. Phys. Chem. 90, 320 (1986).

37. L.G. Piper, M.E. Donahue, and W.T. Rawlins, J. Phys. Chem., 91, 3883 (1987).

38. L.G. Piper, L.M. Cowles, and W.T. Rawlins, J. Chem. Phys. 85, 3369 (1986).

39. L.G. Piper, J. Chem. Phys. 87, 1625 (1987).

40. W.J. Marinelli and L.G. Piper, J. Quant. Spectrosc. Radiat. Transfer 34, 321 (1985).

41. A. Lofthus and P.H. Krupenie, J. Phys. Chem. Ref. Data 6, 287 (1977).

42. D.E. Shemansky and A.L. Broadfoot, J. Quant. Spectrosc. Radiat. Transfer 11, 1385 (1971).

43. R.W. Nichols, J. Atmos. Terrest. Phys. 25, 218 (1963).

44. A.L. Broadfoot, Planet. Space Sci. 15, 1801 (1967).

45. L.C. Lee and D.L. Judge, J. Phys. B: 6, L121 (1973).

46. W.A. Brown and R.K. Landshoff, J. Quant. Spectrosc. Radiat. Transfer 11, 1143 (1971).

47. E.J. Comes and F. Speier, Chem. Phys. Lett. 4, 13 (1969).

48. R.S.F. Chang, D.W. Setser, and G.W. Taylor, Chem. Phys. 25, 201 (1978).

49. D.L. Albritton, A.L. Schmeltekopf, and R.N. Zare, private communication via D.W. Setser (1985).

50. R.A. Gottscho, R.W. Field, K.A. Dick, and W. Benesch, J. Mol. Spec. XX, 435 (1979).

51. E.C.Y. Inn, Planet Space Sci. 15, 19 (1967).

52. D.W. Setser, D.H. Stedman, and J.A. Coxon, J. Chem. Phys. 53, 1004 (1970).

53. D.H. Stedman and D.W. Setser, Chem. Phys. Lett. 2, 542 (1966).

54. M.F. Golde, Chem. Phys. Lett. 31, 348 (1975).

TABLE 1. Franck-Condon Factors of $N_2^+(B^2\Sigma_u^+, v') - N_2(X^1\Sigma_g^+, v'')$.

v'/v"	0	1	2	3	4	5	6	7	8	9	10	11	12	13	14	15
0	0.8836	0.1034	0.0117	0.0012												
1	0.1141	0.6917	0.1611	0.0285	0.0039											
2	0.0023	0.2000	0.5572	0.1854	0.0458	0.0078	0.0012									
3		0.0048	0.2633	0.4694	0.1864	0.0611	0.0122	0.0023								
4			0.0060	0.3087	0.4192	0.1711	0.0736	0.0165	0.0037							
5			0.0006	0.0049	0.3382	0.4008	0.1444	0.0841	0.0199	0.0054	0.0012					
6				0.0018	0.0019	0.3506	0.4098	0.1099	0.0940	0.0217	0.0075	0.0018				
7					0.0043	-	0.3405	0.4422	0.0711	0.1065	0.0211	0.0100	0.0025			
8						0.0079	0.0056	0.2994	0.4904	0.0339	0.13256	0.0171	0.0138	0.0029	0.0017	
9							0.0113	0.0300	0.2198	0.5355	0.0072	0.1580	0.0094	0.0206	0.0027	0.0030

FIGURE CAPTIONS

Figure

1. Flow reactor for studies on the vibrational energy content of active nitrogen.

2. Ratio of the populations of $N_2^+(B, v')$ to $N_2^+(B, v' = 0)$ created in He^* Penning-ionization of $N_2(X, v'')$ as a function of the vibrational temperature of the ground-state nitrogen.

3. Spectrum of the $\Delta v=-2$ sequence of the $N_2^+(B^2\Sigma_u^+-X^2\Sigma_g^+)$ system excited in the Penning-ionization of vibrationally cold nitrogen by $He^*(2\ ^3S)$. The light line is the experimental spectrum; the heavy line shows the best-fit synthetic spectrum.

4. Spectrum of the $\Delta v=-2$ sequence of the $N_2^+(B\ ^2\Sigma_u^+-X^2\Sigma_g^+)$ system excited in the Penning-ionization of active nitrogen by $He^*(2\ ^3S)$. The light line is the experimental spectrum; the heavy line shows the best-fit synthetic spectrum.

5. Spectra of the $\Delta v=-2$ sequence of the $N_2^+(B^2\Sigma_u^+-X^2\Sigma_g^+)$ system excited in the Penning-ionization of active nitrogen by $He^*(2^3S)$ in the presence and absence of SF_6.

6. Comparison between experimental and calculated vibrational distributions of $N_2^+(B)$ created in the Penning-ionization of active nitrogen by metastable helium atoms for a nitrogen mole fraction of 0.011 (p = 1.5 torr, transit time from discharge = 11 ms).

7. Comparison between experimental and calculated vibrational distributions of $N_2^+(B)$ created in the Penning-ionization of active nitrogen by metastable helium atoms for a nitrogen mole fraction of 0.046 (p = 1.5 torr, transit time from discharge = 11 ms).

8. Effective vibrational temperature from the non-equilibrium model versus nitrogen mole fraction through the discharge.

9. Spectra from active nitrogen between 184 and 208 nm in the absence and presence of metastable helium atoms.

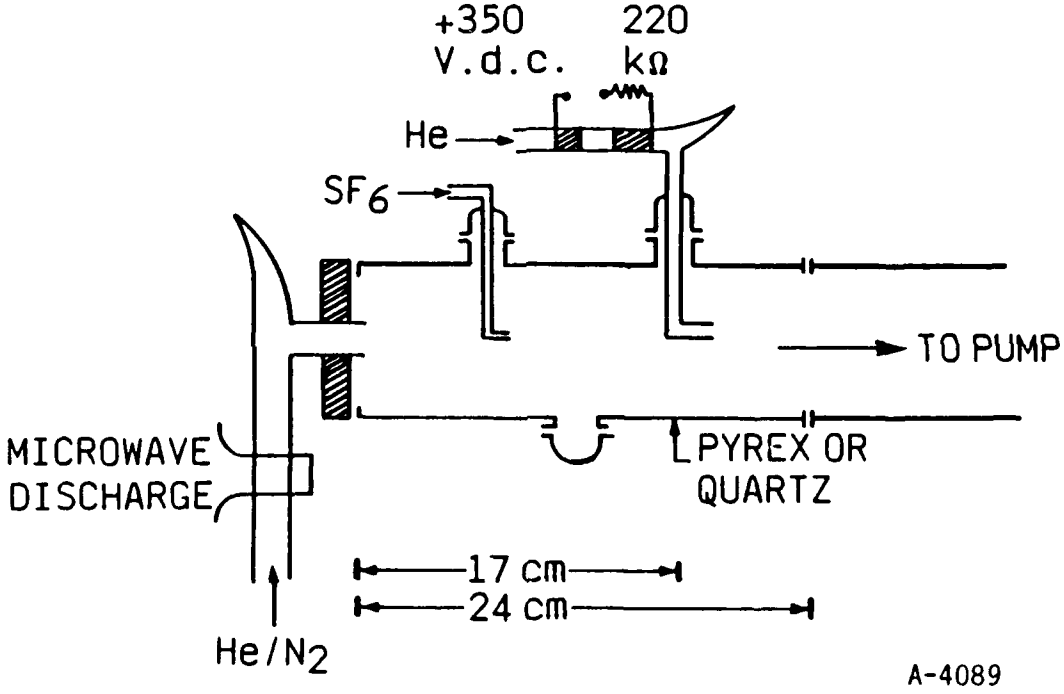

Figure 1. Flow reactor for studies on the vibrational energy content of active nitrogen.

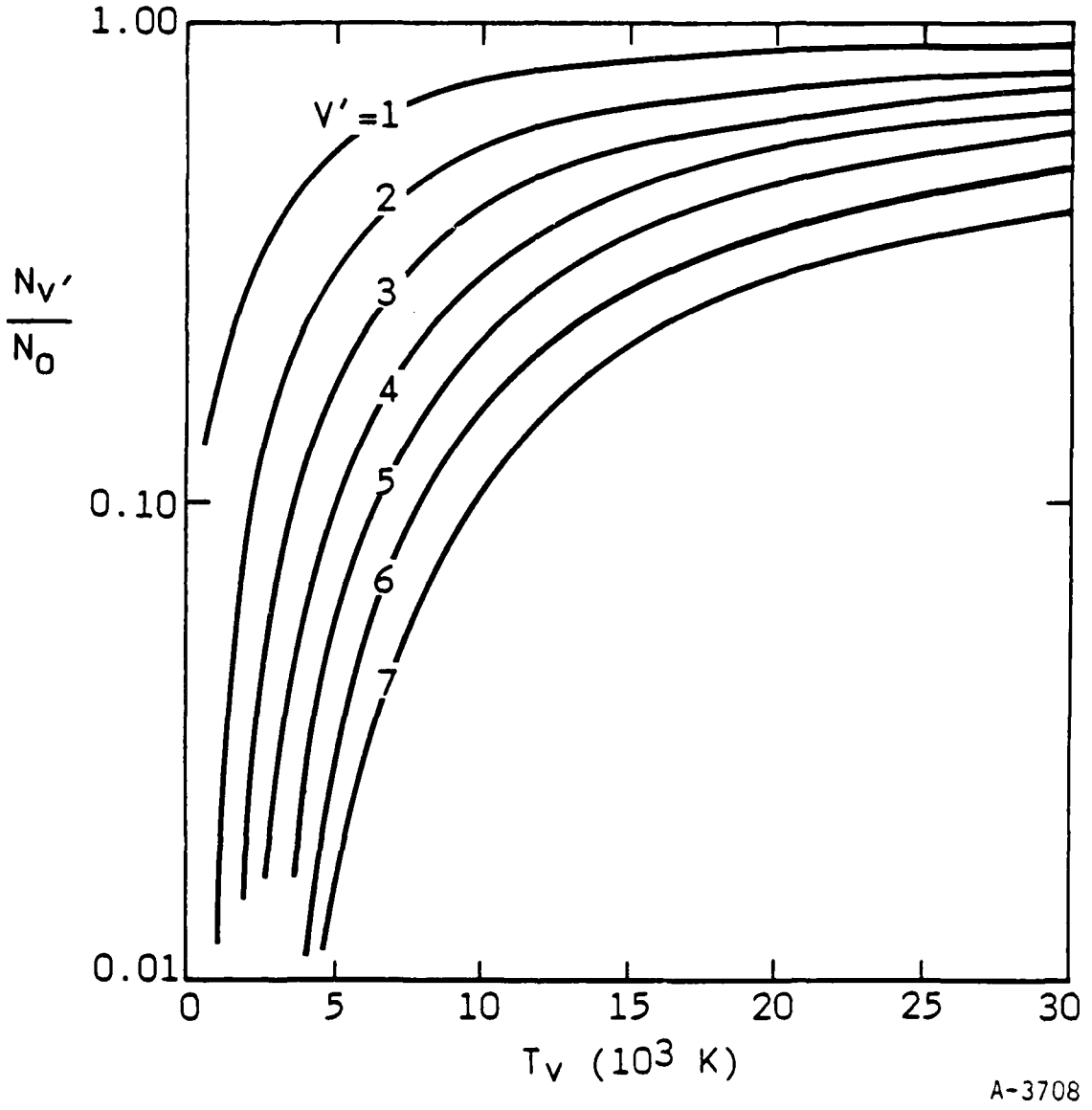

Figure 2. Ratio of the populations of $N_2^+(B, v')$ to $N_2^+(B, v' = 0)$ created in He^* Penning-ionization of $N_2(X, v'')$ as a function of the vibrational temperature of the ground-state nitrogen.

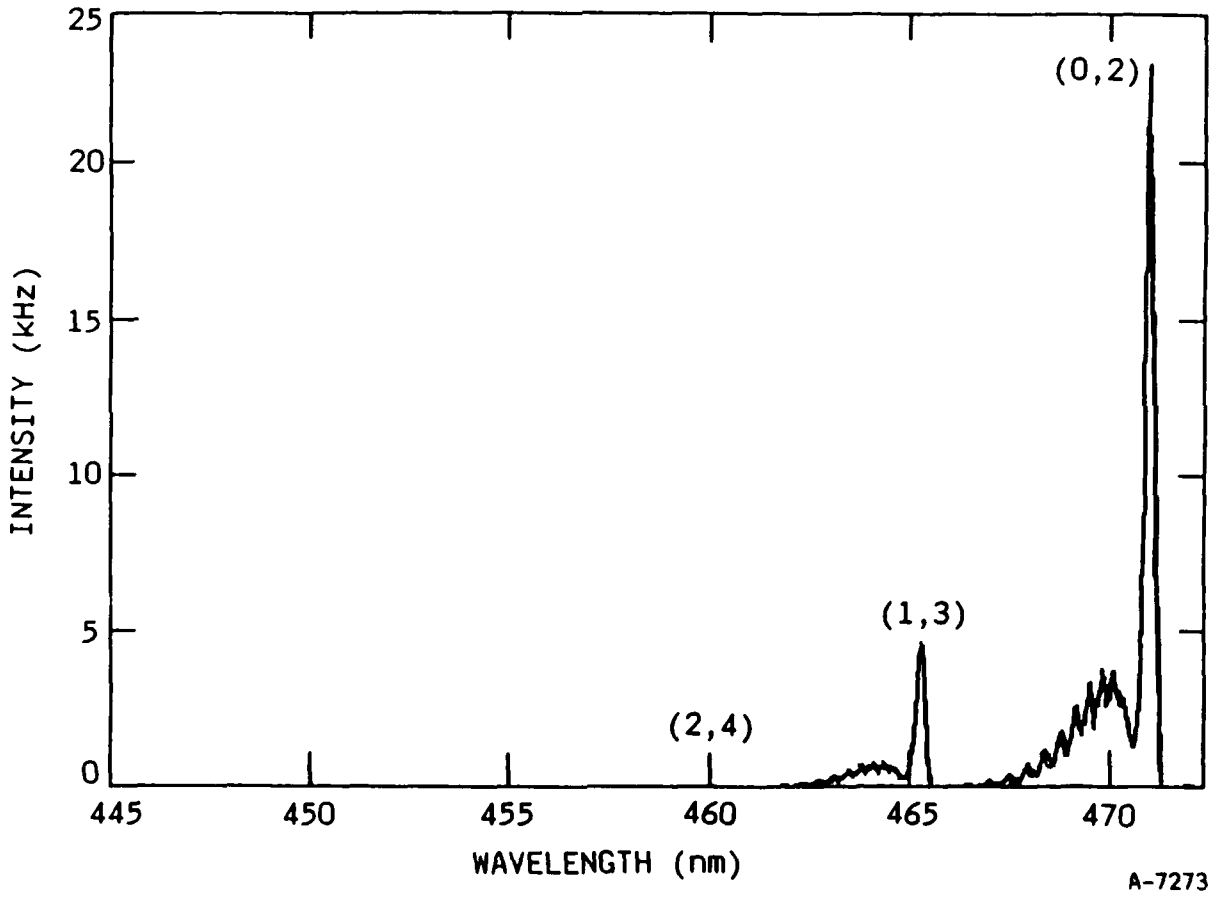

Figure 3. Spectrum of the $\Delta v=-2$ sequence of the $N_2^+(B^2\Sigma_u^+-X^2\Sigma_g^+)$ system excited in the Penning-ionization of vibrationally cold nitrogen by $He^*(2\ ^3S)$. The light line is the experimental spectrum; the heavy line shows the best-fit synthetic spectrum.

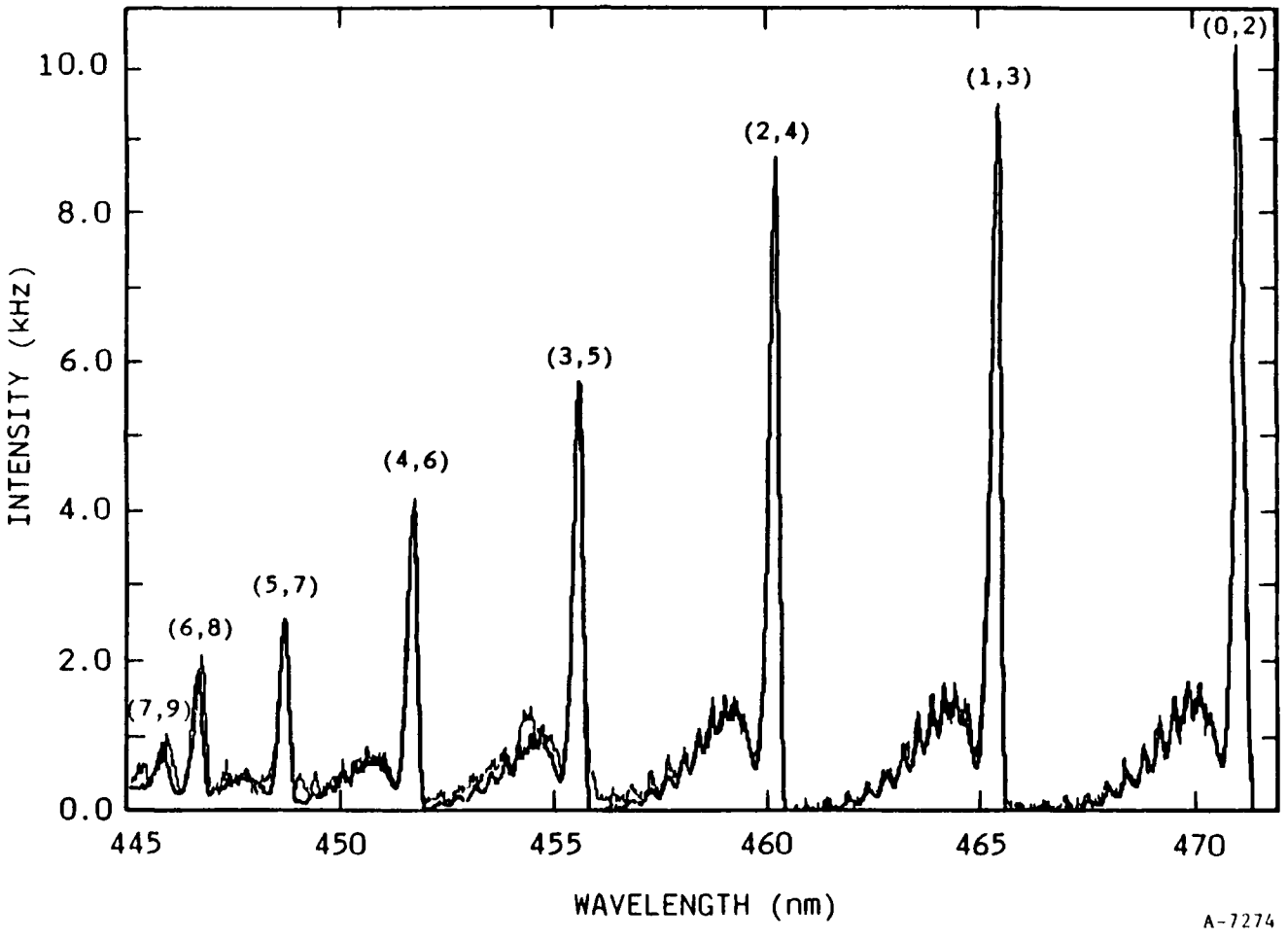

Figure 4. Spectrum of the $\Delta v=-2$ sequence of the $N_2^+(B\ ^2\Sigma_u^+ - X^2\Sigma_g^+)$ system excited in the Penning-ionization of active nitrogen by $He^*(2\ ^3S)$. The light line is the experimental spectrum; the heavy line shows the best-fit synthetic spectrum.

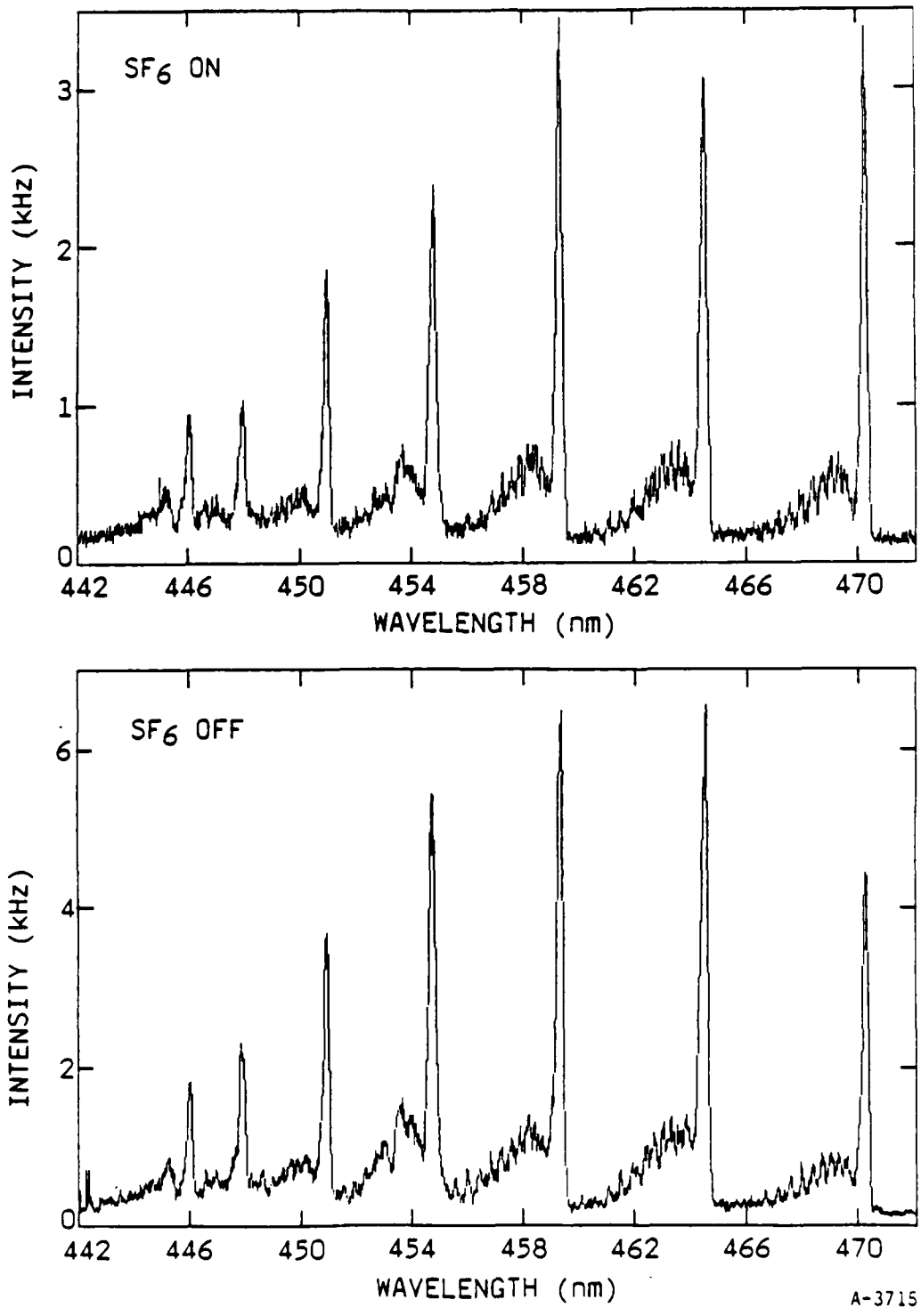

Figure 5. Spectra of the $\Delta v=-2$ sequence of the $N_2^+(B^2\Sigma_u^+-X^2\Sigma_g^+)$ system excited in the Penning-ionization of active nitrogen by $He^*(2\ ^3S)$ in the presence and absence of SF_6.

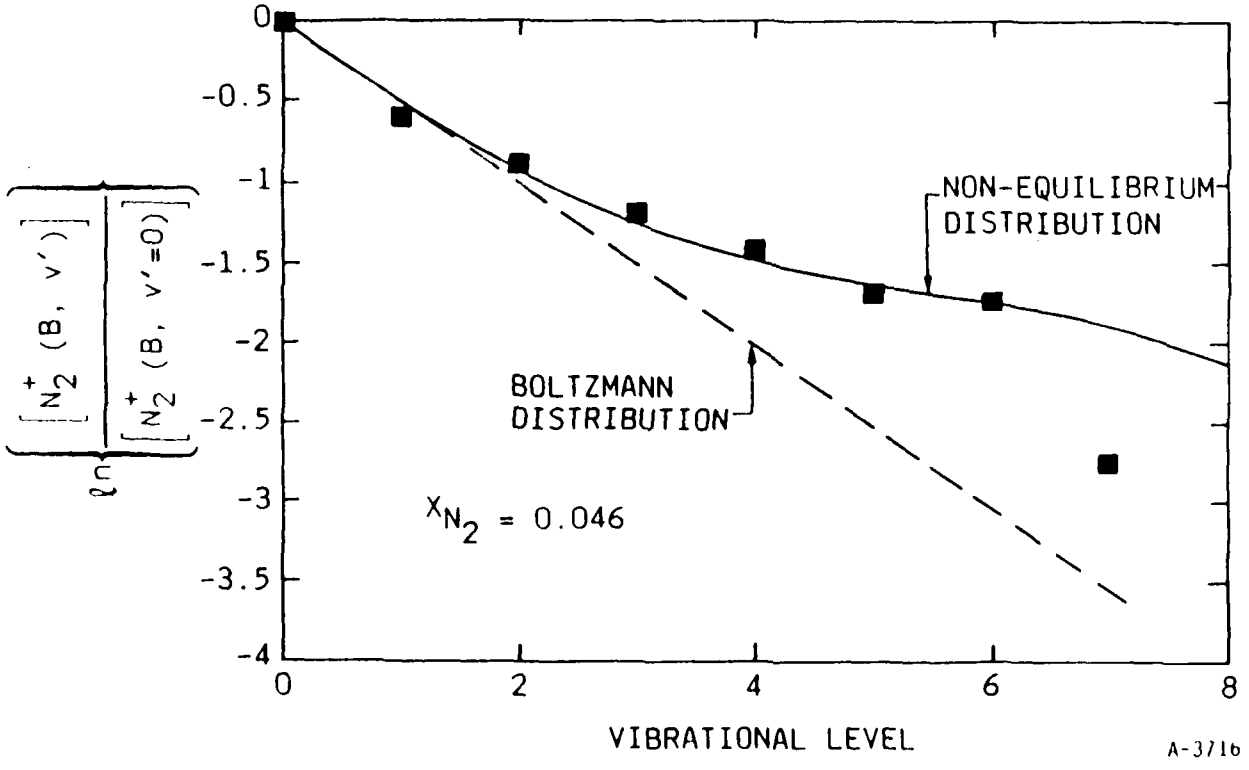

Figure 6. Comparison between experimental and calculated vibrational distributions of $N_2^+(B)$ created in the Penning-ionization of active nitrogen by metastable helium atoms for a nitrogen mole fraction of 0.011 (p = 1.5 torr, transit time from discharge = 11 ms).

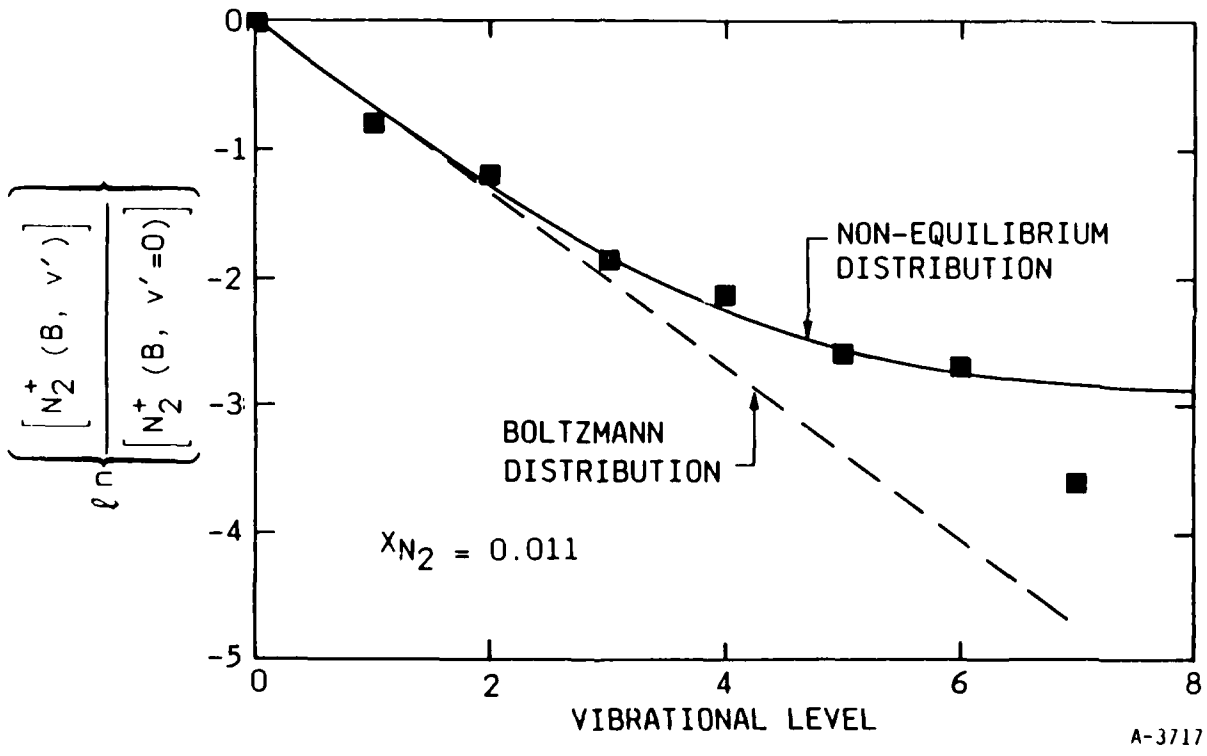

Figure 7. Comparison between experimental and calculated vibrational distributions of $N_2^+(B)$ created in the Penning-ionization of active nitrogen by metastable helium atoms for a nitrogen mole fraction of 0.046 (p = 1.5 torr, transit time from discharge = 11 ms).

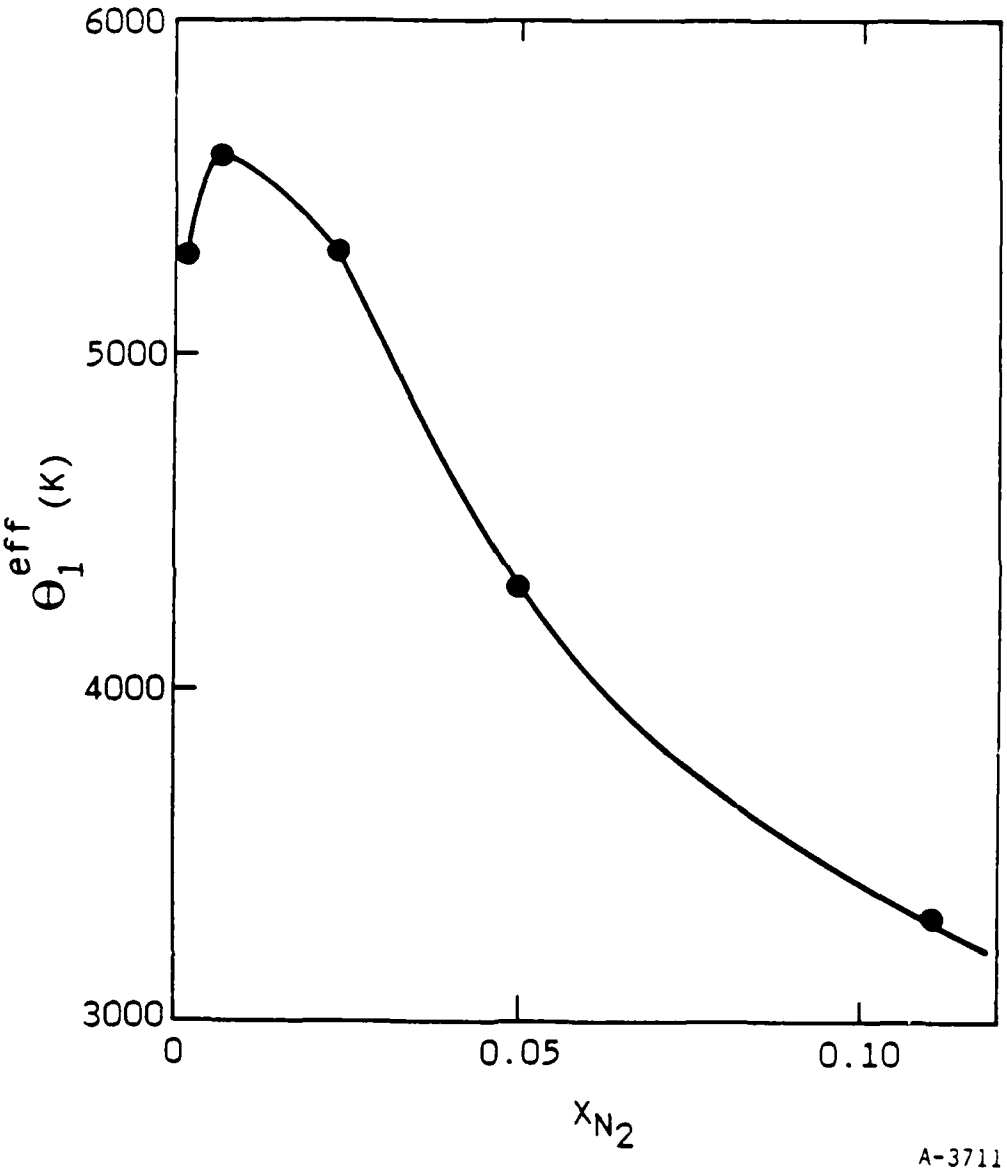

Figure 8. Effective vibrational temperature from the non-equilibrium model versus nitrogen mole fraction through the discharge.

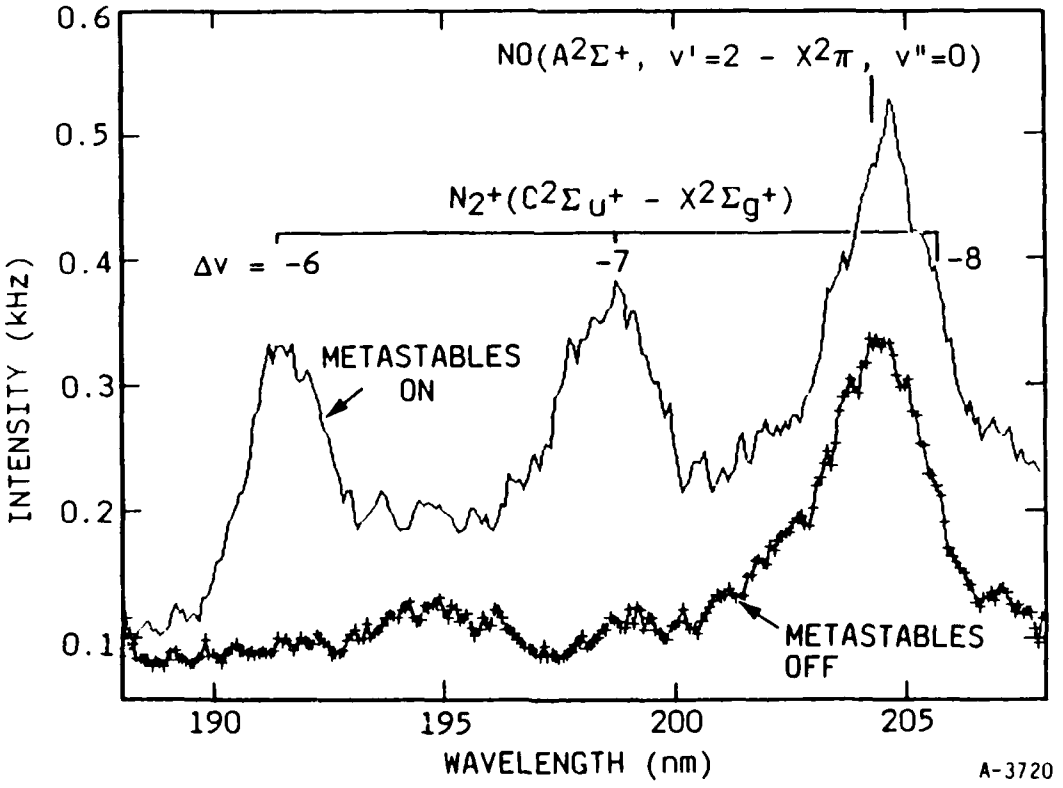

Figure 9. Spectra from active nitrogen between 184 and 208 nm in the absence and presence of metastable helium atoms.

APPENDIX L

(SR-262 reproduced in its entirety)

J. Chem. Phys. 87, 1625 (1987)

PSI-564/
SR-262

Quenching Rate Coefficients for N_2 ($a'^1\Sigma_u^-$)

by

Lawrence G. Piper

Physical Sciences Inc.
P.O. Box 3100
Andover, MA 01810

J. Chem. Phys. 87, 1625 (1987)

ABSTRACT

We have studied the kinetics of the lowest excited singlet state of molecular nitrogen, $N_2(a'^1\Sigma_u^-, v=0)$, in a discharge flow reactor. The metastables were generated in a hollow cathode dc discharge through molecular nitrogen highly diluted in argon, and detected by vuv fluorescence of the forbidden $N_2(a'^1\Sigma_u^- - X^1\Sigma_g^+)$ band system. Observations of the equilibrium between the $N_2(a^1\Pi_g)$ and $N_2(a'^1\Sigma_u^-)$ states in our reactor indicate that the metastable has a radiative lifetime $\gtrsim 23 \, ^{+\ 11}_{-\ 6}$ ms, assuming a radiative lifetime of $80 \, ^{+\ 40}_{-\ 20}$ μs for $N_2(a^1\Pi_g)$. Rate coefficients for quenching by NO, CH_4, CO, and N_2O are approximately gas kinetic, those by H_2, O_2, and CO_2 roughly tenth gas kinetic, and that by molecular nitrogen $(1.9 \pm 0.5) \times 10^{-13}$ cm^3 molecule^{-1} s^{-1}. The interaction between $N_2(a')$ and CO produced $CO(A^1\Pi - X^1\Sigma)$ emission in about $21 \, ^{+\ 10}_{-\ 8}$ percent of the quenching events.

1. INTRODUCTION

Although the lowest excited singlet state of molecular nitrogen, $N_2(a'^1\Sigma_u^-)$, is potentially an important energy carrier in systems involving excited nitrogen, such as nitrogen discharges and aurorae, it has been studied only sparingly. This is probably because its long radiative lifetime, estimated to be between 13 and 500 ms,[1-4] makes it difficult to detect optically. Several authors have shown that it probably is the state to which the much more studied $N_2(a^1\Pi_g)$ state is quenched.[4-8]

Golde[6] developed a discharge technique for studying $N_2(a', v'=0)$. He showed that this state was coupled kinetically to $N_2(a, v'=0)$ which is 1212 cm^{-1} higher in energy. The fact that he could see none of the higher vibrational levels of $N_2(a')$ he took as evidence that the a and a' states were efficiently coupled throughout the nested manifold, and that during the few millisecond transit time between his discharge and his observation vessel all of the higher lying a'-state vibrational levels had relaxed to a-state vibrational levels. Radiation or further quenching deactivated these levels so that some fraction of them ultimately ended in a', v'=0. Later, Casassa and Golde[4] studied the spectroscopy of $N_2(a', v'=0)$, determining the transition moment variation with r-centroid, and reanalyzed the absorption data of Tilford and Benesch[3] to estimate a radiative lifetime of about 17 ms for $N_2(a', v'=0)$. In comparing the ratio of intensities of the a and a' emissions, they estimated a lower limit to the a' lifetime of about 31 ms.

We have studied the kinetics of reactions of $N_2(a', v'=0)$ with a number of molecules in a discharge-flow reactor. A cold-cathode discharge source similar to Golde's produced the metastables. Our observations confirm those

of Casassa and Golde regarding the transition-moment variation of $N_2(a', v'=0)$ and the equilibrium ratio of a to a' emission. We have further determined the rate coefficients for quenching $N_2(a', v'=0)$ by a variety of molecules, and have determined the efficiency with which $N_2(a')$ excites the CO(A - X) bands in an energy-transfer reaction with CO.

2. EXPERIMENTAL

The apparatus used in these studies has been described in some detail in several previous publications.[9-13] Basically it is a 2 in. diameter discharge-flow reactor which incorporates a moveable injector for varying the reaction time between the metastables and the quenchers. A cold-cathode discharge operating at about 390V through a mixture of molecular nitrogen highly dilute in argon produces the metastables. Observation of fluorescence from the forbidden $N_2(a', v'=0 - X, v''=4)$ transition at 171 nm was our primary diagnostic for the metastable number density. Because molecular nitrogen is a reasonably efficient quencher of $N_2(a')$, the mole fraction of nitrogen in the discharge and the total system pressure must be kept low, and transit times between the discharge and the observation region need to be minimized. Typically we operated at a pressure of about 0.95 torr with a nitrogen mole fraction of about 0.007 and a total transit time between the discharge and the detection region of about 13 ms.

Although the discharge source produces some atomic nitrogen, both $N(^4S)$ and $N(^2D)$, and $N_2(A^3\Sigma_u^+)$, none of these species should affect our kinetic results. In principle, $N_2(A)$ could be collisionally excited to $N_2(a')$ in energy pooling reactions involving other metastables which supply at least 2.23 eV. This means $N(^2D)$, $N(^2P)$, $N_2(A)$, and $N_2(X, v>8)$. The absence of emission at 346.6 nm, $N(^2P-^4S)$, shows that $N(^2P)$ number densities are less than 10^6 atoms cm^{-3}. At higher pressures (> 5 torr) and longer flow times from the discharge, we do see some (N^2P) emissions from this source. Presumably, the $N(^2P)$ is excited by the efficient energy transfer between

$N_2(A)$ and $N(^4S)$.[14,15] Metastable helium Penning ionization measurements on the effluents of this discharge source showed that $N_2(X,v)$ also is absent from the gas stream.[16] Our measurements on $N_2(A)$ energy pooling indicated very little, if any, singlet metastable formation.[17] Resonance-fluorescence measurements in the vacuum ultra-violet, however, do indicate the presence of $N(^2D)$ metastables at number densities which could be as high as 10^{10} atoms cm^{-3}. Thus we cannot so easily rule out the possibility of energy pooling between $N_2(A)$ and $N(^2D)$ as a source of $N_2(a')$. Our kinetic observations, however, seem to indicate that this is not the case. For example, CO_2 quenches $N_2(a')$ efficiently but quenches $N_2(A)$ poorly[18] and reacts fairly slowly with $N(^2D)$.[13] Another possible downstream source of $N_2(a')$ could be the three-body recombination of atomic nitrogen.[8] However, N-atom number densities from this discharge source are below 10^{12} atoms cm^{-3}, a number density too small to produce significant $N_2(a')$ emission via three-body recombination at pressures below a torr. We verified this point by failing to find $N_2(a')$ in the afterglow of a microwave-discharge source of atomic nitrogen with atom number densities on the order of 10^{12} atoms cm^{-3} and total pressures below 2 torr.

3. RESULTS

A. Spectral Characterization and radiative lifetime of $N_2(a'^1\Sigma_u^-, v'=0)$

Figure 1 shows the spectrum observed in our reactor. The only significant emissions between 140 and 180 nm are transitions from the lowest vibrational level of the a and a' states. We estimated a relative monochromator response function from the intensities of the various Lyman-Birge-Hopfield bands ($N_2(a - X)$; LBH) assuming a constant transition moment for the a - X emission.[19] With this response function, we could then estimate the relative transition-moment variation for the Ogawa, Tanaka, Wilkinson, Mulliken bands ($N_2(a' - X)$; OTWM) using the Franck Condon Factors given in Lofthus and Krupenie.[20] Not surprisingly, our results agree quite well with those of Casassa and Golde who used a similar procedure. The relative response function, and the transition probabilities calculated with the transition moment variation we had determined allow us to fit the two band systems with our synthetic spectral fitting code.[11] The heavy line in Figure 1 shows the results of the fit compared to the experimental observations which are shown with the light line. Spectral fits to a number of spectra showed that the ratio of the intensities of the LBH to the OTWM bands is 1.71 ± 0.05 at 300K.

Golde[6] has already shown that this ratio is independent of argon pressure over the range 0.5 to 4 torr. Our observations show that quenching the bands significantly by adding N_2O and CO_2 also does not change this ratio. The two emissions are therefore in a steady-state ratio in our reactor. We can use this observation to estimate a lower limit to the lifetime of the $N_2(a')$ state. We need consider only the following three reactions:

$$N_2(a'\,^1\Sigma_u^-) + Ar \underset{k_{-1}}{\overset{k_1}{\rightleftarrows}} N_2(a\,^1\Pi_g) + Ar \qquad (1)$$

$$N_2(a\,^1\Pi_g) + Ar \xrightarrow{k_2} N_2(X) + Ar \qquad (2)$$

$$N_2(a\,^1\Pi_g) \xrightarrow{k_3} N_2(X) + h\nu \quad . \qquad (3)$$

$N_2(a)$ is in steady state within our field of view because its radiative lifetime is only 80 μs.[21-27] The kinetic rate expressions derived from reactions (1) through (3) can be combined, therefore, to give the ratio of number densities of the two singlet metastables:

$$\frac{[N_2(a)]}{[N_2(a')]} = \frac{k_1[Ar]}{(k_{-1} + k_2)[Ar] + k_3} \quad . \qquad (4)$$

Since the ratio of the a to a' emission is independent of pressure,[6] quenching must dominate radiation and the radiative-decay rate, k_3, can be dropped from Eq. (4). The number density is the observed intensity multiplied by the radiative lifetime. The ratio of the rate coefficients k_i/k_{-1} is the Boltzmann equilibrium ratio,

$$\frac{k_1}{k_{-1}} = 2\, e^{-1212\ cm^{-1}/kT} \quad , \qquad (5)$$

where the factor of two accounts for the lambda doubling in the pi state. With these last three points in mind, we can rearrange Eq. (4) to get

$$\frac{I_a}{I_{a'}} = \frac{k_1}{k_{-1} + k_2} \frac{\tau_{a'}}{\tau_a} \quad . \qquad (6)$$

In the limit that deactivation to the a' state is the only significant pathway for a-state quenching, we can set a limit on the radiative lifetime of the a' state in terms of that of the a state:

$$\tau_{a'} \geq \frac{k_{-1}}{k_1} \frac{I_a}{I_{a'}} \tau_a \quad . \tag{7}$$

The radiative lifetime of $N_2(a)$ is still somewhat in doubt,[21-27] but a value of $80 \begin{smallmatrix} +40 \\ -20 \end{smallmatrix}$ μs apparently encompasses the correct value. Thus we find that

$$\tau_{a'} \gtrsim 23 \begin{smallmatrix} +11 \\ -6 \end{smallmatrix} \text{ ms} \quad . \tag{8}$$

This analysis is similar to that given by Casassa and Golde.[4] They used a different lifetime for $N_2(a^1\Pi_g)$, however, and reported $\tau_{a'} \geq 32$ ms. Their reanalysis of the experiments of Tilford and Benesch[3] yielded a lifetime of 17 ms. Thus they concluded that the true lifetime probably lay between 17 and 40 ms. We feel that the analysis of the ratio of a to a' intensities should give a more accurate assessment of the radiative lifetime than does the vuv absorption measurement of Tilford and Benesch which involves a comparison of densitometer tracings of $a'^1\Sigma_u^-$ and $A^3\Sigma_u^+$ absorptions rather than a direct curve-of-growth measurement. The major uncertainty in the present approach is the radiative lifetime of $N_2(a^1\Pi_g)$. Clearly what is needed is a good determination of that value.

B. Quenching Rate Measurements

The reactions important in our kinetic analysis involve quenching of the $N_2(a')$ by the species of interest, Q, diffusion to the walls of the reactor with subsequent deactivation, and quenching by the N_2 and Ar bath gas:

$$N_2^* + Q \rightarrow N_2(X) + Q' \tag{9}$$

$$N_2^* + \text{wall} \xrightarrow{k_w} N_2(X) + \text{wall} \tag{10}$$

$$N_2^* + X_i \rightarrow N_2(X) + X_i^* \ , \tag{11}$$

where X_i represents other quenching species such as N_2, Ar, etc. The differential equation describing the rate of change in the number density of the metastables with time is

$$\frac{d[N_2^*]}{dt} = - \left\{k_9[Q] + \sum_i k_{11}^i[X_i] + k_w\right\} [N_2^*] \ . \tag{12}$$

Because the number density of the quenchers is much larger than that of the metastables, it remains constant (it would in any event if the reaction involves energy transfer rather than reaction). Thus we can solve Eq. (12):

$$\ell n \frac{[N_2^*]}{[N_2^*]_o} = - \left\{k_9[Q] + \sum_i k_{11}^i[X_i] + k_w\right\} t \ . \tag{13}$$

Keeping the reaction time fixed and varying the number density of the quencher gives the decay coefficient ,Γ, defined by

$$\frac{d\ \ell n[N_2^*]}{d[Q]} = - k_9\ z/\bar{v} = \Gamma(z) \ , \tag{14}$$

where the reaction time is given by the ratio of the distance from the injector to the observation region, z, to the bulk flow velocity, $\bar{v}$. Finally, the rate coefficient results from the slope of a plot of Γ versus z:

$$k_9 = -\bar{v} \frac{d\Gamma}{dz} \ . \tag{15}$$

This procedure corrects for imperfect mixing at the injector. Figure 2 shows semilog plots according to Eq. (14) for the quenching of $N_2(a')$ by NO at three different reaction times. Figure 3 shows plots of decay coefficient versus z for three different quenchers.

The above analysis assumes plug flow. The rate coefficients derived from plots according to Eqs. (14) and (15) must be divided by 0.62 to correct for the coupling of a radial density gradient in the metastable number density with a parabolic velocity profile. A number of papers in the literature discuss this effect in detail.[28-31]

Wall deactivation and relatively efficient quenching by molecular nitrogen constrained the experimental conditions to fairly low pressures and short reaction times. Several of the most inefficient quenchers, therefore, required fairly large additions of gas to the reactor in order to obtain adequate decays. In order to correct for any possible perturbation to the metastable number densities caused by injecting large mass flows of gas into the main flow, we measured apparent decays when comparable amounts of argon were added through the injector. We then corrected the measured decay coefficients of the quenchers of interest by subtracting the effective argon decay coefficients from them. This correction procedure assumes that argon is an inefficient quencher of $N_2(a')$. The decrease in the effective argon decay coefficient with increasing reaction time indicates this assumption is valid. The molecules N_2, CF_4, and SF_6 were corrected in this manner. This large addition of gas was still $\lesssim$ 7 percent of the total gas flow, so it did not perturb the flow field sufficiently to change the flow correction factor.

Table 1 summarizes our results. The error bars on the rate coefficients include the contributions from the standard deviations in the least squares

fits according to Eqs. (14) and (15), our estimates of the uncertainties involved in the calibrations of our flow meters, pressure gauge, thermometer, etc., and our estimate of the basic reproducibility of our measurements as determined in other kinetic investigations which involved multiple determinations of rate coefficients under a number of different conditions of pressure, total gas flow rate and flow velocity.[9,12,13]

C. The excitation of CO(A) by energy transfer from $N_2(a')$

When carbon monoxide is added to the metastables, emission from the CO fourth-positive system, $CO(A^1\Pi - X^1\Sigma)$, is observed. Golde and Thrush[32,33] have shown that CO fourth-positive emission is excited in the energy transfer between $N_2(a)$ and CO. In our system, however, the low steady-state number density of the $N_2(a)$ precludes that state as being the source of the observed CO(A) emission (see below). We conclude therefore, that it arises from energy transfer from $N_2(a')$:

$$CO(X^1\Sigma) + N_2(a'^1\Sigma_u^-) \rightarrow CO(A^1\Pi) + N_2(X^1\Sigma_g^+) \quad (16)$$

$$CO(A^1\Pi) \rightarrow CO(X^1\Sigma) + h\nu \quad . \quad (17)$$

The extremely rapid radiative lifetime of the CO(A)[34] prevents its being deactivated by electronic quenching under our conditions. Thus the CO(A) is in steady state in our observation region, and we can write

$$\frac{[CO(A)]}{I_{N_2(a')}} = \frac{k_{16}}{k_{17}} \tau_{a'} \quad . \quad (18)$$

We scanned the spectrum between 140 and 185 nm for varying amounts of added CO. We determined the number density of the emitting CO(A) molecules and the $N_2(a')$ and $N_2(a)$ emission intensities by spectral fitting. Figure 4 shows one such spectrum with its associated fit. The data derived from the

fits are plotted according to Eq. (18) in Figure 5 for vibrational levels 0-2 of CO(A). Excitation-rate coefficients derived from the slopes of the lines in Figure 5, assuming a radiative lifetime for $N_2(a')$ of $23 \pm {}^{11}_{8}$ ms, are given in Table 2. The results indicate that only $21 \pm {}^{10}_{8}$ percent of the quenching events between $N_2(a')$ and CO result in CO electronic excitation.

If the a-state rather than the a' state were responsible for exciting $CO(A^1\Pi)$, then our data would indicate an excitation rate coefficient of 5×10^{-9} cm^3 $molecule^{-1}$ s^{-1}, more than ten times gas kinetic. Golde and Thrush[33] previously have established that the rate coefficient for exciting CO(A) by $N_2(a)$ is only 1.5×10^{-10} cm^3 $molecule^{-1}$ s^{-1}. Thus we can confidently assign $N_2(a')$ as the precursor for CO(A) excitation in our system.

4. DISCUSSION

Dreyer and Perner[35] excited $N_2(a')$ with a pulsed relativistic electron beam in nitrogen gas and observed its temporal behavior via resonance absorption on the fifth-positive system of nitrogen. They analyzed their data to determine a rate coefficient for $N_2(a')$ quenching by molecular nitrogen of $(2.21 \pm 0.14) \times 10^{-13}$ cm^3 molecule^{-1} s^{-1} in excellent agreement with our value. Van Veen et al.[7] used a laser to excite $N_2(a\,^1\Pi_g, v'=0,1)$ via two-photon pumping. The variation in the fluorescence decay lifetimes with nitrogen pressure over the range of 0.05 to 10 torr indicated complete coupling between $N_2(a)$ and $N_2(a')$ at pressures above 1 torr, so that observed decays in that pressure region were diagnostic of $N_2(a')$ behavior. They reported a rate coefficient for quenching $N_2(a')$ by nitrogen of $(2.3 \pm 0.2) \times 10^{-13}$ cm^3 molecule^{-1} s^{-1}, again in excellent agreement with the present results.

Golde and Thrush[8] observed the behavior of $N_2(a)$ and $N_2(a')$ under various conditions in a flow of recombining nitrogen atoms and concluded that ratio of the rate coefficients for $N_2(a')$ quenching by Ar to that by N_2 was unity and that the similar ratio for CO_2 quenching to that by N_2 was 117 ± 20. Our results clearly indicate that quenching of $N_2(a')$ by argon must be much less efficient than quenching by nitrogen. If the argon quenching rate coefficient were the same as our nitrogen value, we calculate that the metastables would have a lifetime against quenching of 0.28 ms at the argon number density in our reactor. Thus it would not survive the 13 ms traversal time from the discharge to the observation region. The fact that $N_2(a')$ is observed in the observation region shows that $N_2(a')$ quenching by Ar is more than an order of magnitude slower than is quenching by N_2. Our results give a ratio of the CO_2

rate coefficient to that for N_2 of 129 ± 21 in good agreement with Golde and Thrush's observation.

We are unaware of any other quenching data on $N_2(a')$. Our rate coefficient for quenching by molecular oxygen indicates that quenching would be comparable to radiative decay at an altitude just below 105 km (assuming a radiative lifetime of 23 ms). Thus one cannot neglect the importance of $N_2(a')$ as a metastable energy carrier in modeling energy degradation in the disturbed upper atmosphere.

ACKNOWLEDGEMENTS

We appreciate support from the Defense Nuclear Agency and the Office of Scientific Research through contracts with the Air Force Geophysics Laboratories. We thank Lauren Cowles, Margrethe DeFaccio, and Bill Cummings for helping with the data analysis.

REFERENCES

1. P.G. Wilkinson and R.S. Mulliken, J. Chem. Phys. 31, 674 (1959).

2. S.G. Tilford, P.G. Wilkinson, and J.T. Vanderatice, Astrophys. J. 141, 427 (1965).

3. S.G. Tilford and W.M. Benesch, J. Chem. Phys. 64, 3370 (1976).

4. M.P. Casassa and M.F. Golde, Chem. Phys. Let. 60, 281 (1979).

5. W.J. Marinelli and B.D. Green, Manuscript in preparation.

6. M.F. Golde, Chem. Phys. Let. 31, 348 (1975).

7. N. Van Veen, P. Brewer, P. Das, and R. Bersohn, J. Chem. Phys. 77, 4327 (1982).

8. M.F. Golde and B.A. Thrush, Proc. R. Soc. A. 330, 79 (1972).

9. L.G. Piper, G.E. Caledonia, and J.P. Kennealy, J. Chem. Phys. 74, 2888 (1981).

10. L.G. Piper and W.T. Rawlins, J. Phys. Chem. 90, 320 (1986).

11. L.G. Piper, W.J. Marinelli, W.T. Rawlins, and B.D. and Green, J. Chem. Phys. 83, 5602 (1985).

12. L.G. Piper, L.M. Cowles, and W.T. Rawlins, J. Chem. Phys. 85, 3369 (1986).

13. L.G. Piper, M.E. Donahue, and W.T. Rawlins, J. Phys. Chem. 91, XXXX (1987).

14. J.A. Meyer, D.W. Setser, and D.H. Stedman, J. Phys. Chem. 74, 2238 (1970).

15. L.G. Piper, manuscript in preparation.

16. L.G. Piper and W.J. Marinelli, PSI TR-591 (1986) and manuscript in preparation.

17. L.G. Piper and M.A. DeFaccio, manuscript in preparation.

18. W.G. Clark and D.W. Setser, J. Phys. Chem. 84, 2225 (1980).

19. M.J. Mumma, J. Opt. Soc. Amer. 62, 1459 (1972).

20. A. Lofthus and P.H. Krupenie, J. Phys. Chem. Ref. Data 6, 113 (1977).

21. D.E. Shemansky, J. Chem. Phys. 51, 5487 (1969), and private communication (1986).

22. R.F. Holland, J. Chem. Phys. 51, 3940 (1969).

23. W.L. Borst and E.L. Zipf, Phys. Rev. A 3, 979 (1971).

24. R.S. Freund, J. Chem. Phys. 56, 4344 (1972).

25. M.J. Pilling, A.M. Bass, and W. Braun, J. Quant. Spectrosc. Radiat. Transfer 11, 1593 (1971).

26. L.J. Curtis and P. Erman, J. Opt. Soc. Amer. 67, 1218 (1977).

27. F. Dahl and J. Oddershede, Phys. Scr. 33, 135 (1986).

28. E.E. Ferguson, F.C. Fehsenfeld, and A.L. Schmeltekopf, Adv. in Atomic and Molec. Phys. V (1970).

29. R.C. Bolden, R.S. Hemsworth, M.J. Shaw, and N.D. Twiddy, J. Phys. B 3, 45 (1970).

30. R.W. Huggins and J.H. Cahn, J. Appl. Phys. 38, 180 (1967).

31. J.H. Kolts and D.W. Setser, J. Chem. Phys. 68, 4848 (1978).

32. M.F. Golde and B.A. Thrush, Proc. R. Soc. Lond. A. 330, 97 (1972).

33. M.F. Golde and B.A. Thrush, Proc. R. Soc. Lond. A. 330, 109 (1972).

34. R.W. Field, O. Benoist d'Azy, M. Lavollee, R. Lopez-Delgado, and A. Tramer, J. Chem. Phys. 78, 2838 (1983).

35. J.W. Dreyer and D. Perner, Chem. Phys. Let. 16, 169 (1972).

Table 1. Results of $N_2(a'^1\Sigma_u^-)$ Quenching Studies

MOLECULE	QUENCHING RATE COEFFICIENT (cm^3 $molecule^{-1}$ s^{-1})
N_2	$(1.9 \pm 0.5) \times 10^{-13}$
O_2	$(2.8 \pm 0.6) \times 10^{-11}$
CO_2	$(2.5 \pm 0.6) \times 10^{-11}$
NO	$(3.6 \pm 0.8) \times 10^{-10}$
N_2O	$(1.7 \pm 0.4) \times 10^{-10}$
CH_4	$(3.0 \pm 0.8) \times 10^{-10}$
CO	$(1.1 \pm 0.3) \times 10^{-10}$
H_2	$(2.6 \pm 0.6) \times 10^{-11}$
CF_4	$(2.4 \pm 1.0) \times 10^{-13}$
SF_6	$(7.8 \pm 1.8) \times 10^{-14}$

Table 2. Results of $CO(A^1\Pi)$ Excitation by $N_2(a'^1\Sigma_u^-)$

v'	k_{ex} (cm^3 $molecule^{-1}$ s^{-1})*
0	$(11.7 \begin{smallmatrix}+ 5.5\\- 4.4\end{smallmatrix}) \times 10^{-12}$
1	$(6.8 \begin{smallmatrix}+ 3.1\\- 2.5\end{smallmatrix}) \times 10^{-12}$
2	$(3.8 \begin{smallmatrix}+ 1.7\\- 1.4\end{smallmatrix}) \times 10^{-12}$
3	$(0.8 \begin{smallmatrix}+ 0.5\\- 0.4\end{smallmatrix}) \times 10^{-12}$
TOTAL	$(23.1 \begin{smallmatrix}+ 10.8\\- 8.7\end{smallmatrix}) \times 10^{-12}$

*Assumes lifetime of $23 \begin{smallmatrix}+ 11\\- 6\end{smallmatrix}$ ms for $N_2(a'^1\Sigma_u^-)$

Figure 1. Spectrum of $N_2(a'^1\Sigma_u^-)$ and $N_2(a^1\Pi_g)$ 13 ms downstream from the discharge. The light line shows the experimental spectrum, the heavy line the synthetic best fit to the data.

Figure 2. The decay of $N_2(a'^1\Sigma_u^-)$ with added [NO] for three different reaction times.

Figure 3. Decay coefficients plotted against reaction time for $N_2(a'^1\Sigma_u^-)$ quenching.

Figure 4. Spectrum of $CO(A^1\Pi)$ excited by energy transfer from $N_2(a'^1\Sigma_u^-)$. The experimental spectrum is the light line, the synthetic best fit to the experimental data is the heavy line.

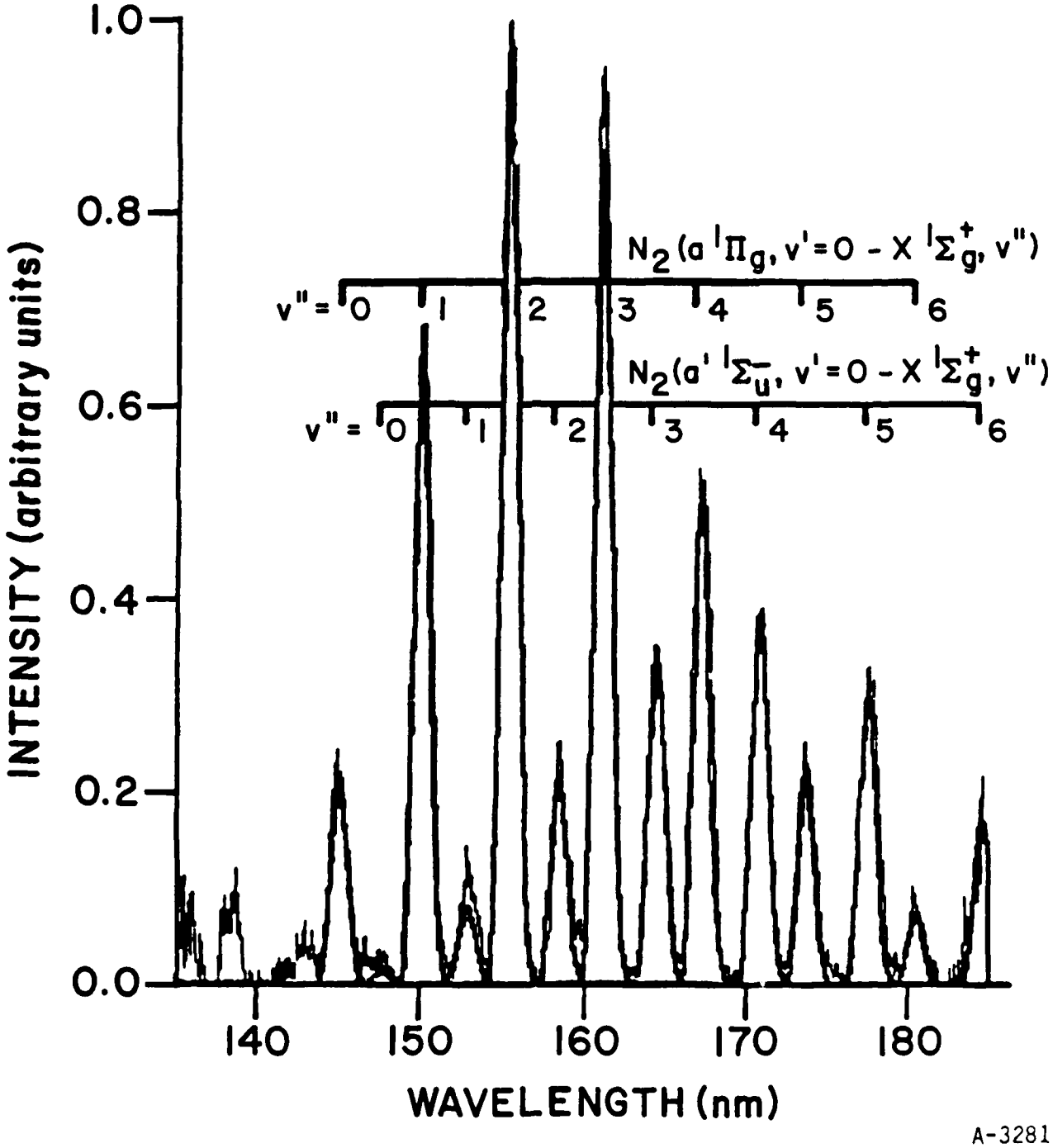
1.0
0.8
0.6
0.4
0.2
0.0
INTENSITY (arbitrary units)
$N_2(a\,^1\Pi_g, v'=0 - X\,^1\Sigma_g^+, v'')$
v" = 0 1 2 3 4 5 6
$N_2(a'\,^1\Sigma_u^-, v'=0 - X\,^1\Sigma_g^+, v'')$
v" = 0 1 2 3 4 5 6
140
150
160
170
180
WAVELENGTH (nm)
A-3281

FIGURE 1

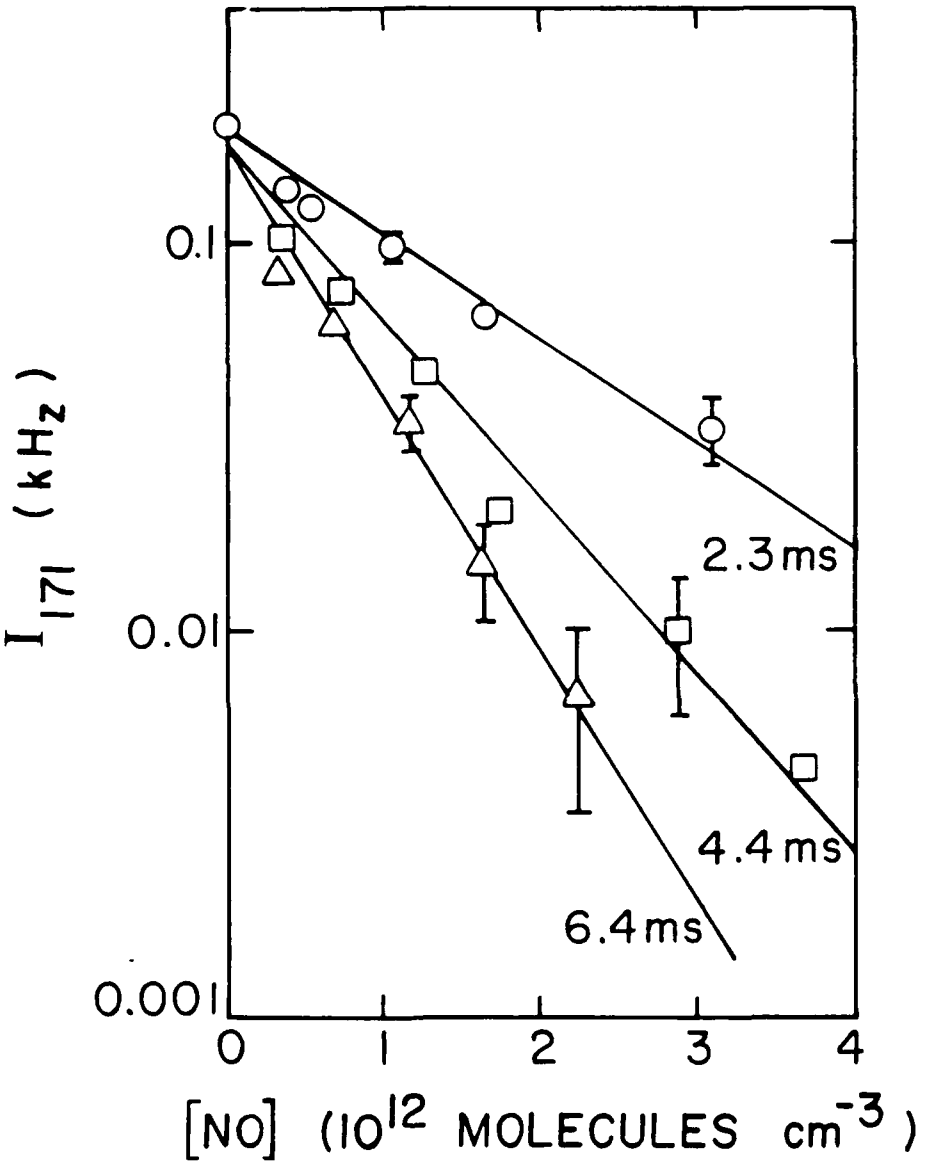
0.1
0.01
0.001
I_{171} (kHz)
2.3ms
4.4ms
6.4ms
0
1
2
3
4
[NO] (10^{12} MOLECULES cm^{-3})
A-3169

FIGURE 2

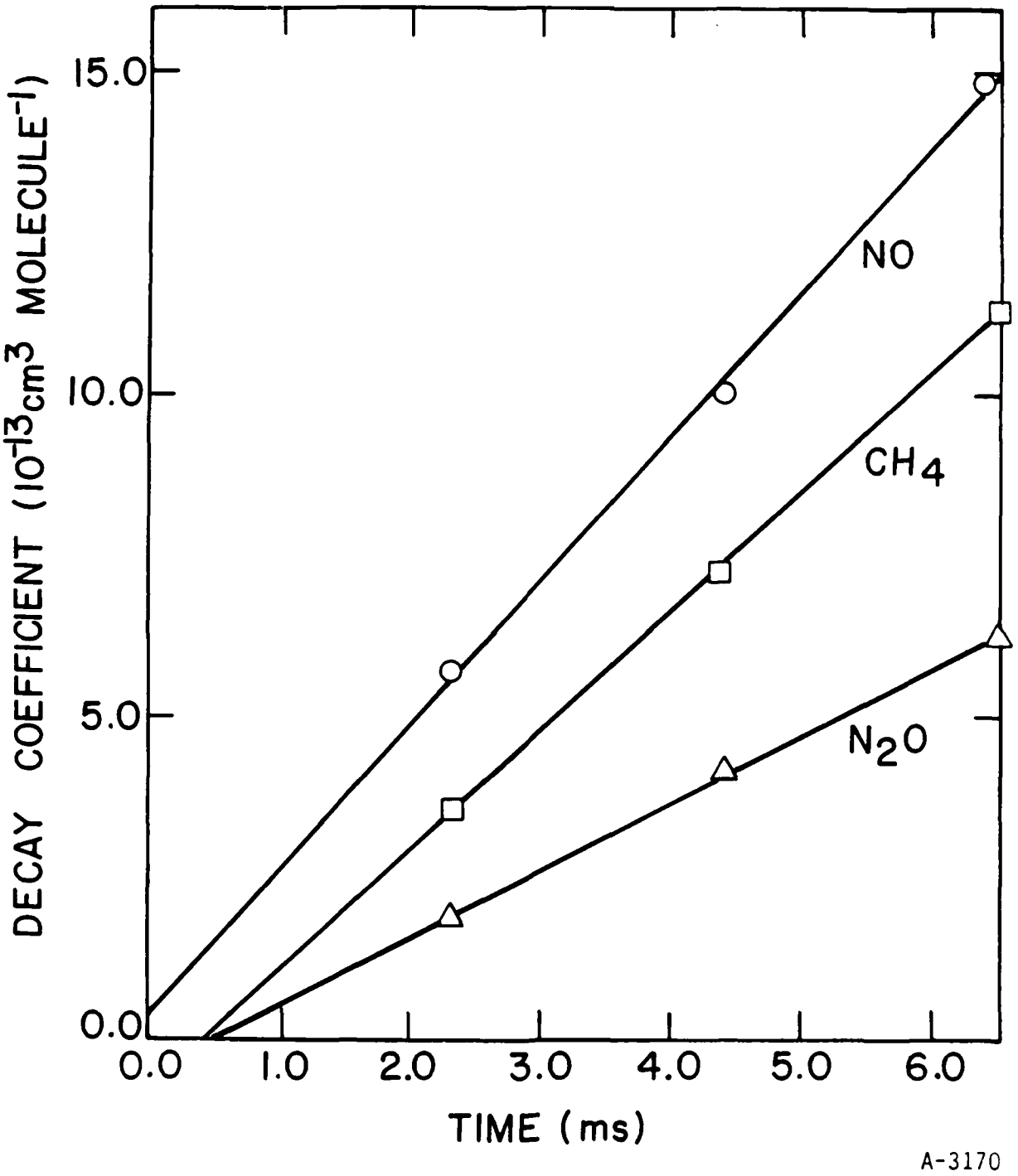
DECAY COEFFICIENT (10^{-13}cm^3 MOLECULE^{-1})
15.0
10.0
5.0
0.0
0.0
1.0
2.0
3.0
4.0
5.0
6.0
TIME (ms)
NO
CH_4
N_2O
A-3170

FIGURE 3

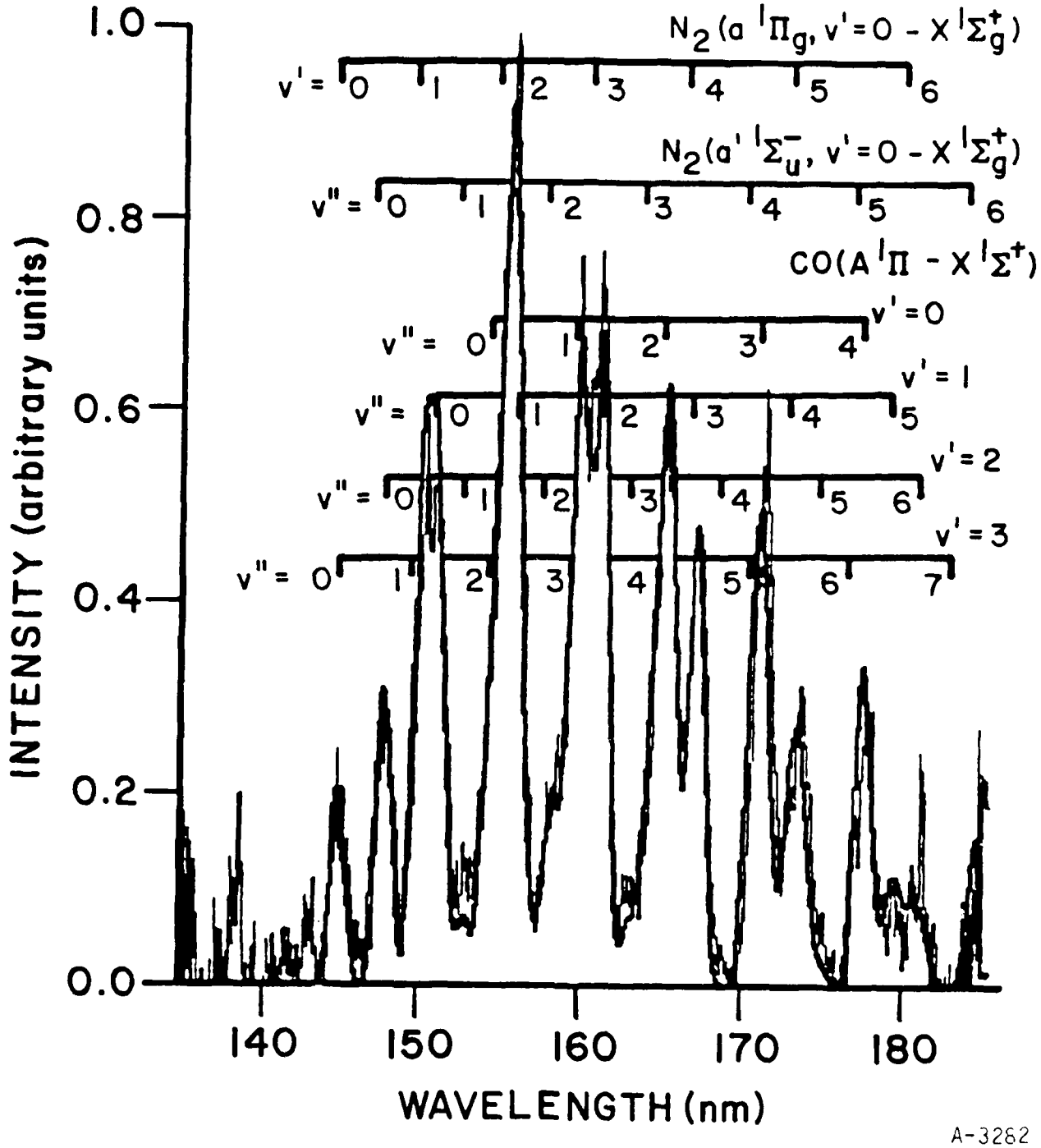
1.0
0.8
0.6
0.4
0.2
0.0
INTENSITY (arbitrary units)
140
150
160
170
180
WAVELENGTH (nm)
N2(a 1Πg, v'=0 - X 1Σ+g)
v' = 0 1 2 3 4 5 6
N2(a' 1Σ-u, v'=0 - X 1Σ+g)
v" = 0 1 2 3 4 5 6
CO(A 1Π - X 1Σ+)
v' = 0
v" = 0 1 2 3 4
v' = 1
v" = 0 1 2 3 4 5
v' = 2
v" = 0 1 2 3 4 5 6
v' = 3
v" = 0 1 2 3 4 5 6 7
A-3282

FIGURE 4

APPENDIX M

(SR-353 reproduced in its entirety)

J. Chem. Phys. 90, XXXX (1989)

PSI-9057
SR-353

EXPERIMENTAL DETERMINATION OF THE EINSTEIN COEFFICIENTS FOR THE $N_2(B-A)$ TRANSITION

Lawrence G. Piper, Karl W. Holtzclaw, and B. David Green
Physical Sciences Inc.
Research Park, P.O. Box 3100
Andover, MA 01810

and

William A.M. Blumberg
Air Force Geophysics Laboratory/LSI
Hanscom Air Force Base, MA 01731

January 1989

ABSTRACT

We have used a branching-ratio technique to measure the relative variation in the transition-dipole moment with internuclear separation for the N_2(B-A) transition. Our spectral observations cover the range from 500 to 1800 nm, and use several different detectors and excitation sources. The data from different sets are consistent in the regions of spectral overlap. Using well established values for the radiative lifetimes of N_2(B,v'>5) allows the relative dipole-moment function to be placed on an absolute basis. From the dipole-moment function and a set of RKR-based Franck-Condon factors which we have computed, we derive Einstein coefficients covering the range v'=0-12 and v"=0-20. Our results indicate that currently accepted lifetimes for N_2(B,v'=0-2) should be revised upwards by 20 to 40 percent.

I. INTRODUCTION

The currently accepted experimental values for the N_2(B-A) Einstein coefficients (i.e., as tabulated in Lofthus and Krupenie[1]) rest upon the variation in the electronic transition moment as a function of internuclear separation determined by Shemansky and Broadfoot.[2] Using a branching-ratio technique and the r-centroid approximation,[3] they determined the relative variation in the transition moment with internuclear separation between 1.30 and 1.55Å. They placed this relative curve on an absolute basis by adjusting it to give a lifetime for $v'=3$ which agreed with one they determined directly by measuring real-time fluorescence decays following excitation of N_2 by a pulsed, electron beam.

This procedure gave lifetimes for $N_2(B^3\Pi_g)$ in modest accord (±15 percent) with those derived from most,[4-6] but not all,[7] recent theoretical transition-moment functions for $v' \geq 5$. The theoretical lifetimes all become increasingly longer than those derived from Shemansky and Broadfoot's work, however, for the lowest vibrational levels. This discrepancy reaches 50 percent for $v'=0$. Even for the higher vibrational levels, where the agreement in the total radiative lifetimes between theory and experiment is adequate, the branching ratios for radiation from a given upper vibrational level to the various lower levels differ greatly between theory and experiment.

Shemansky and Broadfoot's Einstein coefficients for the lowest vibrational levels of N_2(B) result from extrapolations of their transition-moment curve well outside the region of the measurements used to establish it. This procedure is prone to systematic error. To reconcile experiment and theory we have redetermined the relative transition-moment variation as a function of internuclear separation, using a procedure similar to that used by Shemansky and Broadfoot, but with measurements extending over a much greater range, 1.15 to 1.70Å.

The first-positive bands arise from the $N_2(B^3\Pi_g - A^3\Sigma_u^+)$ transition, and are among the most prominent in nitrogen and air discharges of various types, in the disturbed upper atmosphere,[8,9] and in a number of chemiluminescent reactions.[10-14] In addition, laser oscillation has been observed from these bands.[15,16] In order to understand excitation mechanisms of the various first-positive sources or to quantify first-positive band lasing, one must have accurate Einstein coefficients. Furthermore, a complete set of Einstein coefficients allows one to predict emissions accurately in one region of the electromagnetic spectrum based upon observations in another region, e.g., infrared radiances can be estimated from visible intensities.

II. THEORETICAL BASIS FOR MEASUREMENTS

The r-centroid approximation was first put forth by Fraser[3] and has been used extensively over the last three decades to evaluate the transition-moment function of a large number of molecular systems experimentally. Although this method has been criticized, several authors have demonstrated that it is generally accurate for most molecules having only slowly varying transition-moment functions[17-19] (hydrides and deuterides appear to be an exception).

The intensity of a molecular emission, in units of photons cm^{-3} s^{-1}, is given by

$$I_{v'v''} = N_{v'} A_{v'v''} \tag{1}$$

where $N_{v'}$ is the number density in the upper-state vibrational level and $A_{v'v''}$ is the Einstein coefficient,

$$A_{v'v''} = \frac{64\pi^4 \nu_{v'v''}^3}{3h} |\langle v'|R_e(r)|v''\rangle|^2 \quad . \tag{2}$$

Here $\nu_{v'v''}$ is the transition frequency in cm^{-1}, the integral is of the wavefunctions over the electric dipole-moment operator, and the constants have the usual meanings. This matrix element usually can be separated into two parts. One part represents the overlap of the wavefunctions of the two levels with each other, and is called the Franck-Condon factor. The other is the electronic transition moment which is a function of internuclear separation.

Fraser showed that the electronic transition moment could generally be represented adequately at discrete points by a function (usually polynomial or exponential) of the r-centroid. This quantity is an average r for each ($v' \rightarrow v''$) transition and is defined as

$$\bar{r}_{v'v''} = \frac{\langle v'|r|v''\rangle}{\langle v'|v''\rangle} \qquad (3)$$

By measuring the relative intensities of a number of bands with a common upper vibrational level, one can map out relative values for the electronic-transition moment at various r-centroids, and thereby determine the variation in the transition moment with internuclear separation. Combining Eqs. (1) and (2) and separating the dipole-moment matrix into its component parts gives

$$I_{v'v''} = \frac{64\pi^4 \nu_{v'v''}^3}{3h} N_{v'} q_{v'v''} \left|R_e(\bar{r}_{v'v''})\right|^2 \quad , \qquad (4)$$

where the Franck-Condon factor is

$$q_{v'v''} = \left|\langle v'|v''\rangle\right|^2 \quad . \qquad (5)$$

The ratio of measured band intensities to the product of the Franck-Condon factor times the cube of the transition frequency for each transition then gives a set of reduced intensities which should vary one from the other in the same way that the electronic transition moment varies with internuclear separation:

$$\frac{I_{v'v}/q_{v'v}\nu_{v'v}^3}{I_{v'v''}/q_{v'v''}\nu_{v'v''}^3} = \frac{\left|R_e(\bar{r}_{v'v})\right|^2}{\left|R_e(\bar{r}_{v'v''})\right|^2} \quad . \qquad (6)$$

This technique gives only the relative transition-moment variation. The transition-moment function is made absolute by normalizing to experimental lifetime or oscillator strength data.

The sum of the Einstein coefficients from a given upper level to all accessible lower levels equals the reciprocal of the radiative lifetime of that upper vibronic level

$$\sum_{v''} A_{v'v''} = 1/\tau_{v'} \quad . \tag{7}$$

Knowing the radiative lifetimes of $N_2(B,v)$ allows one to put the relative transition-moment function on an absolute basis (vide infra).

Oscillator-strength data can establish one Einstein coefficient from the set of relative Einstein coefficients absolutely:

$$A_{v'v''} = \frac{8\pi^2 e^2}{m_e c\, \lambda^2_{v'v''}} \frac{d}{d_u} f_{v'v''} \quad . \tag{8}$$

In Eq. (8) m_e is the electron rest mass, e its charge in esu, c the velocity of light, $\lambda_{v'v''}$ the transition wavelength in cm, d_u and d the electronic degeneracies of the upper and lower states, respectively, and $f_{v'v''}$ the oscillator strength. We are unaware of reliable oscillator-strength measurements for N_2 first-positive transitions.

We have measured the intensities of a number of first-positive bands over the wavelength region between 500 and 1700 nm. This set of sequences covers the $\Delta v=6$ through $\Delta v=-2$ sequences and samples a range of internuclear separations between about 1.15 and 1.7 Å. We have placed our relative measurements on an absolute scale using the experimental lifetimes of Eyler and Pipkin.[20]

III. EXPERIMENTAL

The experimental procedure involved determining first-positive spectra over the appropriate spectral regions under several different sets of conditions using monochromators with photoelectric detectors. Individual band intensities, $I_{v'v''}$, for each spectrum were determined using a computerized spectral-fitting procedure (see below). This procedure greatly reduces uncertainties introduced by spectral overlap with other first-positive bands or with other nitrogen band systems.

Three different monochromator/detector combinations and three different excitation sources were used in these studies. This allowed us to make multiple determinations of the data in the regions of spectral overlap. In addition, different excitation sources emphasize the formation of different vibrational levels. This allowed matching the source to the most appropriate wavelength region.

One approach consisted of looking at the excitation of nitrogen, at pressures on the order of a few millitorr, by a high energy electron beam of 4.5 kV and about 15 mA. The apparatus for these observations, the LABCEDE facility at the Air Force Geophysics Laboratory (AFGL), has been described in detail previously.[21] Basically it consists of a cylindrical vacuum chamber, 1m diameter by 3.4m long. The electron beam enters perpendicular to the chamber axis about 1.2m from the viewing port in one end. Gas flows through the region irradiated by the electron beam in a few milliseconds. This prohibits the buildup of beam-created species within the irradiated volume. A 0.3m monochromator with an S-1 photomultiplier monitored fluorescence in the chamber between 570 and 1050 nm. This spectral region encompasses the $\Delta v=4$ through $\Delta v=0$ sequences of the nitrogen first-positive system.

The second approach, which emphasized the short-wavelength region of the spectrum, involved observing atomic nitrogen recombination in a He/N_2 discharge afterglow. This source tends to emphasize excitation of the highest levels of

$N_2(B)$, $v'=9-12$. A 0.5m monochromator coupled to a thermoelectrically cooled photomultiplier with a GaAs photocathode was used for these measurements. They encompassed the spectral region between 500 and 850 nm, covering principally the $\Delta v=6$ through $\Delta v=2$ sequences of the first-positive system.

The third approach consisted of infrared observations of a low pressure (0.1-20 Torr), low power (10-20 Watts) microwave-discharge lamp in nitrogen. In these studies a 0.5m monochromator with an intrinsic Ge detector scanned the spectral region between 700 and 1700 nm. This covered the $\Delta v=2$ through $\Delta v=-2$ sequences of the nitrogen first-positive system.

All systems were calibrated for relative spectral response using a standard quartz-halogen lamp. The lamp and its power supply were obtained from Optronic Laboratories. When set up as prescribed on the calibration sheet, the lamp irradiance is certified to have an uncertainty of ± 2 percent between 500 and 1600 nm, and ± 4 percent between 1600 and 2500 nm. In the latter two systems, the light from the lamp was reflected off a $BaSO_4$ screen before passing through the entrance slit of the monochromator. The $BaSO_4$ screen is a uniform, diffuse reflector. Its reflectivity is 99 $\pm$ 1 percent between 300 and 1000 nm, and declines only slightly at longer wavelengths (94 percent at 1700 nm).[22,23] We did correct for the decrease in reflectivity at the longer wavelengths.

The reason for using the $BaSO_4$ screen is to ensure the monochromator optics are filled. When the monochromator views the lamp directly, only a small portion of the grating is illuminated, and the location of the lamp image on the grating becomes a sensitive function of lamp placement. Irradiaing small grating imperfections could distort the response of the instrument to the radiation. Under filling the monochromator optics also can affect the location of the lamp image on the detector element. Any non-uniformities in detector responsivity with position across the detector surface, therefore, could lead to a distorted response-function calibration. The $BaSO_4$ screen eliminates these potential difficulties.

We confirmed the response function of the latter two systems with a second quartz-halogen lamp (also from Optronic Laboratories) and with a 1250 K black body (from Infrared Associates). Relative response functions derived from all three standard sources agreed to within ±5 percent. As a final crosscheck of the relative response of the latter two systems, we compared observed intensities of the O/NO air afterglow continuum with published values.[24-29] Good agreement was found in the region between 400 and 650 nm,[24-27] but not in the infrared.[28-29] Apparently most published values for the relative variation of air afterglow intensity as a function of wavelength are erroneous for $\lambda > 900$ nm. Recent observations by Bradburn and Lilenfeld[30] over this same spectral region support our findings.

IV. FITTING PROCEDURE

Individual band intensities were calculated from vibrational level populations determined by a spectral fitting technique.[31] We fit regions containing only one prominent transition from the level of interest, i.e., fitting single sequences. The spectral fitting code determines vibronic-level number densities within an electronic state and corrects for spectral overlap between different bands. The general procedure involves calculating synthetic spectra whose magnitudes correspond to unit population for the bands of interest. The populations of these emitters are then adjusted in a linear least-squares fitting routine to reproduce the observed spectrum.

Spectral simulation begins by calculating line positions and their relative intensities following the methods of Kovacs.[32] This procedure generates a stick spectrum which is then convoluted with a triangular slit function whose full width at half maximum equals the monochromator band pass. We confirmed the appropriateness of a triangular slit function by scanning the monochromator over the atomic-line spectrum emanating from a pen-ray lamp, and then measuring the shapes of the spectral lines.

We used the spectroscopic constants of Roux et al.[33] to calculate band positions and found them to agree with our observations. Synthetic spectra generated from the constants tabulated in Lofthus and Krupenie[1] could not adequately reproduce the wavelengths of the higher v′ levels (even after correcting for the sign error on $\omega_e y_e$ for the A state in Lofthus and Krupenie).

The distribution of rotational populations was taken to be Boltzmann. Rotational temperatures for the microwave discharge spectra were chosen to give the best match to the observed rotational contours of the bands. These rotational temperatures varied between 450 and 1000 K in accord with our observations on microwave-discharge lamps using other techniques.[34] The other two excitation sources produced spectra with a room temperature, 300 K, rotational distribution.

Spectral overlap is a problem in all band sequences. Generally bands from higher vibrational levels of the $\Delta v=n-1$ sequence overlap with the lower vibrational levels in the $\Delta v=n$ sequence. This problem is particularly severe for the $\Delta v=+3$, $+2$, $+1$, and 0 sequences. The infrared afterglow system ($B'^3\Sigma_u^- - B^3\Pi_g$) and several sets of atomic-nitrogen lines contaminate the microwave-discharge spectra. The infrared afterglow system also affects the atom-recombination data. In addition, overlap with $\Delta v=n-1$ first-positive bands is particularly severe in these data due to the larger relative populations of the high v' levels. The N_2^+ Meinel bands ($A^2\Pi_u-X^2\Sigma_g^+$) are prominent in the electron-impact excitation spectra. Spectral constants of Roux et al.[35] and Lofthus and Krupenie[1] were used to calculate the line positions of the B'-B and A-X systems, respectively.

The extent of the overlap determined the fitting strategy. In instances of partial overlap, the code determined the populations of all emitting species directly. With complete overlap or overlap from more than one band system, populations of the contaminating species were estimated by fitting adjacent regions of the spectrum which afforded more reliable estimates. These populations were then used to generate a synthetic spectrum of interfering emissions in the region of interest that subsequently was subtracted from the data. Fitting the residual spectrum then determined the intensities of interest. Bands for which the relevant feature coincided with another band of comparable or greater intensity, or which were severely overlapped with a significant band for which no independent population estimate could be made, were not used in the transition-moment determination.

Figures 1 and 2 illustrate the capabilities of the spectral fitting procedure. They show successive approximations in the fitting of the $\Delta v=0$ sequence in the data taken on LABCEDE. The data are displayed as the light line, the fit as the smoother, darker line. In Figure 1 only the $v'=0-5$ levels of $N_2(B)$ and some atomic lines were included in the fit. Large discrepancies are evident in the fit, particularly around 920 and 950 nm. These regions contain the 1,0 and 2,1 Meinel bands. Including the Meinel bands

in the fit and estimating contributions from the 7,8 and 6,7 first-positive bands gives the result displayed in Figure 2. The entire spectral region is fit excellently, lending confidence to the accuracy of the intensity determinations.

Situations involving subtraction of interfering emissions could result in systematic errors. The particular Einstein coefficients used in the estimates determined the magnitudes of the intensities to be subtracted.[36] In regions of the spectrum where such subtraction has the potential to produce significant errors, there is overlap of data using at least two excitation methods that produce spectra with markedly different characteristics. Systematic errors would be manifest, therefore, as differing trends in the $R_e(\bar{r})$ curves from the different data. All systems showed similar trends, however, indicating the relatively minor role of such systematic errors.

The r-centroids and Franck-Condon factors necessary for the evaluation of the reduced intensities and the construction of the $R_e(\bar{r})$ curve were calculated by W.J. Marinelli and T. Quagliaroli of PSI using a procedure outlined previously.[37] Rydberg-Klein-Rees potentials were first calculated for both electronic states using the spectroscopic constants of Roux et al.[35] and the approach of Tellinghuisen.[38] The numerical eigenfunctions were then evaluated using the Numerov-Cooley procedure[39] to solve the radial Schrodinger equation. The overlap integrals in the r-centroid and Franck-Condon-factor calculations were evaluated using Simpson's Rule. The results, which cover the range of $v'=0-12$ and $v''=0-24$, are more extensive than other calculations,[1,35] but agree quite well with them in regions of overlap. We have tabulated them elsewhere.[40]

V. RESULTS

The reduced intensities were averaged for all spectra taken with a given excitation method. A total of four spectra were analyzed for the discharge data, three for the atom-recombination data, and two for the data taken with the LABCEDE facility. The data were combined to form the relative transition-moment curve by minimizing the sum of the squares of the differences of the normalized reduced intensities for each progression from the analytical expression which best represented all the data. In practice, we determined the best fit of a given analytical form to the reduced intensities of one progression, e.g., $v'=2$ or $v'=10$, and then varied the intensity normalization factor of each of the other progressions to obtain the minimum least-squares deviation from that analytical expression. We then recomputed the best-fit analytical expression to the adjusted progressions. This defined a new line, and the individual progressions were again adjusted to match this line. After several iterations, further adjustment of the progressions did not significantly improve the fit between all of the data and the analytical form which best represented them. The final result was independent of the initial progression chosen to begin the fitting procedure.

We tried both linear and quadratic expressions to represent R_e as a function of $\bar{r}_{v'v''}$. The fitting procedure showed the quadratic term not to be statistically significant. A few trials with a cubic function also did not improve the fit. The best linear fit was

$$R_e(\bar{r}_{v'v''}) = (1.67 \pm 0.04) - (0.654 \pm 0.030)\ \bar{r}_{v'v''} \quad . \tag{9}$$

Figure 3 shows the relationship between this line and the experimental data.

The relative transition-moment curve shown in Figure 3 was placed upon an absolute basis by multiplying Eq. (9) by a normalization factor, ζ, that would bring radiative lifetimes calculated from our set of Einstein coefficients into congruence with the experimental values of Eyler and Pipkin.[20] That is

$$\zeta \sum_{v''} q_{v'v''} \nu^3_{v'v''} \left|R_e(\bar{r}_{v'v''})\right|^2_{rel} = \frac{1}{\tau_{v'}} \quad . \tag{10}$$

We found a value of $\zeta = (1.89 \pm 0.03) \times 10^{-7}$ provided agreement between our calculations and all of Eyler and Pipkin's experimental lifetimes. These lifetimes, which cover the range v'=5-12, should be the most accurate available because they were determined via laser-induced fluorescence in a molecular beam under collision-free conditions. We note, however, that this set of lifetimes appear to be 10 to 15 percent shorter than those determined in the most reliable of the other experimental[2,41-44] or theoretical studies.[3-5] Our selection of a different set of lifetimes would alter our transition-moment curve by five to seven percent. We discuss lifetimes further in the next section.

The normalization factor, ζ, and the constants in Eq. (4) allow us to re-normalize the relative transition-moment variation given by Eq. (8) so that R_e can be expressed in Debye:

$$R_e(D) = (1.30 \pm 0.03) - (0.508 \pm 0.02)\, \bar{r}_{v'v''} \quad . \tag{11}$$

The normalization procedure requires summing over all significant transitions. The best test for completeness is to sum the Franck-Condon factors from a given v' over all v". The resultant sum should be close to unity. For v'=0-10, $\sum_{v''=0}^{20} q_{v'v''} \geq 0.9$, so our set of relative Einstein coefficients is sufficiently complete for accurate normalization in Eq. (10). While the sum for v'=11,12 is somewhat smaller, our results still are sufficiently complete. Even if the Franck-Condon factor for transitions to v"=21 made up the balance of the difference between the Franck-Condon factor sum up to v"=20 and unity, the ν^3 term in Eq. (4) is so small that for these additional transitions our twenty-one term sum over the relative $A_{v'v''}$ would be augmented by less than one percent.

In practice a small correction to the sum in Eq. (10) should be made to include radiative transitions to other electronic states, in this case $W^3\Delta_u$ and $B'^3\Sigma_u^-$. Werner et al.[5] indicate that the largest of these corrections range from about five percent for $v'=12$ to less than three percent for $v'=5$. Their incorporation into our analysis will yield a normalization factor, ζ, which is the same within experimental error as the value we have used. We have chosen, therefore, not to make these corrections.

Table 1 contains a complete set of N_2(B-A) Einstein coefficients.

VI. DISCUSSION

A. Transition-Moment Functions

The present results agree much better with theoretical calculations[3-6] of the transition-moment function than with the results of previous empirical investigations.[2,45-49] In all cases agreement on the shapes is quite good over the range 1.1 to 1.7 Å. Agreement with absolute magnitudes of the transition-moment function is also quite good, generally within 10 to 15 percent. Our measurements appear to have resolved the major discrepancies between theory and experiment.

Figure 4 compares our experimentally derived variation in electronic transition moment with internuclear separation with that determined by Shemansky and Broadfoot and with the theoretical calculation of Werner et al.[5] The shape of our curve matches that of Werner et al. quite well. Consequently, our results agree quite well with theirs on the relative variation of lifetimes as a function of vibrational level and on the radiative branching ratios from a common upper vibrational level to the various lower levels. In contrast, Shemansky and Broadfoot's transition-moment function has a much different slope which results in a much different variation in lifetimes with vibrational level and set of branching ratios.

Werner et al. have reviewed the various experimental and theoretical transition-moment functions. All of the previous empirical values[45-49] diverge even more widely from our results than those of Shemansky and Broadfoot.[2] These discrepancies can result from a number of factors depending upon the approach taken. For example, measurements of band intensities require extreme care in determining instrument response function, in separating out contributions to the apparent band intensity from overlapping radiators, and in avoiding experimental pitfalls such as self reversal which apparently can be a problem using high intensity sources.[49-51]

Accurate response-function determinations require uniformly filling the optical system with the calibration lamp output as well as with the radiation source being measured. Monochromator optics usually cannot be filled by placing a tungsten strip lamp in front of the entrance slit. Rather, illumination from the strip lamp must be reflected into the monochromator from a diffuse white source such as a $BaSO_4$ screen[22,23] or a Spectralon® target.[51]

The first-positive system is subject to significant overlap from interfering radiators. This interference is so pervasive that accounting for it requires spectral-fitting capability. Shemansky and Broadfoot did use spectral fitting in their analysis. Other groups measuring band intensities did not.

Jeunehomme[46] tried to infer a transition-moment function from lifetime measurements of various vibrational levels. Generally, radiative lifetimes cannot be determined accurately enough for this procedure to prove successful. In even the best circumstances, radiative lifetime variations with v' are fairly insensitive to the form of the transition-moment function. This is because the total radiative decay rate (the inverse of the radiative lifetime) is the sum of a number of components which, taken together, sample a wide range of internuclear separations. Comparing to experimental variations in radiative lifetime, however, provides a good cross check to a transition-moment function derived from other measurements (vide infrared).

Several groups also have attempted to measure transition moments by observing the radiation emitted by high temperature gases in thermal equilibrium.[49,53-56] In this approach, the gas generally is heated by a shock wave or high current arc. These measurements often are plagued by interfering impurity emissions, and generally lead to overestimates of transition probabilities. Such measurements have proven to have uncertainties of factors of two to three.

B. Radiative Lifetimes

Figure 5 compares lifetimes calculated from the present results with those of Shemansky and Broadfoot[2] as well as the recent measurements of Eyler and Pipkin[20] and the theoretical calculations of Werner et al.[5] Our transition-moment function reproduces quite well the change in lifetime with vibrational level observed by Eyler and Pipkin. The discrepancy between our results and those of Shemansky, on the other hand, is considerable. Although somewhat different in magnitude, our relative changes in lifetime with vibrational level match those calculated by Werner et al.

We scaled Werner et al.'s results to Eyler and Pipkin's lifetimes by first fitting their transition-moment variation to a quadratic function. This quadratic function was used as a relative R_e function to calculate relative transition probabilities. The relative probabilities were then made absolute by applying the procedure given by Eq. (10). This resulted in a nine percent increase in Werner et al.'s transition-moment curve at every point. The result of this procedure is a set of lifetimes which agree with ours to better than five percent.

Similar treatment of the theoretical transition-moment functions of Yeager and McKoy[3] and Weiner and Öhrn[4] result in even smaller increases in the magnitude of their functions. Rizzo et al.'s[6] function, on the other hand, requires a 12 percent decrease in magnitude for it to come into congruence with ours. Their transition-moment function results in a set of radiative lifetimes more than 20 percent shorter than those measured by Eyler and Pipkin.[20]

A number of groups have reported experimental values for radiative lifetimes of various vibrational levels of $N_2(B)$.[20,41-44,57,58] Table 2 summarizes some of them. In most instances the measurements involved fitting multiexponential decays at a number of pressures and extrapolating one of the decay components to zero pressure. This approach generally is hazardous unless the lifetimes of the various components in the decay differ greatly. The $N_2(B)$

state is collisionally coupled to various levels of the $B'^3\Sigma_u^-$, $W^3\Delta_u$, and $A^3\Sigma_u^+$ states.[42,44,58-63] Coupling effects are manifest even at pressures as low as a mTorr.[42,44,63] This coupling typically leads one to overestimate the radiative lifetime. Eyler and Pipkin's measurements, having been made by laser-induced-fluorescence techniques in the collision-free environment of a molecular beam, should be free from these effects of interstate coupling.

Our results indicate lifetimes for vibrational levels 0 and 1 $N_2(B)$, that are 36 percent and 24 percent longer, respectively, than those given by Shemansky and Broadfoot.[2] The discrepancy could be even greater since Shemansky and Broadfoot's values for the highest vibrational levels are 10 to 15 percent longer than ours. Scaling their results down accordingly would lead to discrepancies greater than 50 percent for $v'=0,1$. Ortiz et al.[57] and Heidner et al.'s[58] experimental values of 13 ± 1 μs and 10 ± 2 μs, respectively, for the radiative lifetime of $v'=0$ appear to confirm our result of 12.1 μs.

VII. SUMMARY AND CONCLUSIONS

We have determined the variation in the transition moment with internuclear separation for the N_2(B-A) transition. Our approach relies on the redundancy of intensity measurements from several different sources using several different detection systems to reduce possible systematic errors. We have made extensive use of spectral fitting to reduce uncertainties in band-intensity determinations caused by overlap with other bands or band systems. Our results agree well with several recent theoretical calculations, but show that substantial revision of currently accepted experimental values is necessary.

Number densities of N_2(B,v) determined in experiments on N_2(B) excitation by various sources result from dividing measured band intensities by the appropriate Einstein coefficient. Our results indicate that using the Einstein coefficients in Lofthus and Krupenie will result in <u>over</u> estimates of 30 to 60 percent for the number densities in v'=10-12 but <u>under</u> estimates of 20 to 30 percent in the lowest levels. This means that relative number densities of vibrational levels 0 and 12 could differ by 100 percent or more using our Einstein coefficients compared to previous values.

ACKNOWLEDGMENTS

We appreciate financial support from the Air Force Office of Scientific Research (Task 2310G4) and the Defense Nuclear Agency (Project SA, Task SA/SDI, Work Unit 00175) through contracts with the Air Force Geophysics Laboratory F19628-84-C-0057 and F19628-85-C-0032. W.J. Marinelli and T. Quagliaroli calculated the Franck-Condon factors used to reduce the data. Experimental and analytical contributions of H.C. Murphy and M.A. DeFaccio proved invaluable as did discussions with W.J. Marinelli and W.T. Rawlins.

REFERENCES

1. A. Lofthus and P.H. Krupenie, J. Phys. Chem. Ref. Data 6, 113 (1977).
2. D.E. Shemansky and A.L. Broadfoot, J. Quant. Spectrosc. Radiat. Transfer 11, 1385 (1971).
3. P.A. Fraser, Can. J. Phys. 32, 515 (1954).
4. D.L. Yeager and V. McKoy, J. Chem. Phys. 67, 2473 (1977).
5. B. Weiner, and Y. Öhrn, J. Chem. Phys. 80, 5866 (1984).
6. H.J. Werner, J. Kalcher, and E.A. Reinsch, J. Chem. Phys. 81, 2420 (1984).
7. A. Rizzo, R.L. Graham, and D.L. Yeager, J. Chem. Phys. 89, 1533 (1988).
8. A. Vallance Jones, Sp. Sci. Rev. 11, 776 (1971).
9. A. Vallance Jones, R.R. Meier, and N.N. Shefor, J. Atmos. Terr. Phys. 47, 623 (1985).
10. R.D. Kenner and E.A. Ogryzlo, Chemi- and Bioluminescence, J.G. Burr ed., New York: Marcel Dekker, 45 (1985).
11. S.J. David and R.D. Coombe, J. Phys. Chem. 89, 5206 (1985).
12. S.J. Davis and L.G. Piper, J. Phys. Chem. (submitted) (1989).
13. L.G. Piper, J. Chem. Phys. 88, 6911 (1988).
14. L.G. Piper, J. Chem. Phys. 91, XXXX (1989)
15. L.E.S. Mathias and J.T. Parker, Appl. Phys. Lett. 3, 16 (1963).
16. D.L. Franzen, B.L. Danielson and G.W. Day, IEEE J. Quant. Electron. 14, 402 (1978).
17. R.W. Nicholls, J. Quant. Spectrosc. Radiat. Transfer 14, 233 (1974).
18. J.L. McCallum, J. Quant. Spectrosc. Radiat. Transfer 21, 563 (1979).
19. S.M. Yazykova and E.V. Butyraskaya, J. Phys. B 13, 3361 (1980).
20. E.E. Eyler and F.M. Pipkin, J. Chem. Phys. 79, 3654 (1983).
21. L.G. Piper, B.D. Green, W.A.M. Blumberg and S.J. Wolnik, J. Chem. Phys. 82, 3139 (1985).

22. F. Grum and G.W. Luckey, Appl. Opt. 7, 2289 (1968).

23. F. Grum and T.E. Wightman, Appl. Opt. 16, 2775 (1977).

24. A. Fontijn, C.B. Meyer and H.I. Schiff, J. Chem. Phys. 40, 64 (1964).

25. M. Sutoh, Y. Morioka and M. Nakamura, J. Chem. Phys. 72, 20 (1980).

26. M. Vanpee, K.D. Hill and W.R. Kineyko, AIAA J. 9, 135 (1971).

27. A.M. Pravilov and L.G. Smirnova, Kinet. Catal. 19, 202 (1978).

28. M.F. Golde, A.E. Roche and F. Kaufman, J. Chem. Phys. 59, 3953 (1973).

29. A.T. Stair, Jr. and J.P. Kennealy, J. Chim. Phys. Chim. Biol. 64, 124 (1967).

30. G. Bradburn and H. Lilenfeld, J. Phys. Chem. 92, 5266 (1988).

31a. L.G. Piper, W.J. Marinelli, W.T. Rawlins, and B.D. Green, J. Chem. Phys. 83, 5602 (1985).
b. M.E. Fraser, W.T. Rawlins, and S.M. Miller, J. Chem. Phys. 88, 538 (1988).

32. I. Kovacs, Rotational Structure in the Spectra of Diatomic Molecules, London: Adam Hilger (1969).

33. F. Roux, F. Michaud and J. Verges, J. Mol. Spectrosc. 97, 253 (1983).

34a. M.A.A. Clyne and L.G. Piper, JCS Faraday 72, 2178 (1976).
b. W.T. Rawlins and L.G. Piper, Proc. Soc. Photo-Opt. Instrum. Engn. 279, 58 (1981).

35. F. Roux, D. Cerny, and J. Verges, J. Mol. Spectry. 94, 302 (1982).

36. The Einstein coefficients used in determining populations of the $v'>5$ overlapping first positive levels (overlap of the $\Delta v=n$ and $\Delta v=n-1$ sequences) as well as the infrared afterglow system are those found in Reference 5. Fitting involving the Meinel or Wu-Benesh bands did not require subtraction nor did more than one band from any v' occur in any fit, hence the values assumed for the Einstein coefficients of those systems are immaterial.

37. W.J. Marinelli and L.G. Piper, J. Quant. Spectrosc. Radiat. Transfer 34, 121 (1985).

38. J. Tellinghuisen, Comput. Phys. Commun. 6, 221 (1974).

39. J. Eccles and R. Malik, Quantum Chem. Prog. Exch. Bull. 13, 407 (1981).

40. B.D. Green, W.J. Marinelli, K.W. Holtzclaw, B.L. Upschulte, L.G. Piper and H.C. Murphy, LABCEDE Final PSI TR-756, (1988). Available from the authors upon request.

41. M. Jeunehomme, J. Chem. Phys. 45, 1805 (1966).

42. T.A. Carlson, N. Duric, P. Erman, and M. Larsson, Physica Scripta 19, 25 (1979).

43. M. Holstein, D.C. Lorents, J.R. Peterson, and J.R. Sheridan, Can. J. Chem. 47, 1858 (1969).

44. D.E. Shemansky, J. Chem. Phys. 64, 565 (1976).

45. R.G. Turner and R.W. Nicholls, Can. J. Phys. 32, 475 (1954).

46. M. Jeunehomme, J. Chem. Phys. 45, 1805 (1966).

47. B.E. Cunio and R.E.W. Jansson, J. Quant. Spectrosc. Radiat. Transfer 8, 1763 (1968).

48a. D.C. Jain and R.C. Sahni, J. Quant. Spectrosc. Radiat. Transfer 7, 475 (1967).
b. D.C. Jain, J. Quant. Spectrosc. Radiat. Transfer 12, 759 (1972), re-analysis of the measurments of Ref. 45

49. N.E. Kuzmenko, L.A. Kuznetsova, A.P. Monyakin, and Yu. Ya. Kuzyakov, J. Quant. Spectrosc. Radiat. Transfer 24, 29 (1980) and references therein.

50. M.E. Pillow and S.E.F. Smallwood, Proc. Phys. Soc. 80, 562 (1962).

51. D.C. Tyte, Proc. Phys. Soc. 80, 1354 (1962).

52. Labsphere, Inc., N. Sutton, NH.

53. J.C. Keck, J.C. Camm, B. Kivel and T. Wentink, Ir., Ann. Phys. 7, 1 (1959).

54. P.A. Allen, J.C. Camm, and J.C. Keck, J. Quant. Spectrosc. Radiat. Transfer 1, 269 (1961).

55. W.H. Wurster, J. Quant. Spectrosc. Radiat. Transfer 3, 355 (1963).

56. K.L. Wray and T.J. Connolly, J. Quant. Spectrosc. Radiat. Transfer 5, 111 (1965).

57. M. Ortiz, A. Perez, and J. Campos, Physica C 150, 440 (1988).

58. R.F. Heidner, III, D.G. Sutton, and S.N. Suchard, Chem. Phys. Lett. 37, 243 (1976).

59. N. Sadeghi and D.W. Setser, Chem. Phys. Lett. 77, 304 (1981).

60. A. Rotem, J. Nadler and S. Rosenwaks, Chem. Phys. Lett. 83, 281 (1981).

61. N. Sadeghi and D.W. Setser, J. Chem. Phys. 79, 2710 (1983).

62. A. Rotem and S. Rosenwaks, Opt. Engn. 22, 564 (1983).

63. B.D. Green, W.J. Marinelli, L.G. Piper and W.A.M. Blumberg, manuscript in preparation.

Table 1. Einstein Coefficients and Wavelengths for $N_2(B-A)$ Transitions[a]

v'/v" =	0	1	2	3	4	5	6	7	8	9	10	11	12	13	14	15	16	17	18	19	20	ΣAv'v"	τv'(μs)
0	4.756 1046.9	2.500 1231.7	0.797 1489.5	0.166 1874.1	0.026 2308.6	0.003 3752.8																8.284	12.12
1	7.481 888.4	0.038 1017.9	1.347 1187.8	0.990 1420.2	0.369 1757.0	0.088 2288.4	0.014 3250.7	0.001 5521.6														10.33	9.68
2	3.962 773.2	5.218 869.6	0.964 990.6	0.210 1147.1	0.747 1357.2	0.490 1653.9	0.178 2104.1	0.041 2867.5	0.005 4442.9													11.82	8.46
3	1.024 685.8	7.500 760.6	1.901 851.6	2.262 964.8	0.059 1109.2	0.275 1299.8	0.429 1562.5	0.235 1947.5	0.077 2565.3	0.016 3717.0	0.002 6614.8											13.78	7.26
4	0.154 617.3	3.292 677.2	8.069 748.5	0.147 834.5	2.382 940.4	0.578 1073.9	0.015 1247.1	0.255 1480.8	0.248 1812.7	0.117 2320.8	0.034 3194.7	0.005 5047.7										15.30	6.54
5	0.017 562.2	0.688 611.4	5.842 668.9	6.835 736.8	0.232 818.1	1.585 917.3	1.162 1040.8	0.075 1198.7	0.074 1407.3	0.189 1695.5	0.137 2118.9	0.058 2800.8	0.014 4079.4	0.002 7339.2								16.91	5.91
6	0.001 516.8	0.076 558.2	1.579 605.7	8.105 660.8	4.479 725.5	1.380 802.5	0.610 895.4	1.369 1009.8	0.368 1153.9	--	0.095 1592.4	0.128 1949.1	0.075 2492.8	0.262 3421.4	0.005 5362.5							18.30	5.46
7	--	0.003 514.2	0.200 554.3	3.060 600.1	9.536 653.0	2.180 714.7	2.610 787.5	0.059 874.6	1.146 980.7	0.691 1112.4	0.075 1280.3	0.019 1501.1	0.086 1804.2	0.079 2245.3	0.040 2944.8	0.012 4220.9	0.002 7275.9					19.80	5.05
8	--	--	0.013 511.7	0.477 550.5	4.655 594.7	9.952 645.4	0.582 704.2	3.259 773.1	0.094 854.8	0.671 953.2	0.861 1073.8	0.261 1225.0	0.004 1419.6	0.034 1679.1	0.066 2041.8	0.049 2583.4	0.022 3476.9	0.006 5225.3	0.001 10157.9			21.00	4.76
9	--	--	--	0.030 509.2	0.891 546.8	6.661 589.4	9.158 638.0	0.006 694.1	3.140 759.2	0.635 835.9	0.224 927.2	0.803 1037.8	0.465 1174.2	0.076 1346.3	0.002 1569.9	0.037 1871.6	0.048 2299.7	0.030 2953.3	0.012 4070.5	0.003 6405.6		22.22	4.50
10	--	--	--	0.001 474.4	0.072 506.8	1.524 543.2	8.506 584.3	7.736 630.9	0.340 684.3	2.435 745.9	1.335 817.8	0.005 902.7	0.554 1004.1	0.581 1127.3	0.206 1280.0	0.015 1473.6	0.009 1726.8	0.033 2070.9	0.033 2564.5	0.019 3329.1	0.007 4628.3	23.41	4.27
11	--	--	--	--	0.001 473.0	0.129 504.5	2.336 539.9	10.03 579.3	5.752 624.0	1.330 674.8	1.470 733.1	1.862 800.6	0.116 879.3	0.274 972.4	0.562 1084.0	0.344 1219.7	0.083 1388.1	0.001 1602.1	0.014 1882.4	0.027 2264.1	0.024 2798.3	24.35	4.11
12	--	--	--	--	--	0.004 471.6	0.232 502.2	3.338 536.3	11.24 574.4	3.657 617.2	2.383 665.5	0.546 720.8	2.025 784.0	0.475 857.2	0.041 942.6	0.413 1043.6	0.419 1164.5	0.181 1311.5	0.029 1493.6	--	0.015 2017.5	25.00	4.00

a. The order of entries is Av'v" in units of 10^4 s^{-1}
λv'v" in units of nm

Table 2. $N_2(B^3\Pi_g)$ Lifetimes in Microseconds

v'	This Work	Shemansky[44]	Eyler and Pipkin[20]	Jeunehomme[41]	Carlson et al.[42]	Holstein et al.[43]
0	12.1			9.0		
1	9.7			7.5		
2	8.5	7.6±0.5		7.0	8.3±0.5	7.5±0.2
3	7.3	6.6±0.2		6.8	7.4±0.5	6.6±0.3
4	6.5	6.1±0.2		6.5	7.0±0.5	
5	5.9	5.4±0.2	5.9±0.2	6.2	6.9±0.5	6.1±0.3
6	5.5	5.7±0.3	5.3±0.2	6.0	5.9±0.5	
7	5.1	5.3±0.3	5.0±0.2	5.3	5.7±0.5	
8	4.8	4.8±0.2	4.7±0.2	5.1	5.3±0.5	
9	4.5	5.0±0.2	4.4±0.2	4.8	5.4±0.5	4.9±0.3
10	4.3	5.2±0.3	4.3±0.2	4.4	5.9±0.5	
11	4.1	4.7±0.2	4.2±0.2		5.0±0.5	
12	4.0	4.5±0.3	4.1±0.2		4.6±0.5	4.1±0.2

FIGURE CAPTIONS

Figure 1. $\Delta v = 0$ Sequence Data (light line) and Fit (dark line) for $N_2(B-A)$ and Atomic Lines

Figure 2. $\Delta v = 0$ Sequence Data and Fit for $N_2(B-A)$, $N_2^+(A-X)$, and Atomic Lines with Estimated Contributions from Other $N_2(B-A)$ Sequences Subtracted

Figure 3. Experimentally Determined Variation in the Electronic-Transition Moment with r-centroid for the N_2 First-Positive System

Figure 4. Variation in Electronic Transition Moment with Internuclear Distance for the $N_2(B-A)$ Transition

Figure 5. Variation in $N_2(B)$ Radiative Lifetimes as a Function of Vibration Level

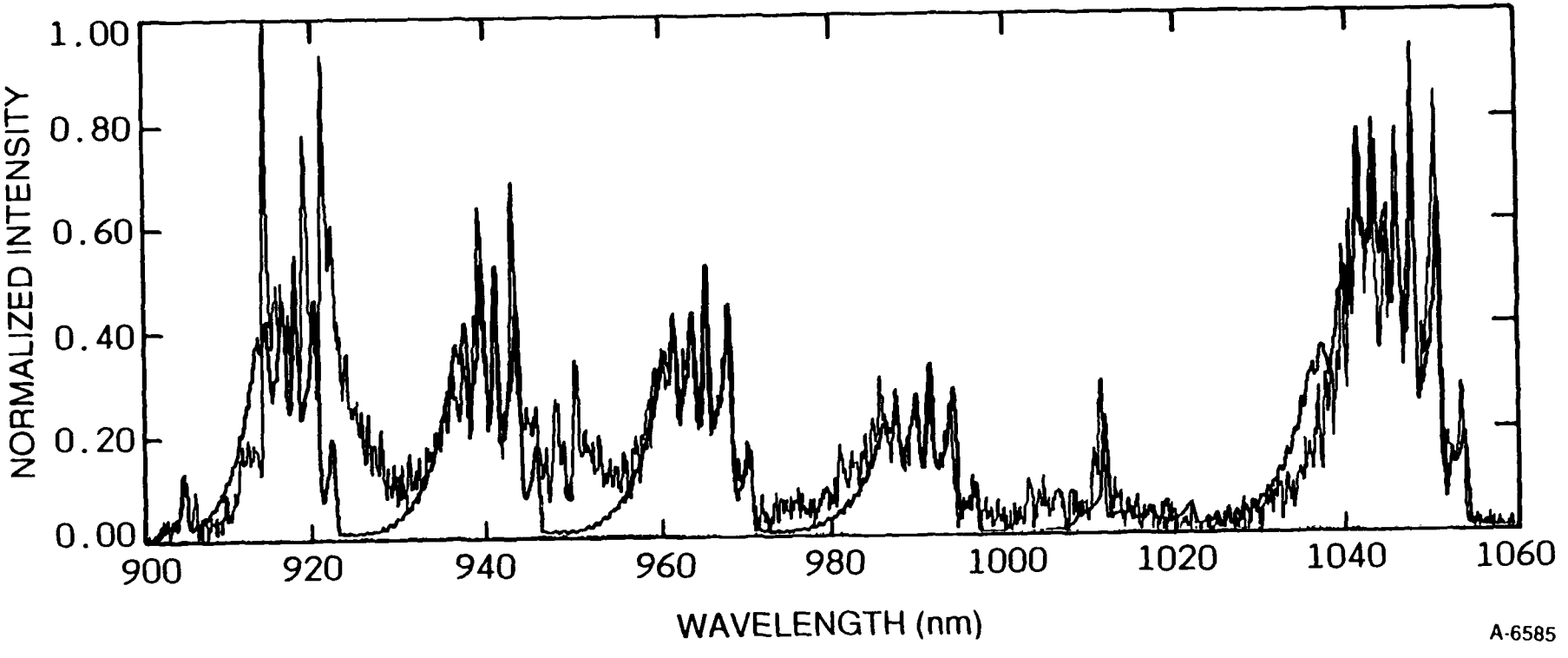

L.G. Piper et al.
J. Chem. Phys.
Figure 1

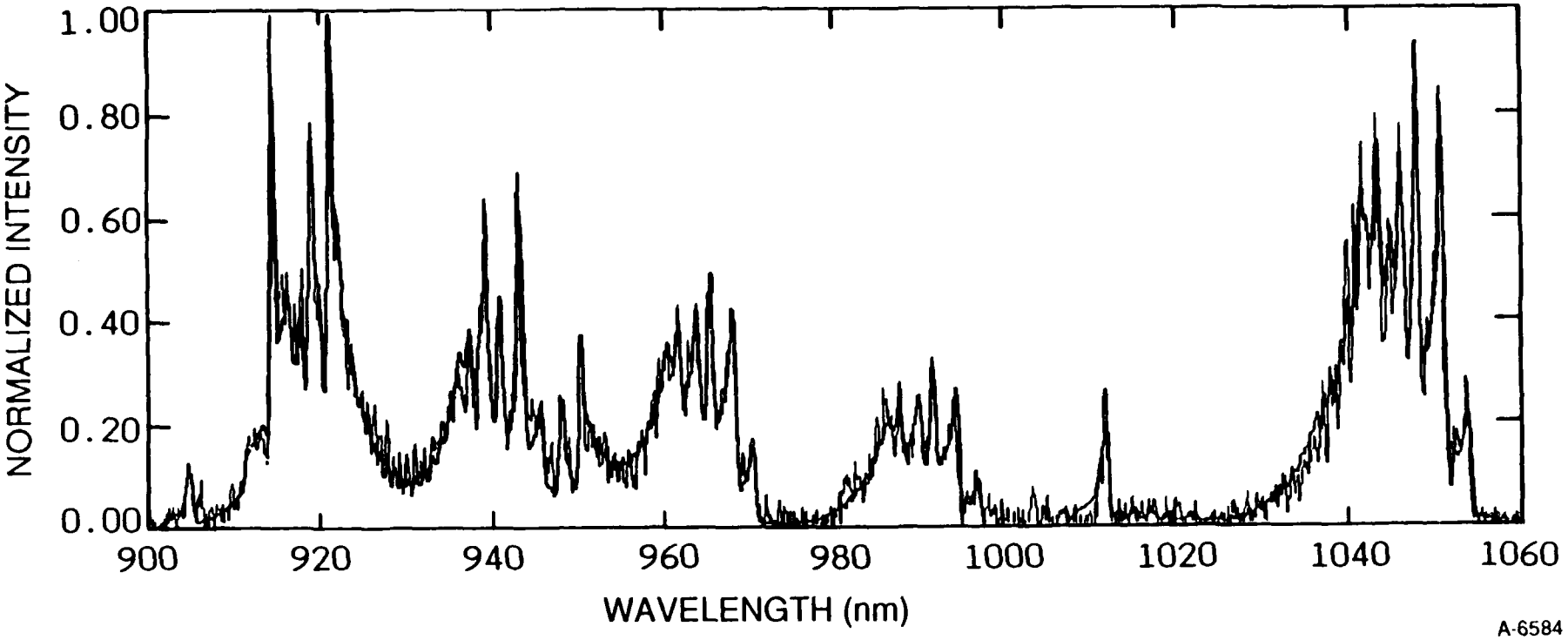

L.G. Piper et al.
J. Chem. Phys.
Figure 2

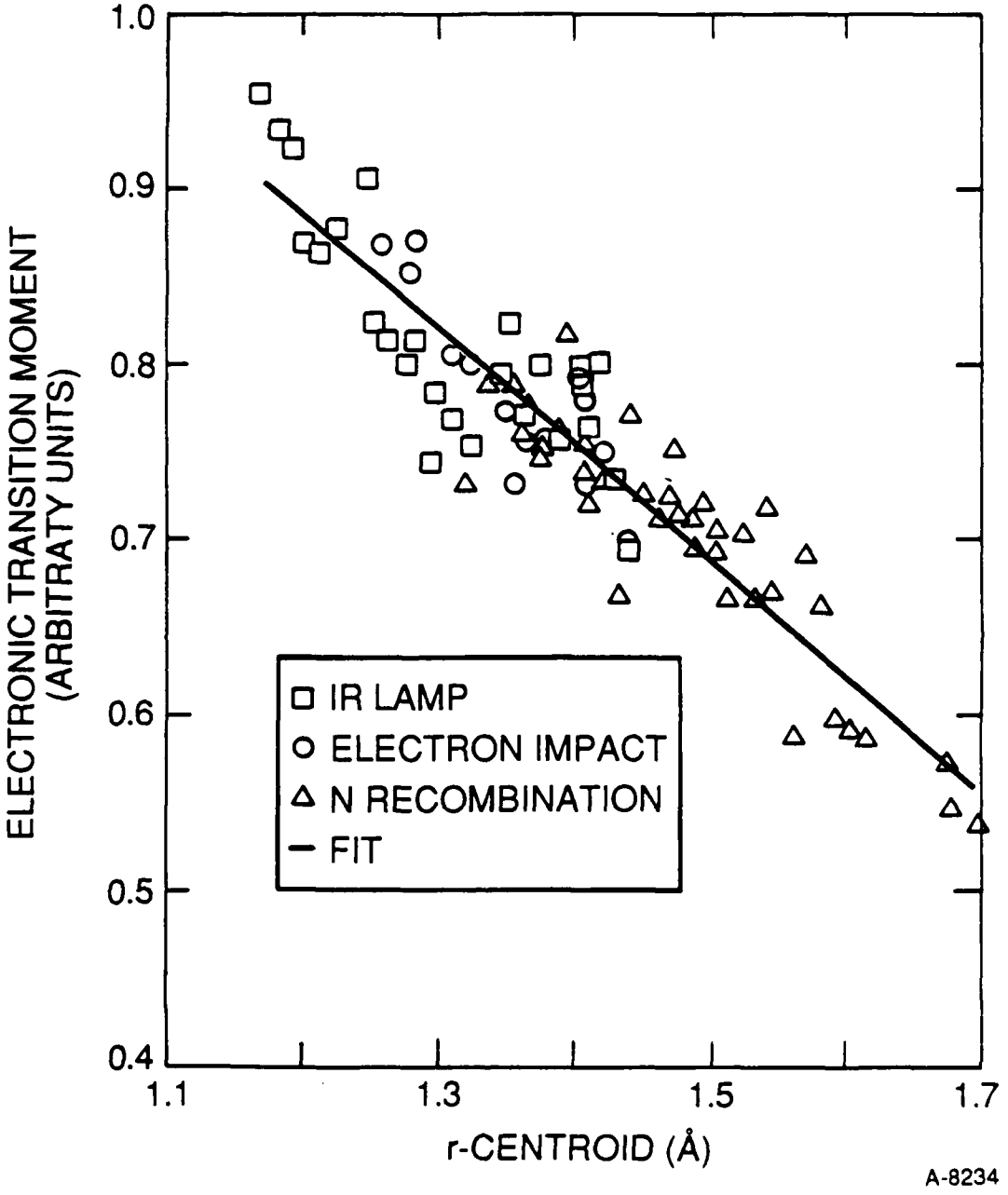

L.G. Piper et al.
J. Chem. Phys.
Figure 3

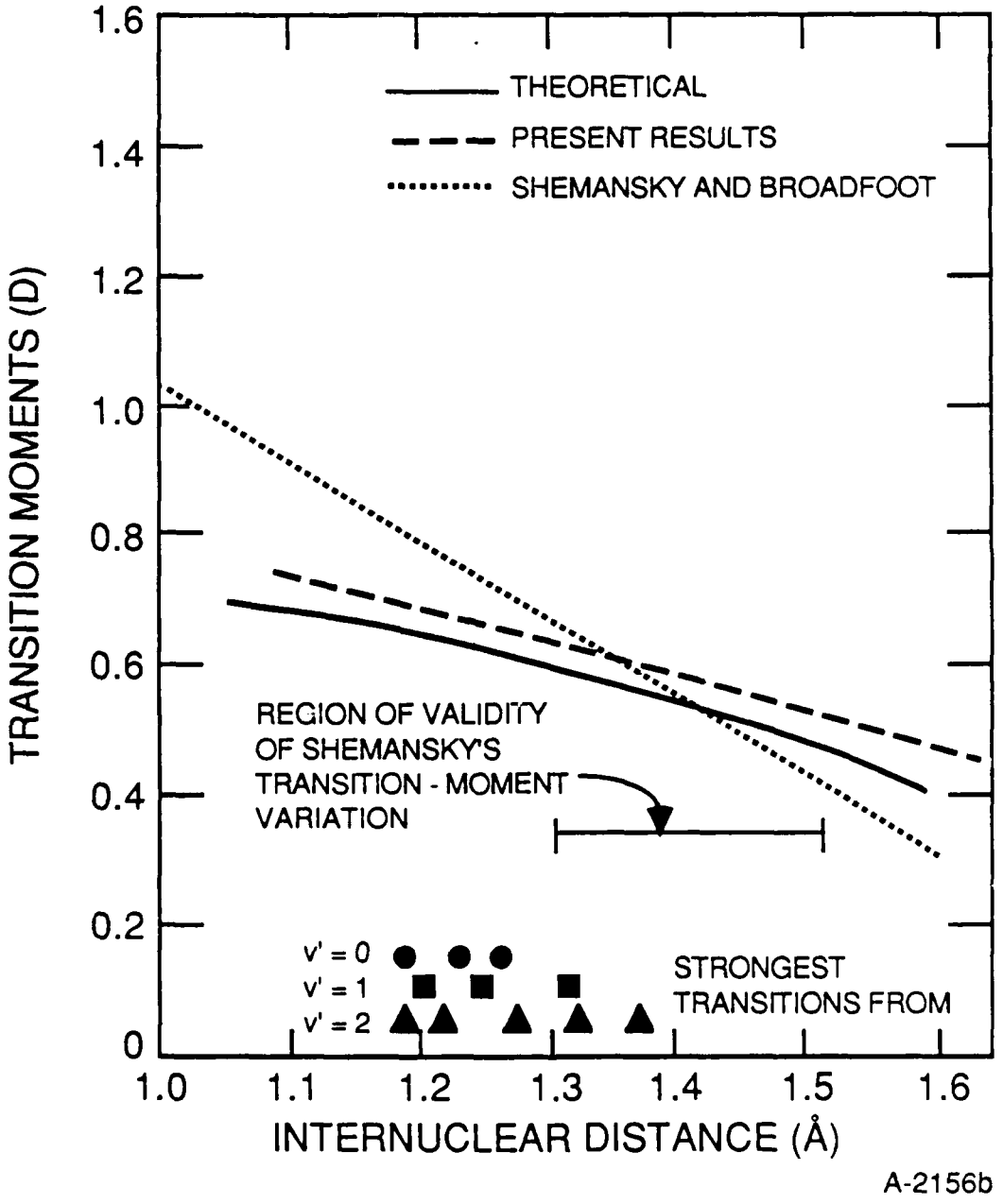

L.G. Piper et al.
J. Chem. Phys.
Figure 4

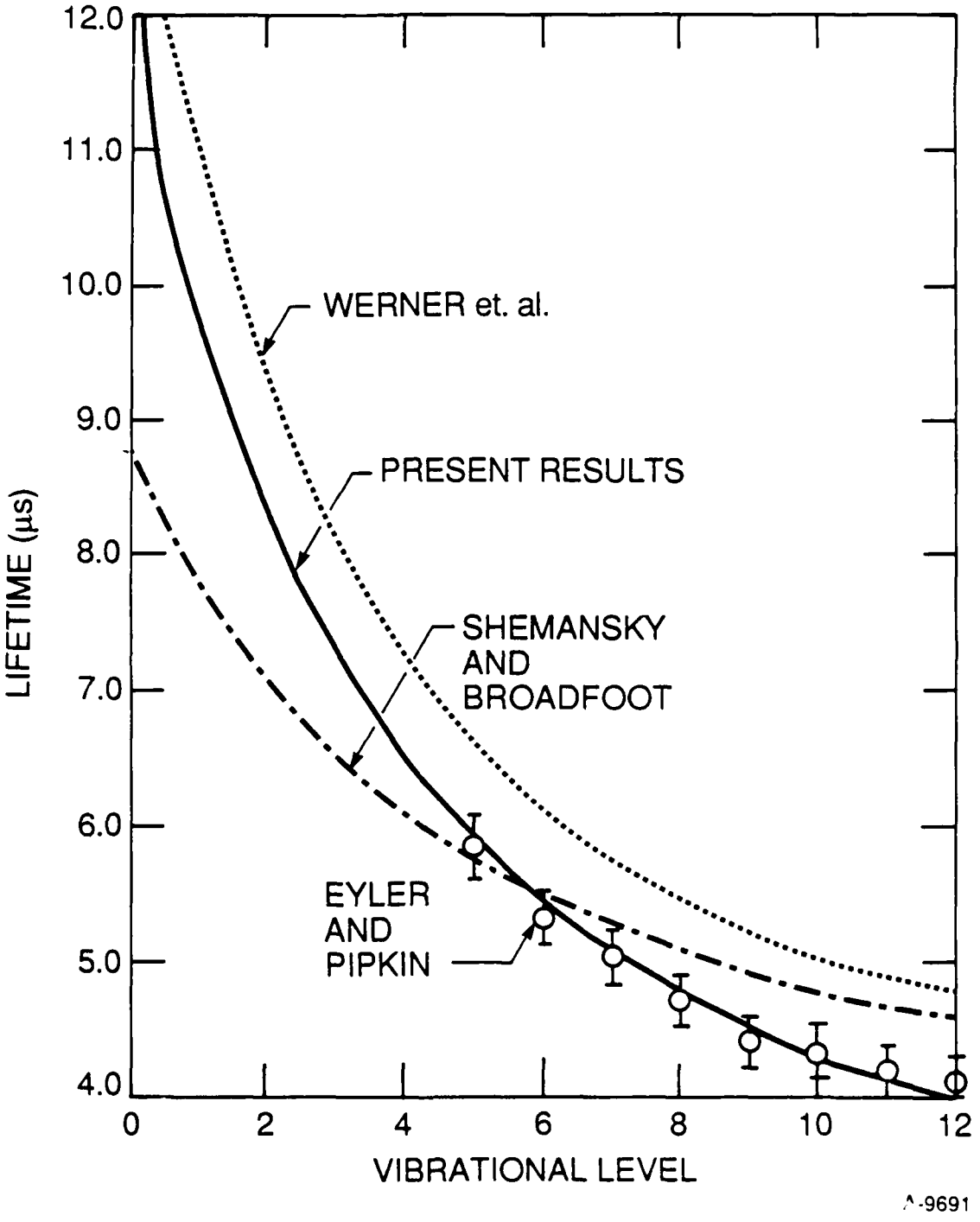

L.G. Piper et al.
J. Chem. Phys.
Figure 5

APPENDIX N

(PSI-032/TR-572 reproduced in its entirety)

PSI-032/
TR-572

COCHISE OPERATING MANUAL

Quarterly Status Report No. 5

For the Period

1 April 1986 to 30 June 1986

Under Air Force Contract No. F19628-85-C-0032

Prepared by:

M.E. Fraser, H.C. Murphy, and W.T. Rawlins

Sponsored by:

Air Force Geophysics Laboratory
Air Force Systems Command
U.S. Air Force
Hanscom Air Force Base, Massachusetts 01731

August 1986

TABLE OF CONTENTS

LIST OF ILLUSTRATIONS

LIST OF ILLUSTRATIONS (Continued)

LIST OF TABLES

LIST OF CHECKLISTS

1. INTRODUCTION

1.1 An Overview of the COCHISE Apparatus

The COCHISE facility, situated at the Air Force Geophysics Laboratory, is, in the simplest terms, a relatively large, cryogenically cooled test chamber which may be used to study the state of the reaction products created as the result of a variety of possible gas phase reactions such as chemi-excitation processes,

$$A + BC \rightarrow AB^* + C \qquad (1)$$

$$A + B \xrightarrow{M} AB^* \qquad (2)$$

or vibrational exchange or electronic-state quenching reactions

$$A^* + B \rightarrow A + B^* \quad , \qquad (3)$$

where the quantities A, B, C are meant to represent atoms or molecules and the asterisk implies electronically or vibrationally excited states.

The predominant IR active mode of excitation of AB^* is vibrational; however, some atmospheric species (most notably N_2 and O_2) possess electronic states which can radiate in the IR. It is often difficult to deduce detailed information about these processes from in situ atmospheric measurements of IR emission; such data often have low spectral resolution and contain contributions from competing thermal and scattering mechanisms. However, laboratory investigations of individual chemical processes under carefully controlled conditions can provide detailed mechanistic and spectroscopic information; this information can, in turn, be used in conjunction with atmospheric models to both interpret in situ data and define further measurements.

Infrared emission spectroscopic experiments designed to investigate gas phase chemiexcitation reactions require: 1) high sensitivity to the relatively weak molecular radiation from the products of reactions (1) and (2);

2) adequate resolution to allow conclusive spectral analysis; and 3) specificity to the chemiexcitation process under investigation, i.e., negligible interference from radiative, collisional, and surface relaxation processes. These conditions work against each other; the achievement of condition (3) necessitates the use of small pressures and/or product yields, which results in low radiation levels and increases the difficulty of achieving conditions (1) and (2). Furthermore, the limitation of IR detection sensitivity by thermal background radiation in the field of view severely inhibits spectrally resolved observations of long-wavelength radiation from important atmospheric species such as CO_2 (15 μm) and O_3 (10 μm). Previous IR chemiluminescence methods, such as arrested relaxation[1-3] and discharge flow[4,5] coupled with the use of circular-variable-filter spectrometers,[5] grating monochromators,[2] and Fourier transform spectrometers,[1-4] have been highly successful in studies of chemiexcitation at wavelengths less than ~5 μm.[6] In general, however, these methods suffer from thermal background limitations; for example, at 10 μm, the spectral radiance from a typical AB^* species at a column density of $\sim 10^8$ cm^{-2} (often representative of such experiments) would be ~9 orders of magnitude less than that from a room temperature blackbody.

Infrared detectivity can be dramatically improved by resorting to a cryogenic background, as shown in Figure 1. Since the limiting noise mechanism is the statistical fluctuation in the photon flux associated with the detector's environment, the detectivity of the system is inversely proportional to the square root of that flux. The results plotted in Figure 1 are normalized to the detectivity at 293 K. Although considerable enhancement in detectivity is obtained with an 80 K background, the effects of background radiation can be virtually eliminated by cooling the entire reaction chamber/detection system to temperatures below 40 K. As a further benefit of cryogenic temperatures, rapid cryopumping of reagent gases can be attained near 20 K, and radiation leakage from the external vacuum system can then be eliminated by isolating the reaction/detection system during the experiments.

COCHISE is designed for partial simulations and detailed experimental

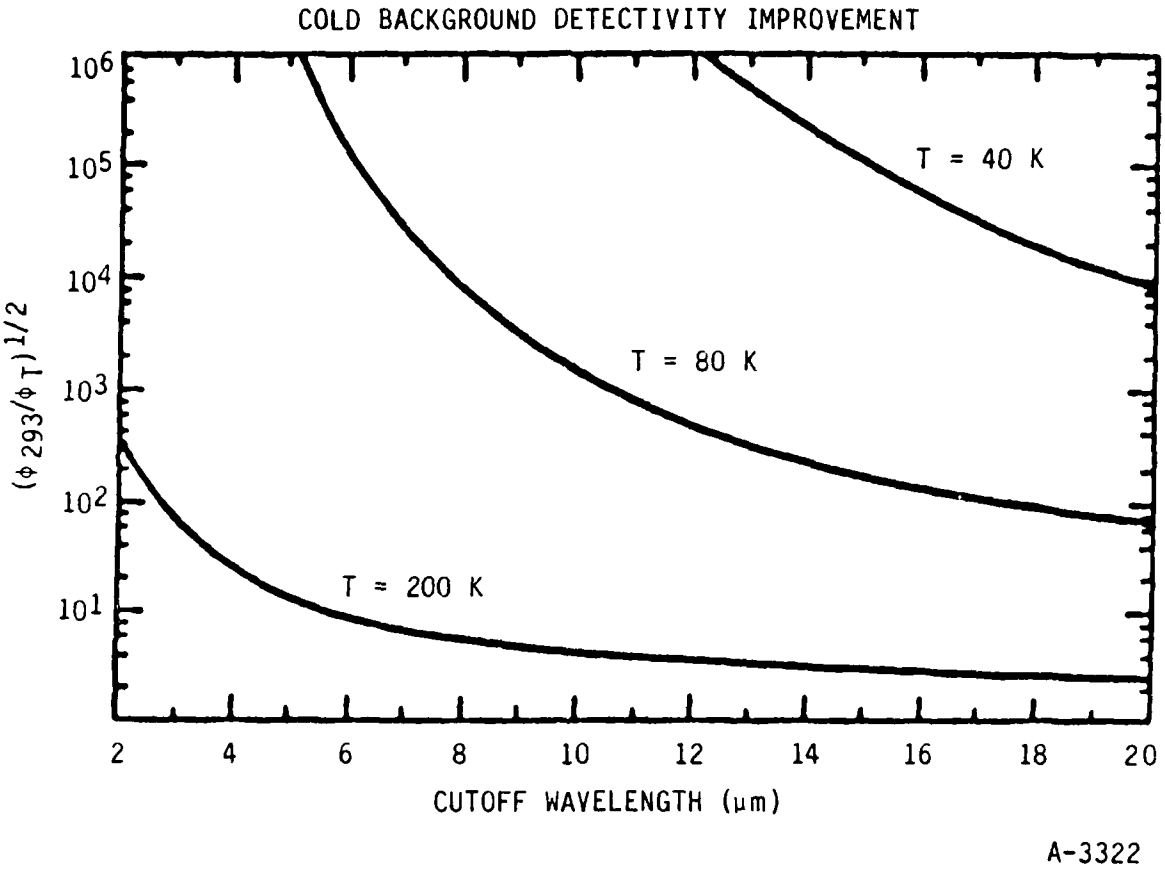

Figure 1. Reduction in Background Photon Flux by Cyrogenic Operation

studies of high-altitude IR excitation phenomena, particularly chemiexcitation and excitation transfer processes. The primary design objective for the apparatus was to eliminate the limitations to IR detectivity outlined above. The experimental direction taken in the development of Cold Chemiexcitation Infrared Simulation Experiment (COCHISE) has been to reduce the temperatures of both the reaction chamber and the detection system to ~20 K to optimize the benefits of cold background and cryopumping. A state-of-the-art IR detector and a cryogenic scanning monochromator are coupled to a long-path reaction cell to allow spectrally resolved detection of IR radiation (2 to 20 μm) from emitting species at concentrations below 10^6 molecules cm^{-3}. The techniques of discharge flow and arrested relaxation are combined to allow mixing of the reacting species in the field of view at steady-state pressures near 3 mTorr, so that, in most cases, the chemiexcited products can be formed and observed under nearly single-collision conditions. The high-speed cryopumping of the reaction vessel removes the excited species from the field of view of the detection system before radiative or collisional relaxation can occur and eliminates contamination by back-diffusion from the chamber walls.

A schematic of the entire COCHISE apparatus is given in Figure 2. The reaction cell and detection system are enclosed within a cryogenic thermal shroud, which is, in turn, enclosed by a main vacuum chamber to minimize conductive losses. All surfaces within the shroud, with the exception of selected optical components and reagant gas lines, are held at temperatures as low as ~20 K; this allows rapid cryopumping of all reagent and background gases except He and H_2. The reagent gases enter the reaction cell through four sets of opposing jets (see also Figure 3) and interact along the center line of the cell; the resulting radiation is viewed along the center line through a lens by a grating monochromator detection system. The data processing, temperature control, and system housekeeping are performed by an external computer. The various components of the system are described in more detail in later sections.

The COCHISE facility as described above thus provides a unique capability for the study of the fundamental kinetic paths and product distributions

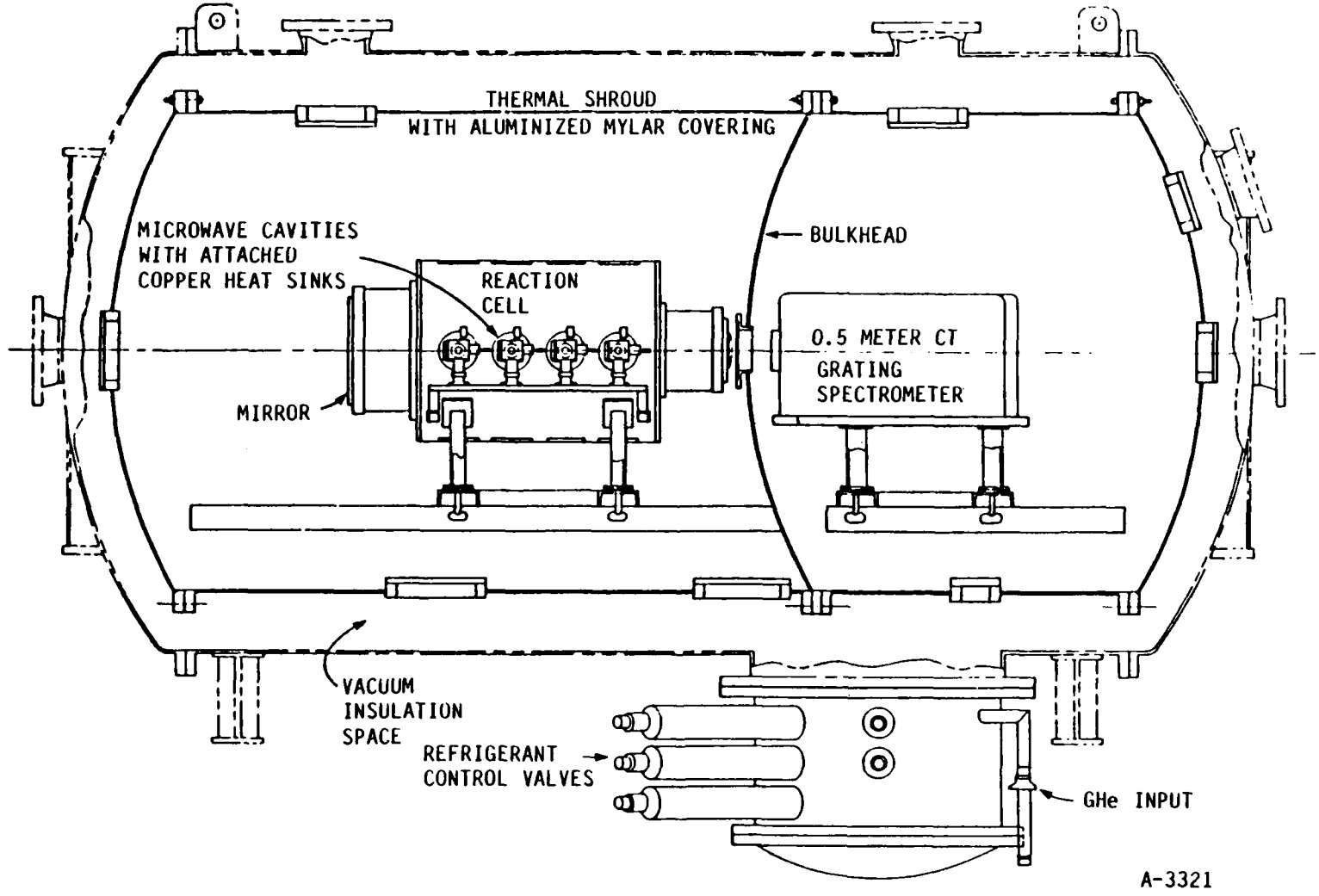

Figure 2. Schematic of COCHISE Facility

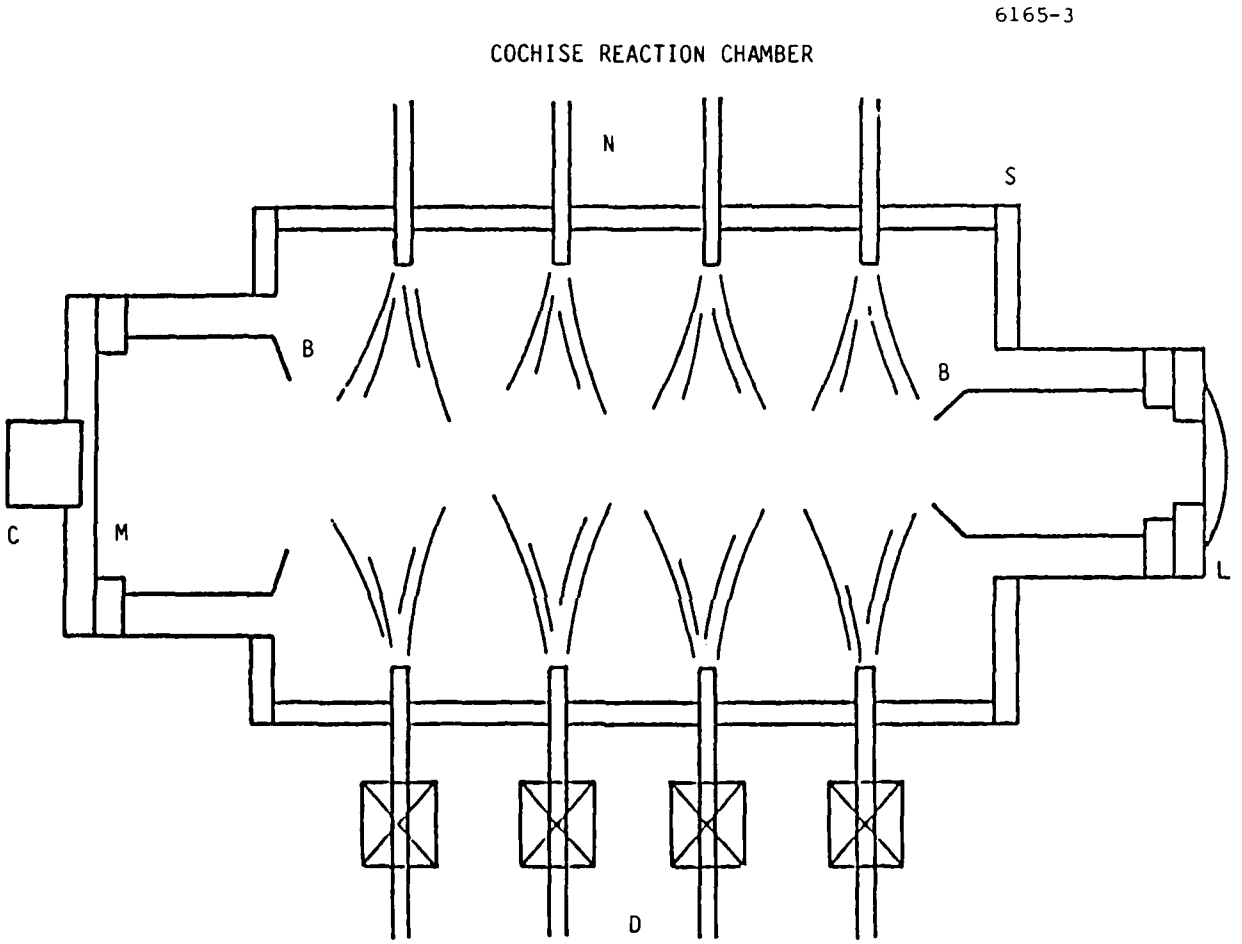

Figure 3. Scale Drawing of Chemiluminescence Reaction Cell. Ar/N_2 or Ar/O_2 mixtures are excited by microwave discharges, D, and mix with the counterflow of O_2 from nozzles N in an axisymmetric reaction zone at the chamber center. Baffles, B, restrict detection system field-of-view to the on-axis reaction volume. M is the plane mirror which increases the intensity of the radiation collected by lens L. Spectral response calibration is performed using blackbody source, C, embedded behind a small hole in the end mirror.

produced by chemical reactions between various excited species, free radicals, and neutral molecules. Such studies, although of basic interest in their own right, can prove to be invaluable in the understanding of radiative/energy transfer phenomenology occurring at rarefied gas densities such as auroral or nuclear phenomena in the upper atmosphere. To the best of our knowledge, the COCHISE device is the only facility in the nation which can provide such detailed information on these fundamental chemical processes.

1.2 Applications and Accomplishments

The COCHISE facility has been used to develop an extensive data base on the spectroscopy of infrared (2 to 16 μm) fluorescence from the effluents and interactions of microwave-discharged N_2/Ar and O_2/Ar mixtures.[7] Some results of these measurements include the formation of NO(v) from the interaction of discharged N_2/Ar and O_2,[8] the formation of O_3(v) from discharged O_2/Ar,[9,10] and the excitation of high-lying Rydberg states of Ar in the discharge.[11] Studies currently under way include the interaction of discharged N_2/Ar with CO and the potential for formation of N_2O(v) from various processes.[12]

Discharged N_2/Ar mixtures provide a wealth of energy-rich states of nitrogen. The most prominent effluents of such discharges are the atomic species N(^4S, ^2D, ^2P), the principle molecular metastable $N_2(A^3\Sigma_u^+)$, and vibrationally excited N_2(v). Other excited triplet and singlet forms of N_2, e.g., $B^3\Pi_g$ and $a^1\Pi_g$, have relatively short radiative lifetimes (1 to 100 μs) and thus may be expected to disappear soon after exiting the active discharge if there are no other source terms besides direct excitation. These excited species can give rise to vibrationally excited NO and CO through exoergic reaction or energy transfer with atmospheric species such as O_2, CO, and CO_2. Our previous and current experiments have examined the interaction of discharged nitrogen, N_2^*, with O_2 and CO, which occurs primarily through the N(^2D) metastable.[12] COCHISE will further examine the potential effects of N(^2P) in these systems, as well as to more completely characterize the N_2^*-CO interactions. Our present studies of the N_2^*-CO system indicate at least three different excitation processes responsible for emission in the 4 to 6 μm

region. One reaction, which results in excitation of CO(v), is probably energy transfer from $N(^2D)$:

$$N(^2D) + CO \rightarrow CO\ (v \leq 9) + N(^4S)$$

A second, unidentified process, which is most apparent at low CO concentrations, appears to excite CO($v \leq 23$) with extremely low (< 10 K) rotational temperatures. However, the COCHISE data base at this time is still too sparse to permit a useful characterization of this process. This extraordinary combination of high vibrational and low rotational excitation is intriguing, and may be related to gas-surface interactions at the wall of the cryogenic reaction chamber. We propose to obtain a more complete data base as a function of CO concentration and surface aging. An additional manifestation of the N_2^*-CO interaction is an unidentified band system occurring between 4.3 to 4.5 μm. The spectroscopic parameters for this band system are remarkably similar to those for ground-state N_2($v = 1$-6), which is not supposed to radiate in the gas phase. Thus, if this assignment is correct, an excitation process on the cryogenic surface is indicated. We propose to obtain more data for a variety of N_2 and CO conditions, and to perform a conclusive spectroscopic analysis of these bands. In addition, we propose to examine the effects of $N(^2P)$ via the reactions

$$N(^2P) + CO \rightarrow N(^2D) + CO(v \leq 4)$$

$$\rightarrow N(^4S) + CO(v \leq 15)$$

While $N(^2P)$ cannot be isolated from $N(^2D)$, the ratio of the two species can be varied to some extent by adjusting the N_2 mole fraction and discharge power, so a parametric study of CO(v) fluorescence will indicate whether $N(^2P)$ excites CO(v). We are planning to extend this type of investigation to other atmospheric collision partners, e.g. CO_2 and N_2O. Active nitrogen is known to be highly reactive with these species,[13] and we will examine the IR fluorescence spectrum for emission from vibrationally excited CO_2 (4.3, 15 μm), N_2O (4.5, 7.8, 17 μm), CO (4.7 μm), and NO (5.3 μm). These experiments will

require the development of techniques for heating the reagent lines sufficiently to prevent condensation of CO_2 and N_2O; this capability was designed into COCHISE, but has never been implemented.

Recent COCHISE measurements have also provided new spectral data on N_2 electronic emission in the short-wavelength infrared (SWIR), seemingly excited in the microwave discharge.[6] The $W^3\Delta_u \rightarrow B^3\Pi_g$ transitions are clearly indicated between 2 and 5 μm,[14] some $B^3\Pi_g \rightarrow A^3\Sigma_u^+$ transitions appear to be present, and several other features are unidentified as yet. We will pursue these studies, using a combination of parametric experiments with varying N_2 flows and counterflow gases and a spectral fitting analysis, to characterize the excitation and quenching of this emission and its spectroscopic distributions and branching ratios in the infrared.

In addition to N_2^*, metastable and vibrationally excited forms of O_2, O_2^*, are potential precursors to atmospheric IR phenomena, but are relatively poorly understood in terms of kinetics and reaction paths.[15] COCHISE experiments indirectly point to excitation of $O_3(v)$ by energy transfer from $O_2(b\ ^1\Sigma)$ and/or $O_2(v)$, and auroral enhancements in $O_3(\nu_3)$ and $CO_2(\nu_2)$ radiation as observed by HIRIS may be related to similar processes.[16-18] We are planning to examine O_2^* interactions with the same reactive species used for N_2^*, namely CO, CO_2 and N_2O, to survey the potential of various forms of O_2^* as precursors to infrared radiation. O_2^* will be generated by microwave discharge of O_2/Ar. The O_2 states of interest include $O_2(a^1\Delta_g, b^1\Sigma_g^+, c^1\Sigma_u^-, A^3\Sigma_u^+, A'^3\Delta_u)$ and $O_2(v)$. Spectral surveys will cover the range 2 to 17 μm, with emphasis on potential IR radiators such as NO, CO, N_2O, CO_2 and O_3. This exploratory work will be used to identify key O_2^* states and reactions for further study.

The potential for chemical generation of N_2O in the upper atmosphere is a subject of continuing debate. However, reactions of atmospheric species which can result in formation of N_2O at low pressures have yet to be conclusively identified. The possible reactions would require at least one excited-state reactant species, and thus may occur most prominently in

laboratory discharges or strong aurorae. Furthermore, these reactions are sufficiently exoergic to produce vibrationally excited N_2O, resulting in infrared chemiluminescence near 4.5 (ν_3), 7.8 (ν_1), and 17 (ν_2) μm. We are using the COCHISE facility to investigate these phenomena, and have observed emission from $N_2O(\nu_3)$ formed in microwave discharges of flowing, dilute mixtures of $N_2/O_2/Ar$ at ~1 Torr.[12] Other measurements of the interactions of discharged O_2/Ar with N_2 and of discharged N_2/Ar with O_2 give no measureable formation of $N_2O(v)$. These results contraindicate the formation of $N_2O(v)$ from the reactions of $O_3(v)$ with N_2, metastable O_2 with N_2, and metastable N_2 with O_2. We suggest that excited and/or metastable forms of <u>both</u> N_2 and O_2 are required in the critical reaction(s). This could entail reactions of one of the forms of N_2^* with O_2^* or perhaps $O_3(v)$. We propose to pursue this issue in further COCHISE experiments. The first step in this investigation is to examine the IR spectra of discharged $N_2/O_2/Ar$ mixtures over a wide range of N_2 and O_2 partial pressures, temperature and total pressure, to ascertain under what conditions $N_2O(v)$ formation in the discharge is optimized. These results should give some clues as to the identities of the key N_2O precursors, since we know from separate experiments how the production of O_2^*, N_2^*, and $O_3(v)$ varies with these conditions. Such measurements will, of course, provide similar information on NO, O_3, and NO_2 formation which would be applicable to discharged air.

A further and necessary development of this line of research will require the modification of COCHISE to permit discharge excitation of the counterflow gas. Owing to the difficulty of dissipating heat from high-power (~50W) microwave units, this modification would probably take the form of a lower powered, DC discharge. Such a modification permits the study of <u>in situ</u> fluorescence resulting from the direct interactions of two or more different excited species. Example reactions which could be studied in this configuration include $N_2(A) + O$ (to look for NO(v) formation), $N_2(A) + O_3(v)$, $N_2(A) + O_2(^1\Delta, ^1\Sigma)$, etc. Such reactions are little-known but could play an important role in strong electron bombardments where metastable production rates are large. Thus this proposed modification to COCHISE, while rather extensive, would significantly increase the power of the facility to study high-energy atmospheric phenomena.

The observation in COCHISE of IR emission from high-lying Ar Rydberg states excited in the microwave discharges has opened the possibility for performing similar studies of O(I) and N(I) radiation. Based on the results of the Ar(I) experiments, these measurements would use discharged O_2/Ar and N_2/Ar mixtures at ~0.1 Torr, with the highest possible diatomic partial pressure. The Ar is required for the discharge to persist, and its spectral interference will have to be removed by subtracting background Ar spectra. Also, it will probably prove advantageous to reconfigure the field of view such that the discharge tubes are more directly viewed by the detection system. This can be done by a combination of re-orienting the reaction cell and introducing reflective surfaces into the chamber. These measurements would provide information on the spectroscopy and excitation mechanisms for these states in microwave discharges, and the resulting data base could be linked to other on-going plasma experiments at AFGL.

2. THE COCHISE APPARATUS

2.1 The Chamber

A schematic of the COCHISE apparatus is shown in Figure 2. The cryogenic portion of the apparatus is thermally isolated inside a cylindrical main vacuum chamber ~3m long and ~1.5m in diameter (Figure 2). The thermally insulating vacuum enclosure is maintained at $\sim 10^{-10}$ atm by a 50-cm (20-in.) cold-baffled diffusion pump (Consolidated Vacuum Corp.) backed by a large two-stage mechanical pump (Leybold-Heraeus DK-200). The light-tight aluminum shroud, ~2.5m long and 1.25m in diameter, is supported on stainless steel and phenolic standoffs and is completely surrounded by a multilayer thermal shield to provide insulation from the 300 K thermal radiation of the outer wall. This shield consists of 19 alternating layers of aluminized Mylar, Dacron bridal veil, and 0.76 mm (0.030 in.) Scott Industrial Foam and permits a total radiative load of < 50W from the 300 K outer wall to the 20 K shroud. This corresponds to a net reduction of over 2 orders of magnitude in the radiative heat flux, allowing a hugh increase in the efficiency and load-carrying capacity of the cooling system. The shroud, reaction cell, and detection system are cooled to ~20 K by a 600W closed-cycle helium refrigeration system (Cryogenic Technology, Inc.). Extended-stem valves permit control of coolant flow in three independent loops supplying the shroud, reaction cell, and microwave discharge heat sink (see below).

Component temperatures are monitored at roughly 25 locations by calibrated platinum resistance thermometers. Direct current voltage is supplied from an external source; the resulting voltage drop across each sensor is amplified, processed by analog-digital conversion in a PDP-8E (Digital Equipment Corp.) computer, converted to absolute temperature, and displayed on various storage oscilloscopes or hard copy devices. Temperatures of gas flow lines and optical components are controlled in 13 different areas by resistive heaters mounted on the appropriate hardware. Temperature-controlled portions are isolated from surrounding areas by stainless steel or phenolic standoffs. Power to the heaters is percentage-controlled by the computer via solid-state

switches so that the temperature of each heat station is independently sampled and regulated to within ±0.5 K.

Because the internal cryogenic chambers are rapidly cryopumped, they may be vacuum-isolated from each other and from the external vacuum system during the measurements to seal off external light leaks. This is accomplished by means of specially modified, cryogenic, latching solenoid valves of a type not commercially available. These valves, which are operated from an external control panel, can be opened and closed by separate solenoids and will remain in either position in the absence of applied power; microswitches mounted on the valve shafts provide positive readouts of the valve positions.

The physical arrangement shown in Figure 2 emphasizes flexibility in use of the apparatus. The main vacuum chamber and cryogenic shroud have full-opening end doors and a number of access ports through which all the services for the experiments, e.g., cryogenic coolant, microwave power, reagent gases, and instrumentation, are introduced. All diagnostic and control devices are mounted externally. The ready availability of extra access ports and vacuum feedthroughs allows a high degree of adaptability to future-diagnostic concepts, such as use of lasers or atomic resonance line sources. Details of the chamber subsystems, i.e., the reaction chamber, refrigerator system, etc., will be presented in later sections.

2.2 Reaction Cell and Reagent Gas Lines

A schematic of the chemiluminescence reaction chamber is given in Figure 3. The copper reaction cell is cylindrically symmetric, 60 cm in length, 40 cm in diameter. To control the cryopumping speed (and thus the reagent gas residence time - see below), the reaction cell temperature can be independently varied; temperature uniformity to ±0.1 K over the entire surface is achieved through proper positioning of coolant flow lines and heater elements.

The reagent gases are metered into the system by motorized Granville-Phillips leak valves; flow rates are monitored by calibrated mass flowmeters (Brooks). One gas mixture flows through four sapphire microwave discharge sidearms on one side of the cell; another gas mixture flows through four counterflow sidearms on the opposite side of the cell. Up to three gases can be mixed prior to introduction into the discharge cavities; two gases can be separately mixed for the counterflow. Upon penetration of the outer vacuum chamber, the room-temperature gases undergo a two-stage heat exchange process. The first stage, outside the shroud, is a copper plate cooled with liquid nitrogen; the second stage, inside the cryogenic shroud, permits variable temperature selection over the 30 to 500 K range. The gases then pass through temperature-controlled copper lines to the appropriate inlet sidearms and into the reaction volume. Just prior to entering the reaction cell, gases in the sapphire discharge tubes are ionized and excited by four modified McCarroll-Evenson[7] microwave discharge cavities (Opthos Instruments) powered by Raytheon PGM 10 power supplies (2450 MHz, 100W) with a variable duty cycle. Typical operation is at 50 to 90 percent of maximum power with duty cycles of either 100 or 50 percent at 23 Hz, creating steady-state conditions while the discharges are on; all four discharges are driven by a single pulse generator to insure synchronous operation to within a few microseconds. Excess heat generated by the discharge plasmas is transmitted to a copper heat sink plate where it is removed by the helium coolant; the heat transfer rate is controlled via an extended-stem valve on the coolant as described above. In normal operation, the discharges are held at the desired gas temperature (typically 80 to 100 K in experiments to date) to within 1 or 2 K.

As shown in Figure 3, the reagent gases are expanded into the interaction volume, with equal mass flow rates, through four sets of diametrically opposed inlet jets which are equally spaced along the cylindrical cell. Flow conditions in the reaction cell have been modeled[8] for a range of experimental conditions; free expansion occurs in the reaction cell, and the gas reaches a limiting velocity in which nearly all the thermal energy in the inlet tube is converted into kinetic energy. Near the cylinder axis, an axisymmetric stagnation point occurs, and the thermal energy of the gas molecules returns to

that of the gas in the inlet tubes. Gas density variations along the cylinder axis (reaction volume) are predicted to be < 10 percent. The pressures in the reaction zone and in the sidearms are monitored by MKS Baratron capacitance manometers.

At typical flow rates used in the past, ~4 standard liter/min of various $Ar/N_2/O_2$ combinations on each side, the resulting pressures are ~1 Torr in each sidearm and ~3 mTorr in the reaction zone; the corresponding gas residence times are ~2 msec from the discharge to the expansion region, ~0.5 msec from the expansion region to the field of view, and ~0.3 msec in the field of view.[9]

The chemiluminescent reactions occur primarily in the stagnation region where the opposing flows meet. The IR radiation is viewed by the detection system through a 7.6 cm (3 in.) f/5 antireflection (AR)-coated germanium lens; the resulting observed volume is roughly cylindrical along the optical axis so that only radiation occurring within ~4 cm of the axis is observed. A polished gold mirror at the far end of the cell enhances the collection efficiency of the system. Internal baffles on the mirror and lens discriminate against scattered light from the discharges. The walls of the reaction cell are not in the field of view. The spectral response of the optical system is routinely calibrated with a variable-temperature blackbody source imbedded in the center of the mirror.

2.2.1 Gas Manifold and Flow Calibration

A diagram of the gas manifold is shown in Figure 4. The solenoid valves are located on the high pressure side of the lines and the controlling switches are on the COCHISE control panel. There are two solenoid valves, one for discharge gases and another for counterflow. Similarly, there are two pump out valves; also one each for discharge and counterflow. Figure 4 shows the gas manifold for each gas line. There are currently three lines on the discharge side (Ar, N_2, and/or O_2) and two on the counterflow side (Ar, N_2 or O_2 or CO).

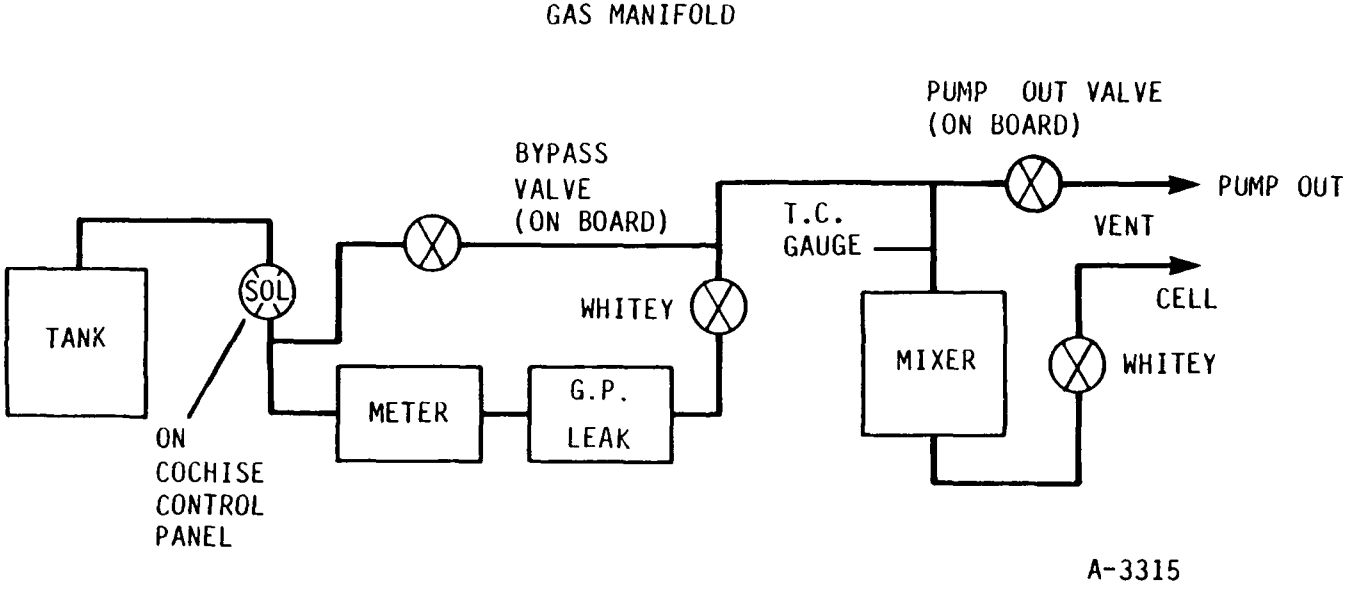

Figure 4. Gas Manifold

In order to pump out the lines, the pump-out valve must be engaged and the Whitey and board valves open as well. This is the mode in which the discharge and counterflow lines are leak-checked. A rate of rise in the TC readout is monitored with the pump-out valve closed. Typical values are < 0.1 micron/min. The lines may be pumped out up to the pressure gauges on the gas cylinders by opening the solenoid valves. This is typically done each morning prior to beginning experiments.

To operate the gas manifold system, the following should be done in order: 1) pump out the lines up to the cylinder regulator , 2) close the bypass valve, 3) set up the desired flows by adjusting the leak control switches on the COCHISE control panel (be sure to turn on the flow meters), and 4) close the pump-out valves and open the reaction cell valves (there are a total of eight, four each, for counterflow and discharge).

Typical total mass flow rates are 0.11 g/s from each of the counterflow and discharge. This corresponds to flow rates of ~4 standard liters/min from each. It is important for mass balance to be maintained so whenever one component of the discharge counterflow is changed the other component must also be adjusted. Figures 5 through 14 show the calibrations for the gases Ar, O_2, N_2(CO) for each of the flow meters. The units in Figures 5 through 8 are g/s while those of the other curves are in μmoles/s or cm^3/min.

2.2.2 Field of View

In order to discriminate against surface emissions, it is critical for the field of view to underfill the mirror. The lens and position of the monochromator were chosen to accomplish this goal but until recently there was no experimental verification. Two different configurations were used; one for simplicity, the other for accuracy. The configurations are shown in Figures 15a and b, respectively.

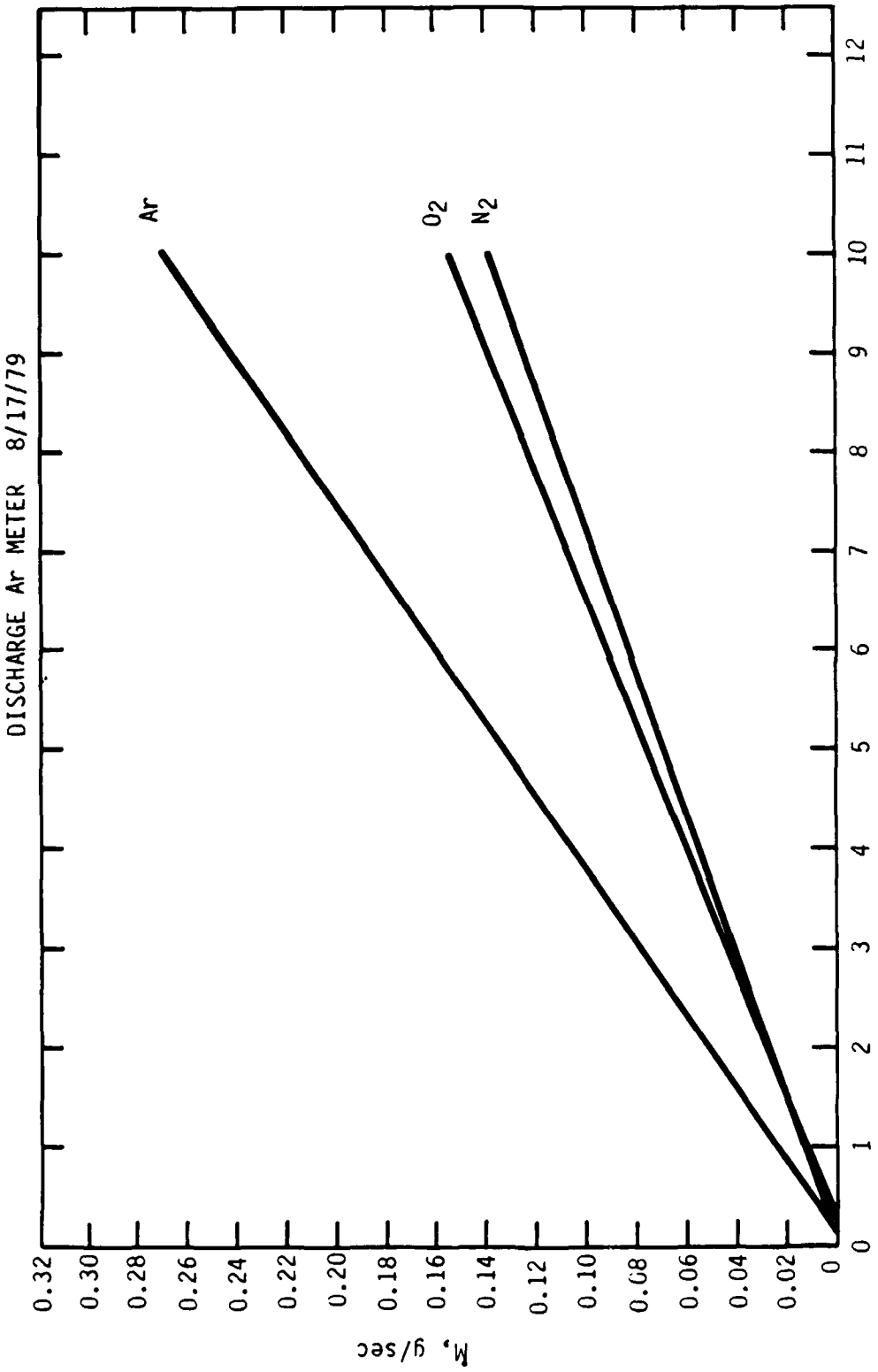

Figure 5. Discharge Ar Meter, g/s units

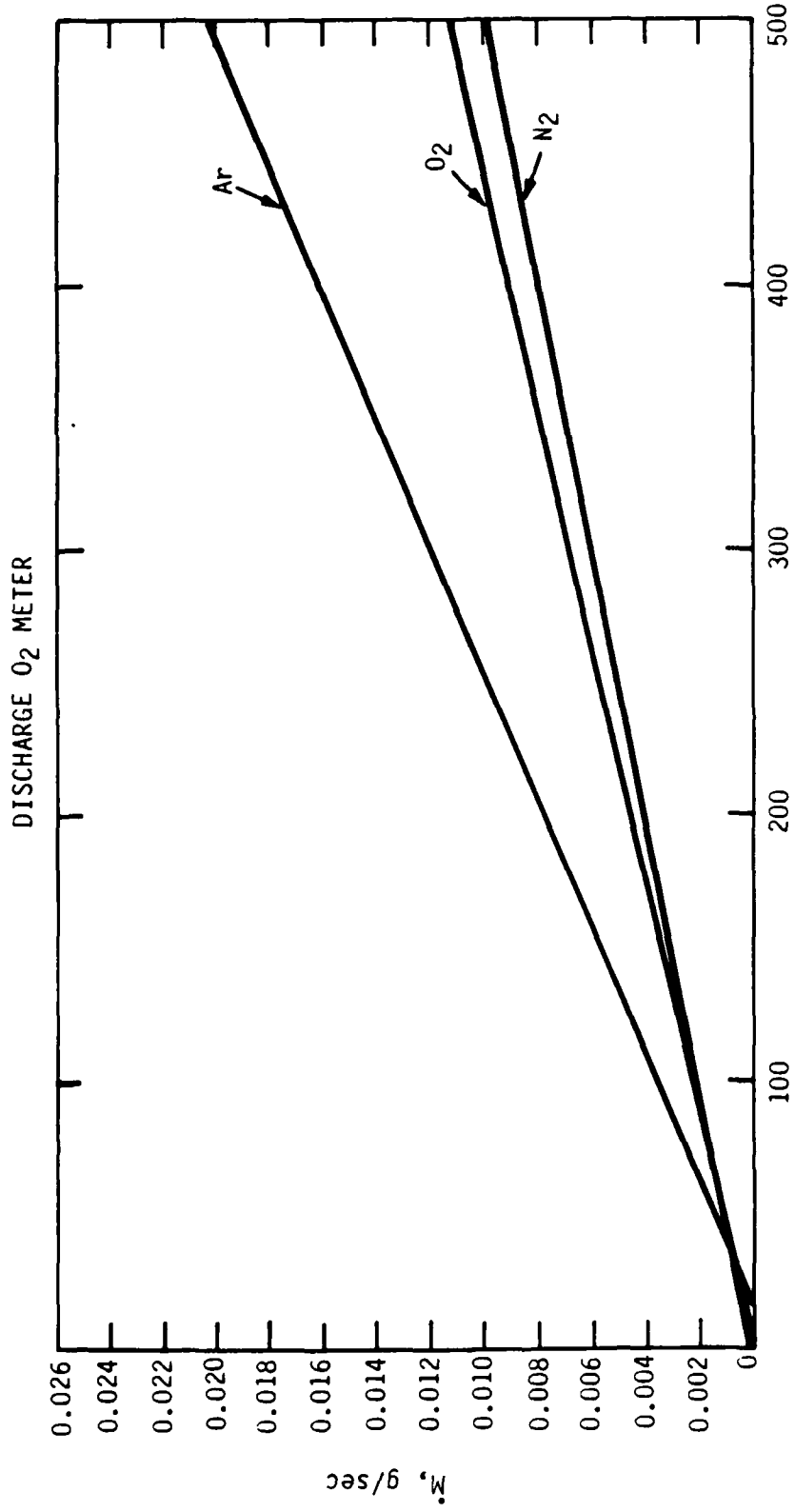

Figure 6. Discharge O_2 Meter, g/s units

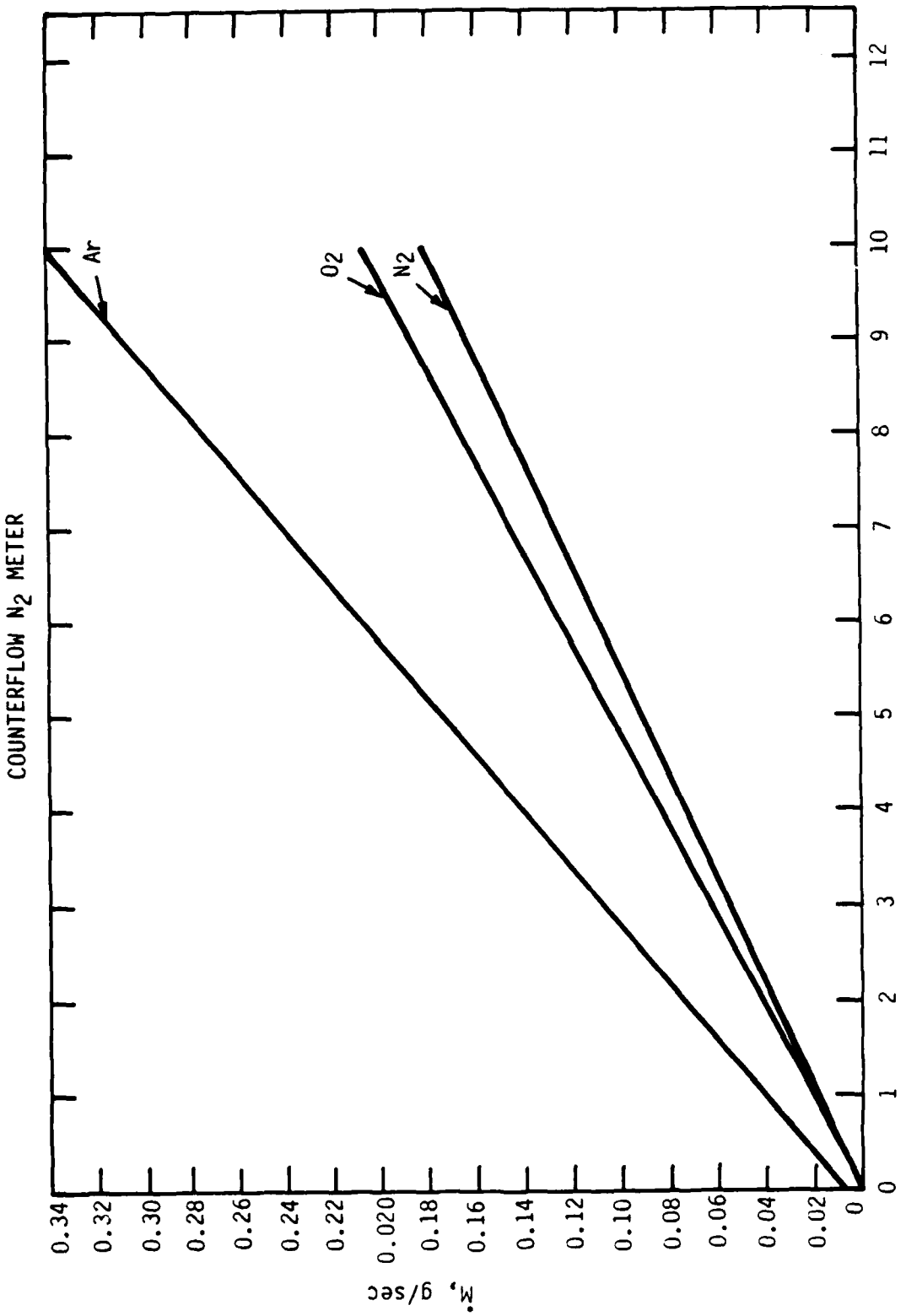

Figure 7. Counterflow N_2 Meter, g/s units

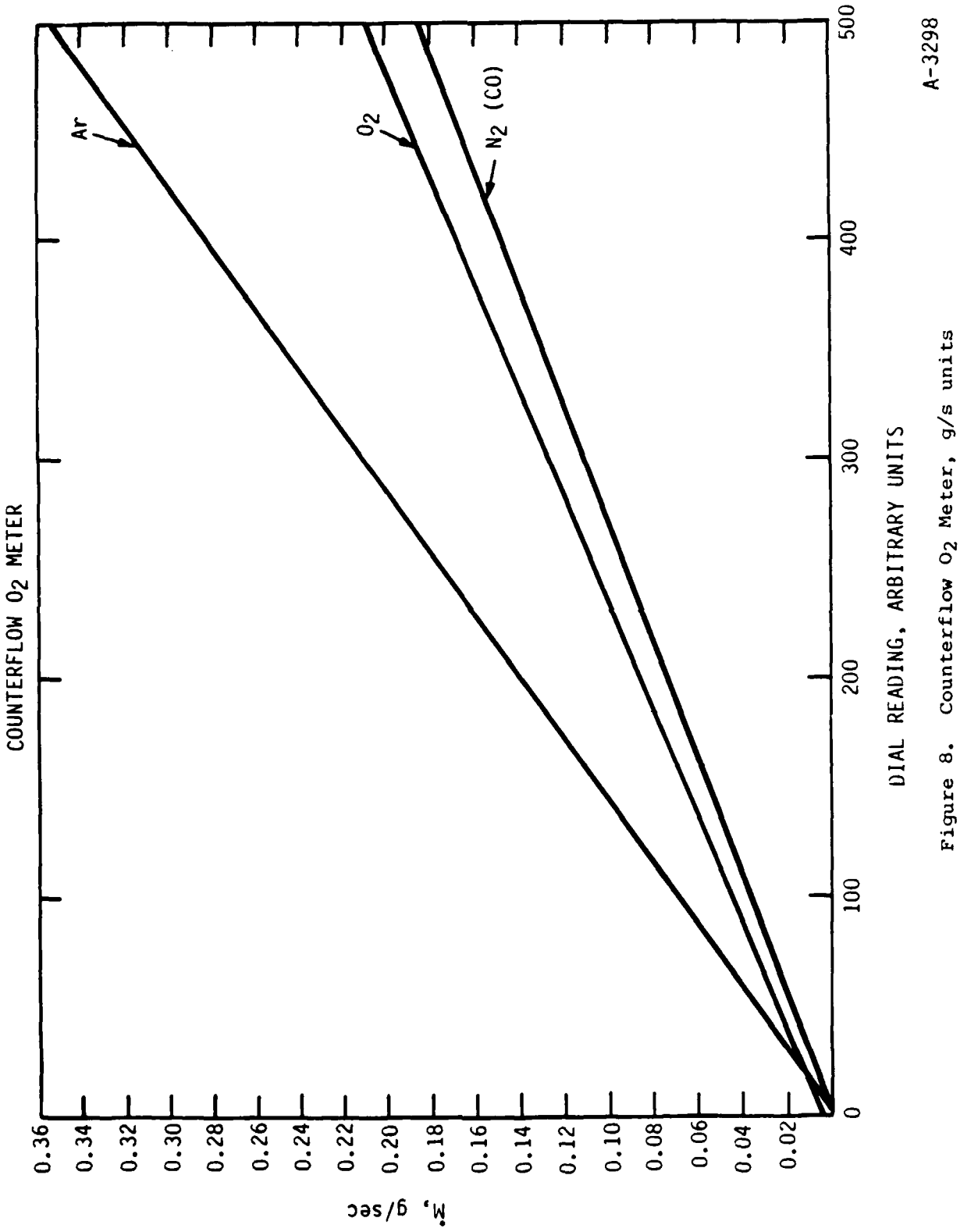

Figure 8. Counterflow O_2 Meter, g/s units

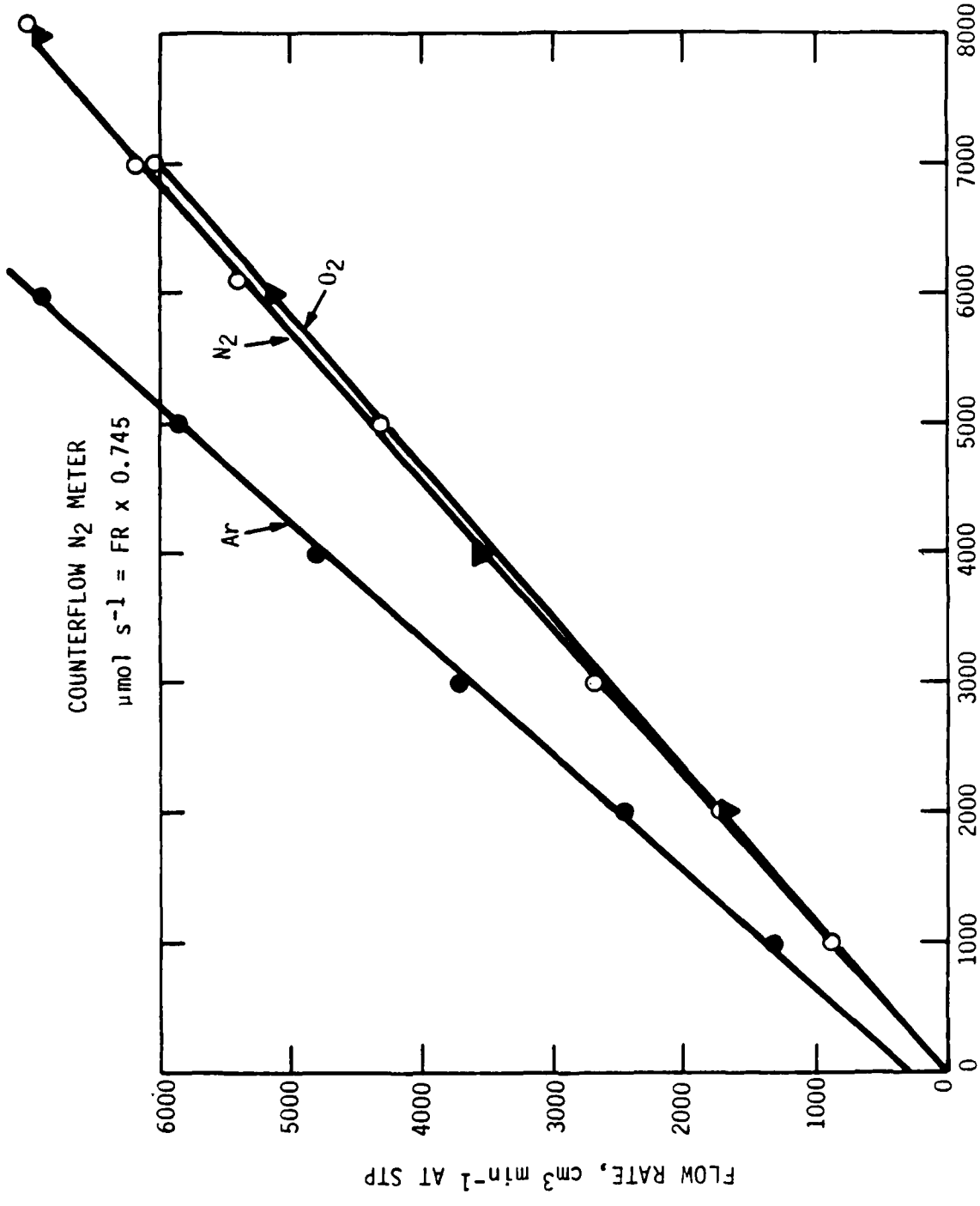

Figure 9. Counterflow N_2 Meter, cm^3/min units

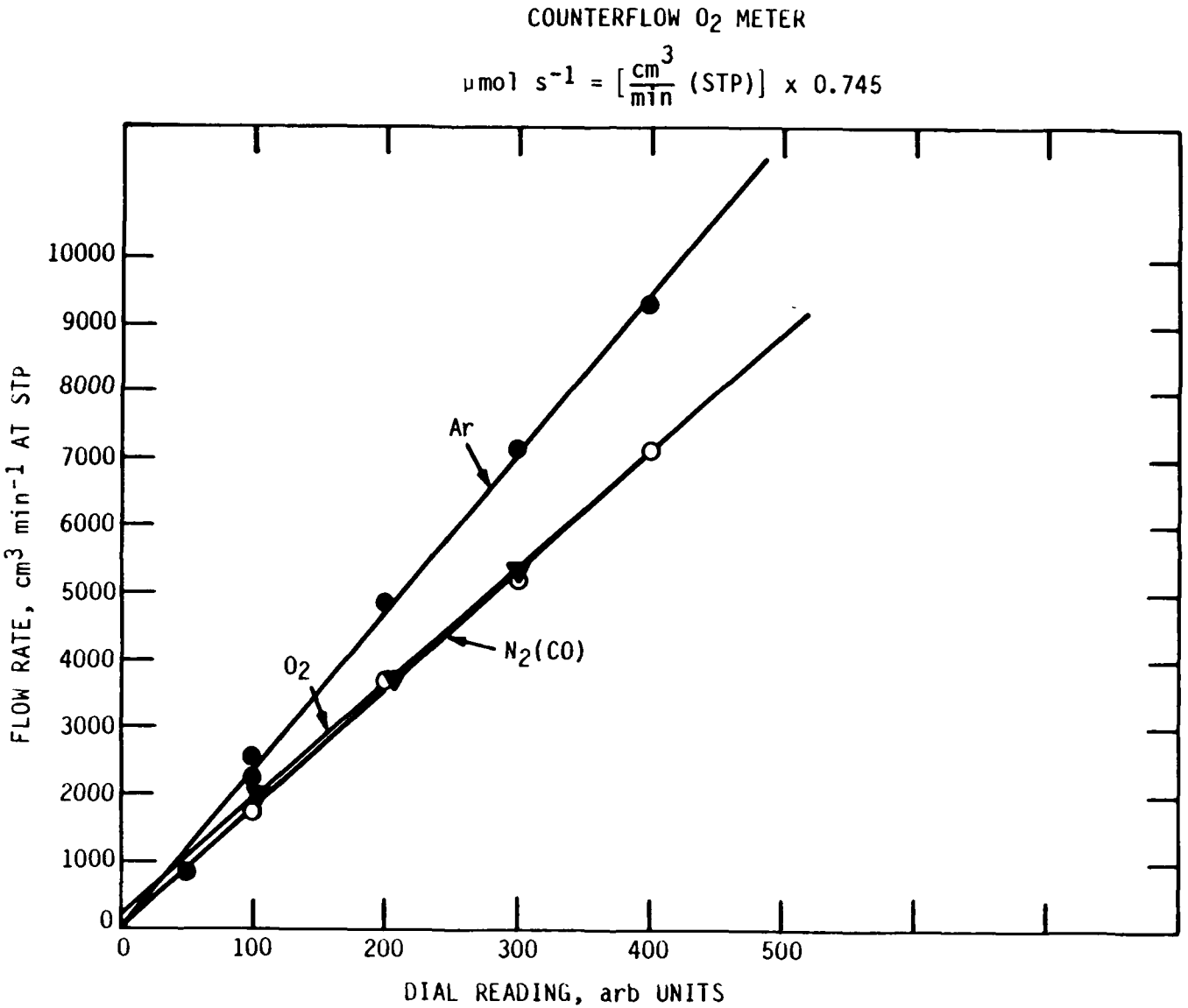

Figure 10. Counterflow O_2 Meter, cm^3/min units

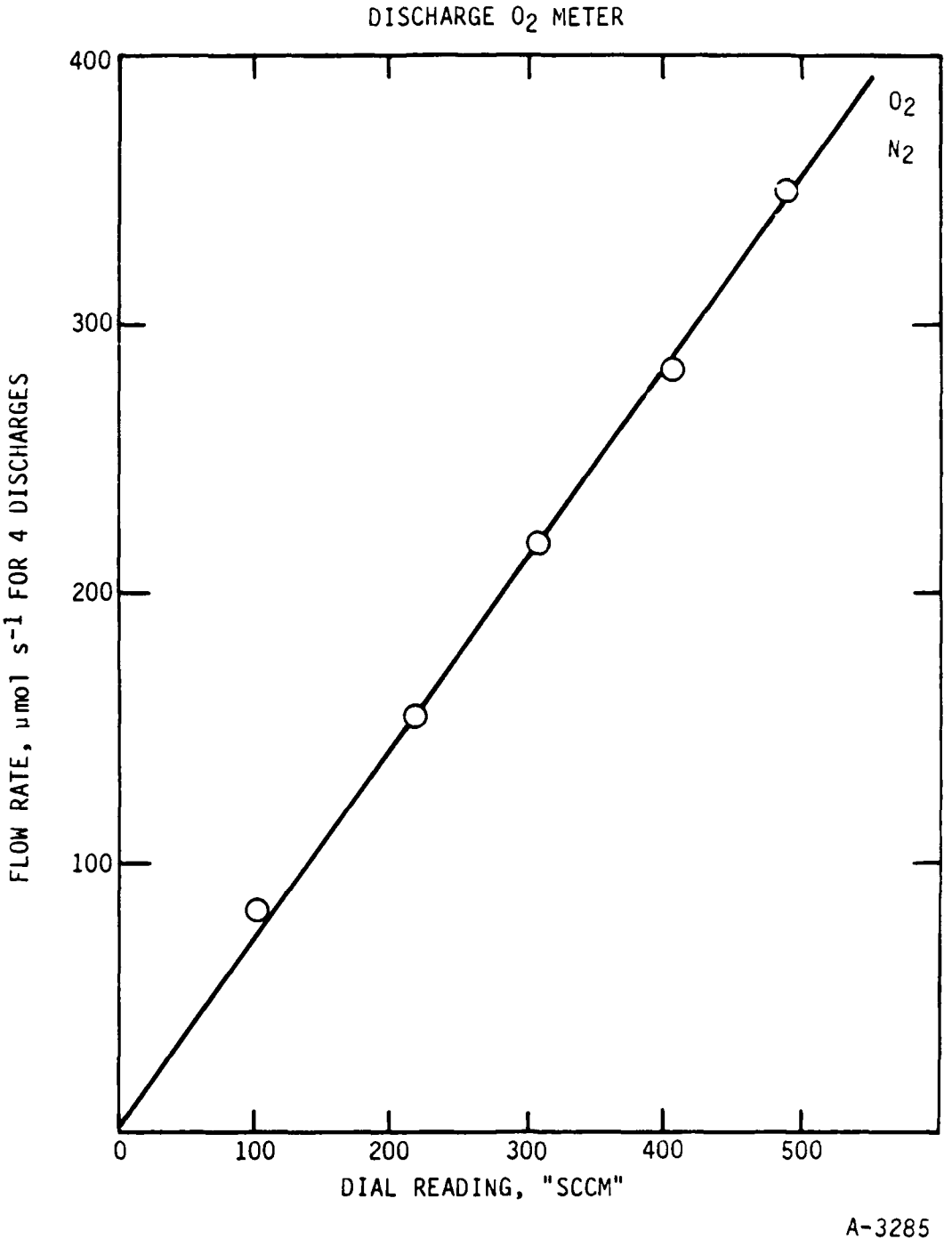

Figure 11. Discharge O_2 Meter, µmol/s units

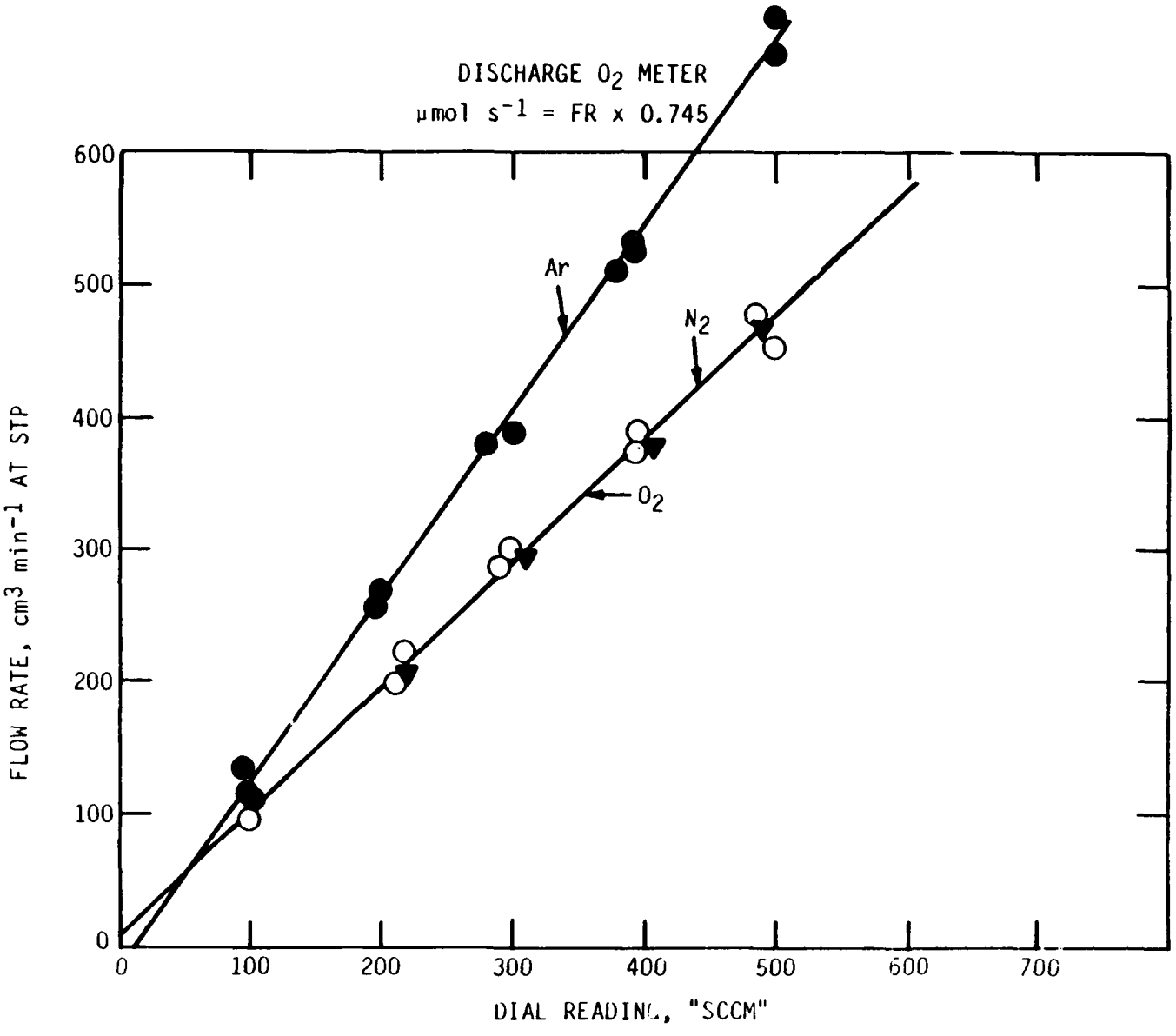

Figure 12. Discharge O_2 Meter, cm^3/min units

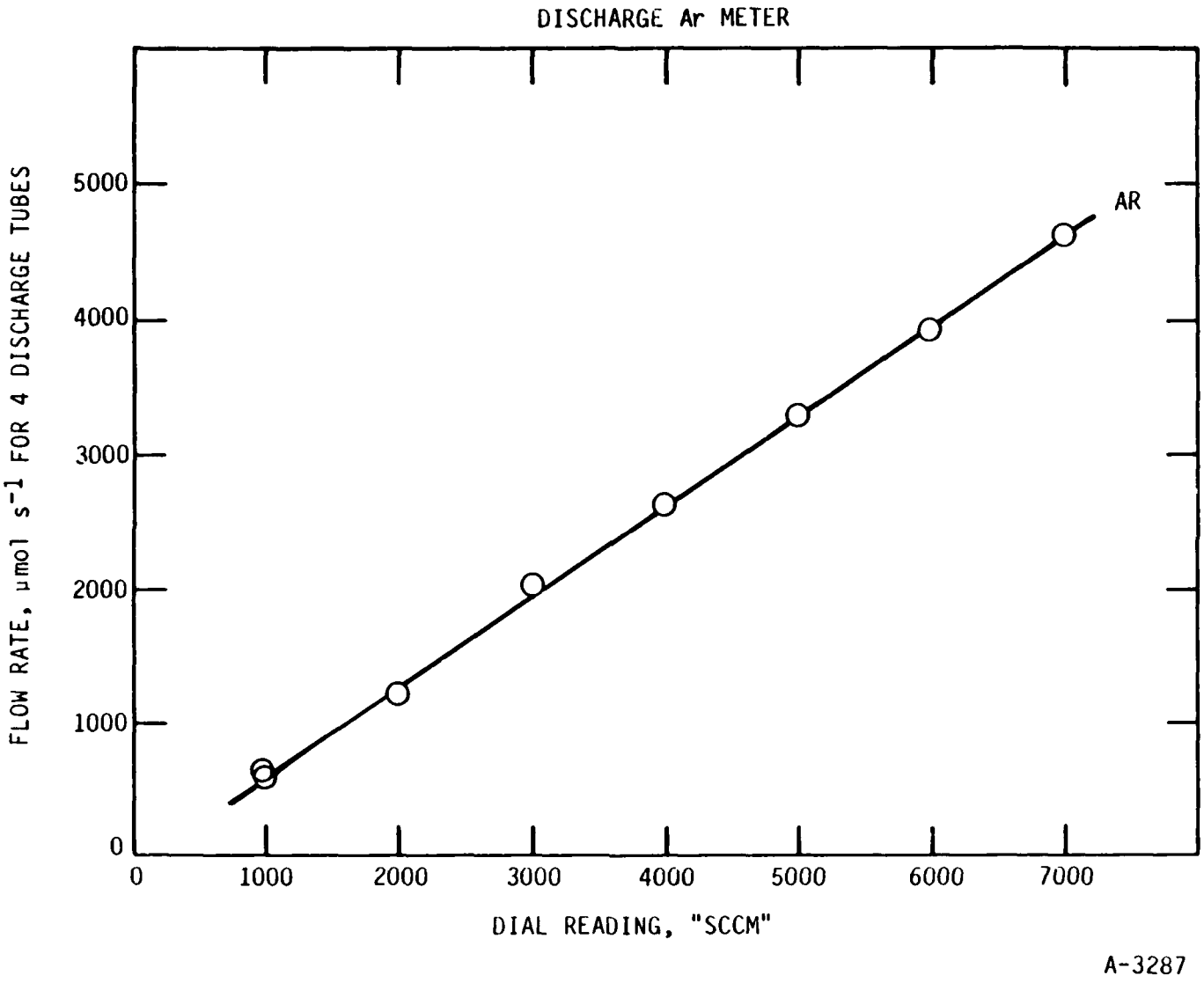

Figure 13. Discharge Ar Meter, µmol/s units

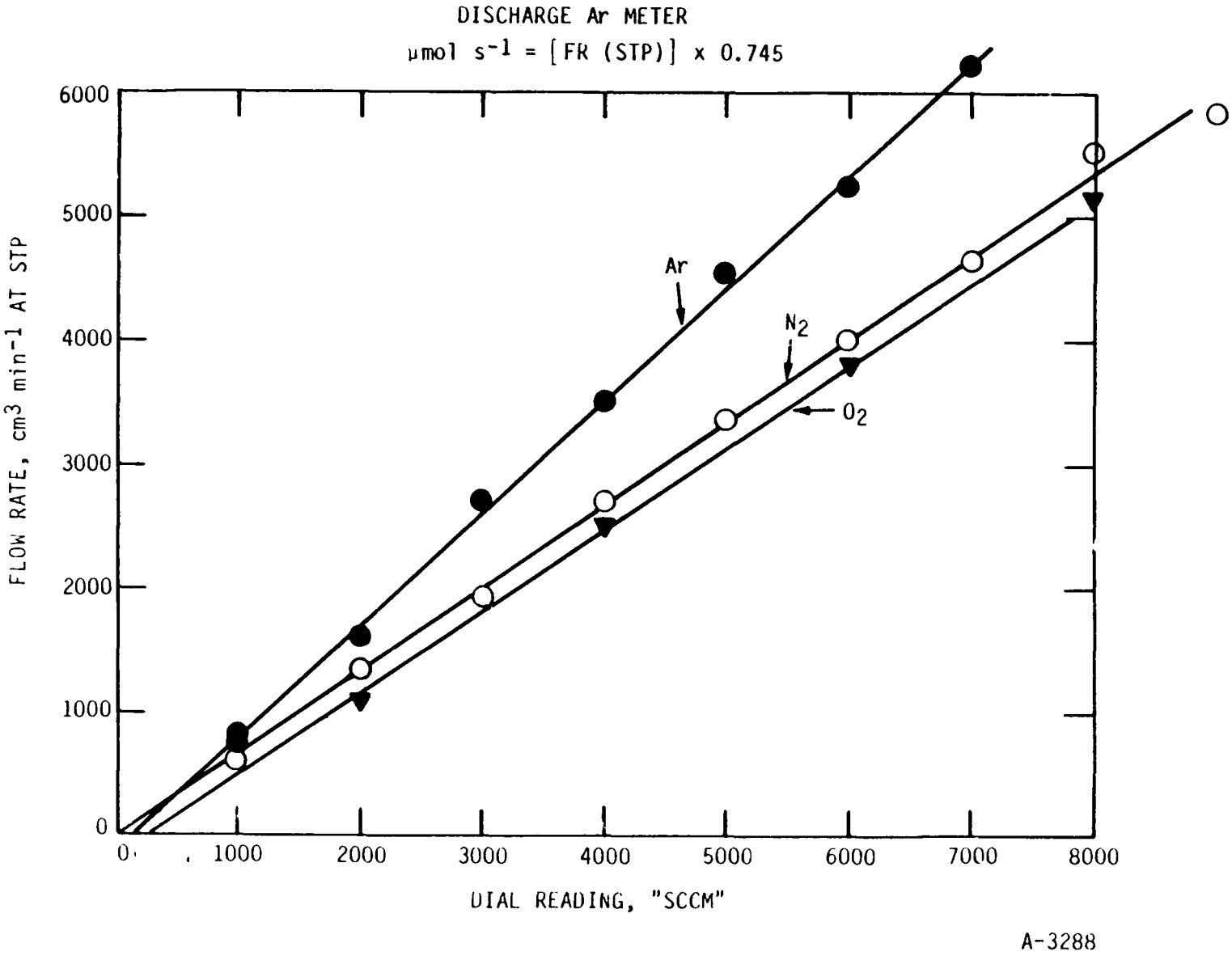

Figure 14. Discharge Ar Meter, cm^3/min units

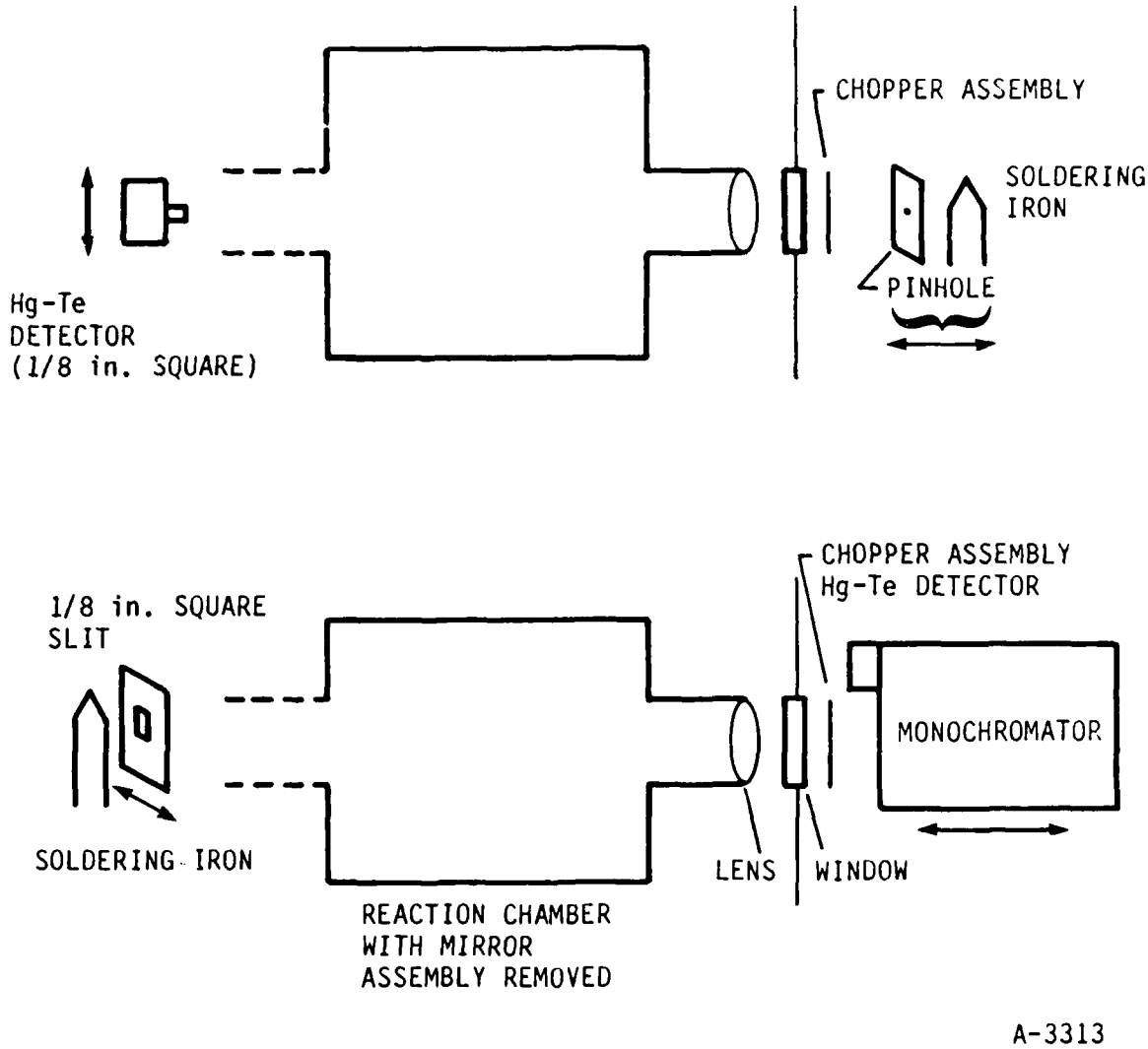

Figure 15. Field-of-View Appratus Configurations

The apparatus configuration shown in Figure 15a was the easiest to construct and so was tried first. With the detector placed along the horizontal diameter of the reaction cell at the position the mirror would occupy, the curve in Figure 16 was obtained. This figure shows the field of view to be ~6 to 8 cm wide. Since the mirror is 10 cm wide, it is clearly underfilled. With the source moved 2 in. farther away from the lens, Figure 17 was obtained. The intensity has increased in the field of view but the width of the field has decreased. Figure 18 illustrates the results for a position of the source displaced out of the line of sight by 1/2 in. The field of view is offset and the intensity reduced.

The studies with this configuration, although informative, do not accurately represent the true field view. What is required is a configuration similar to that in Figure 15b. The monochromator was put in zeroth order with the slits wide open (3 mm) and a source placed at the position of the mirror. Using a 1/8 in. square source, Figure 19 was obtained. This figure shows a narrower field of view than Figures 16 through 18. Signal-to-noise limitations prevented more than one full decade of data. Nevertheless, the results indicate that the mirror is underfilled and that COCHISE is unlikely to directly observe surface emissions.

2.3 Detection System and Signal Processing

2.3.1 Spectral Detection System

The detection system is isolated from the reaction system by an aluminum bulkhead which blocks scattered radiation from the cell and prevents the passage of reagent gases into the detection system. Infrared radiation emanating from a cylinder ~8 cm in diameter centered along the axis of the reaction cell (or from the blackbody source in the center of the end mirror, in the case of calibration measurements) passes through the reaction cell lens into the detection system via a 7.6 cm AR-coated germanium window in the center of the bulkhead. The radiation then passes through an order-sorting filter and an optional tuning fork chopper into a cryogenic grating monochromator, where it is dispersed and focussed onto a liquid-helium cooled detector.

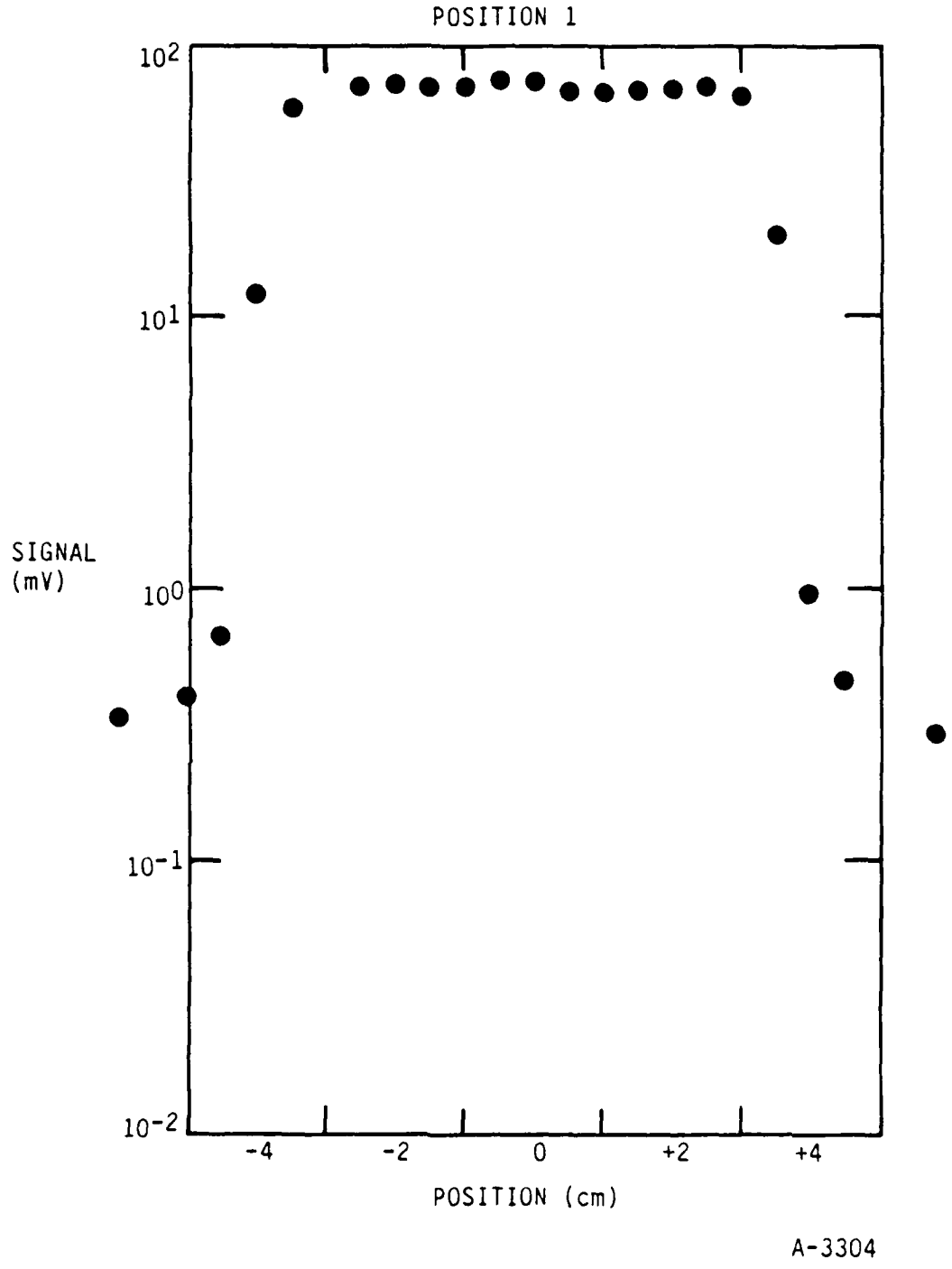

Figure 16. Position 1

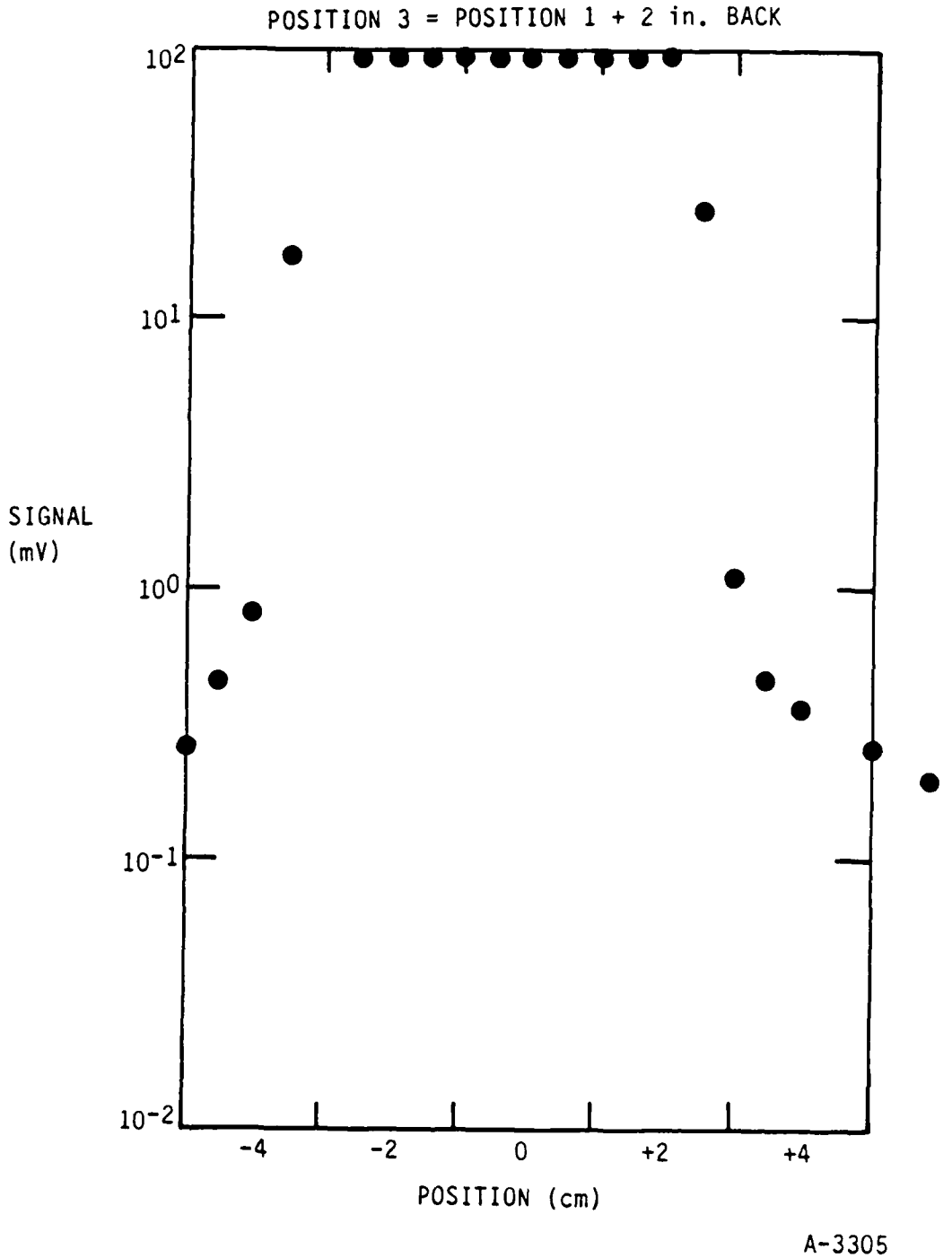

Figure 17. Position 3 - Position 1 plus 2 in. back

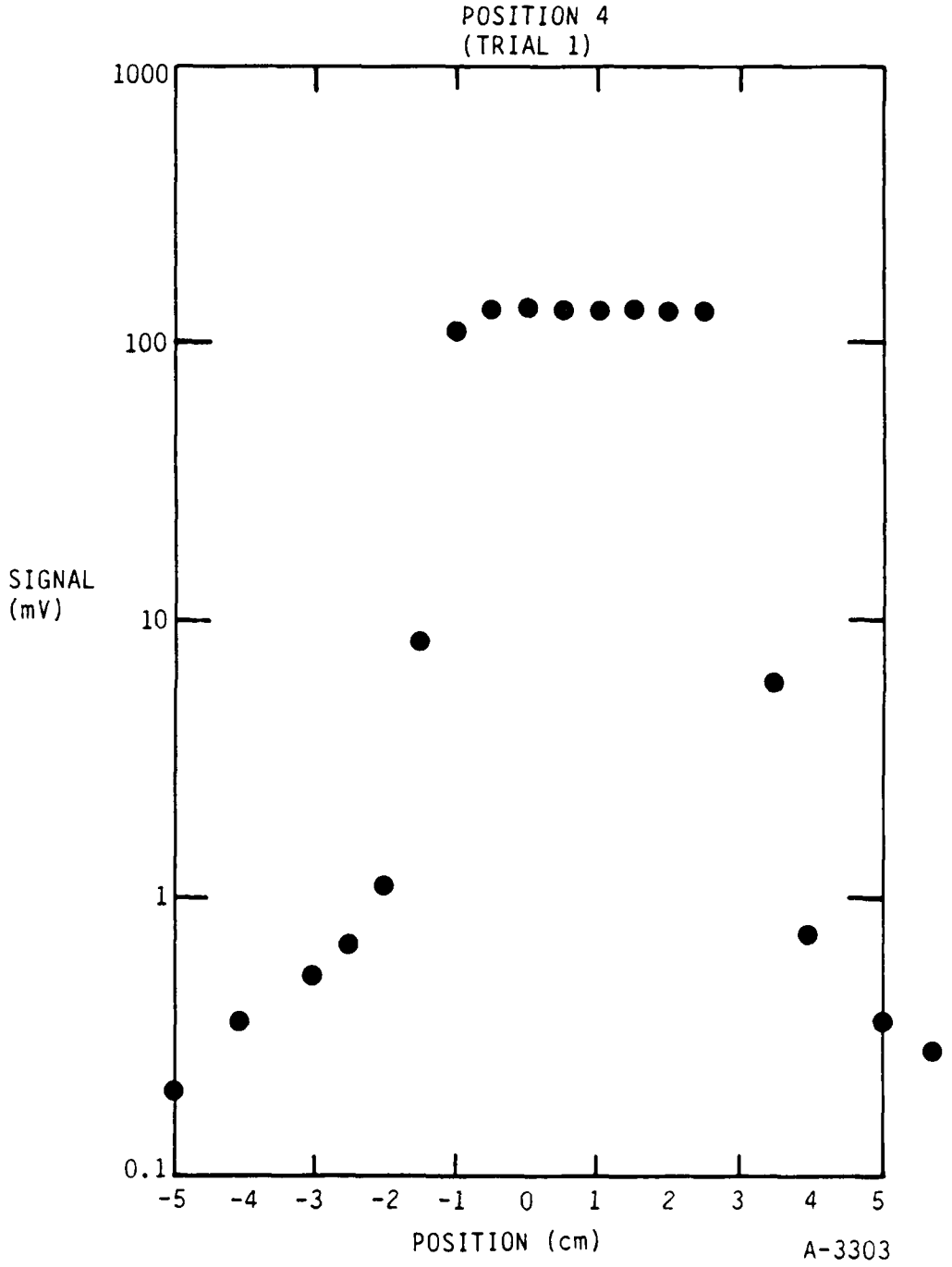

Figure 16. Position 4

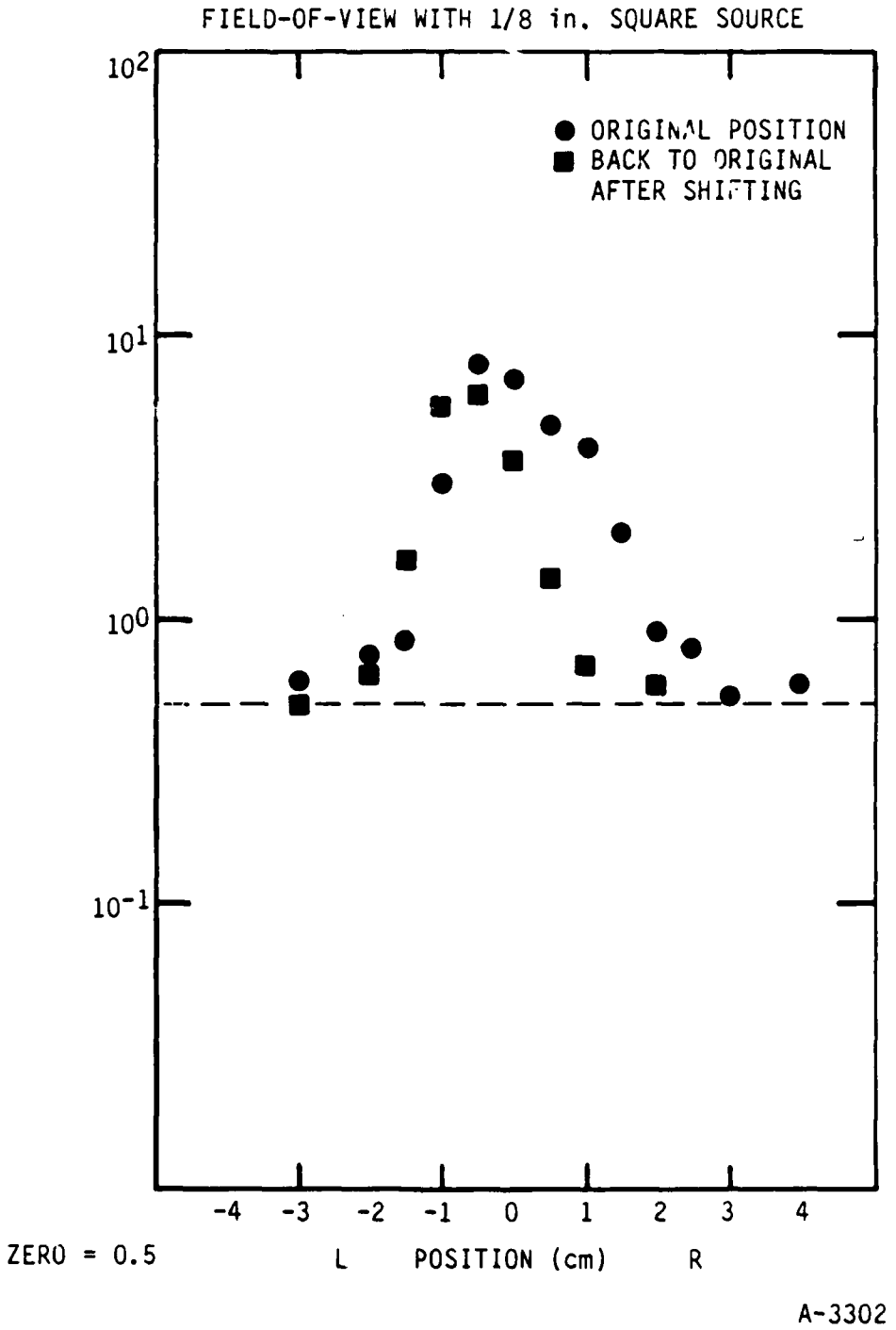

Figure 19. Field of View with 1/8 in. Square Source

2.3.2 Foreoptics

A series of long-wavelength-pass and/or bandpass filters is deployed by a specially constructed, solenoid-driven, rotating filter wheel. For most applications to date, long-wavelength-pass filters with sharp short-wavelength cutoffs at nominally 2, 4, and 8 μm have been used to isolate the corresponding first-order spectral regions of 2-4, 4-8, and 8-16 μm.

A 23 Hz tuning fork chopper (American Time Products type L40 or Philamon type TFLC 34CH-7178) positioned in front of the monochromator entrance slit can be used to modulate the incoming radiation. This chopper is used in all blackbody measurements and is optional in the chemiluminescence measurements, as will be described below.

2.3.3 Cryogenic Monochromator

In the development of a cryogenic spectrometer system for the COCHISE facility, a scanning grating monochromator proved to be the most straightforward, reliable, and economical approach. The instrument chosen was a 0.5m asymmetric Czerny-Turner system (Minuteman 305 CM), which is mounted on a Invar frame to minimize distortion at low temperatures. The spherical collecting and focusing mirrors and the grating are mounted in Invar supports, which are in turn mounted directly to the basic frame. The entire assembly is covered with a light-tight aluminum housing and is held at ~20 K during normal operation.

Two interchangeable replica gratings are employed, their selection depending on the wavelength region of interest. Both gratings are 6.4 cm square, which gives the instrument an aperture ratio of f/6.9. For wavelengths below 8 μm, a grating blazed at 3 μm with 150 lines/mm (at room temperature) allows a nominal first-order reciprocal dispersion of 0.013 μm/mm in the exit slit plane; for longer wavelengths, a grating blazed at 10 μm with 75 lines/mm gives 0.027 μm/mm. Thus, for a slit width of 0.5 mm, the

resolution element is ~2.6 cm^{-1} at 5 μm and ~1.4 cm^{-1} at 10 μm. Such resolution permits not only determination of detailed vibrational structure for most small atmospheric molecules (typical vibrational spacings of ~25 cm^{-1}) but also the observation of some rotational structure in many cases.

The entrance and exit slit assemblies consist of rotatable disks containing a series of fixed 2 cm high slits ranging in width from 0.1 to 3.0 mm (2 mm exit slit has sapphire insert); the slits can be independently indexed by manual controls outside the vacuum chamber. The grating is rotated by a conventional sine-drive mechanism using a precision ball screw designed specifically for cryogenic service; the scan drive controls are located outside the vacuum system. Three shafts penetrate the outer and inner walls of the system and are coupled to the slit assemblies and grating drive screw via stainless steel bellows.

2.3.4 Cryogenic Infrared Detector

The IR preamplifier-detector module was designed and fabricated at the Electrodynamics Laboratory of Utah State University. The photovoltaic detector element is an arsenic-doped silicon cube, 3.0 mm on an edge (Santa Barbara Research Center); an f/0.25 parabolic reflector images the monochromator exit slit onto the detector and thus permits collection of virtually all radiation passing through the slit. A contiguous preamplifier unit utilizes an integrated JFET operational amplifier (Burr-Brown 3521R) in a direct-coupled negative-feedback operational scheme that previously has been applied successfully to ultrahigh impedance cryogenic detectors.[10] The module also contains an IR emitting diode, temperature monitors, and associated electronic elements and devices. The preamplifier and detector are maintained at temperatures of ~220 and 9 K, respectively, by proportional control systems. An external console provides system control functions, detector bias, signal conditioning circuitry, and output indicators and terminals. This detector, when operated at ~9 K, is sensitive to 1.2 to 22 μm radiation and has a peak noise equivalent power of ~10^{-16} $W/Hz^{1/2}$.

Liquid helium cooling of the detector package is provided by a 20-liter liquid helium vessel suspended from a port on the top of the vacuum chamber. The neck of the vessel, which serves as a fill-and-vent line, is flexibly connected by a bellows to a port in the 20 K shroud to effect a light-tight penetration. Thermal coupling between the detector and the liquid helium vessel is accomplished by a copper bar and thermal strap, with sapphire electrical standoffs to isolate the detector-preamplifier case.

2.3.5 Signal Processing

The detector output is processed by phase-sensitive detection to discriminate against random-phase background noise. The radiation reaching the detector is modulated in one of two ways. In most chemiluminescence observations, the microwave discharges are pulsed at ~23 Hz with a square wave, 50 percent duty cycle; since chemical reaction does not occur in the absence of the reactive species formed in the discharge plasma, this results in a square wave oscillation in the chemiluminescence signal (provided the chopping frequency is slow enough relative to the flow speed so that diffusional blurring of the waveform does not occur). An alternate method of data collection is to operate the discharge continuously and modulate the radiation with the chopper. However, the pulsed discharge method has the advantage of discrimination against stray radiation, which is not directly linked to species produced in the discharge plasma. The chopper is also used to modulate the radiation from the internal blackbody source during calibration measurements.

The ac detector output passes through an optional bandpass amplifier (PARC Model 113) and into a lock-in amplifier (PARC Model 124) which is synchronized either to the frequency of the chopper pickup coil or to the external pulse generator used to pulse the microwave discharges. The final demodulated signal is digitally averaged, displayed, and stored in real time by the PDP-8/E computer. The combination of grating scan rate, electronic time constant, and digital averaging for a given spectral scan is carefully chosen so that there are at least seven averaged data points and three time constants per spectral resolution element; these criteria insure that the

apparent spectral detail is indeed limited by the instrument resolution. The data are initially stored on disk by the PDP-8/E computer and are subsequently transferred via magnetic tape to other computers for detailed analysis.

2.3.6 Spectral Responsivity

The spectral responsivity of the COCHISE optical/detection system, as determined from calibrations with the internal blackbody source, is plotted as a function of wavelength in Figure 20. The 2 to 16 μm spectral region was traversed by means of two gratings and three long-wavelength-pass filters. The solid curves were obtained using a 10 μm blazed grating. First-order measurements employ a 4 μm long-pass filter (5 to 9 μm) and an 8 μm long-pass filter (8 to 16 μm), while second-order measurements can be made using a 4 μm long-pass filter together with a sapphire window (4 to 8 μm). The dashed curves were obtained in first order using a 3 μm blazed grating with 2 and 4 μm long-pass filters. Since the noise level of the instrumentation is $\sim 10^{-6}$V, the maximum responsivity, at ~10 μm, corresponds to an optimum NESR near 10^{-12}W cm^{-2} sr^{-1} μm^{-1} or $\sim 10^{6}$ photons cm^{-3} s^{-1} μm^{-1} for the effective optical path length of 100 cm. For typical species of interest (e.g., O_3), the transition probability is ~10 s^{-1}, and the bandwidth is ~1 μm; thus the minimum detectable concentration of such vibrationally excited species is of the order of 10^5 molecules cm^{-3}. This unsually high sensitivity at such long wavelengths is due to the absence of noise from thermal background radiation and to the long optical path which is available for the measurements.

2.4 Refrigeration System

COCHISE requires a rugged, high capacity refrigeration system in order to cool down and maintain a chamber temperature of ~16 K. The refrigeration system chosen was a Cryogenic Technology Model 1400 which is capable of providing gaseous He at the required temperature and mass flow. Pictorial diagrams of the refrigerator can be found in the system operation manuals which are kept in the COCHISE work space. A diagram of the plumbing of the refrigeration system illustrating those components relevant to COCHISE operation is shown in

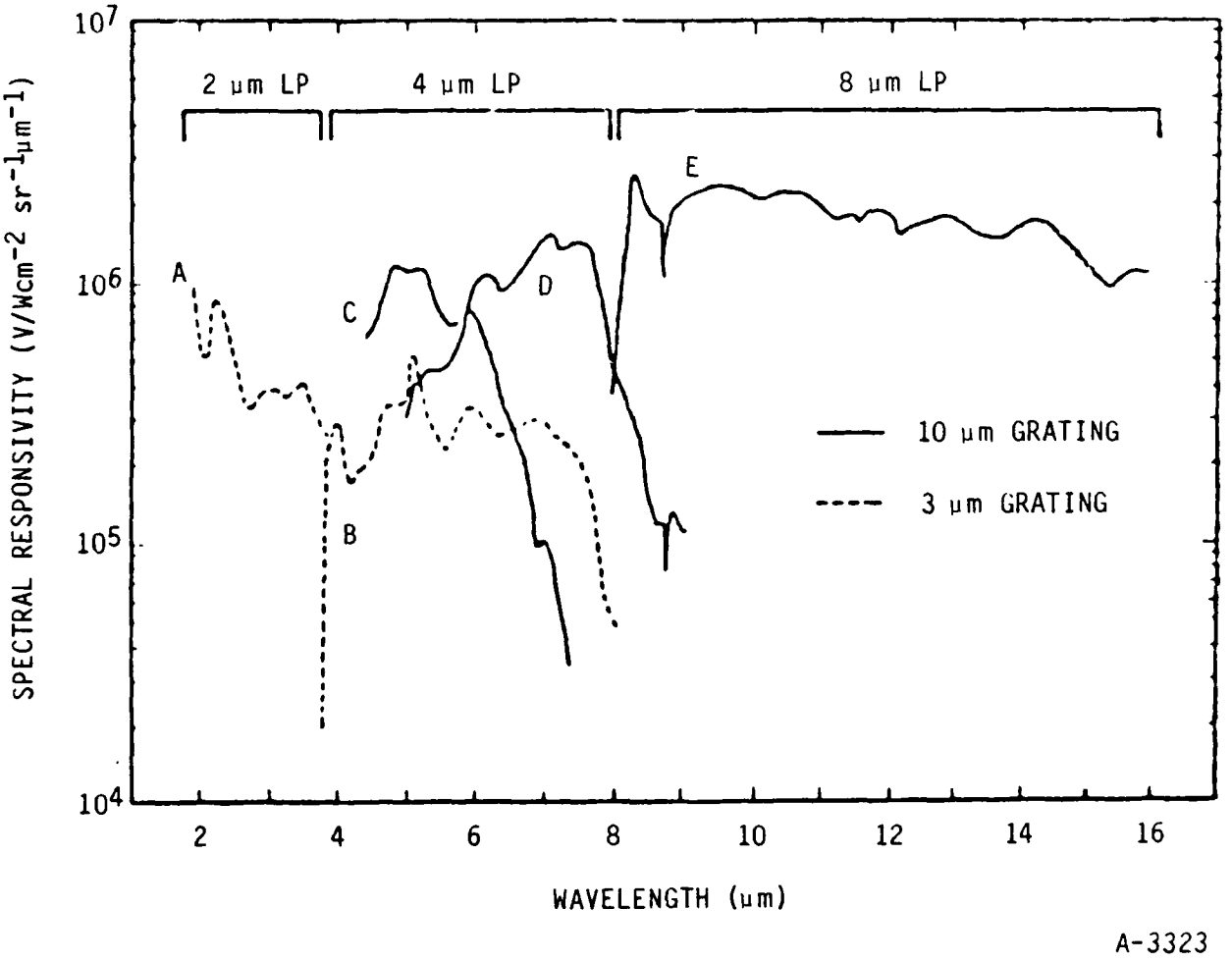

Figure 20. Approximate Spectral Responsivity of COCHISE Optical System for Two Grating Blaze Wavelengths and Three Order-Sorting Long-Pass Filters as Indicated. Curves A,B,D,E were obtained in first order; curve C was obtained in second order using a sapphire long-wavelength cutoff filter.

Figure 21. Figure 22 shows, in greater detail, the plumbing of the refrigerator lines entering the chamber. Each of the indicated valves (shroud, heat sink plate, and reaction cell) allow individual control of refrigerant flow to these subsystems. These valves are physically located underneath the COCHISE chamber and are evident in Figure 2. Labelled photographs of the refrigerator system may be found in the manuals stored in the COCHISE work space.

Typical operation of the refrigerator system is decribed below. The system operates in two basic modes: normal and cooldown. Normal operation will be described first:

Normal: (low speed, 1 or 2 compressors)

- He from supply manifold and low-P return gas from RF (5 to 9 psig) go into compressor(s).

- Compressed He is regulated at 230 to 240 psig by "bypass regulator"; excess goes through recovery/bypass valve (in recovery position) into storage tank.

- Storage tank should be at 25 to 50 psig. If pressure is too low (as when gas gets cold in cooling lines, then some bleeds from tank into low P side), the low side P cannot be controlled by low side regulator. If this happens, let some in from the supply manifold. This gas goes through the compressor(s) and the excess is shoved through the bypass regulator into the storage tank.

- High P return He enters four-stage heat exchangers. Valve V806 controls amount which goes through LN_2 first stage. Other stages use heat transfer with outgoing He.

- Cooled compressor gas undergoes expansion in parallel engines. Inlet and outlet valves for each engine are operated by big cam on top of RF cabinet. These valves need to be adjusted so that they open and shut properly; adjust best when cold.

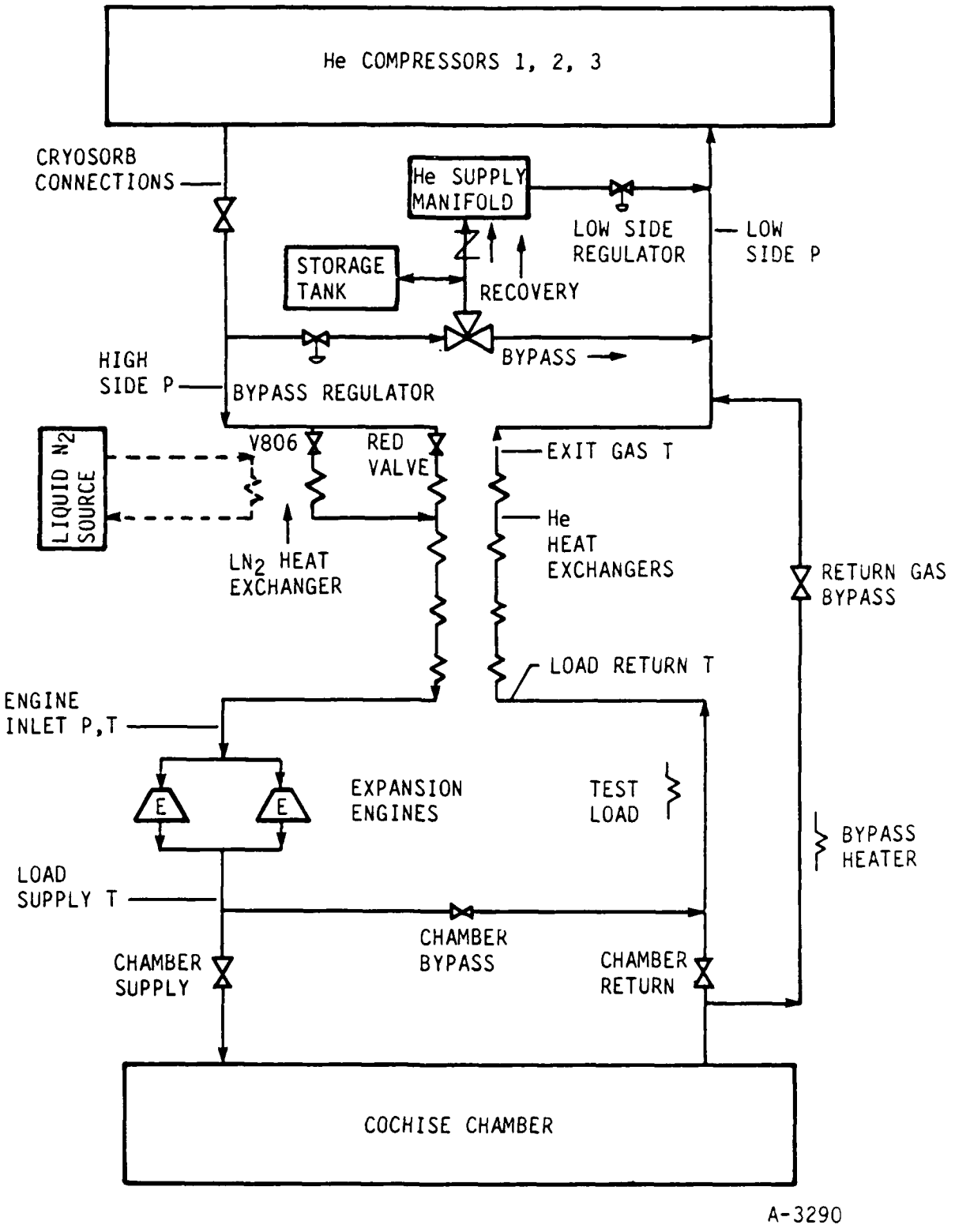

Figure 21. Refrigerator System

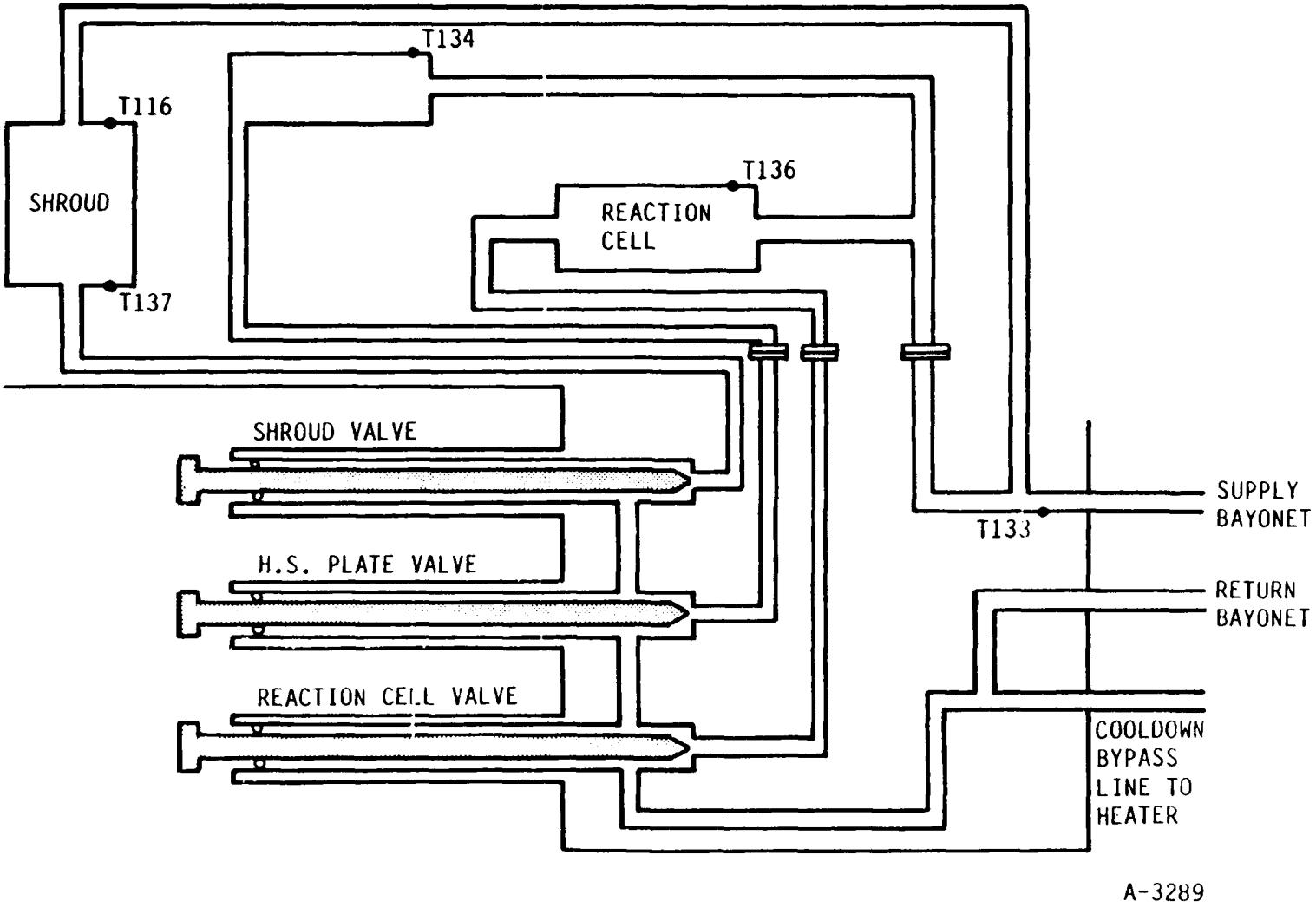

Figure 22. COCHISE Refrigerant Valves

- P drop between high side and engine inlet should be ~(235 to 180) psig, the smaller the better. Too much P drop is robbing you of efficiency, and may be due to freeze-up of contaminants in heat exchangers.

- Low P, cold (~10 K) He passes through load and returns to RF at ~15 to 20 K.

- Return coolant He (low P) passes through heat exchangers and cools high P gas coming from compressor(s). For best efficiency, the temperature at the exit of the heat exchangers should be -15° to -20°C. This temperature is controlled by valve V806, which diverts some of the high P gas through as LN_2 first stage. If this valve is open too far, there is too much cooling by LN_2 and not enough warming of the low P He. The result is that LN_2 is wasted and the low P He is too cold going to the compressors. In this event, the Cu pipe will frost up. The best setting for V806 is ~50 percent open (fully open = 9 turns).

- Warmed, low P (5 to 9 psig) He returns to the compressor and gets compressed; the cycle starts over again.

- Reducing low side P from 9 to 4 psig decreases the efficiency but may be easier on the compressors. This is an attempt to prolong the life of the seal on the compressor inlet, the most failure-prone part of the compressor. Use when load is small, i.e., no discharges.

- Note: Never operate <4 psig; operation <0 psig can cause damage to the compressors.

- If high P side exceeds ~245 psig, the compressor relays will start to make a godawful noise as they cut in and out in order to not exceed maximum P. Keep the setting <u>below</u> 240, since this tends to drift up over several hours. 235 is best.

Cooldown: (high speed, 1 compressor: an option) but typical operation now low speed, 2 compressors

- Recovery system set up as in normal; high P He from compressors regulated at ~230 to 240 psig and storage tank stays at 25 to 50 psig.

- High P He from compressors goes entirely through LN_2 first stage. This is done by closing the red-handle ball valve up inside plumbing. This is all the precooling that the gas gets, since there is no return gas on the other side of the heat exchangers.

- High P He, cooled by LN_2, undergoes expansion in parallel engines. Optimum P drop is the same as in normal.

- Cold, low P He goes through system load.

- The gas returning from the load bypasses the heat exchangers and goes directly to the compressors, as follows. Return valve on RF is closed. All He from load passes through Cu tubing out of plenum, through the parallel heaters (variable control), through the bypass ball valve (which is closed for normal) next to the platform and directly to the compressors. The return gas and heat exchanger exit gas temperature monitors are bypassed and therefore their readings are meaningless. The bypass is continued until the gas returning from the load is cold enough to do some good in the heat exchangers.

- In bypass mode, plug in bypass line heater. This heater is thermostatted for 50 °F to keep this line from freezing.

- Bypass mode should be maintained until the shroud is ~100 K.

- When shroud warm end ~100 K or at the end of the day, begin transition to normal (turn off heater, close bypass). REMEMBER TO TURN OFF HEATER SEVERAL MINUTES BEFORE CLOSING THE BYPASS VALVE, OR AN EXPLOSION WILL RESULT

- Once bypass is closed, system will cool fast except for spectrometer. To speed this up, backfill with He. Watch P in vacuum space as well as in spectrometer and do not exceed $\leq 10^{-5}$ Torr on ionization gauge. This will correspond to ~100 mTorr in the spectrometer which will slowly decrease. Repeat every time this gets below ~10 mTorr.

- IMPORTANT: remember to purge LHe dewar with He during the entire cooldown in order to prevent icing.

- Start with LN_2 on automatic throttle. After 1 hr, switch to unthrottled LN_2. Reinstall LN_2 flow controller when switching over to normal.

2.5 Temperature Diagnostics and Control

Not all of the COCHISE components can be operated at cryogenic temperature. The gas lines (discharge heat sinks, counterflow and discharge manifolds, and pressure port plate) are typically operated at 90 K to avoid condensation of reagent gases. Figure 23 shows the vapor pressure of all the gases used in COCHISE experiments at various temperatures. Operation at 90 K is adequate for most commonly used gases (N_2, CO, Ar, and O_2) but much higher temperatures are required for NO, N_2O, and CO_2.

The optical components (bulkhead window, reaction cell lenses, reaction cell mirror) are typically operated 40 to 80 K in order to prevent condensation of reagent and product gases. Since these components are within the field of view operation at 40 to 60 K is preferred to minimize the thermal background.

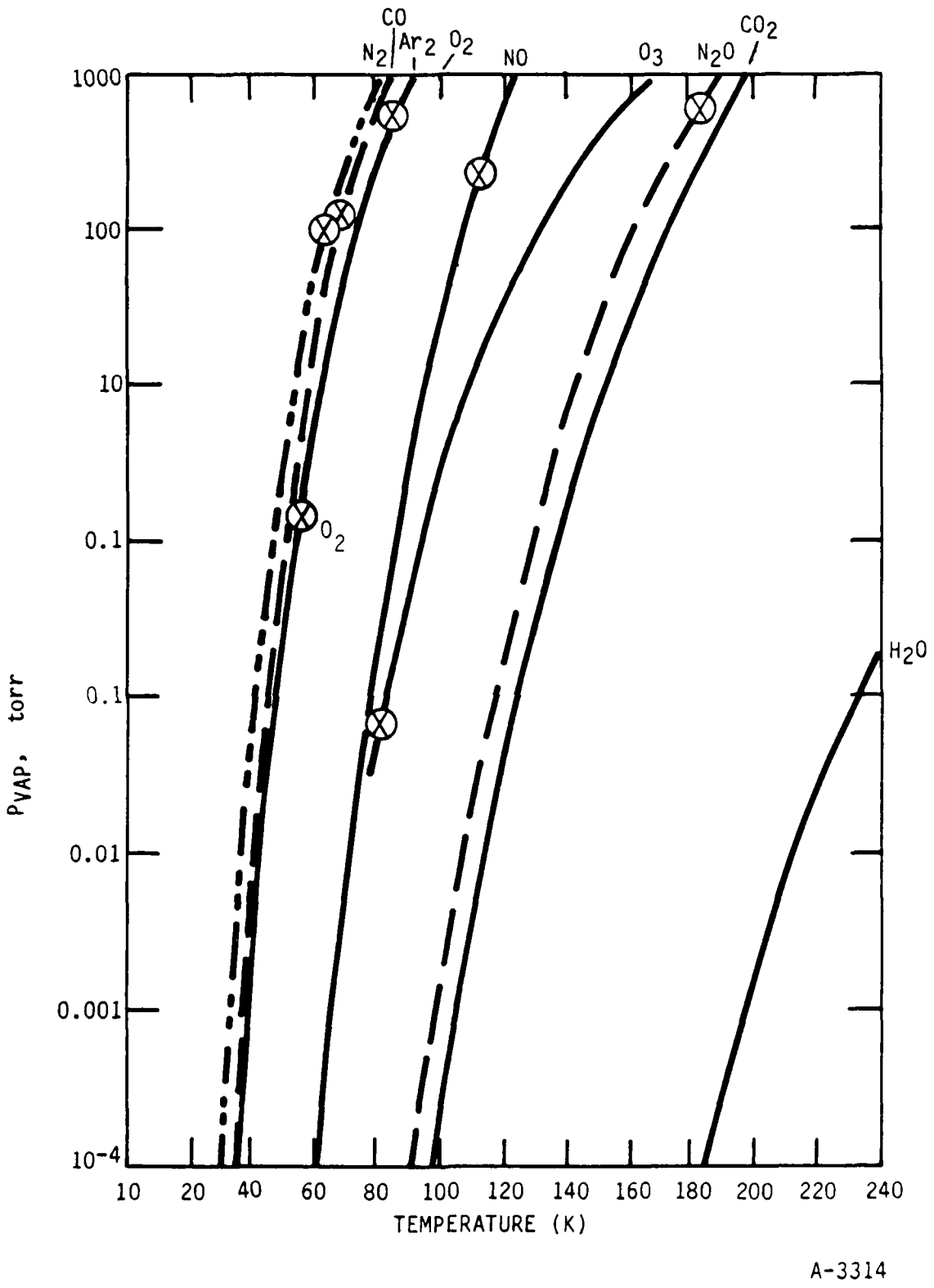

Figure 23. Vapor Pressure of Reagent Gases; ⊗ indicates melting temperature

The various channel assignments for the temperature monitor/controls are listed in Table 1. Control and readout is possible only when the program MOTHER is running. The teletype prints the refrigerator, shroud, reaction chamber, heat sink and spectrometer temperatures every 5 min. Output of these sensor readings are necessary during cooldown and warmup and cannot be altered. Readings of any of the other sensors, including those output to the teletype, may be displayed on the two console screens by setting the A/D numbers into the six locations beneath the left console. A total of six channels may be monitored simultaneously. One note of reference, the second channel can accept only an even A/D valve.

The temperature sensors used in COCHISE have a variable resistance with temperature. Figure 24 shows a typical plot. The resistance is linear over the temperature range 40 to 400 K. Below 40 K the resistance is decidedly nonlinear and accurate temperature readings are afforded only above 25 K. This is adequate for most of the COCHISE sensors. However, a much more accurate temperature reading in the 5 to 20 K region is required for the detector. This is achieved with a sensor which increases in resistance with decreasing temperature. A plot of the temperature versus sensor resistance is shown in Figure 25. This sensor is mounted on the copper bar which is thermally attached to the detector. Readout is achieved through a port marked LHe on the console connected to a DVM.

The heater controls are located on the COCHISE console panel. A power switch is located to the left. Each heater unit is composed of a Variac and three-position switch. In the up position, the heater is controlled by the computer. With the switch in the neutral position, the heater is off and in the down position, manual control is permitted. The Variacs may be set to any desired position allowing the heating rate to be adjusted. The spectrometer heater is not located on the console, it is located on the shelf above the gas cylinders. This heater is also controlled by a Variac but has only a manual control. Computer control is not necessary since this heater is only used during warmup to keep the spectrometer warmer than the shroud and reaction chamber thus preventing condensation of gases.

Table 1. Channel Assignments for COCHISE Temperature Monitor/Control

A/D	Heater	Location	Sensor Cabling Identity	Sensor I/O Port
37	--	Shroud, warm end	HP 2	BV (3,4)
36	**	Reaction cell	CT 60	BI (5,6)
35	8	Discharge gas manifold	HP 8	BIV (1,2)
34	--	Discharge master heat sink plate	CT 53	BV (7,8)
33	--	Refrigerant return	CT 61	BVI (1,2)
32	9	Bulkhead window	HP 3	BIV (7,8)
31	10	Reaction cell lens	CT 69	BVI (5,6)
30	7	Reaction cell mirror	CT 56	BVI (7,8)
27*	4	Discharge heat sink #8	CT 65	BIII(7,8)
26	(4)	Discharge heat sink #7	CT 64	BIII(5,6)
25*	3	Discharge heat sink #6	CT 58	BIII(3,4)
24	(3)	Discharge heat sink #5	CT 57	BIII(1,2)
23*	2	Discharge heat sink #4	CT 55	BII (7,8)
22	(2)	Discharge heat sink #3	CT 54	BII (5,6)
21*	1	Discharge heat sink #2	CT 52	BII (3,4)
20	(1)	Discharge heat sink #1	CT 51	BII (1,2)
17	11	Inner hreat exchange plate	HP 5	BIV (5,6)
16	--	Shourd, cold end (spectrometer valve plate)	HP 7	AI (5,6)
15	--	Outer heat exchange plate	HP 1	BV (5,6)
14	6	Pressure port plate	HP 4	BIV (3,4)
13	5	Counterflow manifold	CT 62	BV (1,2)
12	***	Spectrometer interior	HP 6	AI (3,4)
11	--	Spare	CT 67	BI (7,8)
10	12	Blackbody source	CT 59	BVI (3,4)

*Heater channels 1,2,3,4 are controlled by temperature data from heat sinks 2,4,6,8: A/D channels 21,23,25,27.

**Reaction cell temperature is controlled by separate analog device.

***Spectrometer heating is accomplished via CW Variac on side shelf.

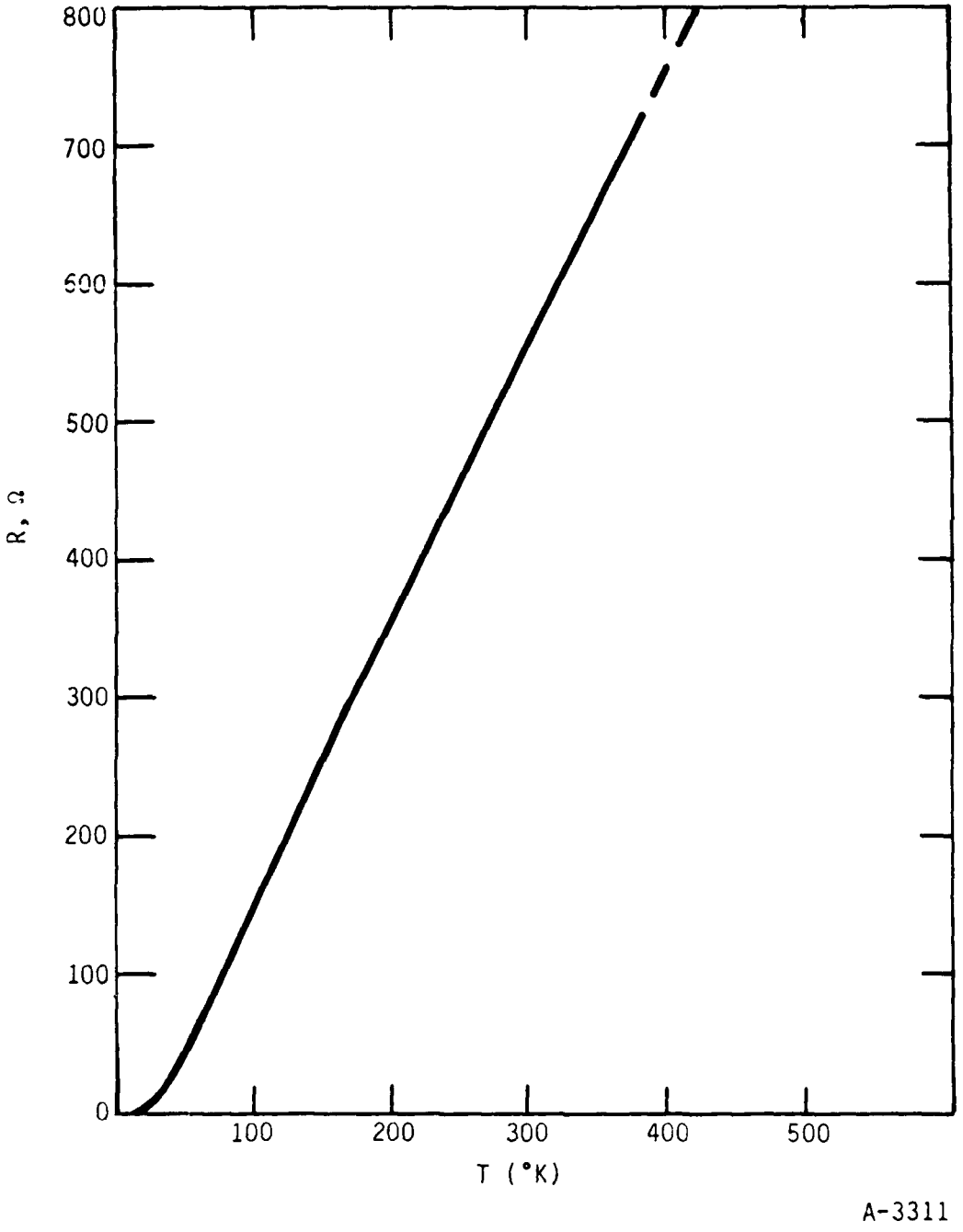

Figure 24. Temperature Sensor

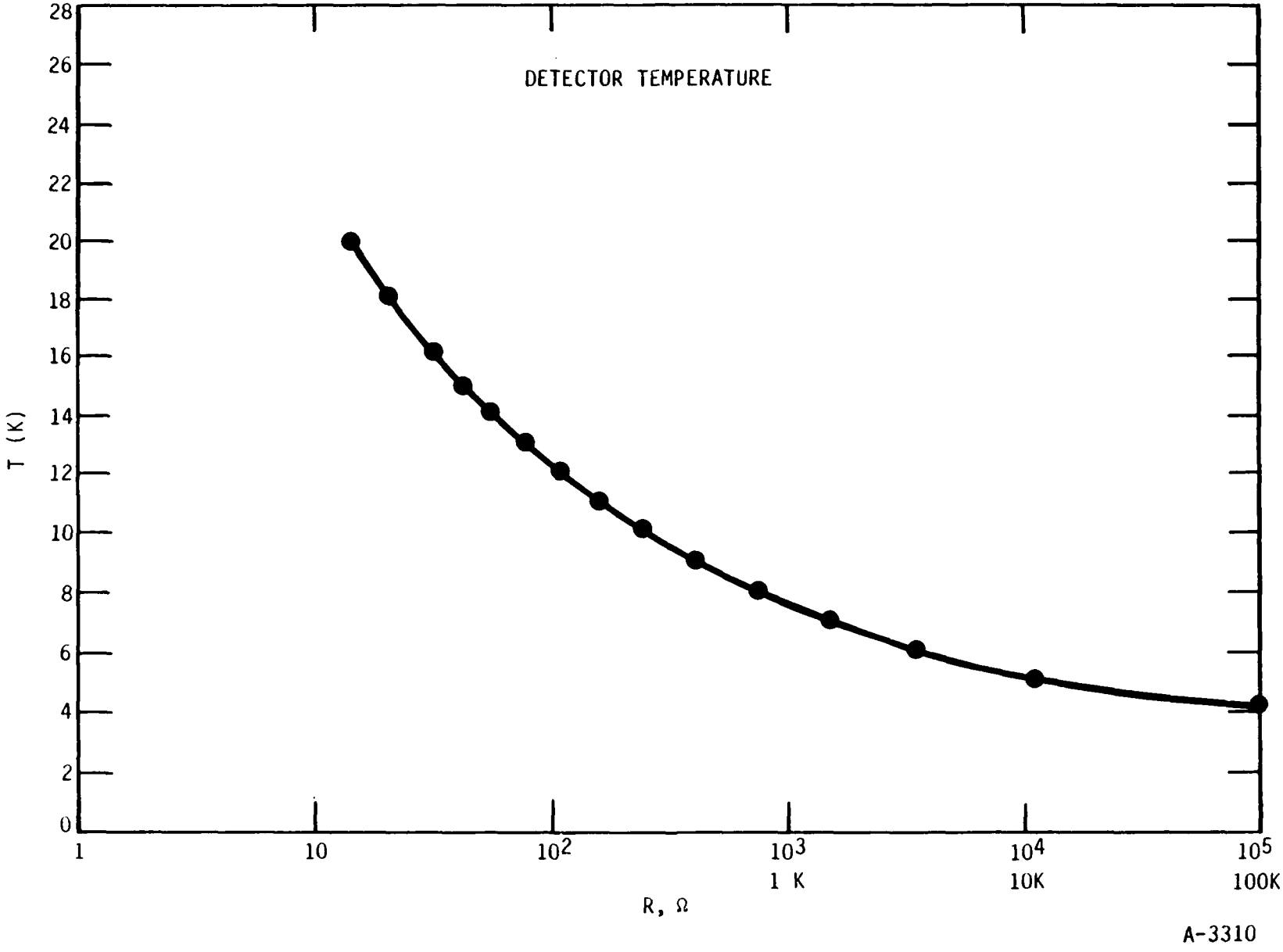

Figure 25. Detector Temperature Sensor

2.6 The Computer System

The PDP-8E computer system is the control and data acquisition system of COCHISE. The program MOTHER affords all of the control and data acquisition tasks necessary to operate COCHISE. This section discusses three aspects relevant to operation of the computer system: 1) booting the computer, 2) Tektronix CRT commands for running MOTHER and data file manipulation, and 3) teletype commands to open data files, start data collection, and affect temperature control.

The booting procedure is shown in Table 2 and is relatively simple and straightforward. If this booting system fails, try again. If the computer will still not operate, there may be a problem in the computer hardware or in the disk drive. A service call to Digital Corp. (273-6630) may be necessary. The identification number of the computer system is 8E (system type), 6631 (serial number).

The Tektronix CRT commands and teletype commands are shown in Tables 3 and 4, respectively. It is important to note that Tektronix CRT commands can only be used when MOTHER is not running, only teletype commands can be entered in MOTHER.

The computer system has a total of four disks, the two sides of the one on top and the two sides of the bottom one. They are numbered sequentially RKA0, RKA1, RKA2, and RKA3. Disk 0 is used to store all of the COCHISE programs including MOTHER. Data storage should not be attempted on this disk. Data storage is automatically perfomed on Disk 1. Disks 2 and 3 are used for backup.

Table 2. Computer Startup Procedure

1. Turn power on
2. Disk drive 0 to run, wait until "RDY-ONCYL" lights illuminated - "WT PROT" light off
3. Switch register to all zeros, press "Ext Addr LD" switch, verify "EMA" lights off
4. Switch register 30 octal, "7,8" up - press "Addr Load" switch
5. Switch register 6743 octal - "0,1,3,4,5,6,10,11" up - raise "Dep" switch
6. Switch register 5031 octal - "0,2,7,8,11" up - raise "Dep" switch
7. Repeat Step 4
8. Press "Clear" switch
9. Press "Cont" switch
10. Monitor dot should appear on Tektronix 4010
11. Type in date in form XX-YYY-ZZ (XX = day, YYY = month, ZZ = year and acceptable years are 70-79)

Table 3. Tektronix CRT Commands

Running MOTHER:

DA XX-YYY-ZZ (CR) - Set date, day (XX), month (YY), and year (ZZ). The acceptable entries for year are 70-79.

DA (CR) - Ask for the current date

R MOTHER (CR) - Run MOTHER

Data File Manipulation:

Dir Tel: <RKA1:/F=5 (CR) List contents of RKA1 disk to printer

Copy RKA3:<RKA1:XXXXXX.YY, etc. (CR). Copy file (up to 5) from Disk 1 to Disk 3

R CVRTBA (CR) - Converts the binary DB files to ASCII DA files. Enter file name including DB with no dot or carriage return. The files must be on Disk 1 (RKA1). This program will have to be run for each DB file to be converted.

Copy TEL:<RKA1:*.DB (CR) - Copy comments of all DB files to terminal. Use only on DB files.

Delete RKA1:*.DA (CR) - Delete files from a disk. Individual file names may be entered or * for all. Verification will be asked for each file. May be used on both DA and DB file types.

R TVDATA (CR) - To inspect an individual file (screen will prompt for name)

Tape Operations:

To load tape:

Plug in power cord to tape drive
Mount tape
Hit load

Copy MTA0:</Z (CR) Zeros directory of tape

Copy MTA0:<RKA1:*.DA (CR) Copies files to tape. Only DA files are desired on tape.

Copy MTA0:*.DA (CR) Lists contents of tape (* may be used for DA)

Type MTA0:XXXXXX.DA (CR) List file from tape on terminal, including comments.

Table 4. Instructions for Data Acquisition in COCHISE MOTHER

Data acquisition is performed utilizing Channel 0, GAIN = 0 (i.e., 10 V.F.S); Channel 0 is sampled at a 120 Hz rate and averaged over NP samples. NP is set at 120 initially, so this leads to a data rate of 1 Hz, where each of these stored data points is an average of NP(120) samples. For example, if the user sets NP = 60, then the data rate is 2 Hz where each of those stored data points is an average over 60 samples. Thus the "stored data" rate is (120/NP) Hz, and each of the stored data points is the average of NP samples.

Teletype commands:

DF (CR)	Which names and opens a file for data storage. MOTHER's response to the "DF" command is: $$$$$$ JJJY## where JJJ is the Julian day of the year, Y indicates the year 197Y, and ## is the serial number of the data file for that date. Calendar information is obtained from the system date. The actual name of the data file will be JJJY##.DA.
$COMMENTS	Input comments which will be written into the data file. Each line of comments must be preceded by the $ sign.
NP XXXX (CR)	Inputs new value of NP; 23<NP<4095
DS (CR)	Instructs MOTHER to being data sampling
DE (CR)	Instructs MOTHER to stop data sampling, write the stored data into the file opened by the last DF command and close the file.
TM nn XXX.X (CR)	Sets A/D station nn to desired temperature
TI mmmm (CR)	Sets clock (24 hr) to correct local time
.(text)	Enters comments on teletype output only - no storage by computer
Control/C	Stops running MOTHER, goes back to monitor

3. TYPICAL OPERATION AND MAINTENANCE

The purpose of this section is to provide detailed instructions and checklists such that someone familiarized with COCHISE will be able to operate the system and acquire data. This section is not intended as a cookbook for a novice; COCHISE is far too complicated to be operated independently without prior experience and the potential danger of damage to the apparatus resulting from inexperience or an error in judgement is substantial. Nevertheless this section will be sufficiently detailed such that it will serve as a valuable learning tool for the novice and a useful guide for the experienced operator.

This chapter is broken up into several subsections including: 1) sealing the tank, 2) pumpdown and cooldown, 3) blackbody calibrations, 4) taking discharge data, 5) overnight and warm-up procedures, and 6) routine maintenance.

3.1 Sealing the Tank

Closing and sealing the tank is itself a rather simple task but there are several procedures to be performed prior to sealing the tank which are necessary to ensure smooth operation. These include replacing the monochromator, verification of detector isolation, and checking all sensors.

The procedures for spectrometer installation are shown in Checklist 1. There are several critical elements which need to be emphasized. Ensure the spectrometer is in zeroth order before putting it back into the chamber. This produces the greatest accuracy in the wavelengths. Locating zeroth order once the chamber is cryogenic results in inferior wavelength accuracy, possibly due to non-uniform changes in the sine bar. Make sure all cables, heat sink straps, and drives have been reattached. Use cable ties at the connection points to make sure cables hold together. Next, make sure the detector is electronically isolated from the rest of the chamber. This may best be checked by checking the resistance between the detector power supply housing (located on top of the chamber) and the chamber itself or the copper bar. Infinite resistance should result in both cases. If not, it is possible that

Checklist 1

Spectrometer Installation Checklist

1. Heater cable and temperature sensor cable from interior attached to their terminal block.

2. Line up both entrance and exit slits at their 3 mm positions (widest).

3. Shine flashlight into one slit and verify that with fiducial marks lined up on the grating drive shaft zero order image emerges center 0 in the other slit.

4. Insert spectrometer into shroud, centered on tracks and butted against backstops on tracks.

5. Verify that external controls are set to:

   a. Entrance slit 3.0
   b. Exit slit 3.0
   c. Grating drive 00000

6. Connect chopper drive thermal block.

7. Attach connecting shafts to slit and grating drive shafts, verifying that no relative motion has occurred before tightening split collars.

8. Attach connecting leads to internal and external temperature sensor blocks.

9. Connect two-pin spectrometer base heater connector to mate on case wiring, connect four-pin connector to mate from bulkhead.

10. Verify that nylon in sapphire spacers remain in detector mounting pads and attach detector to case with nylon studs. Tighten no more than 1/8 turn.

11. Attach detector cover can and apply mylar foil.

12. Insert molecular sieve tray and clamp to frame.

13. Install three hold-down bolts; tighten 1/2 turn.

14. Before closing door, check that grating drive functions, chopper operates, slits may be moved, detector passes warm test, temperature sensors give correct room temperature response.

15. Make sure microdot detector leads are screwed on tigh[illegible], or microphonics will result.

NOTE: When removing unit from shroud, return external grating drive counter to 00000 before disconnecting drive shaft.

some of the sapphire spacers were not replaced and the detector is effectively grounded. This situation must be corrected prior to sealing the tank.

The last item of importance is the verifiction of sensor operation. Turn on the computer, run MOTHER and display all of the sensors. All should read room temperature. The LHe sensor can be checked at the marked port on the COCHISE panel or directly in the chamber (it is mounted on the Cu bar). This sensor should read only a few ohms at room temperature. If a sensor is not operational, check the resistance through the ports on the top of the chamber. Frequently, loose port connections are responsible for anomalous sensor readings. If the port test fails, isolate and test the sensor directly and replace if necessary.

If all is operational, the chamber may be closed up. Check indium seals and replace entirely or only broken sections (the indium seals fit in grooves on the inner chamber). RTV may be used to hold the indium firm while bolting the caps in place. Bolt on the insulated covers and close the outer door. Close the door clamps to hold the outer door firmly shut. The chamber is now ready for pumpdown.

3.2 Pumpdown and Cooldown

This subsection provides detailed checklists for the pumpdown and cooldown cycles of COCHISE. Checklist 2 covers pumpdown, Checklist 3 covers the cleaning of the refrigerant lines (a necessary precursor to cooldown). Checklist 4 lists the procedures for cooldown. Checklist 5 illustrates the technique for cooling the spectrometer by backfilling with helium, and Checklist 6 shows how to fill the detector with liquid helium. The cleaning of the refrigerant lines may be performed at any time prior to cooldown and must be performed prior to every run to remove condensible contaminants (e.g., water, oil, etc.).

Checklist 2

Pumpdown Procedures

1. Make sure right angle, bypass, and foreline valves are closed on COCHISE central panel (see Figure 26).

2. Turn on roughing pump until P = 50μ on foreline gauge.

3. Open bypass to rough-pump the chamber, make sure the spectrometer, bulkhead, and reaction chamber valves are open.

4. Ordinarily the diffusion pump has been left under vacuum. If not, this must be roughed out as well:

   a. Open foreline valve (output of diffusion pump)
   b. Continue pumping diffusion pump and chamber until P $\sim 1 \times 10^{-3}$ Torr

5. Turn on diffusion pump heaters and cooling water pump. The pump will take ~1 hr to warm up before it begins to pump. Sensors will shut down the diffusion pump if it gets too hot. Open right angle valve; bypass closes automatically.

6. Continue pumping for 2 to 3 days.

7. When P $\sim 1 \times 10^{-5}$, the system is ready to be cooled.

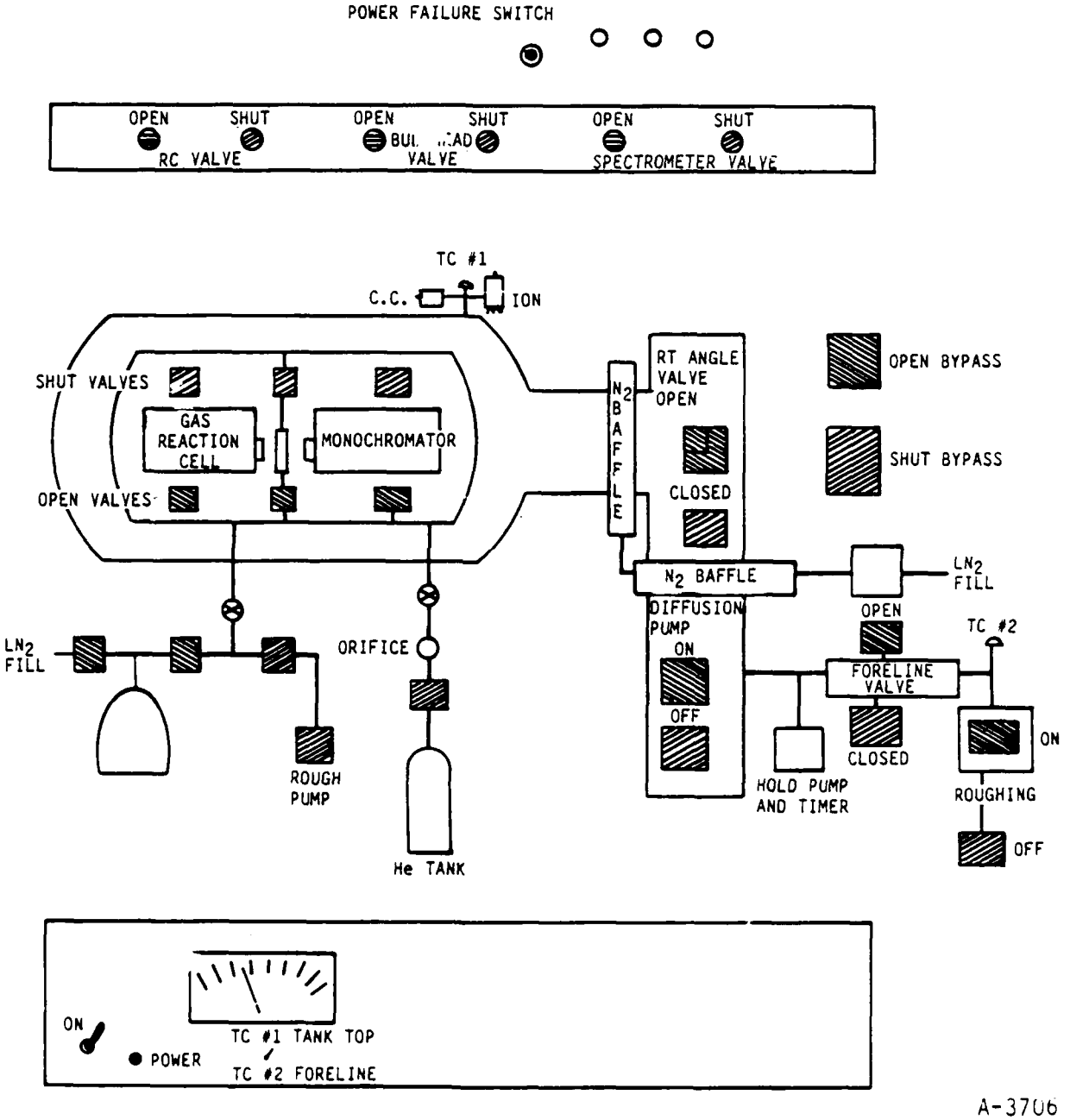

Figure 26. COCHISE Operating Panel; //// = red, ≡ = blue, \\\\ = green

Checklist 3

Cleaning the Refrigerant Lines

1. Make sure chilled water is running to the compressors (water lines located above each compressor).
2. With the 20 liter Dewar:
   a. Using a small pump, pumpdown the 20ℓ Dewar for at least 1/2 hour to remove H_2O
   b. Verify with a TC gauge
   c. Backfill with helium up to 5 to 10 psi to prevent an air leak into the compressor lines when attaching hoses.
3. On the refrigerator:
   a. Put lock-in bar through flywheel to prevent turning
   b. Put in jacking rods (two on each side, four total) to make sure valves stay open
4. Pump out heat exchanger with internal pump to 10-20μ.
5. Close chamber and supply valves so COCHISE is isolated.
6. Open chamber bypass valve.
7. Turn on one of the compressors and allow circulation for several minutes.
8. Fill 20-liter Dewar with LN_2
   a. Typically 20 liters will last only 1 hr
   b. Keep a filled 160-liter LN_2 Dewar nearby
9. Attach Dewar to refrigerator inlet and outlet (near floor) while the system is running.
10. Close valve between refrigerator inlet and outlet (near floor)
11. Run each compressor for ~2 hr.
12. When one is done, turn off and turn on another.
13. With the last compressor done, it is time to clean the COCHISE chamber lines.
14. Open return gas valves (on side near floor)
15. Open chamber supply, close chamber bypass. Run for ~2 hr.
16. After 2 hr, isolate the chamber again by opening the chamber bypass and closing the supply and return gas bypass.
17. We are now back to the original scheme. Open cryosorb valve.
18. Disconnect 20-liter Dewar lines and replace caps. Must be done quickly to minimize He loss. Use spray lubricant if necessary.
19. Shut off compressors, remove all jacks and the locking bar.
20. With experience, this procedure takes 1 full day.

Checklist 4

Cooldown Procedures

1. Turn on computer and run program MOTHER

2. On large He storage tank:

   a. Ensure pressure: 25 to 35 psi

   b. Otherwise fill with He from a cylinder through manifold to the left of the frige.

2a. Start He purge of detector LHe reservoir.

3. Cool down refrigerator first (~1 hr):

   a. Open chamber bypass, turn on LN_2 (line pressure should be ~40 psi)

   b. Remove LN_2 sensor apparatus in refrigerator and replace with bypass tube (ensures maximum LN_2 flow). Leave bypass tube in until the entire system, including the chamber, is out of bypass mode.

   c. Turn on two compressors on low speed (#1, #2, or #3)

   d. Open V806 valve nine turns (full open) and close red-handled valve (see Figure 21). This ensures maximum LN_2 cooling.

4. When refrigerator return temperature ~25 K, put system on chamber bypass (begin cooling chamber, ~1 day). See also section 2.4 for refrigerator operation.

   a. Open return gas bypass
   b. Open chamber supply
   c. Close chamber bypass
   d. Turn on bypass heaters (preset to 50°F)
   e. Open red-handled valve in refrigerator (see Figure 21)
   f. V806 remains a few turns open

5. When the shroud temperature gets to 150 K (exit bypass mode)

   a. Shut heater off and wait 1 min to verify pipes are cool to the touch

   b. Shut off return gas bypass

6. LN_2 sensor apparatus inside the refrigerator may be replaced

7. May begin to cool spectrometer by backfilling with He when shroud is <50 K (see Checklist 5)

8. When all temperatures are <30 K, the detector may be filled with LHe.

9. This procedure should take no more than 4 days and the final chamber pressure should be 1×10^{-7} Torr. Two typical cooldown cycles showing the refrigerator, shroud, and spectrometer temperatures are shown in Figure 27.

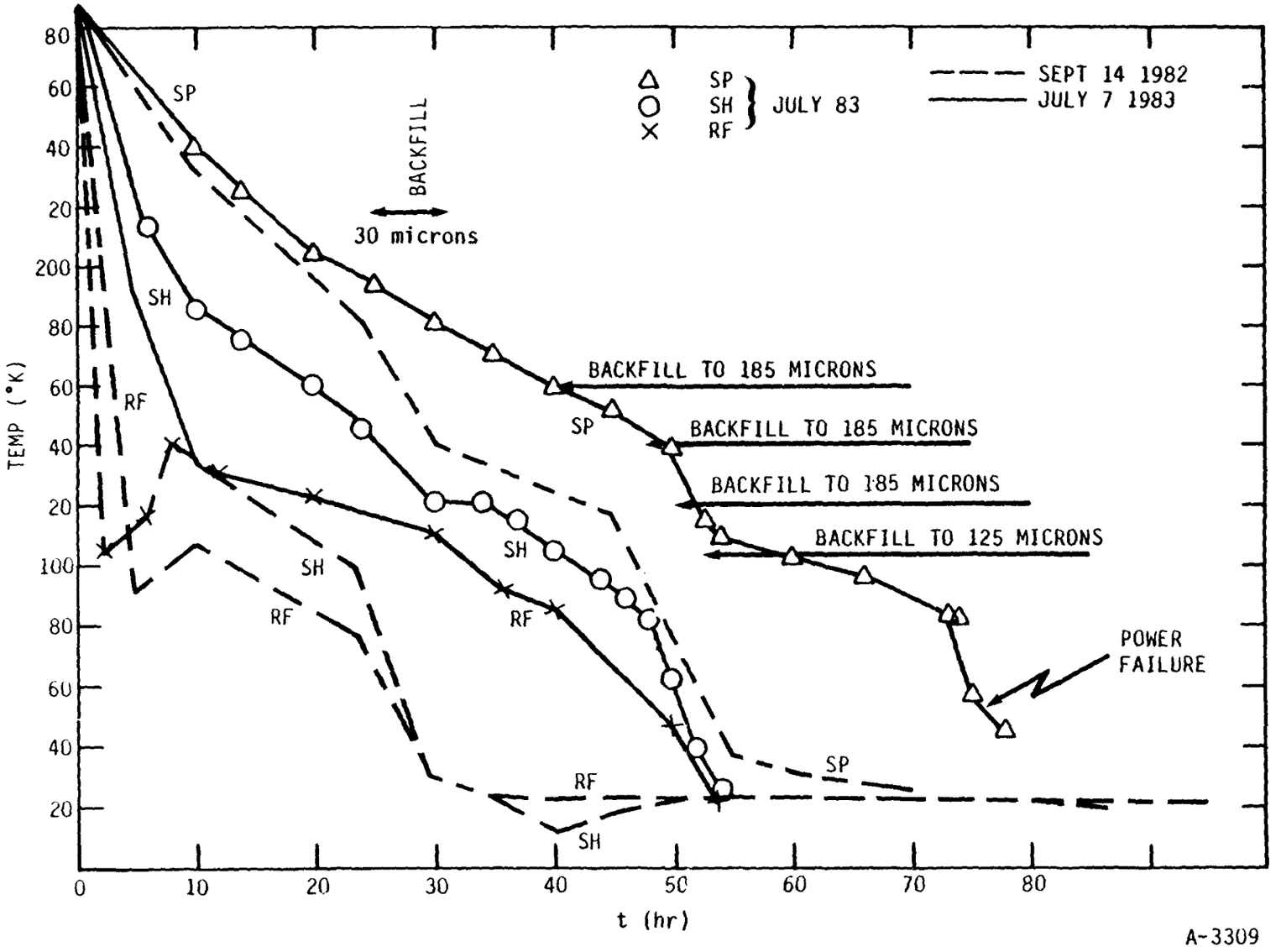

Figure 27. Cooldown Cycle

Checklist 5

Flushing Spectrometer with Helium

1. Close monochromator and bulkhead valves (on central panel)
2. Open He tank valve (on central panel)
3. Flush He line
4. Set baratron to read spectrometer pressure
5. Turn on three-way valve
6. Close monochromator and bulkhead valves
7. Adjust fill valve until pressure = 50 to 60 microns
8. Close He tank valve after each fill
9. Repeat until desired temperature is achieved (<30 K)
10. Re-open monochromator and bulkhead valves when done

Checklist 6

Cooling the Detector with Liquid Helium

1. Place the withdrawal tube in the LHe supply Dewar.

2. Open detector reservoir off gas valve to vent pressure and withdraw gauge assembly from detector LHe reservoir.

3. Attach the metal flexible hose to withdrawal tube and cool.

4. Insert flexible hose end into detector reservoir and tighten O-ring seal. Keep off gas valve open.

5. Attach a He line (<5 psi) to pressurize Dewar and fill reservoir (maintain at 1 to 1-1/2 psig).

5a. Pre-cool the transfer line by flowing LHe before inserting into the reservoir neck.

6. Insert transfer line into reservoir, fill and withdraw when done.

7. Insert LHe reservoir depth detector into reservoir and determine volume from gauge output and calibration shown in Figure 28.

8. Remove LHe depth detector apparatus.

9. Reinstall gauge assembly and close off gas valve.

10. Ensure positive He pressure on reservoir from cylinder to prevent condensation.

11. This procedure will take an hour for the first fill and 30-45 minutes for successive transfers.

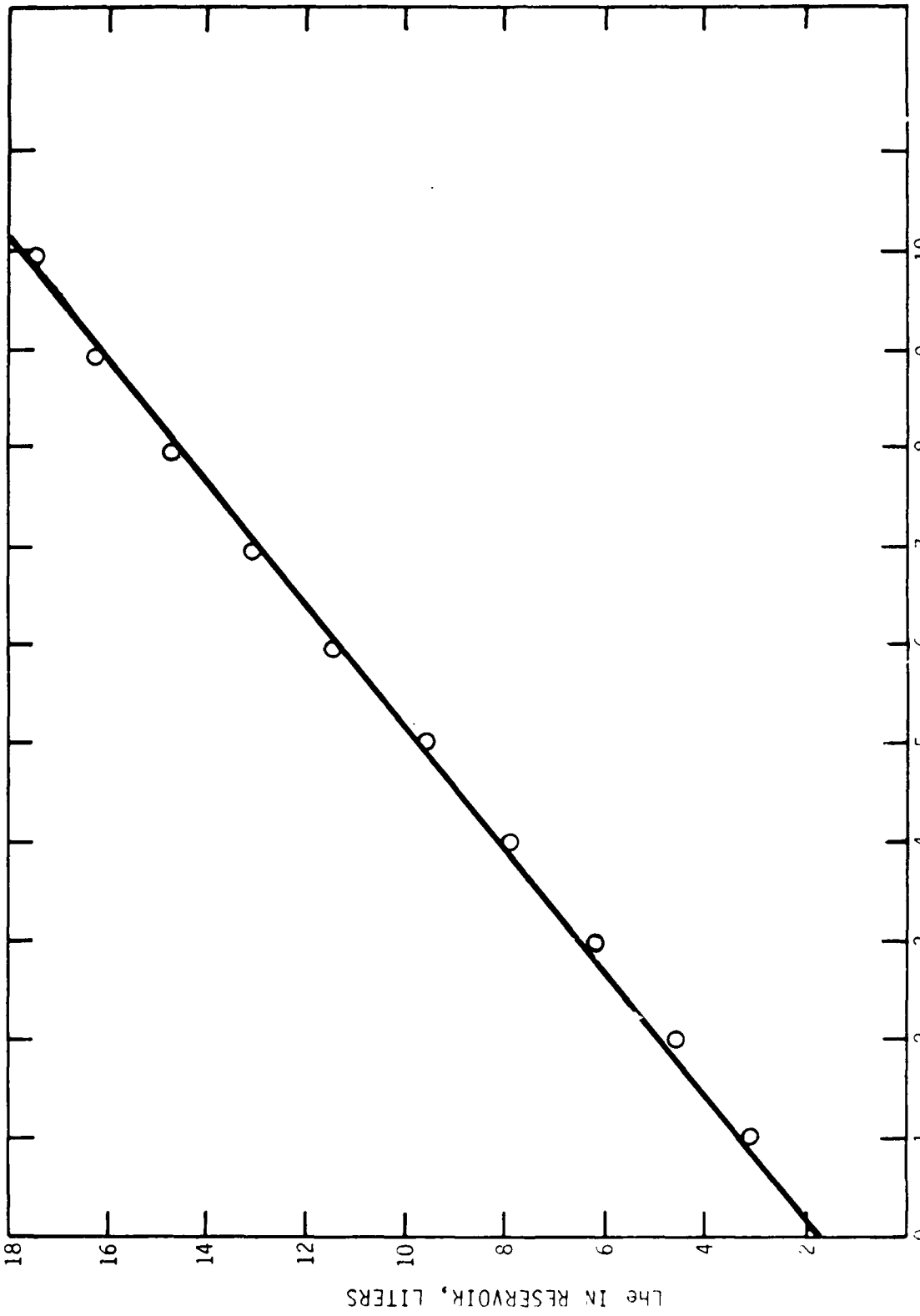

A-3312

Figure 28. LHe Meter Calibration

3.3 Blackbody Calibrations

Before gas is introduced into the chamber, the spectral responsivity of the spectrometer must be determined. This must be done after every cooldown cycle prior to operating the discharges regardless of whether or not the spectrometer had been moved. The movement of COCHISE components during cooldown (absolute magnitude is unknown) requires recalibration of the spectral responsivity for every run. The calibration is achieved by taking spectra of a blackbody at a known temperature for each filter to be used (i.e., SWIR, MWIR, etc.). The blackbody used for this purpose is one of the 330Ω resistive heaters mounted through the center of the mirror with its flat front surface painted black for maximum emissivity.

Taking blackbody spectra is relatively routine; the chore is to take enough such that an accurate spectral calibration results. In this regard, the SWIR 2 to 2.5 μm region poses the only serious difficulty. Even at the highest operable blackbody temperature (370 K, operation above 370 K has been observed to char the epoxy), the intensity drops off rapidly in this wavelength region. The current technique to obtain a SWIR blackbody spectrum is to increase the temperature to ~350 K and obtain several spectra at one of the lower sensitivi' scales (200 or 500 mV). A few spectra are then taken at higher sensitivity (50 mV) and these sections are merged with the reduced sensitivity spectra after implementation of the calibration program. The generalized procedure to take calibration spectra is shown in Checklist 7. Sample MWIR and SWIR blackbody spectra are shown in Figures 29 through 31. Figure 31 shows a spectrum of the 2 to 3 μm section of the SWIR. Figures 32 and 33 show the resulting responsivity curves. Over the years, these curves have not deviated by greater than a factor of four.

Checklist 7

Taking Blackbody Spectra

1. Heat the optics to ~40 K and the blackbody to 300 to 370 K.

   The blackbody may require 3/4 hr to stabilize
   The computer command to set the temperature is shown in Table 4

2. Select the filter (see Checklist 8)

3. Turn on detector

   a. Press power on
   b. Wait till temperature is ~220 K
   c. Turn on bias
   d. Verify bias > 25V otherwise replace batteries

4. Operate in dc mode:

   a. Turn chopper on
   b. Display output on scope
   c. If the chopper is "chattering" turn amplitude down (located on top of the chamber)
   d. Output of detector feeds into PAR channel A
   e. PAR reference to Kron-Hite output

5. Select slit width and scan rate, scale (mV) and RC filtering constant and data collection at (DP)

   a. Table 5 shows recommended scan rates, DP value, and filtering constants for various slit widths

   b. Although we operate in first order, the second order row is appropriate to interpreting Table 5.

6. Prepare to scan:

   a. Set up monochromator near λ start - typical MWIR value is 7.2 (3.6 μm), SWIR is 3.6 (1.8 μm).

   b. Set up data file; include comments, scan rate, DP value, λ start, mV full scale, time constant, and slit width.

   c. Start the monochromator and begin data collection when the monochromator reaches λ start.

7. Stop data collection when desired by entering the DE command followed by (CR).

8. Stop monochromator drive.

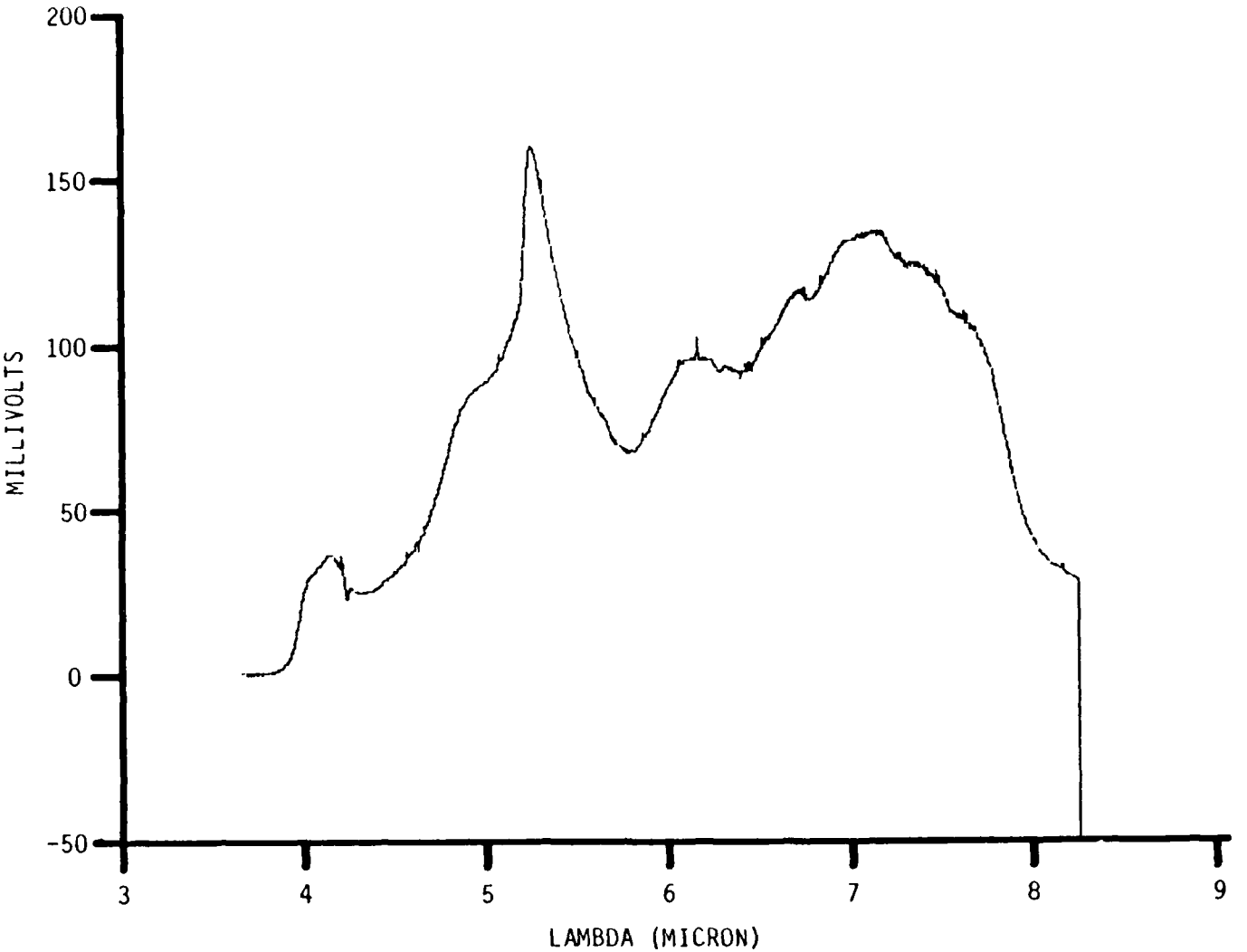

Figure 29. MWIR Blackbody Curve. Data taken at 500 mV Full-Scale, 1s time constant, 1 mm slits, a scan rate of 320/90, and the blackbody temperature was 369.5 K. Data from November 1985

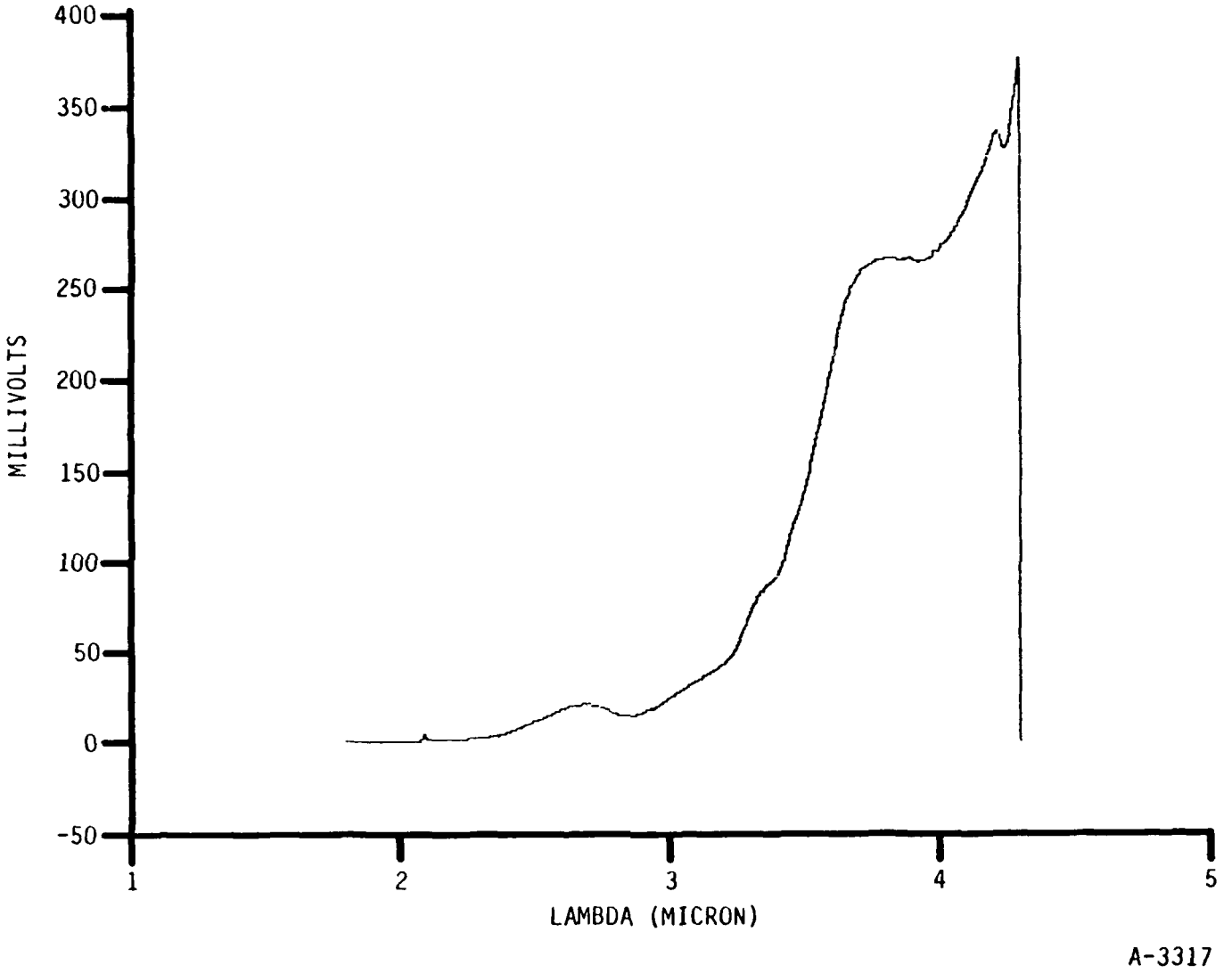

Figure 30. SWIR Blackbody Curve. Data taken at 500 mV full-scale, 3s time constant, 3 mm slits, scan rate of 320/90 and a blackbody temperaure of 369.5 K. Data from November 1985

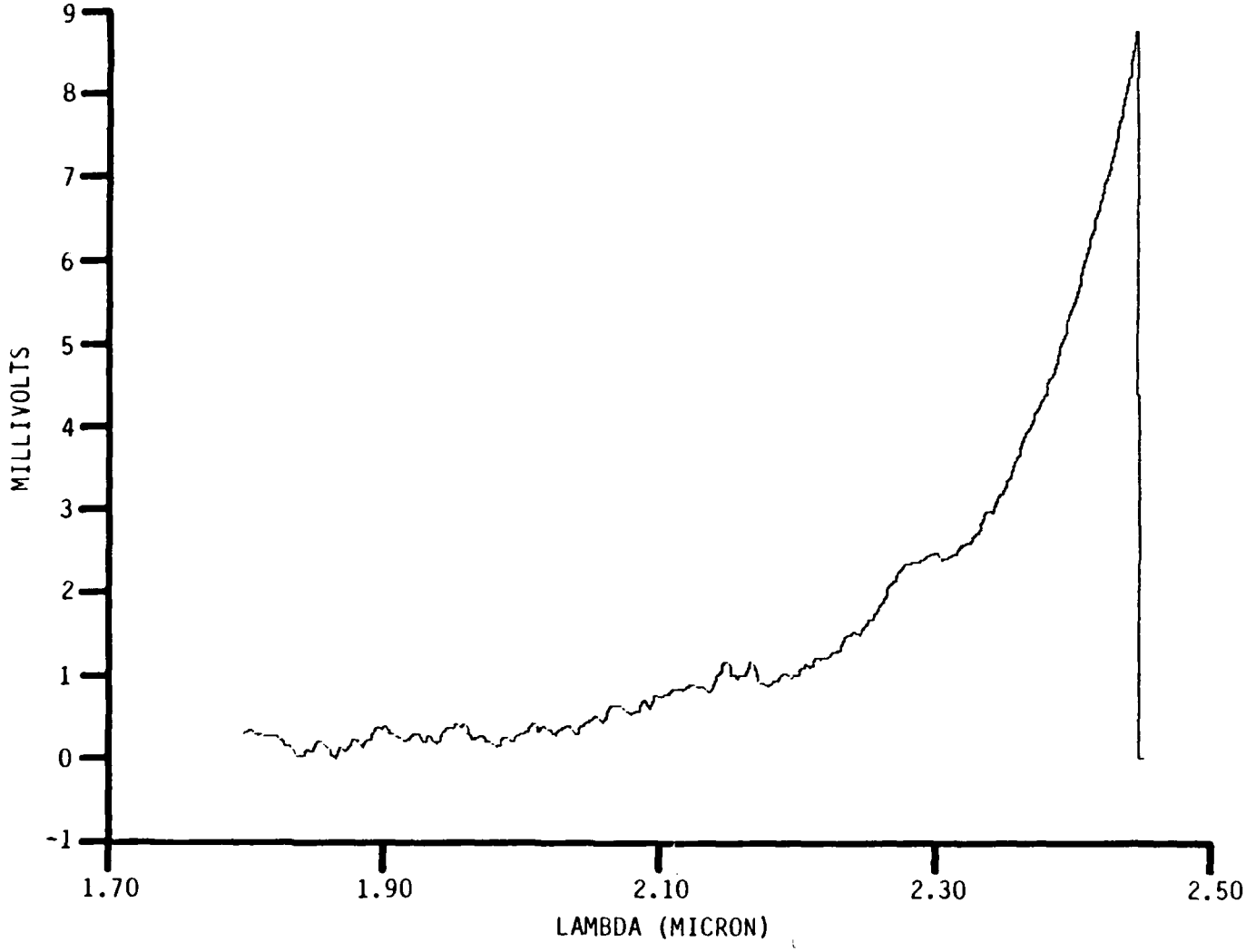

Figure 31. 2 to 3 μm Section of SWIR Blackbody. Data taken at 10 mV full-scale, 3s time constant, 3 mm slits, at a scan rate of 320/90 with the blackbody = 369.5 K. Data from November 1985

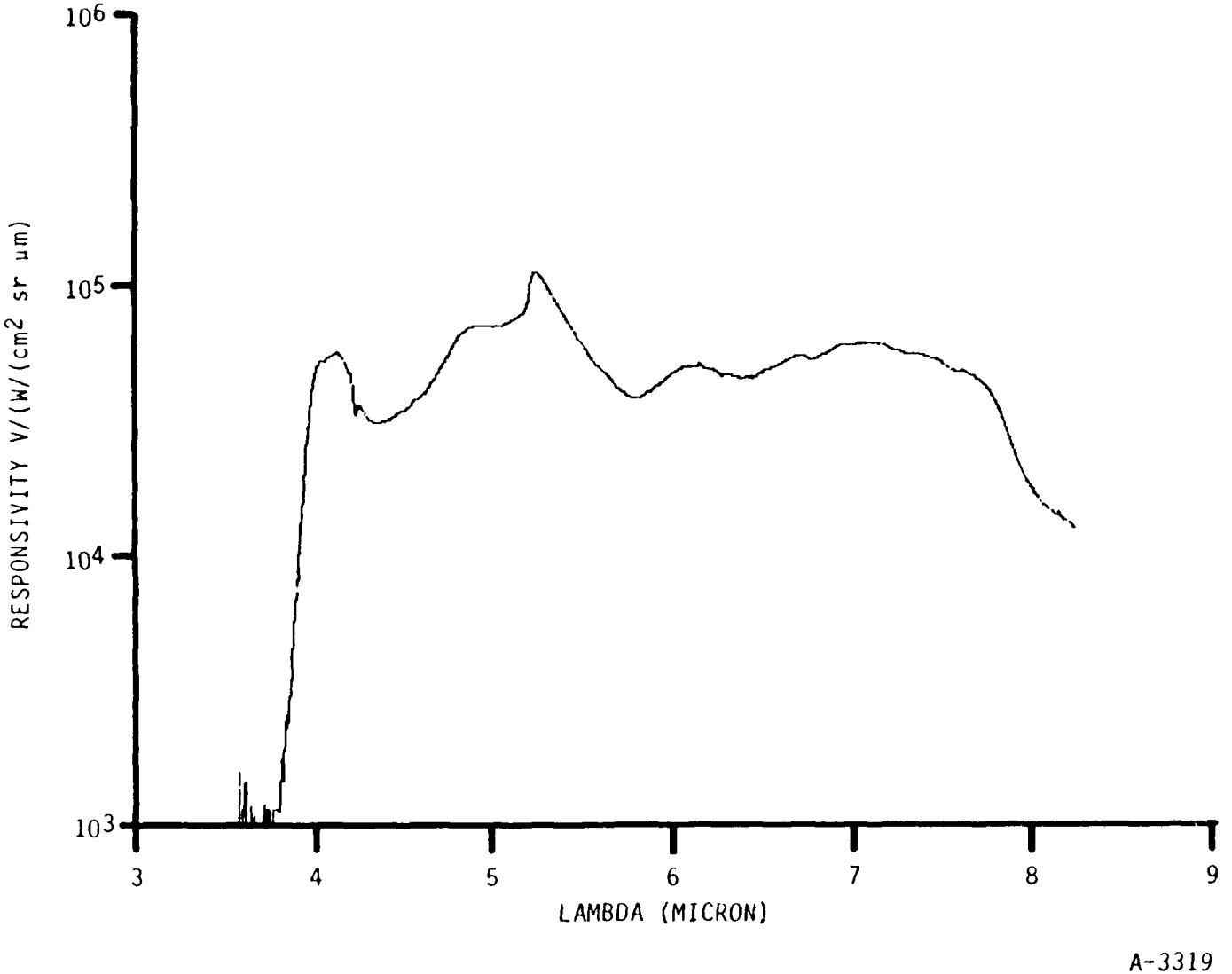

Figure 32. MWIR Responsivity Curve

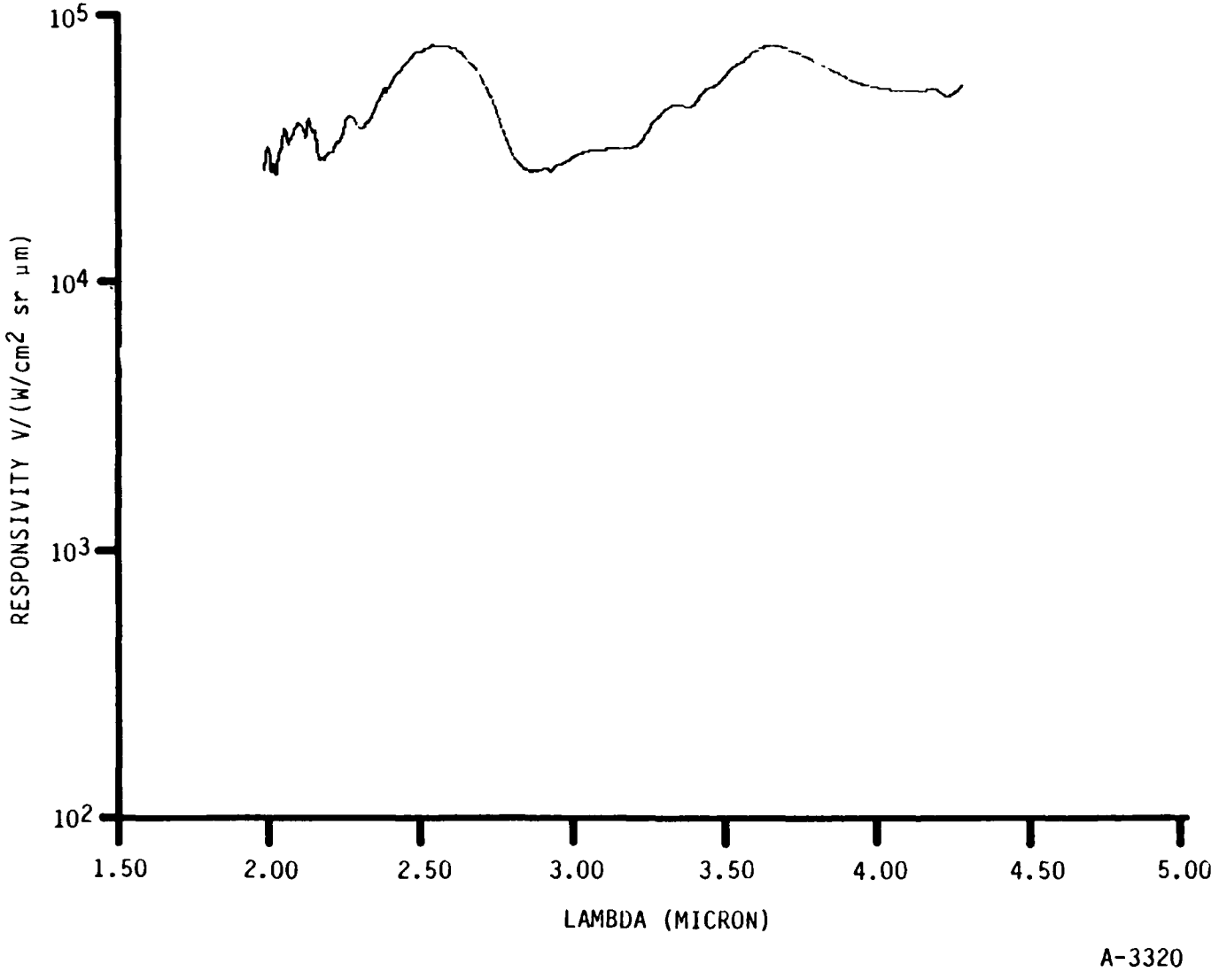

Figure 33. SWIR Responsivity Curve

Checklist 8

The Filter Wheel

1. The filter wheel contains six positions, ostensibly, 2, 4, 6, 8, 10, 12.

2. Currently only positions 2 and 4 contain the appropriate filters. The other positions are either open or blocked.

3. A DVM readout aids in determining the filter wheel position with an analogous resistance for each. However, reliable DVM readings are rarely obtained so the filter wheel position must be recorded.

4. The wheel may be rotated with the adjacent power supply. With this supply on and the voltage set to <5 volts, 10 clicks of the green panel button will move the filter wheel to the next position.

Table 5. COCHISE Data Acquisition Parameters for 0.5m Czerny-Turner Spectrometer

Slit (mm)	ORD	"RES" (μ)	Indicated Scan Rate (nm/min) 800 TR/τ	800 DP	800 DP/120	320 TR/τ	320 DP	320 DP/120	160 TR/τ	160 DP	160 DP/120	80 TR/τ	80 DP	80 DP/120	Spectrum on 4010 Screen (mic/div)
3.0	1	0.80	6/1	90	0.75	15/3	225	1.875	30/3	450	3.75	60/10	900	7.5	1.0
	2	0.40													0.5
2.0	1	0.053	4/1	72	0.60	10/1	180	1.50	20/3	360	3.00	40/3	720	6.0	0.8
	2	0.027													0.4
1.5	1	0.040	3/0.5	36	0.30	7.5/1	90	0.75	15/3	180	1.50	30/3	360	3.00	0.4
	2	0.020													0.2
1.0	1	0.027	2/0.5	36	0.30	5/1	90	0.75	10/1	180	1.50	20/3	360	3.00	0.4
	2	0.013													0.2
0.5	1	0.013	1/0.3	18	0.15	2.5/0.3	45	0.375	5/1	90	0.75	10/1	180	1.50	0.2
	2	0.007													0.1

ORD is the diffraction order in which the grating is being used for all gratings. The 3 μm grating now has twice as many lines/mm so the second order column applies when using this grating.

RES is the spectral resolution, in microns, for the given order.

TR is the scan time per resolution element, in seconds

τ is the PAR time constant (maximum)

DP is the number of samples (at 120 Hz rate) per averaged data point

$\frac{DP}{120}$ = number of seconds per data point

3.4 Taking Discharge Data

Discharge data are the essence of COCHISE research. The experiments are necessarily diverse. However, there are several routine steps which may be described here. Briefly, an experiment is performed as follows: 1) the experimental matrix is always laid out in advance, 2) once the calibrations have been completed, the gas lines are heat soaked for 1 hr at 120 K (all discharge heat sinks, both manifolds, and the pressure port plate) then set to 90 K, 3) the desired gas flows (both discharge and counterflow) are set up and a few preliminary spectra are taken scanning the experimental variables, 4) discharge data is almost always taken AC although DC operation has also been performed, 5) the experimental variables (e.g., percent discharge N_2, percent counterflow of added gas) are examined in detail under varying resolution conditions, 6) with time permitting interesting phenomena from the current or previous runs are also examined, and 7) when the mass loading on the chamber becomes too great ($P > 2 \times 10^{-6}$), it is time for warmup.

The routine aspects of taking discharge data which may be useful to the novice include: 1) setting up the gas flows, 2) operating the discharges, 3) some sample spectra from previous COCHISE experiments, and 4) AC versus DC operation. Each of these will now be discussed.

The gas flows, both discharge and counterflow, are typically set up such that each mass flow rate is 0.11 g/s. The flow calibrations in Figures 5 through 14 will aid in setting the flows of each component. The initial flows are generally set up with the reaction cell valves off and the pump-out valves open. This minimizes gas loading to the chamber. With the flows established and flowing into the reaction chamber, it is time to turn on the discharges.

The power supplies for all four microwave discharges are located in a movable panel. Once the warming cycle has been completed, the power may be turned on and the discharges initiated with a Tesla coil discharge to an exposed wire located beneath the shelf on the COCHISE chamber. Each of the discharges has a forward and reflected power meter so operation may be

verified here as well as by displaying the output on a scope. After each run the discharges are turned off to reduce the heat loading to the chamber.

Each COCHISE run is remarkably different from all previous experiments. There are, however, several common discharge phenomena which are frequently encountered and examined in COCHISE. Sample spectra of these phenomena are shown as a reference guide to the experienced and novice COCHISE user. Figures 34 and 35 show the NO fundamentals and overtones in the MWIR and SWIR, respectively. These data were obtained by reacting Ar/O_2 in the counterflow with discharged Ar/N_2. The CO fundamentals in the MWIR are shown in Figure 36. This spectrum was generated by reacting a counterflow of Ar/CO with discharged Ar/N_2. A flow of Ar/N_2 through the discharges reacting with Ar counterflow will reveal the N_2^* IR transitions. Figure 37 shows the $N_2(w^1\Delta \rightarrow a^1\Pi)$ and $N_2(w^3\Delta \rightarrow B^3\Pi)$ Wu-Benesch emissions in the SWIR obtained in this manner. One last spectrum will be included here for completeness is one which is generated with discharged Ar only, producing Ar(I) emission. Figure 38 shows the Ar(I) emission observed in the SWIR.

One last point to be covered in this section is AC versus DC operation. Most discharge spectra are taken in AC mode in order to discriminate against emitters out of phase with direct discharge excitation but DC data collection has also been performed in order to maximize signal. The differences between AC and DC operation are shown in Table 6.

3.5 Overnight and Warmup Procedures

A large number of systems have to be shut off every evening so a checklist is provided here to ensure that none are forgotten. Checklist 9 shows the overnight shut-down procedures. The most critical of these are turning off all heaters, opening all chamber valves, and turning off the gas flows and the detector. If a compressor were to fail at some point in the evening (which has happened) forgetting to turn off any of the above could lead to a catastrophe. This must be kept in mind whenever the system is left unattended for any period of time.

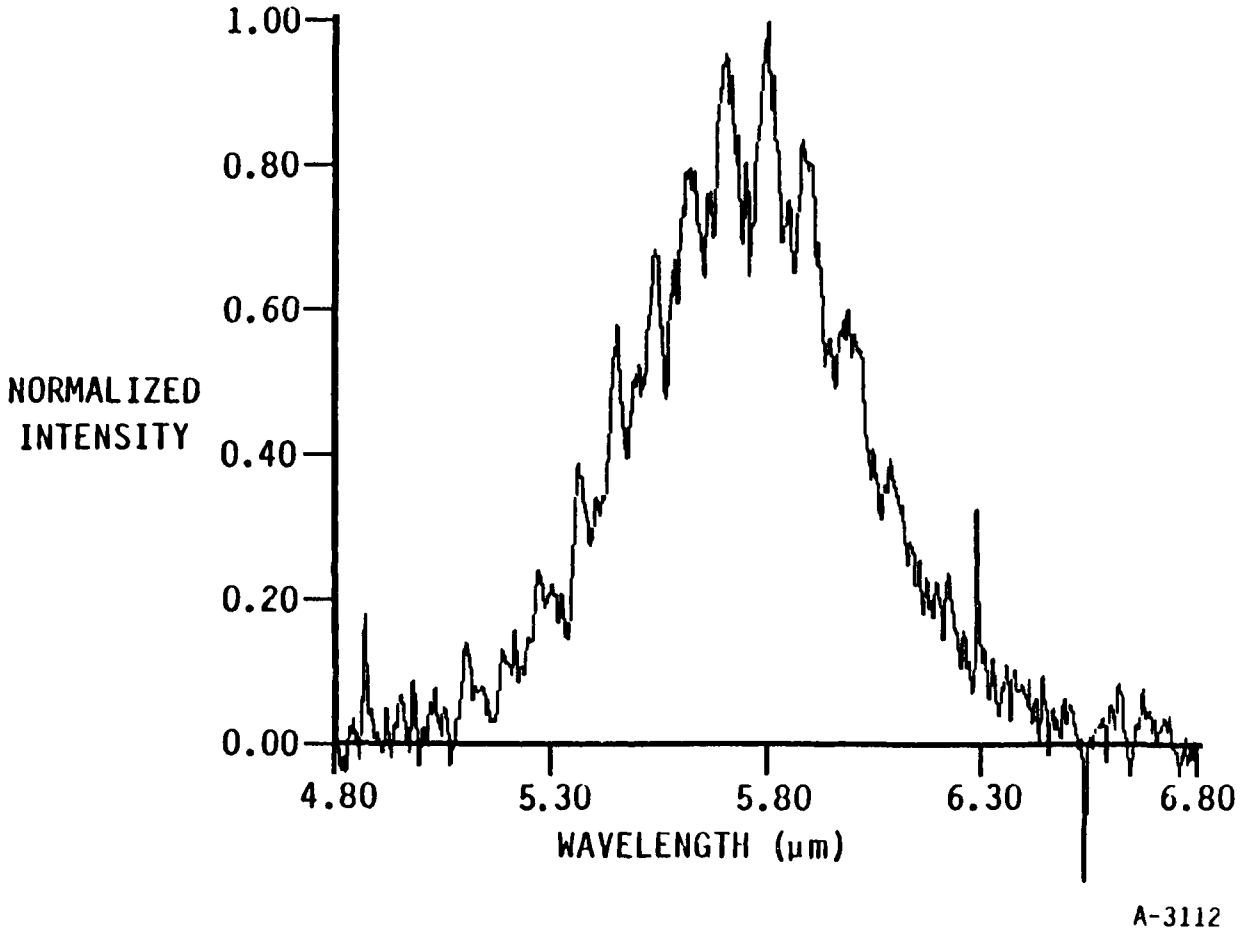

Figure 34. NO Fundamental Emission

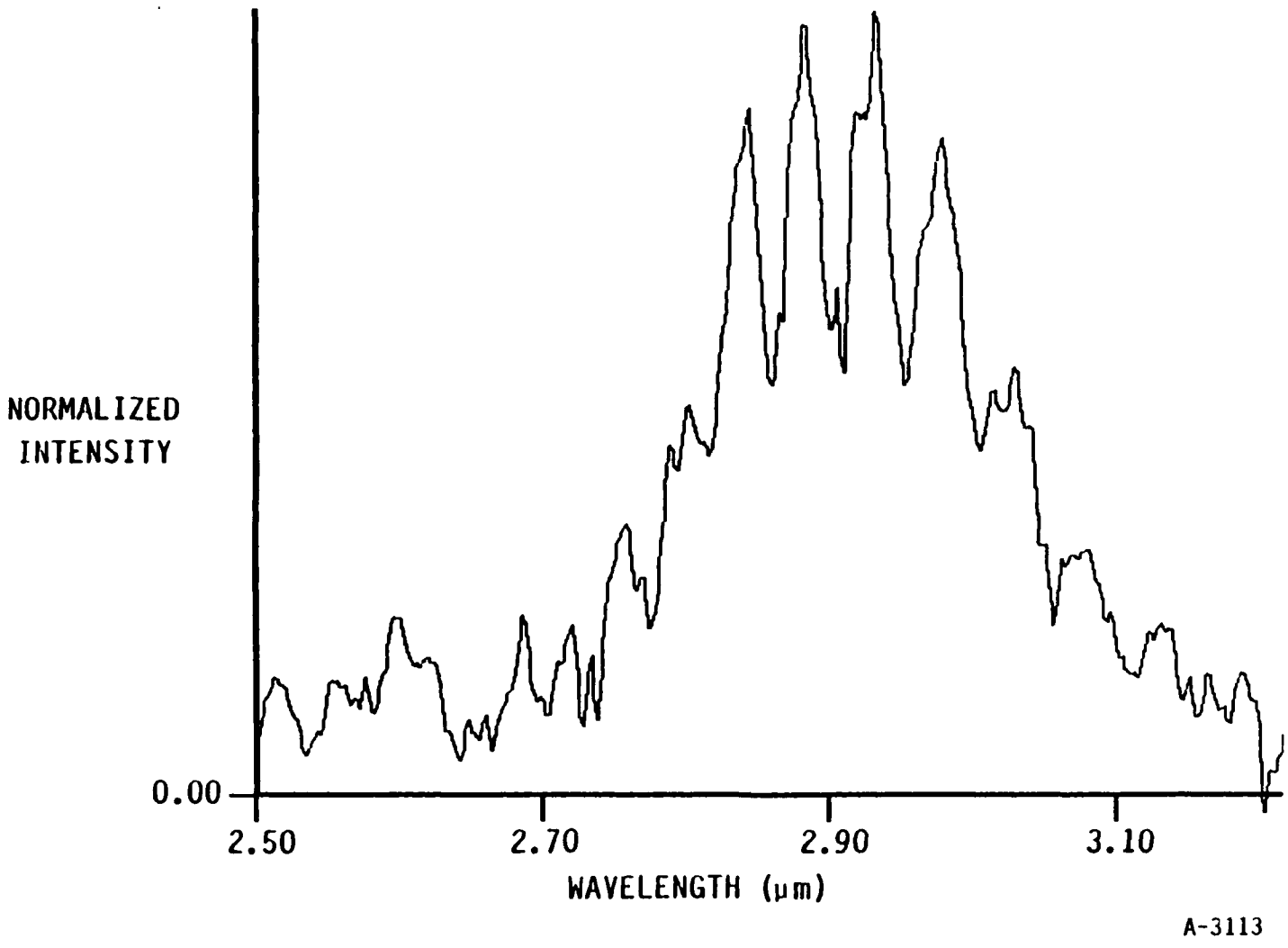

Figure 35. NO Overtone Emission

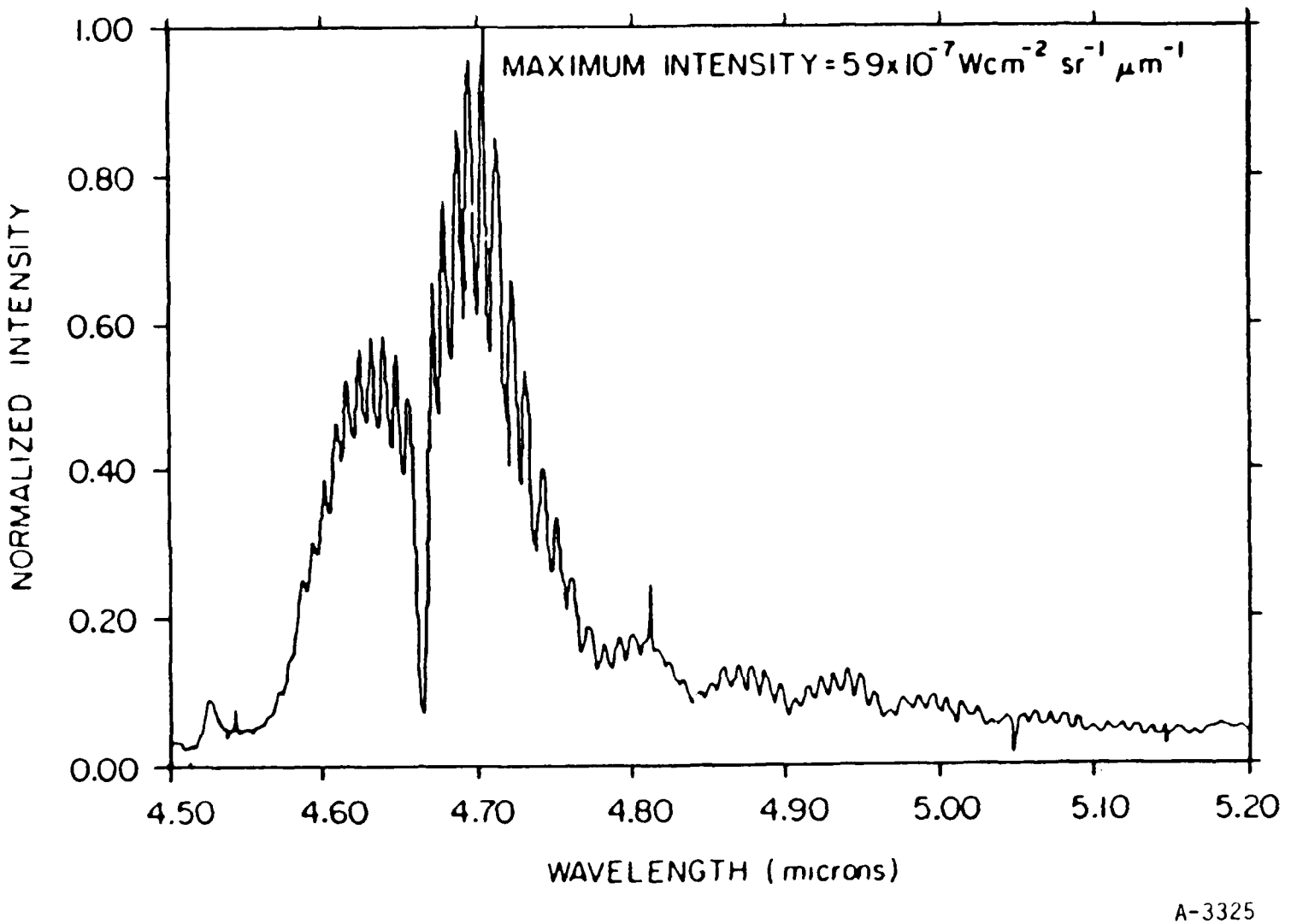

Figure 36. Partial Spectrum of CO ($\Delta v = 1$) Vibraluminescence Observed in the Interaction of Discharged N_2/Ar with Counterflowing CO/Ar at ~80 K, ~3 mTorr. The Spectral resolution is 0.0067 μm.

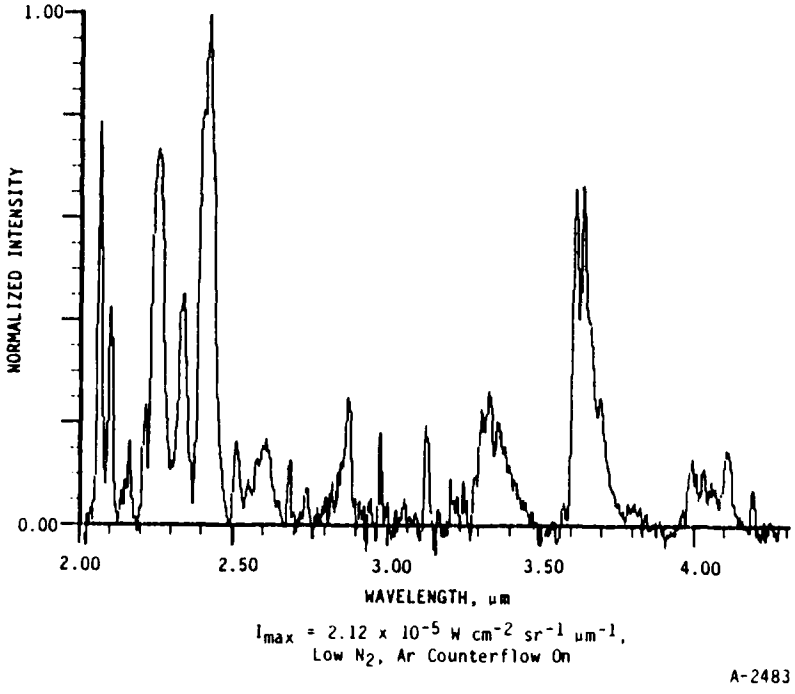

Figure 37a. Spectrum of the AC SWIR Emission Observed from Discharged Nitrogen in Argon with an Argon Counterflow. COCHISE file number 326534. Resolution = 0.013 μm. The flow conditions were 2500 μmole/s Argon, 20 μmole/s nitrogen through the discharge with a flow of 2700 μmole/s of argon in the counterflow.

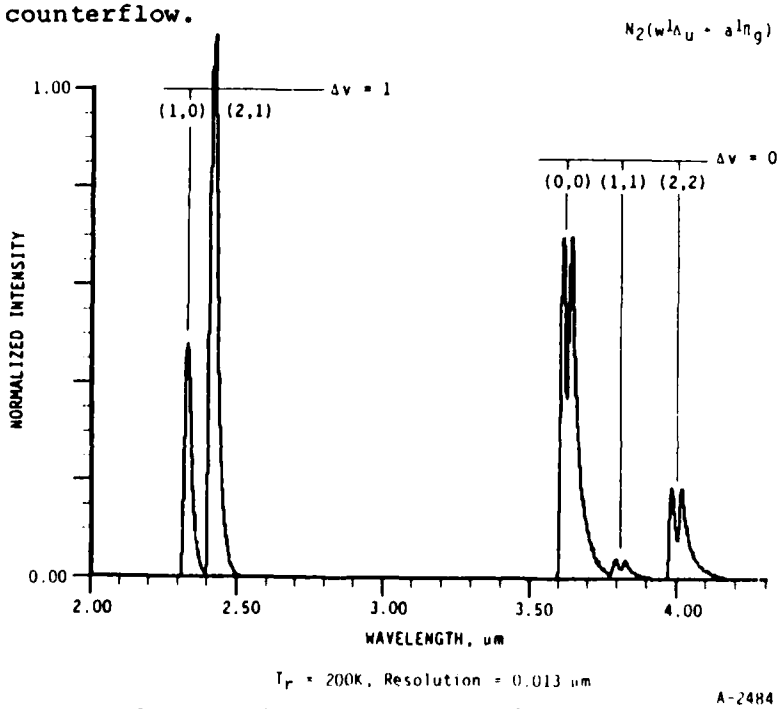

Figure 37b. Calculated Best-Fit Spectrum to the Data Shown in Figure 37a Using $N_2(w^1\Delta_u \rightarrow a^1\Pi_g)$ Emission as a Basis Set. T_r = 200 K, Resolution = 0.013 μm.

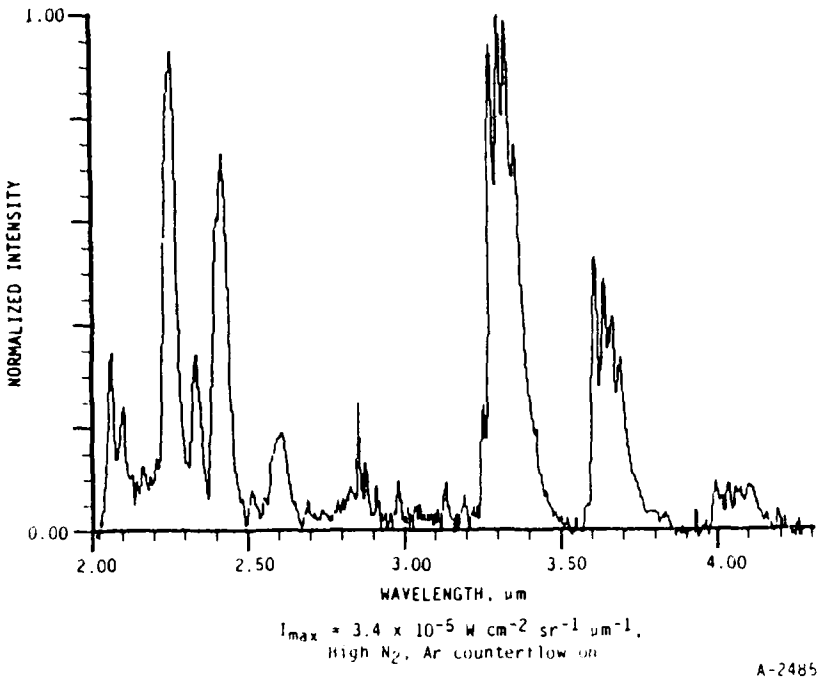

Figure 37c. SWIR Emission Spectrum Observed from Discharged Ar/N_2 with Ar Counterflow Under Conditions of High N_2 Flow. COCHISE file 326531. Resolution = 0.013 μm. The flow conditions were 2500 μmole/s Ar and 250 μmole/s N_2 through the discharge and 2700 μmole/s Ar through the counterflow.

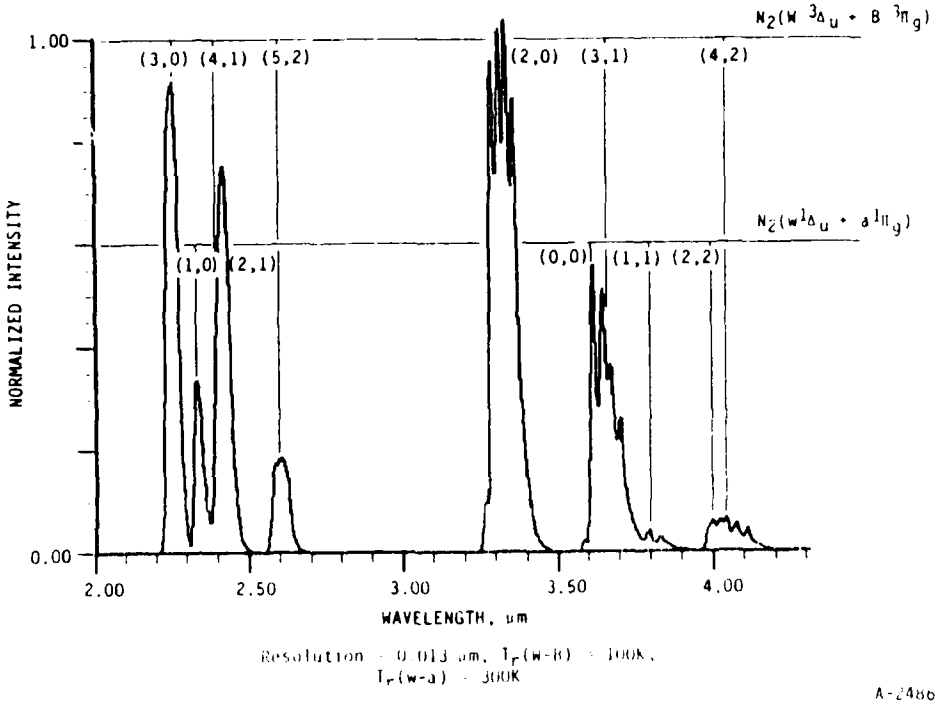

Figure 37d. Calculated Best-Fit Spectrum to the Data Shown in Figure 37c Using $N_2(W^3\Delta_u \rightarrow B^3\Pi_g)$ and $N_2(w^1\Delta_u \rightarrow a^1\Pi_g)$ Emission as Basis Sets. $T_r(W \rightarrow B)$ = 100 K, $T_r(w \rightarrow a)$ = 300 K, resolution = 0.013 μm.

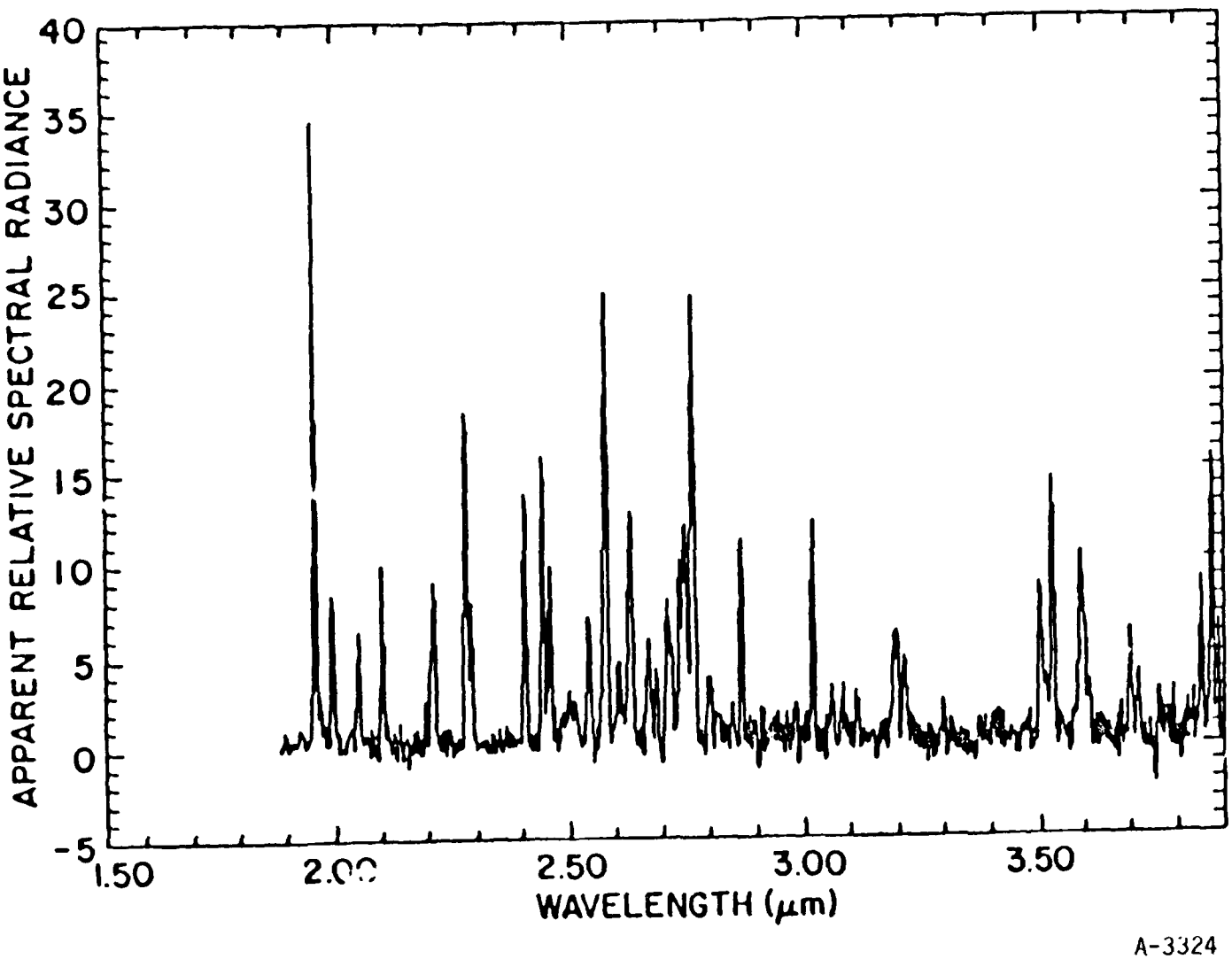

Figure 38. High Resolution Spectrum of Ar Emission from 2 to 4 μm, 0.007 μm Resolution, 0.1 Torr. The spectrum was taken using a 2 μm long-pass interference filter and a grating blazed at 3 μm, operating in first order.

Table 6. AC Versus DC Data Collection

Parameter	AC	DC
Detector output	Channel A PAR	Channel A PAR
PAR reference	Discharge output through light-link board	Krohn-Hite output
Discharge control	Square wave	External drive
Scope 1 (2-channel scope)	Signal output	Chopper output, signal output
Scope 2 (4-channel scope)	Discharge output	Discharge output
Chopper	Off	On

Checklist 9

Overnight Shutdown Procedures

1. Gas flows, solenoid valves, discharges, scan, chart drives off.

2. Disk up, computer locked.

3. Bias, detector off.

4. Console off: PAR
   Chopper/preamp
   Recorder
   RC heat
   Grating drive
   Tektronix two-channel scope
   4-channel scope
   Flowmeters and control board
   Heater control board

5. RC, bulkhead valves, open, SP valve always open, panel locked.

6. Check status of 160 liter Dewar (relevant only if LN_2 cooling of gas line is used)

7. LN_2 to 77 K plate off, exit open (relevant only if LN_2 cooling of gas line is used).

8. Microwave units off.

9. Gas cylinders off, toggle valves closed.

10. Side shelf: Unplug spectrometer heater
    Filter ohm meter voltage source off
    LHe level meter off

11. Refrigerator to overnight condition: two compressors, low speed
    LN_2 valve three turns open

12. Message on teletype (.Goodnight).

With the experiment completed, it is time to warmup the chamber. Great care must be exercised in implementing this procedure as severe explosions causing extensive chamber damage have occurred during warmup in the past. During warmup the critical procedures are turning off all heaters (except the spectrometer heater which must be on) leaving all chamber valves open, and turning off the diffusion pump. Checklists 10 and 11 show the warmup procedure in great detail.

3.6 Routine Maintenance

A section such as this can by no means be complete as further experience will continually add more items to this list. What follows is a compilation of issues, which from current experience, are deemed important to the long-term smooth operation of COCHISE.

1. Grease all refrigerator fittings (with a lithium grease) at least once a year. Do not overgrease.

2. Replace refrigerator activated charcoal traps after 3000 hr of operation.

3. Always keep a positive helium pressure on the detector reservoir. This will keep moisture out.

4. Check bias (detector) batteries before each run (should be >25 volt). Change after every second run.

5. Check and replace spent gas tanks. Order more if needed.

6. Ordering liquid refrigerants:

   LN_2 requires a 2-day lead, deliveries are needed twice a week

   LHe requires a 4 to 5-day lead, one 500 liter Dewer is needed for a complete run.

Checklist 10

Warmup Procedures

1. Go through overnight shutdown.

2. Put Baratron on 1000 Torr head (switch DC output cable in back to 1000 Torr head.

3. Attach Baratron leads to chart recorder:

   Disconnect D/A converter leads
   Use both pens
   Put on slowest speed
   Use two different scales, 100 and 10 Torr
   Set plumbing for Baratron to record Discharge #1 pressure.

4. Raise disks.

5. Leave MOTHER operating.

6. Open spectrometer slits to 3.0 mm

   Plug in spectrometer heater and set to 40 to 50 volts.

7. Monitor in MOTHER

   Shroud - warm end, RC, discharge manifold, RF, shroud - cold end
   37 36 35 33 16

   Spectrometer
   12

8. Turn off diffusion pump heaters on valve board.

9. Turn off LN_2 supply to refrigerator (valve near window).

10. Ensure spectrometer is heating.

11. Turn off the second of two compressors operating (leave compressor #1 on).

12. Turn on recovery switch.

13. Turn off last compressor.

Refrigerator

14. On side shelf, turn off vacuum space vacuum gauge.

Checklist 11

Continued Warmup Procedure

1. All temperatures > 220 K (2 to 3 days).

2. Turn off spectrometer heaters.

3. Close right angle pump valve - on board

   Close foreline valve
   Turn off roughing pump

4. Ensure that all chamber valves are open.

5. Use LN_2 offgas fill line to pressurize chamber to 1/2 atmosphere while monitoring dial gauges for excessive pressure differentials.

6. Monitor 1000 Torr pressure gauge to ensure no large pressure differentials are created.

7. When the temperatures are ~290 K, use LN_2 offgas fill line to bring chamber to 1 atmosphere.

8. Release door lock so it will crack when 1 atmosphere is reached.

9. The pressure may be read on three pressure meters located beneath the chamber door.

10. The chamber may now be opened.

11. Never open chamber below 290 K or severe condensation will result.

7. Changing diffusion pump oil:

The oil may be changed by draining through the bottom viewing port and filling through a port in the side arm after removing the small direct drive pump and its Cu tubing. Make sure the diffusion pump is cool and vented (the whole chamber will have to be vented). The pump requires 1 gal of oil (we currently use 702 silicone fluid). This should be done every 2 or 3 years. The oil does not seriously degrade but the volume does decrease. The drain port seals with a copper washer, be sure to replace this when finished.

8. Normal operation of refrigerator:

High pressure meter should read 225 psi (lower if cold)
Return temperature -10°C to -20°C
Low side pressure 5 to 8 psi

9. All mechanical pumps should have their pump oil changed every year. This includes the gas manifold pump located under the floor boards. The Leybold-Heraeus direct drive forepump (located in the back room, against the far wall) should have its oil changed after every run. To drain, remove drain plug at the base and start the pump (briefly) two or three times. Fill with direct drive pump oil in the fill port on top.

4. CONCLUSIONS AND PROPOSED CHANGES

The goal of this manual has been to provide a thorough discussion of all facets of COCHISE operation. It is by no means exhaustive but it is sufficiently detailed to be a valuable learning tool for the novice and a useful guide for the experienced operator.

Several changes are currently planned for the COCHISE apparatus. These include: installation of a new detector with greater sensitivity and faster response time, replacement of the current grating drive with a stepper motor, complete reconstruction of the gas manifold to reduce system leaks, and the replacement of the PDP-8E computer system with a Micromint for temperature control and an HP-PC for data acquisition. These changes will be performed as a cooperative venture between PSI, AFGL and Utah State University/Stewart Radiance Lab. The involved PSI personnel are the authors of this manual, and the AFGL and USU/SRL scientists are Dr. Steven Miller and Mr. Dale Sinclair, respectively. In view of these proposed changes, it should be recognized that several sections of this manual will be obsolete within a few years and extensive rewriting will be required to keep the manual up to date.

5. REFERENCES

1. Carrington and J.C. Polanyi, MTP International Review of Science, Physical Chemistry, Ser. 1, Vol. 9, J.C. Polany, Ed. (Butterworth, London, 1972), p. 135.

2. B.E. Holmes and D.W. Setser, "Energy Disposal in Unimolecular and Bimolecular Reactions," in Physical Chemistry of Fast Reactions, Vol. 3, I. W.M. Smoth, Ed. (Plenum, London, 1977).

3. J.G. Moehlmann, J.T. Gleaves, J.W. Hudgens, and J.D. McDonald, "Infrared Chemiluminescence Studies of the Reactions of Fluorine Atoms with Monosubstituted Ethylene Compounds," J. Chem. Phys. 60, 4790 (1974).

4. J.P. Sung, R.J. Malins, and D.W. Setser, "Comparison of Rate Constants for Reactions of Hydrogen Atoms with Chlorine, Fluorine, Iodine Chloride, and Chlorine Fluoride," J. Phys. Chem. 83, 1007 (1979).

5. B.M. Berquist, J.W. Bozzelli, L.S. Dzelzkalns, L.G. Piper, and F. Kaufman, "Vibrational Relaxation of Highly Excited Diatomics. I. Method, Analysis, and Application to HCl($v \leq 7$) + CO_2 and N_2O," J. Chem. Phys. 76, 2972 (1982).

6. D. Bogan and D.W. Setser, "Fluorine Containing Free Radicals, Kinetics, and Dynamics of Reactions," ACS Symp. Ser. 66 (1977).

7. W.T. Rawlins, H.C. Murphy, G.E. Caledonia, J.P. Kennealy, F.X. Robert, A. Corman, and R.A. Armstrong, "COCHISE: Laboratory Studies of Atmospheric Infrared Chemiluminescence in a Cryogenic Environment," Appl. Opt. 23, 3316 (1984).

8. J.P. Kennealy, F.P. DelGreco, G.E. Caledonia, and B.D. Green, "Nitric Oxide Chemiexcitation Occurring in the Reaction Between Metastable Nitrogen Atoms and Oxygen Molecules," Journal of Chemical Physics., 69 (4), 1574 (1978).

9. W.T. Rawlins, G.E. Caledonia, and J.P. Kennealy, "Observation of Spectrally Resolved IR Chemiluminescence from Vibrationally Excited $O_3(\nu_3)$," J. Geophys. Res. 86, 5247 (1981).

10. W.T. Rawlins and R.A. Armstrong, "COCHISE Observations of O_3 Formed by Three-Body Recombination of O and O_2," AFGL-TR-82-0273, Air Force Geophysics Laboratory, Hanscom AFB, MA (1982).

11. W.T. Rawlins, A. Gelb, and R.A. Armstrong, "Infrared Spectra (2 to 16 μm) of Ar(I) Rydberg Emission from a Microwave Discharge Plasma," J. Chem. Phys. 82, 681 (1985).

12. W.T. Rawlins, H.C. Murphy, and G.E. Caledonia, "Preliminary Observations of Molecular Fluorescence in COCHISE, 2-8 μm," Physical Sciences Inc., TR-414, Andover, MA (1984).

13. W.T. Rawlins and F. Kaufman, "The Reaction of CO_2 with Active Nitrogen," J. Chem. Phys. 64, 1128 (1976).

14. M.E. Fraser, H.C. Murphy, and W.T. Rawlins, "Dynamics of Atmospheric Infrared Thermochemical Excitation," Quarterly Status Report No. 3, PSI-031/TR-551, February 1986.

15. R.P. Wayne, "Singlet Oxygen Airglow," J. Photochem. 25, 345 (1984).

16. A.T. Stair, Jr., J. Pritchard, I. Coleman, C. Bohne, W. Williamson, J. Rogers, and W.T. Rawlins, "The Rocketborne Cryogenic (10 K) High Resolution Interferometer Spectrometer Flight-HIRIS: Atmospheric and Auroral Infrared Emission Spectra," Appl. Opt., 22, 1056 (1983).

17. W.T. Rawlins, G.E. Caledonia, J.J. Gibson, and A.T. Stair, Jr., "HIRIS Rocketborne Spectra of Infrared Fluorescence in the $O_3(\nu_3)$ Band near 100 km" J. Geophys. Res. 90, 2896 (1985).

18. W.T. Rawlins, "Chemistry of Vibrationally Excited Ozone in the Upper Atmosphere," J. Geophys. Res. 90, 12,283 (1985).

APPENDIX O

(SR-291 reproduced in its entirety)

J. Chem. Phys. 88, 538 (1988)

PSI-032/
SR-291

Infrared (2 to 8 μm) Fluorescence of the $W^3\Delta_u \rightarrow B^3\Pi_g$ and $w^1\Delta_u \rightarrow a^1\Pi_g$ Systems of Nitrogen

Mark E. Fraser and Wilson T. Rawlins

Physical Sciences Inc.

Research Park, P.O. Box 3100

Andover, MA 01810

and

Steven M. Miller

Infrared Technology Division

Air Force Geophysics Laboratory

Hanscom AFB, MA 01731

J. Chem. Phys. 88, 538 (1988)

ABSTRACT

Eleven transitions in the $W^3\Delta_u \rightarrow B^3\Pi_g$ (W-B) and $w^1\Delta_u \rightarrow a^1\Pi_g$ (w-a) systems of nitrogen have been observed in the infrared including the previously unobserved (1,0) and (2,1) W-B features at 6.5 and 7.65 μm, respectively. The fluorescence spectra were observed in a cryogenic reaction chamber at pressures of ~ 3 mtorr (0.4 Pa), following expansion of flowing N_2/Ar mixtures excited by microwave discharges at ~ 1 torr. Einstein coefficients for the w-a system, calculated using a published transition moment function, predict the radiative lifetimes of the lower vibrational levels of the $w^1\Delta_u$ state to be a factor of three longer than earlier estimates. Using a spectral simulation and linear least-squares fitting technique, the published W-B and calculated w-a branching ratios are verified for the transitions observed across the 2 to 4 μm region. The observed vibrational/electronic state distributions are not characteristic of those expected for direct excitation, but appear to result from extensive collisional coupling among excited states of nitrogen which occurs in the high pressure region prior to expansion.

Introduction

There are several nitrogen electronic transitions which give rise to emission in the 2 to 8 μm infrared region.[1-9] These systems include $W^3\Delta_u \rightarrow B^3\Pi_g$, $w^1\Delta_u \rightarrow a^1\Pi_g$, and $a^1\Pi_g \rightarrow a'^1\Sigma_u^-$. Emissions from the $B'^3\Sigma_u^- \rightarrow B^3\Pi_g$ and $B^3\Pi_g \rightarrow A^3\Sigma_u^+$ systems also extend into this spectral region. These systems are commonly observed in nitrogen discharge plasmas and several have been indicated as potential infrared auroral transitions.[10] The detailed excited state populations and vibrational distributions responsible for the observed fluorescence provide information on mechanisms of excitation and energy disposal in excited nitrogen. Interoretation of auroral or plasma spectra for these band systems, however, requires prior verification of the transition branching ratios. We report here observation of emission from several vibrational levels in $W^3\Delta_u \rightarrow B^3\Pi_g$ ($v' = 1$-5) and in $w^1\Delta_u \rightarrow a^1\Pi_g$ ($v' = 0$-2), and verification of their radiative branching ratios across the 2 to 4 μm region.

Experiments

These experiments were performed in the COCHISE (COld CHemiexcitation Infrared Stimulation Experiment) cryogenic discharge afterglow apparatus, which is described in detail elsewhere.[11] Excitation of nitrogen electronic states is produced in four parallel microwave discharges (2450 MHz, 50 W) of flowing N_2/Ar mixtures at ~ 1 torr total pressure. A diagram of the reaction chamber is shown in Figure 1. After exiting the discharge tubes the gas expands into a low pressure (~ 3 mtorr), cryogenically pumped chamber (~ 20 K) where the molecules enter the collimated field of view of a scanning monochromator/infrared detector assembly. Residence times in the discharge tubes are on the order of 3 to 5 ms; an average time of flight of 500 ± 100 μs is required for the gases to exit the discharge tubes and enter

the field of view. Opposing flows of argon are used to create a quasi-static interaction region along the centerline of the field of view, resulting in partial rethermalization of the expansion-cooled rotational distributions. The gas residence time in the field of view is ~ 0.3 ms. Gaseous helium refrigerant maintains all internal temperatures at 20 K, excepting the gas lines and optics which are held at 80 and 40 K, respectively.

The infrared emissions are observed by a cryogenic 0.5 m Czerny-Turner monochromator equipped with a liquid-helium-cooled arsenic doped silicon detector and a grating blazed at 3 μm. The discharges are chopped with a 23 Hz, 50 percent duty cycle square wave, and data collection is performed with a computer-interfaced lock-in amplifier. Data over the 2 to 4 μm region were taken with the phase shift between reference and signal waveforms locked in at the 3.3 or 3.6 μm features. The phase shift for the 4 to 8 μm spectra was locked at the emissions at 6.5 or 7.5 μm.

The absolute uncertainty in the wavelengths (due to monochromator drive error) of the spectral scans is ± 0.003 μm. The data were corrected for instrument responsivity using blackbody calibration spectra taken in the 300 to 370 K range. The uncertainty in the accuracy of the blackbody temperature is ± 3 K, which results in a relative uncertainty of ± 20 percent in the measured 2.5/5.0 μm intensity ratios. This method of calibration has been verified in studies of the fundamental/overtone ratios for NO(v) vibraluminescence.[12]

Spectra were taken for N_2/Ar mixtures with N_2 mole fractions of 0.006 to 0.12, with a mass-balanced counterflow of argon added to thermalize the observed emissions. Spectra were also taken without nitrogen to identify the background ArI Rydberg emission.[13] The data were taken typically at a resolution of 0.013 μm in the 2 to 4 μm region and 0.040 μm for the 4 to 8 μm region.

Spectral Analysis

The interpretation of the 2 to 4 μm discharged nitrogen data is complicated due to the coincidence of several of the $W^3\Delta_u \rightarrow B^3\Pi_g$ (W-B) and $w^1\Delta_u \rightarrow a^1\Pi_g$ (w-a) features. The transitions that are not distinguishable from each other at a resolution of 0.013 μm include the W-B (4,1) and w-a (2,1) at 2.4 μm, the W-B (3,1) and w-a (0,0) at 3.6 μm, and the W-B (4,2) and w-a (2,2) at 4.0 μm. These overlapping bands cannot be identified or quantified by inspection, therefore a spectral fitting technique is required.

The spectral analysis technique used for these studies has also been successfully applied to the analysis of $NO(A^2\Sigma)$,[14] N_2 electronic emission,[15] and $IF(B^3\Pi_{0+})$.[16] The synthetic spectra are generated by a computer code based upon the work of Kovacs[17] and implemented through major modification of a program written by Whiting, et al.[18,19] The program considers singlet-singlet, doublet-doublet, and triplet-triplet dipole transitions for diatomic molecules in the optically thin limit. Line-by-line transition frequencies are computed from energy eigenvalues determined by exact solution of the Schrödinger equation, where the matrix elements of the upper and lower state Hamiltonians are specified from tabulated spectroscopic constants. Following well-established procedures,[17,20] the eigenfunctions of the states are described as linear combinations of eigenfunctions of hypothetical pure Hund's case (a) eigenstates. The transition amplitudes are given by the transformation of the dipole moment function between the upper and lower states.[17,20] The computed infinite resolution emission spectrum is convolved with the instrument scan function (in this case, a symmetric triangle with full width at half maximum as the spectral resolution) to create basis sets for each vibrational level which are then fit to the experimental

spectrum using a linear least squares method. The fitting procedure yields a determination of the product of the upper state number density and the spontaneous emission coefficient of the transition. Rotational distributions are treated by simple Boltzmann expressions, so that band-integrated vibrational state number densities and transition probabilities may be used.

Lambda doubling, which is on the order of 1 cm^{-1} for the $W^3\Delta_u \rightarrow B^3\Pi_g$ system,[21] is not treated in this analysis. The $W^3\Delta_u \rightarrow B^3\Pi_g$ emission system totals 27 branches without lambda doubling. Furthermore, the coupling for the W state is close to Hund's case (b) while the B state coupling exhibits transition from (a) to (b) at higher rotational levels. Despite these complexities, comparison of the line positions of the synthesized $W^3\Delta_u \rightarrow B^3\Pi_g$ (2,0) feature to published high resolution data[21] indicates the positions of principal lines are reproduced to within 1 cm^{-1}. Similarly, the agreement between the synthesized and high resolution[22] $w^1\Delta_u \rightarrow a^1\Pi_g$ (0,0) transition is excellent, < 0.1 cm^{-1}. Since most of the data presented here have been taken and fit to a resolution of 0.013 μm (12 cm^{-1} at 3.3 μm), deficiencies in the spectral synthesis program on the order of 1 cm^{-1} or less are too small to be observed. The spectroscopic data sources for the considered N_2 states were Huber and Herzberg[23] and Roux[22] et al. for $w^1\Delta_u$ and $a^1\Pi_g$, Cerny[24] et al. for $W^3\Delta_u$ and Effantin[25] et al. for $B^3\Pi_g$.

Each vibrational transition is treated as an independent basis function in a linear least-squares fit to the total spectrum to determine the band-integrated intensities, $N_{v'}A_{v'v''}$. To determine the excited state number densities, accurate values for $A_{v'v''}$ are needed. The transition probabilities used for the W-B system are the ab initio values calculated by Werner et al.[26] and shown in Table 1. These values are more than a factor of two smaller

than the empirical estimates of Covey, Saum, and Benesch,[27] but exhibit essentially the same branching ratios; we prefer the results of Werner et al.[26] owing to their use of a more accurate transition moment function. There are no published transition probabilities for the $w^1\Delta_u \rightarrow a^1\Pi_g$ system. Consequently, we calculated them using the Franck-Condon and r-centroid data tabulated in Lofthus and Krupenie[28] and the transition moment function determined by Yeager and McKoy.[29] The results are shown in Table 2. The radiative lifetimes for the first five vibrational levels are predicted to be 1500, 830, 470, 430, and 360 μs, respectively, at variance with earlier estimates[28] of 500 to 100 μs. These radiative lifetimes are more than an order of magnitude longer than those used by Cartwright[10] for auroral modeling predictions.

Using the spectral synthesis linear least-squares fitting technique described above, eleven bands from the $N_2(W^3\Delta_u \rightarrow B^3\Pi_g)$ and $N_2(w^1\Delta_u \rightarrow a^1\Pi_g)$ systems have been identified. Inclusion of the $B^3\Pi_g \rightarrow A^3\Sigma_u^+$, $B'^3\Sigma_u^- \rightarrow B^3\Pi_g$, $a^1\Pi_g \rightarrow a'^1\Sigma_u^-$, and $B^3\Pi_g \rightarrow W^3\Delta_u$ systems of nitrogen in the fits indicated no evidence of emission from these systems in the observed spectra. This is consistent with the rapid radiative decay expected for the $N_2(B,B',a)$ states in transit from the discharge exits to the field of view.

The rotational temperatures, T_r, used in the fits were determined empirically by comparison of intensity distributions and branch structures of the data with theoretical spectra. The (2,0) band was used for the W-B system with the result T_r = 100 K, indicating this emission system is nearly rotationally thermalized. With the rotational temperatures of the W-B system fixed at 100 K, simultaneous W-B and w-a fits were used to determine the rotational temperature for the w-a system. The optimal T_r was chosen as that which best reproduced the intensity distribution of the first two branches of

the 3.6 μm emission feature which corresponds, in large part, to the R and Q branches of the w-a (0,0) emission. The result for w-a was T_r = 300 K, although 200 K produced better fits in some data taken at low nitrogen mole fraction. The deviation in the calculated populations incurred using w-a basis sets with T_r = 200 K versus T_r = 300 K is <10 percent in the w-a populations and <5 percent in the W-B populations.

Results

Identification of the observed spectral features was facilitated by a variation of the relative W-B and w-a intensities as a function of nitrogen mole fraction. At low nitrogen mole fraction the w-a features are more prominent allowing unambiguous identification. Under these conditions the dominant spectral feature at 3.6 μm is the (0,0) w-a transition. Figure 2 shows the data and best fit to the 3.5 to 3.9 μm region of data obtained at a nitrogen mole fraction of 1.2×10^{-2}. The figure also shows the contributions to the fit from each of the w-a and W-B basis sets. The best fit was obtained for a w-a basis set with T_r = 200 K. At higher nitrogen mole fractions the W-B features predominate, in particular the (2,0) feature at 3.3 μm. Figure 3 shows data taken at high nitrogen mole fraction and fit to both W-B and w-a systems over the full 2 to 4 μm region. Six transitions in the W-B system are identified, three from the $\Delta v = 3$ series and three from the $\Delta v = 2$ series. The W-B (5,3) band at 4.5 μm cannot be distinguished from the noise level, in keeping with its small transition probability relative to that for the (5,2) band (cf. Table 1). No W-B emission from vibrational levels higher than $v' = 5$ is observed under any nitrogen mole fraction condition. Five transitions in the w-a system are also identified, the (1,0) and (2,1) bands in the $\Delta v = 1$ sequence and the (0,0), (1,1), and (2,2) bands in the $\Delta v = 0$ sequence.

No clearly identifiable emission from v' = 3 in the w-a system is observed. All additional features in Figure 3 are due to ArI Rydberg emission, which appears as scattered light from the discharges. We have reported on these emissions previously.[13]

Spectra taken of discharged nitrogen in the 6 to 8 μm region also show evidence of W-B features. Fits to the data provide unambiguous identification of the previously unobserved (1,0) and (2,1) transitions at 6.2 to 6.8 μm and 7.4 to 8 μm, respectively. Figures 4a and 4b show data and fit to the W-B (1,0) and (2,1) W-B features respectively. The W-B (2,1) feature is the only emission observed with this apparatus in the 7 to 8 μm wavelength range.

Figure 5 shows the determined populations in the v' = 3 level of the $W^3\Delta_u$ state and v' = 0 of the $w^1\Delta_u$ state as a function of nitrogen mole fraction. The W-B and w-a emission systems coexist in the effluent of a microwave discharge under all nitrogen mole fraction conditions. Both systems exhibit similar kinetic behavior except at N_2 mole fractions in excess of 10 percent. Under these conditions the $w^1\Delta_u$ (v' = 0) population drops off more rapidly than the $W^3\Delta_u$ (v' = 3). The W-B (2,0) feature exhibits dissimilar and variable temporal behavior as measured by phasing relative to the other W-B, w-a emission features as a function of nitrogen mole fraction. The W-B (2,0) feature is in phase only at the higher nitrogen mole fractions. At the lower N_2 mole fractions, the phase lag of the (2,0) band is on the order of π (22 ms), corresponding to cessation of the discharge pulse. Since the radiative lifetime of the $W^3\Delta_u$ (v' = 2) level is short (1200 μs) compared to the modulation frequency (23 Hz), and is comparable to the radiative lifetimes of other observed states which exhibit no phase lags, radiative decay effects have been ruled out as the cause. Investigations of the (1,0) and (2,1) W-B bands also

indicate variable phasing between these emissions. These two emissions are in phase with each other only at low nitrogen mole fractions. No phase shift effects are encountered with the w-a emissions or with the W-B ($v' > 3$) bands.

The relative population distributions for the vibrational levels of the $W^3\Delta_u$ and $w^1\Delta_u$ states are shown in Figures 6a and 6b, respectively. Also shown in Figures 6a and 6b are the distributions back-corrected for the 500 μs radiative decay which is incurred during transit from the end of the discharge tubes to the field of view. In the absence of collisional feed sources in the reaction cell, the corrected distributions are those which would exist at the discharge exits. Both $W^3\Delta_u$ and $w^1\Delta_u$ states exhibit strongly relaxed distributions, with the maximum population occurring at the lowest vibrational levels. Also shown in Figures 6a and 6b are the determined upper limit relative populations for $W^3\Delta_u$ ($v' = 6$) and $w^1\Delta_u$ ($v' = 3$). The value for $W^3\Delta_u$ ($v' = 6$) corresponds to the noise level of the data. The w-a (3,2) band corresponds to a distinguishable feature which lies at 2.5 μm, but the observed intensity appears to be principally attributable to a coincident ArI Rydberg line.[13] (The w-a (3,3) band at 4.2 μm is not observable owing to its very small relative transition probability (cf. Table 2)).

Emission from $v' > 1$ levels in the $N_2(a^1\Pi_g \rightarrow a'^1\Sigma_u^-)$ system also occurs in the 2 to 4 μm region. Owing to the short radiative lifetime of the $a^1\Pi_g$ state (~100 μs), observation of this band system in the field of view due to discharge excitation is unlikely. Fits to the data of the a-a' ($v' = 1$-3) features indicate none of these features are distinguishable from the noise level in the data, with determined upper limit populations of $< 2 \times 10^6$ cm^{-3}. This is consistent with the anticipated production of $N_2(a, v' > 1)$ in the field of view by the observed w-a radiative cascade. Similarly, the absence

of identifiable emission in the $B'\Sigma_u^- \rightarrow B^3\Pi_g$ system gives an upper bound of $\sim 10^6$ cm^{-3} for the $N_2(B')$ number density in the field of view.

Discussion

In comparison of the data and the predictions of the spectral synthesis code, we observe only minor disagreements in spectral position and branch intensity distribution. Discrepancies in the reproduction of the branch head positions are within the spectrometer drive error of 0.003 μm. Failure to exactly match the relative branch intensities within a given band may be partially due to non-Boltzmann rotational temperature distributions. Assumption of a single Boltzmann distribution may also cause discrepancies in the detailed reproduction of the relative branch intensities. The magnitude of these discrepancies is small, and at low resolution ($\delta\lambda > 0.013$ μm) the band shapes and integrated intensities are relatively well reproduced. Because the w-a and W-B systems can be discriminated at different nitrogen mole fractions, the fits confirm the (3,0)/(3,1), (4,1)/(4,2) W-B and (1,0)/(1,1), (2,1)/(2,2) w-a branching ratios, obtained from Tables 1 and 2, to ± 20 percent.

The observed vibrational and electronic state distributions are quite different from those one might expect for discharge-flow excitation under the conditions of these experiments. Typically, at low N_2 mole fractions, the residence time in the active discharge plasma (~ 2800 cm/s at 1.4 torr in each tube) is 3 to 5 ms, with the discharge region extending essentially to the end of the tube. For N_2 mole fractions near 0.1, the discharge region "shrinks" to about 2 ms, allowing 1 to 2 ms of flow time downstream of the dosed volume prior to expansion into the observation volume. For typical conditions of this type of discharge ($[e^-] \sim 10^{11}$ cm^{-3}, $E/N \sim 10^{-16}$ V cm^2, characteristic electron energy ~ 6 to 8 eV), we expect the principal excitation mechanism for

$N_2(W,w)$ to be via direct electron impact on ground state nitrogen. This production term would be balanced by losses due to electron impact processes (dissociation, superelastic de-excitation), collisional deactivation, radiative loss, and flow out of the discharge.[30]

For the discharge conditions used in these studies, the dominant loss terms are dissociation, surface quenching, and flow, which should not affect the vibrational/ electronic state distribution formed in the excitation process. Since electron impact excitation gives rise to Franck-Condon vibrational distributions relative to ground state nitrogen, we would expect to observe significant fluorescence from higher vibrational levels ($v' = 4$-9) of the W and w states, with a preponderance of the triplet over the singlet, qualitatively similar to the state distributions predicted by Cartwright[10] for an aurora. In contrast, however, we observe relatively "cold" vibrational distributions with roughly equal populations in the triplet and singlet states, despite their 1.5 eV energy difference. These observations suggest that there are rapid collisional "scrambling" reactions occurring in the discharge which can significantly alter the excited state population distributions. A possible example of such a reaction would be the enhancement of the lower levels of the W state by fast reaction of nitrogen atoms with singlet metastables:

$$N(^4S) + N_2(a'^1\Sigma_u^-) \rightarrow N_2(W^3\Delta_u,\ v \leq 5) + N(^4S) \quad .$$

Similar rapid intersystem crossings may occur through collisions of excited N_2^* with N_2 and Ar. Indeed, previous observations of fluorescence from $N_2(B^3\Pi_g)$ excited by an electron beam gave evidence of strong collisional coupling between the neighboring vibrational levels of the B and W states.[31]

The excitation mechanism for $N_2(w)$ is less apparent owing to its high energy relative to the neighboring states of N_2^*. The non-thermal rotational distributions we observe for the w→a transitions suggest formation of $N_2(w)$ by a reactive collision, although direct energy transfer to N_2 cannot be ruled out. In the latter case, however, the precursor states would have to be medium to high vibrational levels of one or more of the neighboring N_2^* electronic states. An intriguing possibility is excitation of $N_2(w)$ via metastable-metastable interactions, e.g., $N_2^* + N_2^*$ or $N^* + N_2^*$; precursor number densities on the order of 10^{12} cm^{-3} (in the active discharge at 10^{17} cm^{-3} total number density) and a near gas-kinetic rate coefficient would be sufficient to account for the quantity of $N_2(w)$ observed in the field of view.

The large phase lag between $N_2(W, v' = 1,2)$ and the remainder of the excited N_2 states is difficult to understand. Evidently these states are not formed as rapidly (and/or are destroyed more rapidly) in the active discharge as $W(v' = 3\text{-}5)$ and $w(v' = 0\text{-}2)$, but are rapidly formed by collisional energy transfer following cessation of the discharge. This could occur through a relatively inefficient process such as energy transfer with N_2, such that at lower N_2 mole fractions a substantial amount of $N_2(W, v=1,2)$ cannot be formed until after the precursor and $N_2(W)$ loss processes in the active discharge are terminated. The precursor may then be a sufficiently energetic afterglow species such as $N_2(A, v>9)$ or $N_2(X, v>33)$.

The collissional processes for energy redistribution among the states of N_2^* implied by these data must occur with relatively high efficiency, with collision efficiencies ranging from near unity for atom-metastable and metastable-metastable reactions to perhaps 1 percent for collisions with

$N_2(X, v=0)$. Such processes will clearly affect the energy flow in N_2 plasma systems at pressures of a few torr or greater. Furthermore, some of the collisional energy shuffling reactions may be fast enough to affect N_2^* state distributions in the auroral upper atmosphere, particularly in the 80 to 100 km altitude regime where collisional quenching competes with radiative deactivation of excited species. This possibility could be tested by observations of altitude-dependent $N_2(W,w)$ fluorescence in a strong aurora and comparison of the observed vibrational/electronic distributions with those expected for direct auroral excitation.

Conclusions

We have observed infrared (2 to 8 μm) fluorescence from nitrogen in the $\Delta v = 0$ and 1 progressions of the $w^1\Delta_u \rightarrow a^1\Pi_g$ band system and in the $\Delta v = 1$, 2, and 3 progressions of the $W^3\Delta_u \rightarrow B^3\Pi_g$ band system resulting from microwave discharge excitation of N_2/Ar mixtures. Using a spectral synthesis procedure with literature values for the spectroscopic constants provides adequate description of the observed spectra for spectral resolutions with full width at half maximum greater than or equal to 0.007 μm (6.4 cm^{-1} at 3.3 μm). Experimental observations of relative intensities of different transitions arising from a common upper state support the theoretical predictions for the dipole moment functions of Werner[26] for W-B and Yeager and McKoy[29] for the w-a system. We report w-a Einstein coefficients calculated from the data given in Ref. 29; these values differ markedly from those used by Cartwright[10] in his estimation of the relative $N_2(w^1\Delta_u)$ auroral number densities. Recalculation with the new w-a Einstein coefficients leads to an increase in the predicted high-altitude $N_2(w^1\Delta_u)$ relative number density by an order of magnitude.

The identification of the (1,0) and (2,1) W-B bands represents the first time these bands have been experimentally observed. The observed W-B and w-a vibrational distributions provide evidence of complex collisional coupling of the discharge-excited states of N_2, in particular a collisional feed of $W^3\Delta_u$. More detailed time-resolved kinetic studies will be required to resolve this issue.

Acknowledgments

The authors would like to acknowledge advice provided by W.J. Marinelli, L.G. Piper, B.D. Green, and assistance by H.C. Murphy, M.A. DeFaccio, and M. Clawson. The spectral generation code was developed at PSI in large part by P.F. Lewis. This work was performed under Contract F19628-85-C-0032 with the Air Force Geophysics Laboratory, and was sponsored by the U.S. Air Force Office of Scientific Research under Task 2310G4 and by the Defense Nuclear Agency under Project 5A, Task 5A, Work Unit 115.

References

1. R.A. McFarlane, IEEE J. Quantum Electronics QE-2, 229 (1966).
2. H.L. Wu and W. Benesch, Phys. Rev. 172, 31 (1968).
3. W.M. Benesch and K.A. Saum, J. Quant. Spectrosc. Radiat. Transfer 12, 1129 (1972).
4. R.A. McFarlane, Phys. Rev., 140, A1070 (1965).
5. R.A. McFarlane, Phys. Rev., 146, 37 (1966).
6. K.A. Saum and W.M. Benesch, Applied Optics, 9, 195 (1975).
7. E.M. Gartner and B.A. Thrush, Proc. R. Soc. Lond. A 346, 103, (1975).
8. H. Sakai, P. Hansen, M. Esplin, R. Johansson, M. Peltola, and J. Strong, Applied Optics, 21, 228 (1982).
9. W.M. Benesch, J. Chem. Phys., 78, 2978 (1983).

10. D. Cartwright, J. Geophys. Res., 83, 517 (1978).

11. W.T. Rawlins, H.C. Murphy, G.E. Caledonia, J.P. Kennealy, F.X. Robert, A. Corman, and R.A. Armstrong, Applied Optics, 23, 3316 (1984).

12. W.T. Rawlins, M.E. Fraser, and S.M. Miller, "Infrared Branching Ratios for the Fundamental and First Overtone Vibrational Transitions of NO($X^2\Pi$, $v \leq 12$)," manuscript in preparation.

13. W.T. Rawlins, A. Gelb, amd R.A. Armstrong, J. Chem. Phys., 82, 681 (1985).

14. L.G. Piper and L.M. Cowles, J. Chem. Phys., 85, 2419 (1986).

15. L.G. Piper, L.M. Cowles, and W.T. Rawlins, J. Chem. Phys., 85, 3369 (1986).

16. L.G. Piper, W.J. Marinelli, W.T. Rawlins, and B.D. Green, J. Chem. Phys., 83, 5602 (1985).

17. I. Kovacs, "Rotational Structure in the Spectra of Diatomic Molecules," Adam Hilger Ltd., London, (1969).

18. J.O. Arnold, E.E. Whiting, and G.C. Lyle, J. Quantum Spec. Radiat. Transfer, 9, 775 (1969).

19. E.E. Whiting, J.O. Arnold, and G.C. Lyle, NASA TN-D5088, NASA/Ames, Distributed as Cosmic Program #ARC-10221.

20. J.T. Hougen, "The Calculation of Rotational Energy Levels and Rotational Line Intensities in Diatomic Molecules," NBS Monograph 115, National Bureau of Standards, Washington, DC, June 1970.

21. C. Effantin, J. D'Incan, and R. Bacis, J. Mol. Spec., 76, 204 (1979).

22. F. Roux, C. Effantin, and J. D'Incan, J. Mol. Spec., 91, 238 (1982).

23. K.P. Huber and G. Herzberg, Molecular Spectra and Molecular Structure. IV. Constants of Diatomic Molecules, Van Nostrand, New York, (1979).

24. D. Cerny, F. Roux, C. Effantin, J. D'Incan, and J. Verges, J. Mol. Spec., 81, 216 (1980).

25. C. Effantin, C. Amiot, and J. Verges, J. Mol. Spec., 76, 221 (1979).

26. H.J. Werner, J. Kalcher, and E.A. Reinsch, J. Chem. Phys., 81, 2420 (1984).

27. R. Covey, K.A. Saum, and W. Benesch, J. Opt. Soc. Amer., 63, 592 (1973).

28. A. Lofthus and P.H. Krupenie, J. Phys. Chem. Ref. Data, 6, 117 (1977).

29. D.L. Yeager and V. McKoy, J. Chem. Phys., 67, 2473 (1977).

30. G.E. Caledonia, S.J. Davis, B.D. Green, L.G. Piper, W.T. Rawlins, G.A. Simons, and G. Weyl, "Analysis of Metastable State Production and Energy Transfer," AFWAL-TR-86-2078, Air Force Wright Aeronautical Laboratories, Wright Patterson AFB, OH 45433-6563.

31. B.D. Green, W.J. Marinelli, L.G. Piper, and W.A.M. Blumberg, "Excitation and Quenching of the Vibrationally Excited $N_2(B^3\Pi_g)$ State in Electron Irradiated Nitrogen," manuscript in preparation.

Table 1. Einstein coefficients for the $W^3\Delta_u \rightarrow B^3\Pi_g$ transitions (in 10^3 s^{-1}) as calculated by Werner et al.[26]

v'/v"	0	1	2	3	4	5	6
0	0.000						
1	0.221						
2	0.735	0.084					
3	0.868	0.764	0.014				
4	0.649	1.525	0.457	0.000			
5	0.377	1.619	1.554	0.183	0.000		
6	0.187	1.222	2.311	1.157	0.043	0.000	

Table 2. Computed Einstein coefficients for the $w^1\Delta_u \rightarrow a^1\Pi_g$ transitions (in 10^3 s^{-1})

v'/v"	0	1	2	3	4	5	6
0	0.636	0.013					
1	0.979	0.206	0.013				
2	0.660	1.03	0.444	0.010			
3	0.308	1.199	0.767	0.002	0.006		
4	0.117	0.797	1.415	0.466	0.004	0.004	
5	0.040	0.394	1.284	1.362	0.237	0.017	0.002
6	0.013	0.164	0.800	1.600	1.13	0.095	0.028

Figure Captions

Figure 1. Diagram of the COCHISE reaction chamber. The physical dimensions of the cell are 0.6 m in length and 0.4 m in diameter.

Figure 2. Data (light line) and best fit (dark line) (a) to the (0,0) and (1,1) $N_2(w^1\Delta_u \rightarrow a^1\Pi_g)$ and (3,1) $N_2(W^3\Delta_u \rightarrow B^3\Pi_g)$ emission systems at rotational temperatures of 200 and 100 K, respectively. The spectrum was obtained at a discharge nitrogen mole fraction of 1.2×10^{-2} and a resolution of 0.0067 μm. The maximum intensity of the spectrum is 3.45×10^{-7} W cm^{-2} sr^{-1} μm^{-1}. The w-a and W-B basis sets which comprise the best fit in (a) are shown in (b) and (c), respectively.

Figure 3. Data (light line, shown with the best fit and separately above) and best fit (dark line) to the indicated $N_2(w^1\Delta_u \rightarrow a^1\Pi_g)$ and $N_2(W^3\Delta_u \rightarrow B^3\Pi_g)$ emission systems at rotational temperatures of 300 and 100 K, respectively, and at a spectral resolution of 0.013 μm. The spectrum was obtained at a discharge nitrogen mole fraction of 9.1×10^{-2}. The maximum intensity of the spectrum is 3.4×10^{-7} W cm^{-2} sr^{-1} μm^{-1}. The observed features not accounted by the fit are due to ArI Rydberg emission.[12]

Figure 4. Data (light line) and best fit (dark line) to the $N_2(W^3\Delta_u \rightarrow B^3\Pi_g)$ $\Delta v = 1$ transitions. Shown in (a) is the (1,0) band fit at a rotational temperature of 100 K. The spectrum was taken at a nitrogen mole fraction of 7.4×10^{-2} and has a maximum intensity of 2.6×10^{-10} W cm^{-2} sr^{-1} μm^{-1}. Shown in (b) is the the (2,1) band fit at a rotational temperature of 120 K. The spectrum was taken at a nitrogen mole fraction of 1.2×10^{-1} and has a maximum intensity of 3.6×10^{-10} W cm^{-2} sr^{-1} μm^{-1}.

Figure 5. Determined populations for $W^3\Delta_u$ ($v' = 3$) (●) and $w^1\Delta_u$ ($v' = 0$) (o) versus discharge nitrogen mole fraction. Absolute number densities pertain to the 3 mtorr interaction region in the center of the reaction volume.

Figure 6. a) Relative vibrational population distribution for $W^3\Delta_u$ at a discharge nitrogen mole fraction of 1.2×10^{-1} (●) normalized to $v' = 2$. Also shown are the data back-corrected for a 500 μs radiative decay (o). b) Relative vibrational population distribution for $w^1\Delta_u$ at a discharge nitrogen mole fraction of 1.2×10^{-1} (●) normalized to $v' = 0$. Also shown are the data back-corrected for a 500 μs radiative decay (o).

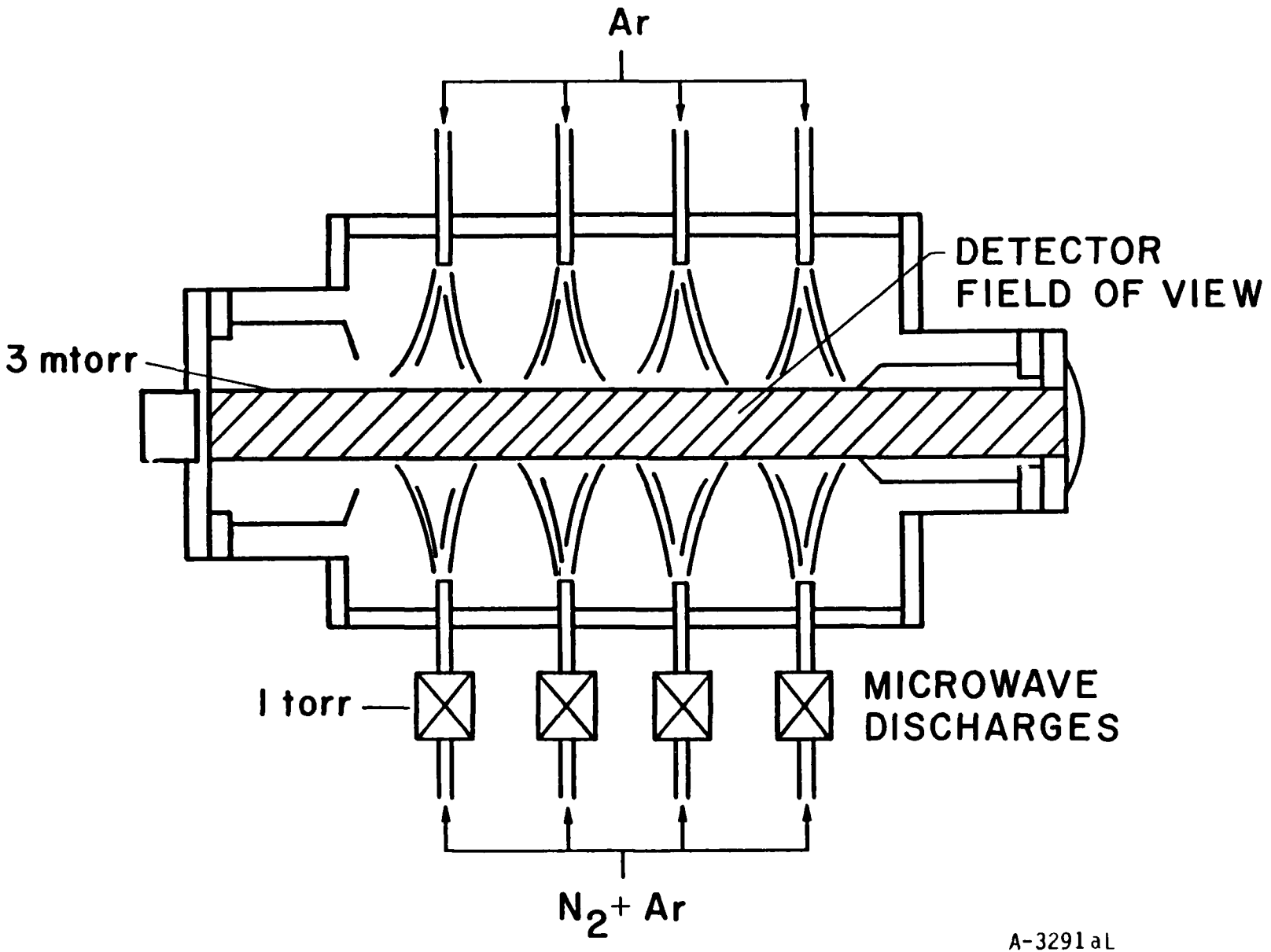
Ar
DETECTOR
FIELD OF VIEW
3 mtorr
1 torr
MICROWAVE
DISCHARGES
N_2+ Ar
A-3291aL

FIGURE 1

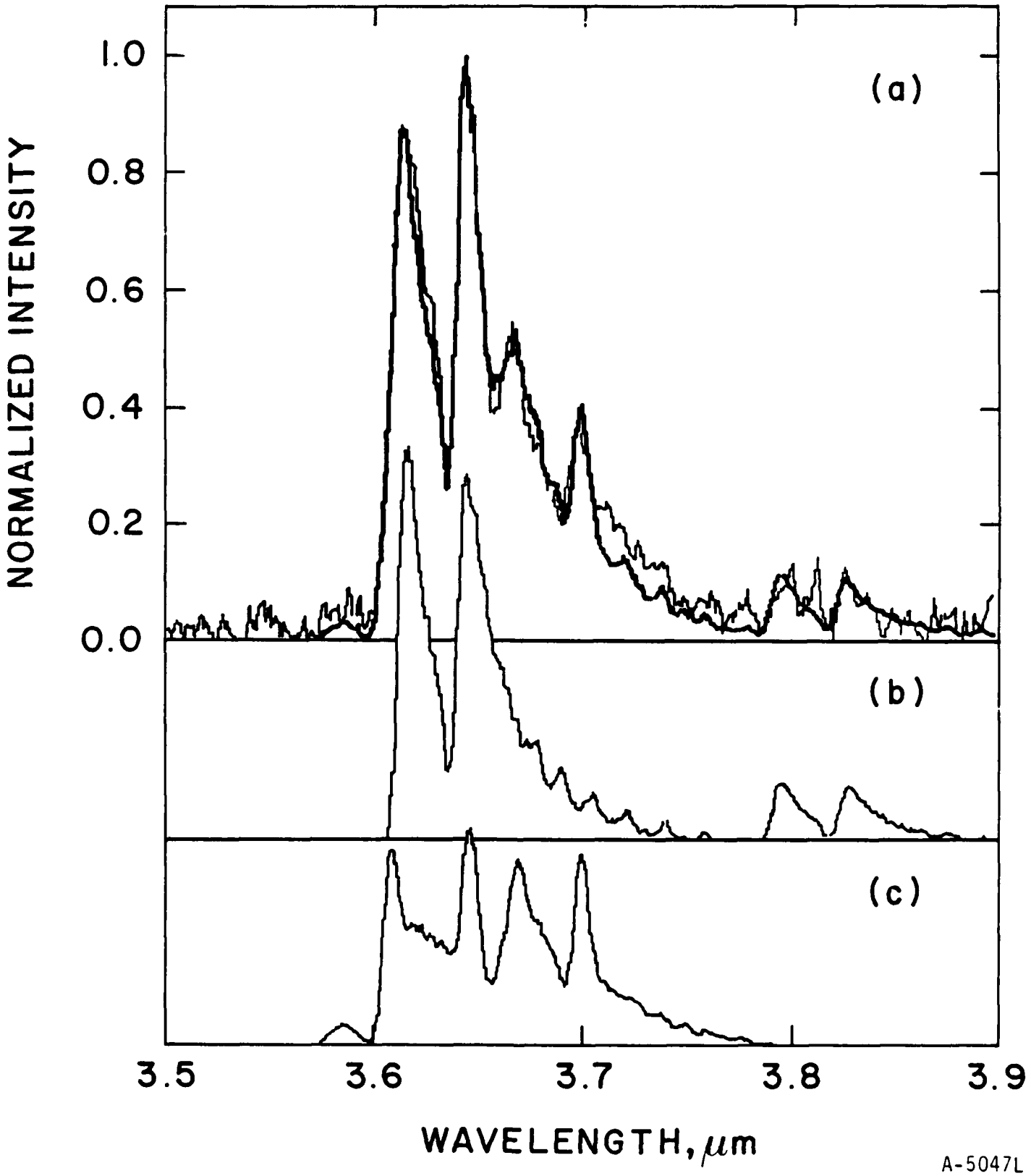
NORMALIZED INTENSITY
1.0
0.8
0.6
0.4
0.2
0.0
(a)
(b)
(c)
3.5
3.6
3.7
3.8
3.9
WAVELENGTH, μm
A-5047L

FIGURE 2

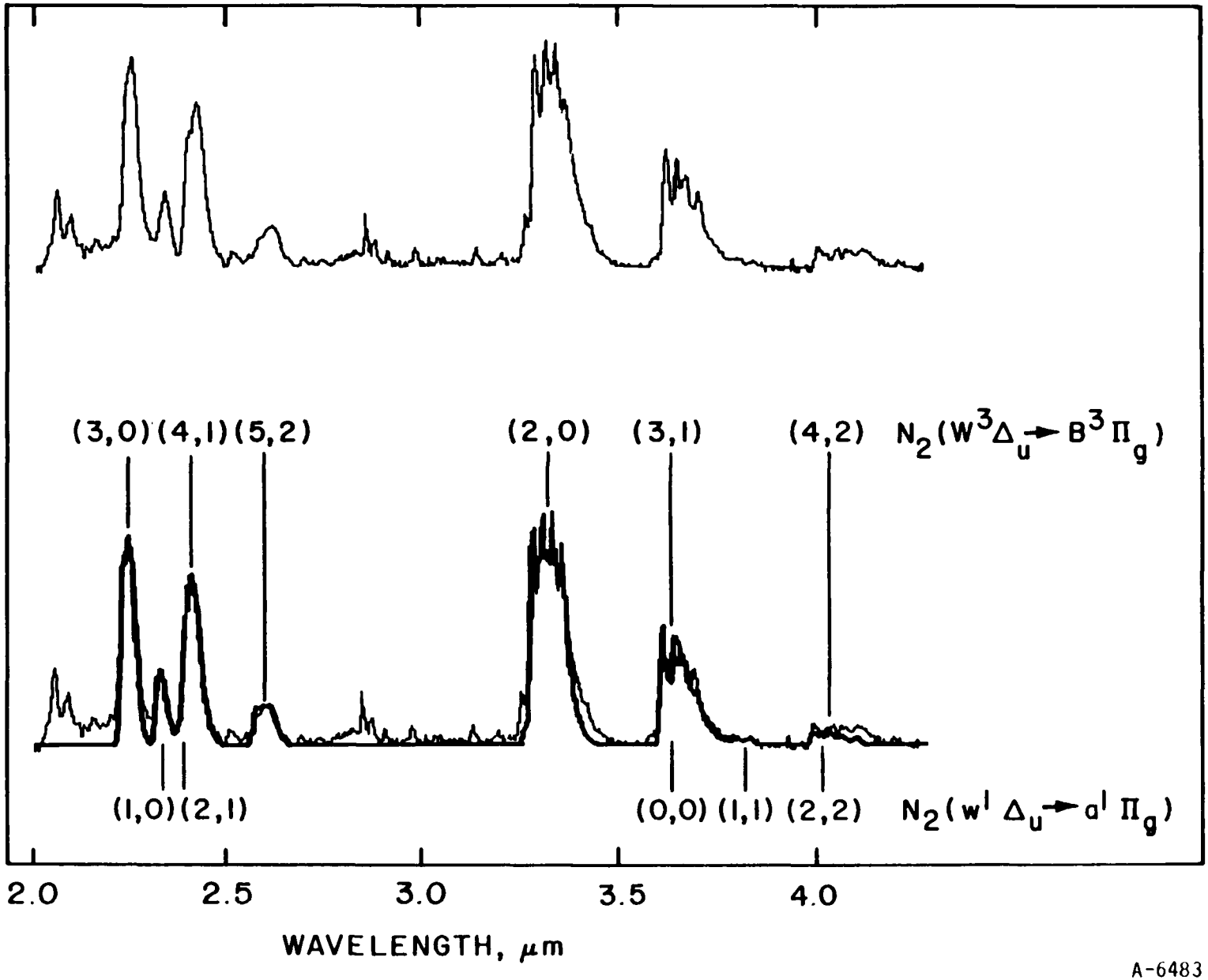

A-6483

FIGURE 3

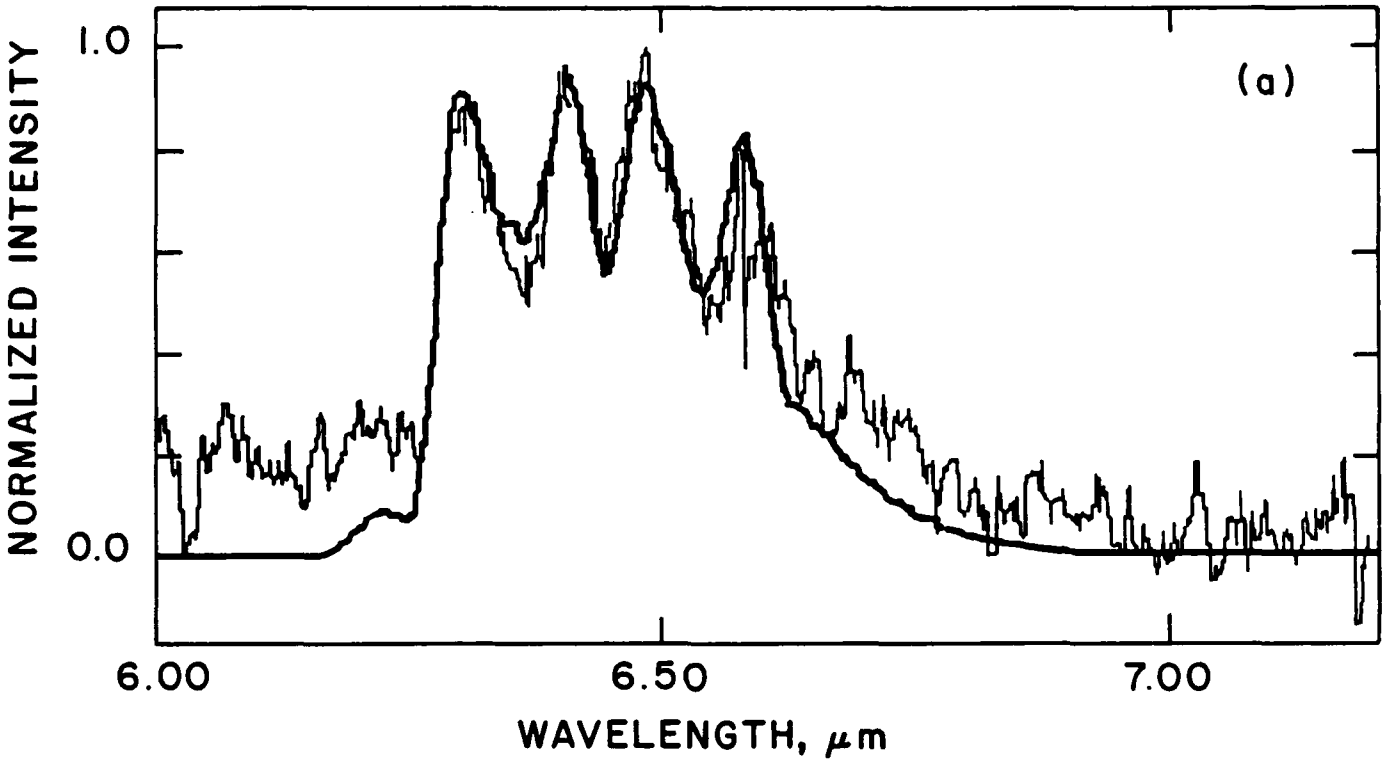

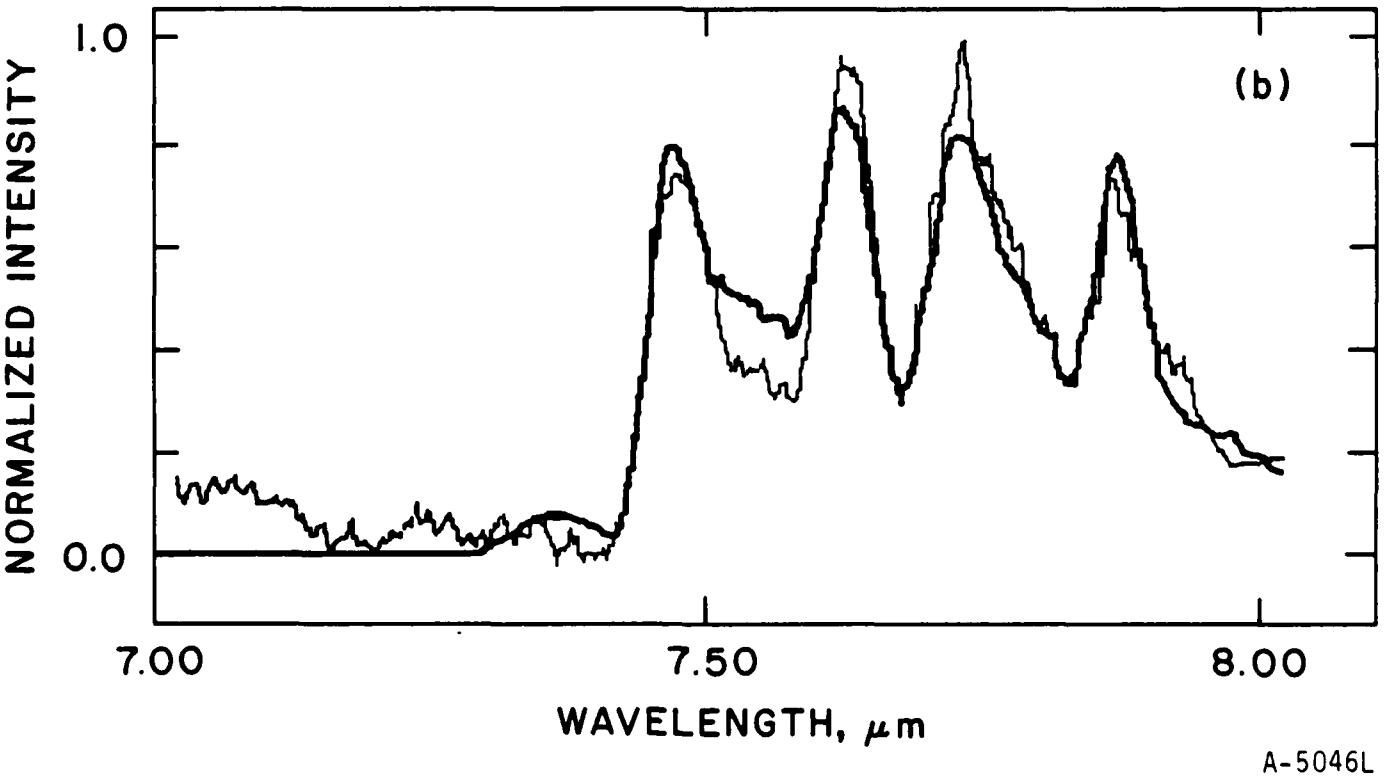

A-5046L

FIGURE 4

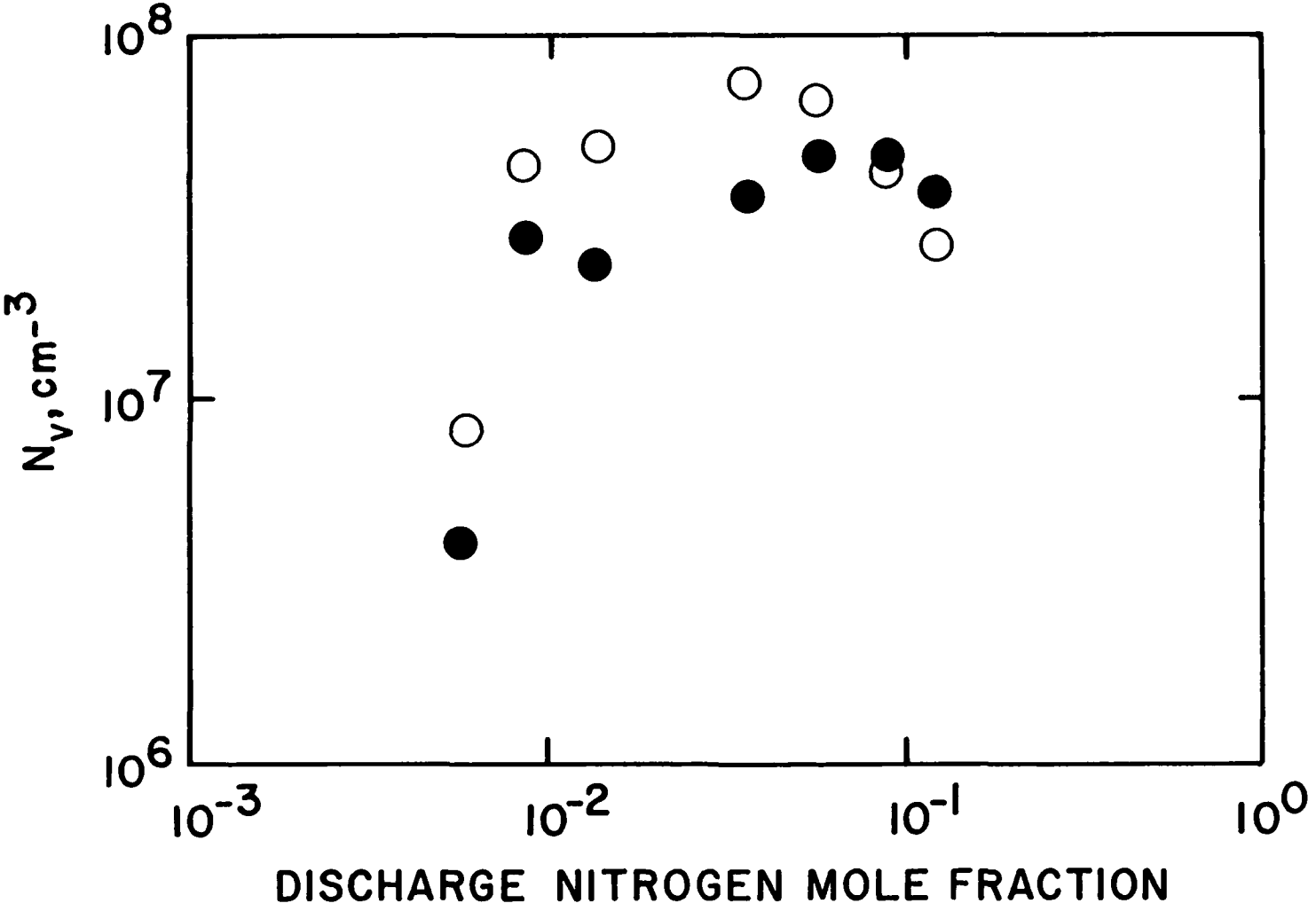

A-4412aL

FIGURE 5

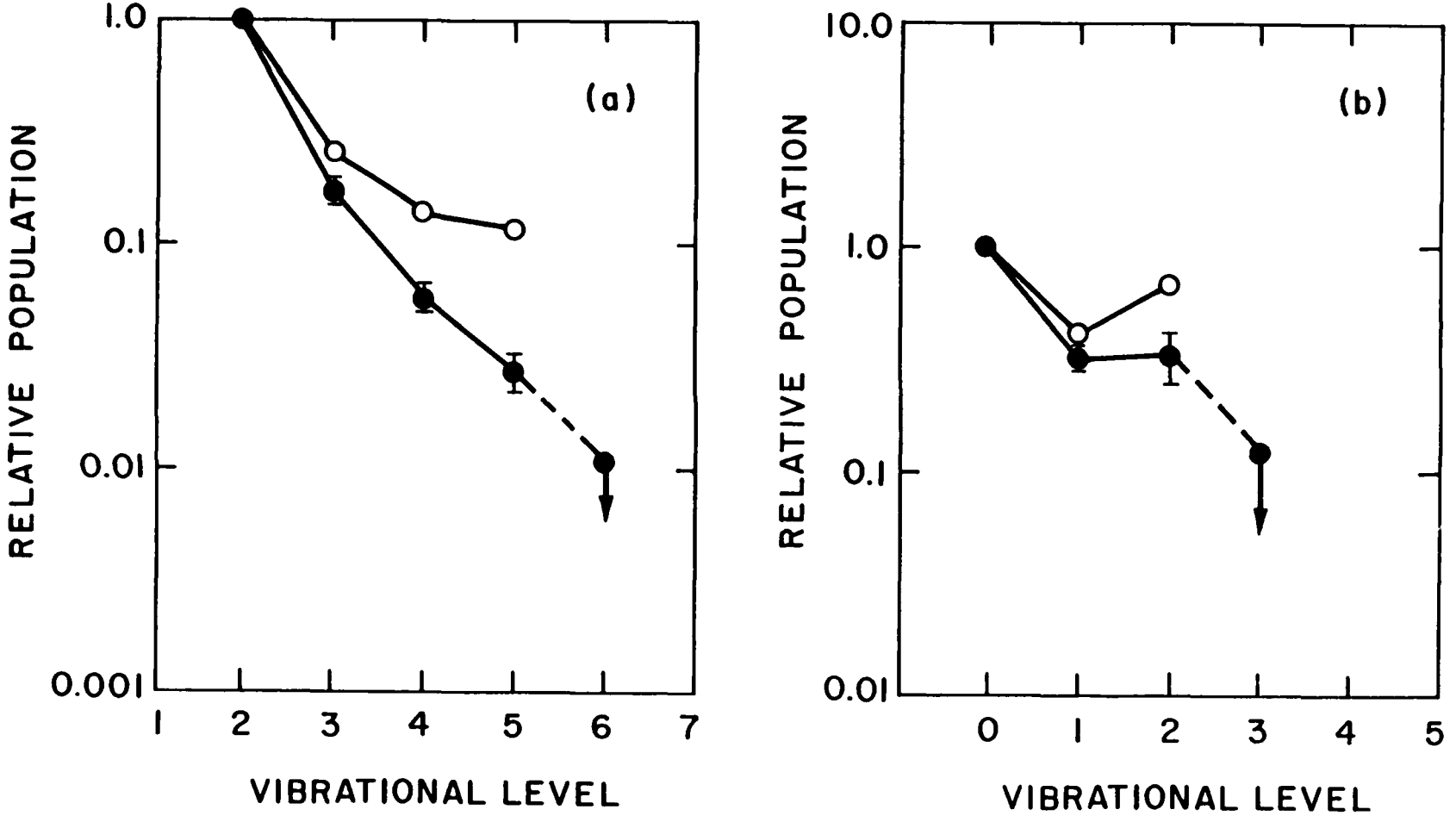

FIGURE 6

A-5426